UNIVERSITÀ DI PISA

DIPARTIMENTO DI INGEGNERIA CHIMICA
CHIMICA INDUSTRIALE E SCIENZA DEI MATERIALI

Ph.D. Thesis

Filler Toughening of Plastics:

Study of the Deformation Mechanism

XUETAO SHI

Supervisor:

Prof. Andrea Lazzeri

Ph.D. candidate in

Ingegneria "Leonardo da Vinci" - Ingegneria chimica e dei materiali

(SSD ING-IND/22)

XXIII cycle

2008-2010

Abstract

Precipitated calcium carbonate nanoparticles (PCC), surface treated with stearin in aqueous medium, were investigated in this thesis as rigid fillers for polymer toughening. The surface characterization of a series of PCC coated with different stearin amount indicated the presence of two different types of calcium alkanoate layers on the surface. One is the chemisorbed monolayer (CSM) bonded to the active sites of PCC surface with a maximum coverage degree of around 72%. The other one is constituted by the physisorbed calcium alkanoate multilayers linked to the CSM by weak intermolecular forces. The micelle adsorption mechanism has been proposed to be the dominating process due to the limited solubility of stearin in water, compared to the coating process in solvent where a full monolayer can be achieved.

The calcium alkanoate molecules, present on the PCC surface as physisorbed multilayers, have been shown to have a complicated thermal behavior. The drying process for PCC particles resulted in molecular rearrangement from the monohydrate α phase to the anhydrous β′ phase. Molecular polymorphism and orientation of calcium alkanoate on the PCC surface are strongly connected with the surface free energy of the coated particles. The coated PCC particles showed a continuously decreasing surface free energy, both for the dispersion and specific components, with an increase in the amount of surface coating. Based on the investigation of the thermal transition and the determination of surface layer thickness, a molecular arrangement model has been proposed suggesting that the CSM is vertical to the PCC surface linked tail-to-tail with the physisorbed multilayers with alkyl chains oriented outwards.

This series of coated PCC nanoparticles were then applied to high-density polyethylene (HDPE) and polylactic acid (PLA) as toughening fillers. The HDPE/PCC nanocomposites achieved the expected balance between the stiffness and toughness. In fact, the yield stress showed a slightly decreasing trend while the impact strength showed a increasing tendency when the surface coating amount on the PCC surface increased. Those mechanical properties were related to the micromorphology and also to the interfacial adhesion between PCC particles and HDPE polymer matrix, which on the other hand connected to the dependence of the surface free energy from the surface coating amount of PCC fillers.

PLA/PCC nanocomposites showed a notable improvement of the elongation-at-break and toughness compared to that of pure PLA. This result can be attributed to both the weaker interfacial adhesion facilitating the debonding process and the plasticizing effect of calcium alkanoate which enhance the deformability of PLA nanocomposites. In fact, the thermal behavior study elucidated that PCC particles acted as nucleating agents for PLA, decreasing the crystallization half-time and the cold crystallization temperature of PLA composites. Also the plasticizing effect of the calcium alkanoate coated PCC nanoparticles was confirmed by the decreased glass transition temperature for PLA/PCC nanocomposites.

Contents

Chapter 1 Introduction

Toughness is a highly desired property for both commodity and engineering polymers. Toughness in most polymer systems depends on the mechanisms promoting energy dissipative processes that delay the fracture process initiated by material flaws or notches. There are several methods for developing the toughness in the brittle polymers, but the most successful is rubber toughening [1-5]. Particulate-filled polymer systems with several types of minerals have been used very early in the history of plastics in many industrial applications due to their low cost and easy processability. In the last two decades, rigid filled polymers have received increasing attention due to the reported improvement in both toughness and stiffness [6-12]. Among rigid fillers, calcium carbonate is the most widely used inorganic rigid filler because of its availability and low cost. At the industrial level, calcium carbonate particles are obtained by milling or quarrying mineral calcite. Alternatively, calcium carbonate can be prepared through the carbonation of a solution of calcium hydroxide, obtained from the calcination of a calcium carbonate containing mineral. The resulting calcium oxide is reacted with water before the carbonation step. In this case, the product obtained is known as the precipitated calcium carbonate. However, particulate filled polymers show some improved properties while some others deteriorate, mainly as a consequence of aggregation causing material flaws leading to brittle fracture. More research work is needed to focus on the optimization of this system in order to take advantage of the potential of particulate fillers, and especially nanoparticles. The structure-property relationship in composites is determined by parameters such as structure and properties of each component and their interfacial adhesions, which are all critical parameters and interconnected with each other.

The improvement in toughness of plastics is of particular interest in many applications of polymeric materials. As mentioned, the rubber toughing system is known as the most effective method for improving the toughness of polymers. Meanwhile, it is also well known that its shortcomings, particularly the decreased overall stiffness of rubber-toughened plastics. Conversely, the use of rigid fillers to toughen plastics started receiving considerable interest. However, the toughness of plastics in the industrial field is one of the most complicated and difficult characteristics to control because of the complexity of the morphological and micromechanical parameters. Some framework concepts and models have been proposed to understand and reveal the mechanisms responsible for the improvement of toughness in modified polymer systems with rubber particles or inorganic

rigid fillers. The main suggested toughening mechanism includes a diffuse plastic deformation process within the polymer matrix, such as multiple-crazing, as well as shear yielding, fibrillation, the stretching or tearing of rubber particles, and the debonding of the inorganic rigid nanoparticles.

1.1 Rubber toughened plastics

The modification of polymers with thermoplastic elastomers or rubbers is a well known common practice to counter the brittleness of polymers. Former studies on rubber-toughened systems have shown that high fracture resistances are mainly related to various parameters such as the morphology of the elastomer phase, the rubber particle size distribution, and rubber concentration and interparticle distance. Wu [3] suggested that, for the nylon-rubber system, the critical interpatricle distance is defined as:

$$d_c = \tau_c \left[(\pi/6\emptyset_r)^{\frac{1}{3}} - 1 \right]^{-1} \tag{1.1}$$

where $\emptyset_r$ is the rubber concentration, d_c is the critical rubber particle diameter, and τ_c is the critical surface-to-surface interpatricle distance. His experimental results are reported in the following Fig. 1.1. Wu even suggested that a polymer-blend would still be brittle in the case that the interparticle distance was bigger than the critical value.

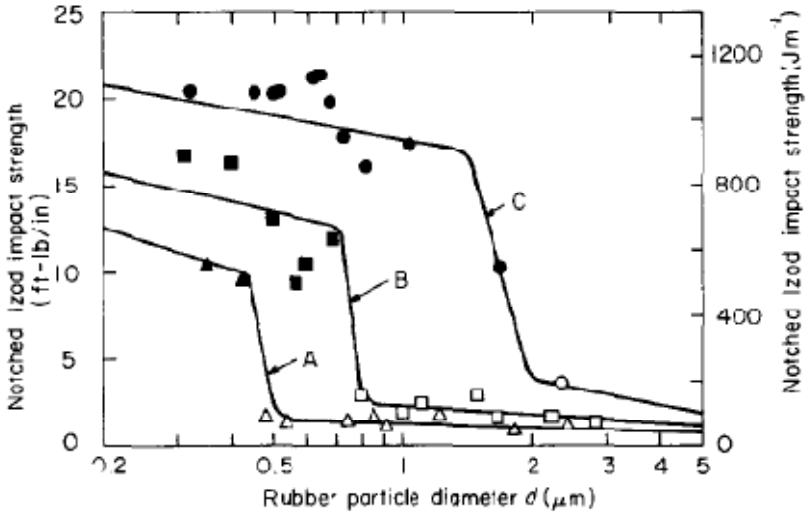

Figure 1.1 From reference [3] Notched Izod impact strength versus PR-rubber number-average particle diameter $d_n$at constant adhesion $Ga \approx 8100\ J \cdot m^{-2}$ and constant rubber contents curves A: 10%; B: 15%; C: 25% by weight.

According to this theory, the critical interpatricle distance is a material property and independent of the rubber volume fraction and particle size at a given deformation mode,

strain rate and temperature. In a later work [13, 14], Wu suggested that the surface-to-surface interparticle distance tended to focus on the rubber particles. However, the main mechanism of energy dissipation in polymer/rubber blends is the yielding of the matrix. Therefore, τ_c is renamed to be the matrix-ligament thickness, which was only the ratio of the center-to-center distance (L) to the diameter of the particle (d).

Yee and co-workers [15, 16] first proposed the importance of the rubber particle cavitation. Although the major energy absorption mechanism is suggested to be the massive plastic deformation of the polymer matrix in some literature work [17-19], rubber cavitation is the initiation process for the further cavitations of rubber particles or the shear deformation and then the whole fracture process.

Muratoglu et al. [4, 20-22] also studied rubber toughened Nylons and postulated that in the blending process the rubber first underwent phase separation, and subsequently nylon crystallized preferentially with low energy and low plastic resistance crystal planes parallel to the rubber-nylon interface. Those lamellae were organized perpendicular to the interfaces while the hydrogen-bonded planes of low slip resistance are aligned parallel to the interfaces. They studied the ductile-brittle transition as a function of temperature, rubber weight fraction and particle size. The analysis of the fracture surface revealed unique morphologies for various regions of toughness by the SEM technique. In the brittle region, the fracture surface is patchy; in the transition region, there are occasional striations present on the fracture surface, along with the brittle fracture morphology; in the ductile region, the surface is fully covered by the striations.

Lazzeri and Bucknall [23-27] have elucidated the toughness mechanism for the rubber-toughened polymer based on a quantitative model for cavitation and consequent dilatational yielding in multiphase plastics. The model indicates that cavitation can occur by debonding at phase boundaries or by the nucleation of voids within a soft polymeric phase when the stored volumetric strain energy density within the rubber phase exceeds the critical value. This model is related to the critical volume strain required for cavitation to the properties of particles: its size, shear modulus, surface energy and failure strain in biaxial extension.

The cavitation model assumed that rubber particles under positive hydrostatic stress will cavitate when the stored volumetric strain energy density U_o:

$$U_o = \frac{K_r \cdot \Delta_V^{\,2}}{2} \tag{1.2}$$

within the rubber phase exceeds a critical value. In Equ. (1.2), K_r is the bulk modulus of the rubber and Δ_V is the volume strain of the particle. The energy density stored in the particle

after the formation of a void of diameter d is then given by:

$$U_d = \frac{K_r}{2}\left(\Delta_V - \frac{r^3}{R^3}\right)^2 + \frac{6\Gamma}{R}\frac{r^2}{R^2} + \frac{3G_r F(\lambda_f)}{2}\frac{r^3}{R^3} \tag{1.3}$$

where Γ is the surface energy of rubber, R is the rubber particle, G_r is the rubber shear modulus and $F(\lambda_f)$ is a function of the elongation at the break of rubber in a biaxial state of stress. A necessary condition for cavitation is that the energy U_d has to be smaller than the initial energy before cavitation, U_o. The three parts in Equ. 1.3 present the strain energy of the particles, the surface energy of rubber particle and the shear strain energy. Fig. 1.2 shows the relationship between U/U_0 and r/R described by equation (1.3). It is obvious that the cavitation happens at a critical Δ_{V0}, which is inversely related to the particle size. This model predicts that with the increasing stress applied to a rubber-toughened polymer, cavitation will begin in the largest fillers and then progressively affect the smaller ones.

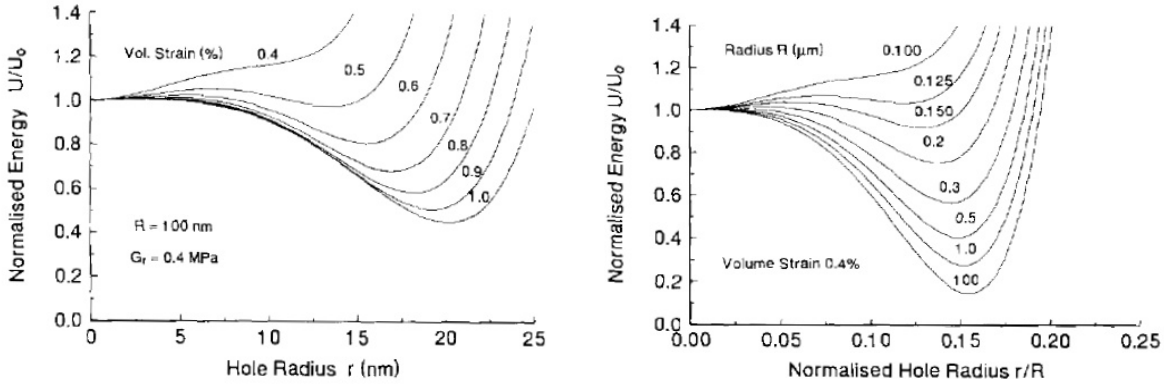

(a) (b)

Figure 1.2 From reference[24] Relationship (a): between energy of rubber particle and void size, calculated from equation (1.3) for a range of initial volume strains; (b) energy of rubber particle and void size for a range of particle size. The Rubber properties: G_r=0.4 MPa, K_r=2GPa, Γ=0.03Jm^{-2} and $F(\lambda_f)$=1.

Lazzeri and Bucknall proposed a modified version of the Gurson yield function to account for the effects of cavitation on the yielding behaviors of rubber-toughened polymers:

$$\sigma_e(\phi_R, f) = \sigma_0(\phi_R, 0)\sqrt{\left(1 - \frac{\mu\sigma_m}{\sigma_0(\phi_R, 0)}\right)^2 - 2fq_1\cosh\left(\frac{3q_2\sigma_m}{2\sigma_0(\phi_R, 0)}\right) + q_3 f^2} \tag{1.4}$$

where ϕ_R is the rubber volume fraction, $\sigma_e(\phi_R, f)$ is the effective (von Mises) yield stress and $\sigma_0(\phi_R, f = 0)$ is the matrix yield stress when the mean normal stress σ_m and the void content f are both zero, while μ is the pressure coefficient of yielding. Factors q_1, q_2 and q_3 are introduced to improve the fit between Gurson's predictions and finite element analysis [28]. This gives a round-nosed cone in stress space, as shown in Fig. 1.3. Equ. 1.4 contains

two term relations to dilatant yielding, one reflecting the flow behavior within the continuous matrix polymer phase, and the other arising from the reduced constraints on yielding of the shear band when voids are present. As the void content f increases, mean stresses within the ligaments remain tensile but become non-uniform, so that the term containing μ is then an approximation. However, the relative importance of this term diminishes with increasing void content, so that any error can be regarded as negligible.

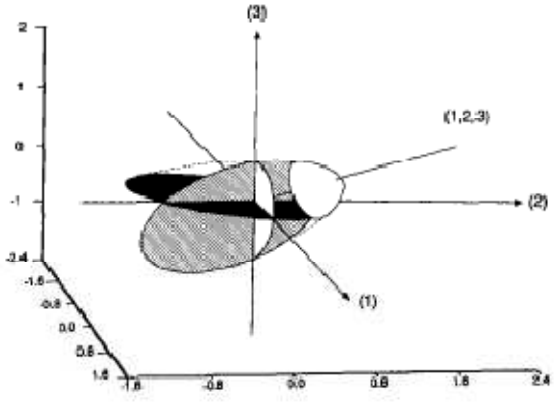

Figure 1.3 From Reference [24], representation in principal stress space of the pressure modified von Mises yield criterion according equation (1.4) for a cavitated polymer containing 20 vol% voids, with μ =0.39.

This proposed dilatational yielding model is applied to a rubber-toughened Nylon-6, and Fig. 1.4 is the transmission electron micrograph of one section from a fractured Charpy specimen of samples. It is clear that the cavitations appear in a line of closely spaced particles in the TEM micrograph, and they are relatively large compared with the rest of the rubber. The Scheme in Fig. 1.4 (b) indicates the combination of normal and shear displacements that have taken place in forming the band, and defines that band angle φ with respect to the principal stress axes.

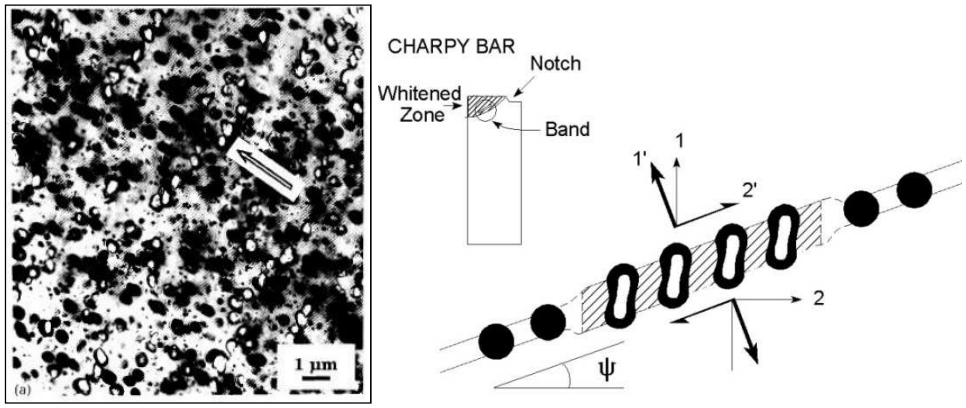

(a) (b)

Figure 1.4 From reference [24] (a) TEM micrograph of OsO_4-stained ultrathin section from a fractured Charpy specimen of rubber toughened Nylon-6, showing a series of dilatation band; (b) Scheme showing locating of band in the broken Charpy bar and the strains within the band.

Those dilatation bands can alter the subsequent stress-strain behavior of the material, especially at the crack tips: cavitated rubber particles respond to dilatational stresses by increasing their volume substantially, whereas uncavitated particles do not. Dilatation bands thus enable the toughened plastics to yield and in some cases to strain-harden by internal cavitation, under conditions that would otherwise cause necking, where the materials are under severe constraints at the tip of the crack, allowing for only a very limited plastic deformation.

In many rubber-toughened systems, the impact strength has been found to be proportional to the volume of the plastic zone [29], and cavitation in the rubber particles causes a lowering of the macroscopic yield stress. This is very important for the study of the rubber-toughened plastics, Lazzeri and Bucknall also worked on the plastic zone size based on the modified equation (1.4), and a first order approximation of the size and shape of the plastic zone in a rubber-toughened polymer is shown in Fig. 1.5. The comparison of the shape zone near a crack tip for a rubber-toughened polymer in the condition among the particle have not cavitated (f = 0) with that of the same polymer at two different levels of microvoids content (f = 0.1 and f = 0.2) in the plain strain. It is obvious that the size of the plastic zone increases significantly with the volume fraction of microvoids. Moreover, during the Izod or Charpy impact test, most energy is dissipated within the plastic zone, and therefore it can be predicted that a polymer blended with rubber, which can cavitate in considerable extent, will show a relatively larger plastic size and subsequently a larger impact strength.

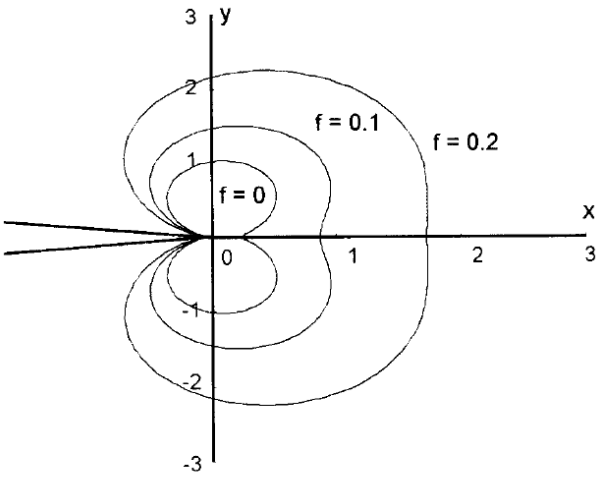

Figure 1.5 From reference [30] Approximate shape of the plastic zone at different void contents

As discussed above, in the modified Gurson equation (1.4) the yielding dilatation model only studies the initial yielding of the material under conditions of random cavitation. However, further deformation is no longer homogeneous and becomes highly localized due

to the initiation of shear instabilities called dilatational bands as shown in Fig. 1.4. The bands can be described as planar arrays of cavitated particles where the matrix between voids is subject to high shear strains and because of the rubber particle cavitation, reduced the constraints on plastic flow. As shown in Fig. 1.4 (b), the plane shear direction is parallel to the plane, and the volume dilatation is normal to it. Then it is possible to calculate the dilatational bands angle ψ between these dilatational bands and the direction of maximum stress on the basis of the modified Gurson relation:

$$\cos(2\psi) = \frac{2\alpha\sigma_0}{\sigma_1 - \sigma_2} \tag{1.5}$$

where σ_1 and σ_2 are the principal stresses on the plane of the band. For a cavitated polymer exhibiting pressure-dependent yielding without strain hardening, α is given by:

$$\alpha = \frac{\mu}{3}\left(1 - \mu\frac{\sigma_m}{\sigma_0}\right) + \frac{f}{2}\sinh\left(\frac{3\sigma_m}{2\sigma_0}\right) \tag{1.6}$$

The angle of the dilatation band, ψ, is thus a function of the void content f and of the level of triaxiality. Once the deformation process has become localized into dilatational bands, further particle cavitation will occur preferentially near band tips. In this case the proposed cavitation model cannot accurately account for the macroscopic yield behavior of the cavitated polymer. The proposed dilatation band model by Lazzeri has been confirmed in the work of rubber-toughened polypropylene [31] with EPR elastomers.

The propagation and the growth of the dilatational bands have been studied by the research work of Hiltner et al. [32, 33]. Their work has examined the dilatation bands present in the polycarbonate toughened with core shell particles. They found that particle outside the dilatation band would not cavitate, while those inside the bands appeared distorted due to the high level of matrix strain in the ligaments, which was estimated to be close to the natural draw ratio of polycarbonate, about 100%. This cooperative cavitation in rubber-modified polycarbonate becomes more likely as the interpatricle distance decreases.

For the rubber-toughened system, it has been proposed by Michler [34, 35] that the dominating mechanism is the single cavitation process in binary blends of PA/BA (polyamide/22 vol% butyl acrylate) systems. Under the conditions of uniaxial tension, a stress concentration builds up inside the rubber phase as the first stage of the whole process. Then the modified particles can be stretched and microvoids occur inside the rubber particles. Meanwhile, shear bands of the polymer matrix form between those microvoids. In the third step, with further straining of the specimen, the voids will become more elongated, and the matrix will be further deformed through shear yielding. They also reported in the

case of the mineral filler $CaCO_3$ that it is not possible for cavitation to occur inside the particles, but void formation at the interfacial region between rigid particle and the polymer matrix is very effective.

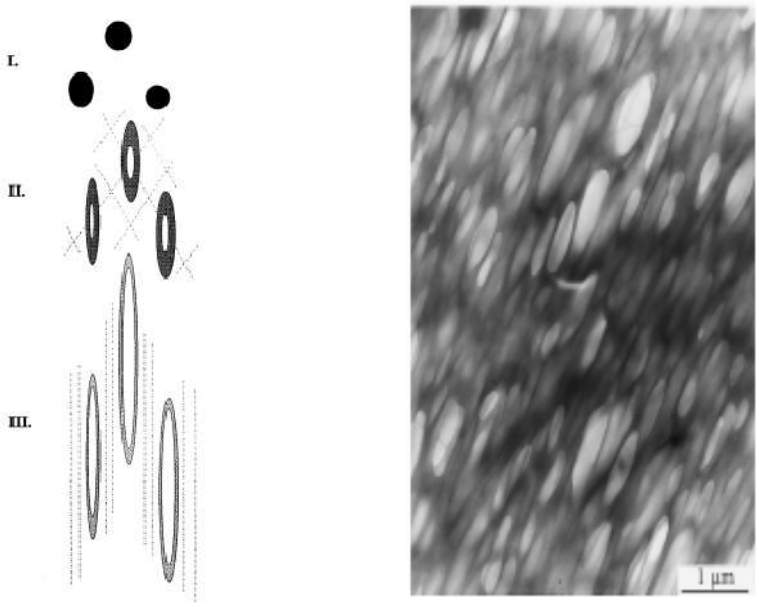

Figure 1.6 From reference [34, 35] single cavitation process in binary blend systems: PA/BA blend

Based on the former knowledge of the rubber toughening mechanism and the proposed models by Wu, Bucknall and Lazzeri, Muratoglu, Michler and so on, the rubber-toughened system basically depends on the rubber particle size, volume fraction and the inter-particle distance, as well as the onset of the cavitation process. However, it is also well known that the cavitation of rubber particle during the deformation process reduces the strength of the polymer system. In other words, the increasing of toughness compromises the stiffness of the polymeric system with rubber particles.

Similar to the requirement of microvoids cavitation process in the rubber-toughening mechanism, a debonding process has been reported in several filled polymer systems. If the volume fractions and random dispersions of particles can be made comparable, it should be more beneficial to use stiff particles such as the calcium carbonate nanoparticles rather than soft rubber particles. This would also then improve the stiffness of the polymer composites filled with rigid particles. Argon and Cohen [11, 12, 36-38] proposed that toughening polymers with rigid filler, could be achieved only if the rigid particles debond from the matrix, creating voids around particles and allowing the interpatricle ligament to deform plastically or even to fibrillate. Michler [34, 35] also proposed that microvoid formation is a major operating mechanism for the initiating plastic deformation similar to the cavitation of rubber particles. They suggested that the microvoid formation can also be caused by the debonding at the interface between rigid particles and matrix, based on their study of the

structure-property relationship of polypropylene/aluminum hydroxide composites. In the following section, the recent research activity in filler toughened plastics is reviewed.

1.2 Filler toughened plastics

In former literature work, semi-crystalline polymer such as polypropylene [39-41], polyethylene [42], polyamide [43, 44], filled with rigid organic fillers in micro or nano-size, for example, $CaCO_3$ [45-49], SiO_2, $Mg(OH)_2$ [50, 51], glass beads [52],carbon nanotubes [53] and layered silicate [54-58], have been studied mainly in order to cope with the obvious limitations of polymers with low stiffness and strength. In the last two decades, the concept of "*filler-toughened polymers*" has received increasing attention due to improvements in the mechanic properties of polymer composites.

In 1989, Levita and Lazzeri [6] published their research work on the strength and fracture properties of a polypropylene filled with ultrafine calcium carbonate (0.07 μm), in the composition range of 0 to 40 percent by volume. Untreated and surface treated (with stearic acid and a titanate coupling agent) grades were compared. The untreated filler caused a decrease of toughness whereas a maximum, about 10 percent, was observed for the treated filler. Bartczak and coworkers [5, 11] compared the modified high-density polyethylene with rubber or nanoparticles based on the critical interpatricle ligament effect. They found a similar result in two systems that the toughness of the polymer nanocomposites increased dramatically when the mean interpatricle ligament thickness of the polyethylene matrix dropped to values below 0.6 μm. This confirmed that the stiff fillers provided the additional benefit of substantially increasing Young's modulus and also the significant improvement of their impact energy. Mai and Xie et al. [59] reported that the optimal properties such as Young's modulus, tensile yield strength, elongation-at-break and Charpy notched impact strength were obtained in PVC by adding only 5 wt% $CaCO_3$ nanoparticles with an average size of 40 nm.

The presence of nanoparticles in the polymer will alter the local stress state of the surrounding matrix due to the specific large surface area. This effect can be attributed to the influence of nanoparticle-polymer interfaces on the polymer chain dynamics in the vicinity of particles. In the literature, detailed discussions can be found about the influence of the particle size, particle/matrix interface adhesion and particle content on the stiffness, strength and toughness of the final particulate polymer composites. Moreover, a basic understanding of the stiffness and toughness mechanism in the nanoparticles-filled polymer composites is necessary to tailor suitable toughened plastics with nanoparticles.

As it is already known, debonding is the required process for the following energy dissipation provided by the polymer matrix deformation that leads to enhanced toughness of polymer nanocomposites. In the work of Michler et al. [35] on the PP/$Al(OH)_3$ system and the work of Gaymans [60] on PP toughened with calcium carbonate nanoparticles, the toughening process as shown in Fig. 1.7 can be summarized in three steps:

(a) *Stress concentration.* Because of the different elastic properties of the rigid nanoparticles with respect to that of the polymer matrix, the nanofillers act as stress concentrators.

(b) *Debonding.* Under the applied uniaxial tension, the stress state around the nanoparticles changes and leads to the debonding on both polar regions of the filler particles. With the continuous growth of voids, the shear bands form in the matrix between the microvoids.

(c) *Shear yielding.* Once the voids form due to the debonding of nanoparticles (similar to the cavitation inside the rubber particles), the triaxial tension can be locally released in the surrounding of voids, especially where the poles of the particle corresponding top and increase the shear component. Consequently, further shear yielding of the polymer is induced.

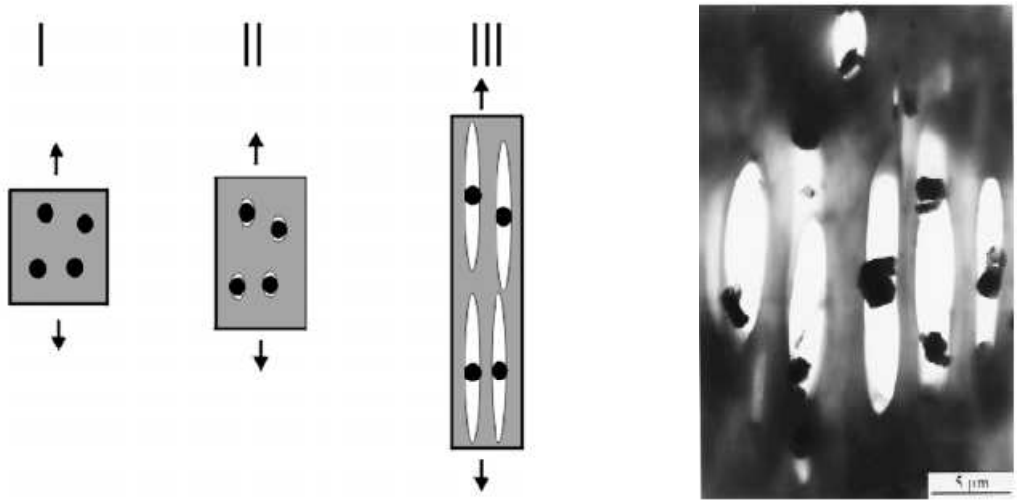

(a) (b)

Figure 1.7 From reference [35, 60] (a) Toughening mechanism of polymer nanocomposites with rigid particles and (b) the TEM micrographs of PP/$Al(OH)_3$ polymer composites

During those three steps of the deformation process, the dominating energy absorption process is in the third stage, which is attributed to the plastic deformation of the polymer matrix. With further increasing of the strain in the specimen, the stress will be further released, by which the plastic deformation of the polymer ligaments is considerably accelerated. However, the initial process that triggers the extensive plastic deformation of the polymer is the formation of microvoids due to the debonding of nanoparticles.

Therefore, a lot of literature work proposed the debonding models for the particulate polymer composites. Argon and Cohen [38] found that the gaps between the particles and the matrix was not completely reversible based on the loading and reloading tests. Thus, they defined the nature of the stress in the modified polymer is induced by the interfacial separation of pre-pressurized particles from the surrounding matrix that clamped down on them. They proposed a simple analytical development about the clamping pressure p on a spherical particle, which is a function of the bulk modulus K_p and volumetric coefficient of the particle γ_p,

$$p = \frac{(\gamma_p - \gamma_c)\Delta T K_p}{\left[1 + \frac{4\mu_c}{3K_p}\right]} \tag{1.7}$$

where μ_c is the shear modulus of the filled composites and the γ_c is the volumetric coefficient of expansion of the filled composites. The γ_c and μ_c themselves depend on the volume fraction c of the rigid fillers and can be determined from the equation by Chow [61, 62].

$$\frac{\mu_c}{\mu_m} = 1 + \frac{\left(\frac{\mu_p}{\mu_m} - 1\right)c}{1 + \left[\left(\frac{\mu_p}{\mu_m} - 1\right)(1-c)\frac{2}{15}\frac{(4-5v_m)}{(1-v_m)}\right]} \tag{1.8}$$

where v_m is the Poisson's ratio of the matrix, μ_p and μ_m are the shear modulus of rigid filler and polymer matrix. Moreover, from Chow:

$$\gamma_p - \gamma_c = -\left(\frac{K_m}{K_p}\right)\frac{(\gamma_m - \gamma_p)c}{1 + \left(\frac{K_m}{K_p} - 1\right)\left[(1-c)\frac{1+v_p}{3(1-v_p)} + c\right]} \tag{1.9}$$

where γ_c and γ_p are the volumetric coefficients of thermal expansion of the composite and that of the rigid fillers. Debonding in the form of a kink on the stress-strain curve will be observable when the negative pressure σ_m inside the particle, induced by the applied tensile stress equals that of the thermal-misfit-induced pressure to make the interface stress free and ready to undergo separation. This gives eventually the tensile debonding stress σ_{db} as,

$$\sigma_{db} = 3p\left[1 + \frac{2(1-4v+v^2)\left(\frac{K_p}{K_c} - 1\right)}{(1+v)\left[2(1-2v) + (1-v)\left(\frac{K_p}{K_c}\right)\right]}\right]^{-1} \tag{1.10}$$

Concerning the debonding process in the filled-polymer composites, Lazzeri [63] has also studied polypropylene composites with the $CaCO_3$ as a filler toughened system. Tensile

dilatometry tests of the polypropylene composites were carried out to study the debonding process and the volume evolution of voids inside the particulate-filled composites. This research work found that the debonding occurred before the macroscopic yield, therefore reducing the plastic resistance of the materials. The debonding would occur earlier as the particle content increased. The volume stain of a series of polypropylene with calcium carbonate fillers with different particle sizes is discussed. This method of volume strain change during uniaxial tensile test has been used to study toughening mechanisms in rubber-toughened polymer in a former work of Lazzeri and Bucknall [26]. As expected, the volume strain of the PP/$CaCO_3$ system shows a clear increase after the yielding points as shown in Fig. 1.8 (a) due to the formation of microvoids after the debonding of nanoparticles from the polymer matrix. A model has been proposed to take the particle size effect into account, based on the formation of an immobilized layer of polymer on the surface of the nanoparticles as shown in Fig. 1.8 (b). The experiment results are consistent with a surface layer of 15-25 nm. The aggregation of the nanoparticles has also been considered in the work when the particle size is about 3.5 micrometers. Their work of the volume strain suggests a very simple and effective method for the characterization of the interphase layer.

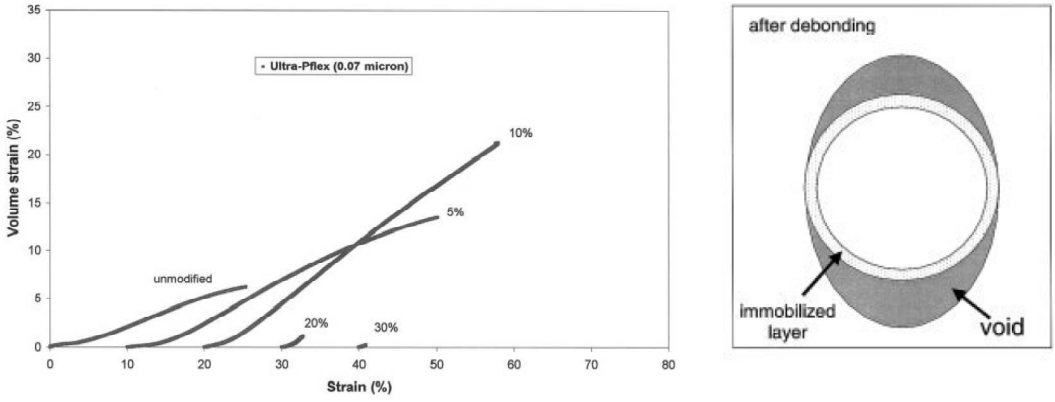

(a) (b)

Figure 1.8 From reference [63] (a) Volume strain-elongation curves for PP/$CaCO_3$ (0.07μm) (b) Model for volume increase due to the debonding between particle and matrix and the cavity growth

Based on the study of debonding process, it is quite clear for the particulate-polymer composites that the improvement of toughness can be achieved with the following requirements:

1. Filler dispersion must be very regular to avoid the formation of crack-initiating large agglomerates.

2. Matrix-debonding must occur to allow unhindered plastic deformation around the particles. In other words, the interfacial adhesion should be at a suitable level to facilitate the debonding process of the particulate polymer composites.

1.3 Mechanical properties of particulate polymer system

In the particulate-polymer composite systems, the mechanical properties such as stiffness, strength and toughness are strongly related to the particle size (large or small aspect ratio), particle-polymer interfacial interaction and the particle loading. Some proposed theoretic models are aimed at predicting the elastic modulus, strength and fracture toughness of the particulate-polymer composites. Besides the influence of nanofillers on the mechanical properties, there are reports [64-67] that the particles can act as nucleating agents for the crystallization of polymer. Meanwhile around or on the particle surface, there will be the transcrystalline layers [5, 68-70], which show different properties from the main polymer matrix.

a. Young's modulus.

The addition of the filler into a polymer matrix results in a heterogeneous system. The stiffness of the composites is usually compared by using Young's modulus, which is ratio of stress and strain in the elastic region in a tensile test. This value is very important and is the main difference between a rubber-toughened and a filler-toughened polymer system because the inorganic rigid particles have a higher stiffness than that of the polymer matrix. Particles having an average size in micrometers and nanometers are compared in many papers considering Young's modulus.

In the work of Bartczak [11], high-density polyethylene composites with calcium carbonate particle with three different sizes of 3.5, 0.70, 0.44 μm in different volume fractions from 5 to 30 percent have been considered. Young's modulus of different composites indicated that the specimens with larger particle size showed a higher Young's modulus than those with smaller particle size. A similar work on polypropylene composites with calcium carbonate is reported by Thio [12]. They found a slightly higher Young's modulus for specimens with larger particles (3.5 μm) than that of the smaller particles (0.7 and 0.07 μm). The particle loading also affects the stiffness of the particulate polymer. The composite modulus consistently increases by increasing the particle contents in the polymer matrix, which is attributed to the rigidity of the inorganic fillers. The most interesting parameter, the interfacial adhesion between rigid particle and polymer matrix, shows no effect on Young's modulus of the composites. This can be explained by the fact that the modulus is a property of a material at a relatively lower deformation before the debonding process occurred, which is related to the interfacial adhesion. In the work of Levita and Lazzeri, the surface coated and uncoated calcium carbonate particles (70 nm) were added

into polypropylene and an increase of the modulus was noted with increasing filler loading. However, no changeable effect of the interfacial adhesion on the elastic modulus was found.

Some theoretical models have been proposed to predict the elastic modulus in the particulate polymer composites. The basic one is Einstein's [71, 72] equation for predicting Young's modulus:

$$\frac{E_c}{E_m} = 1 + 2.5V_P \tag{1.11}$$

where the E_c and E_m are the elastic modulus of the composites and the polymer matrix, and V_P is the volume fraction of the particles. However, this model is valid only at low filler contents and does not consider the effect of particle size. There are some other modification of Einstein's equation. Nielsen [73-75] proposed a modified Einstein's equation:

$$\frac{E_c}{E_m} = \frac{1 + A_1 B_1 V_P}{1 - \psi B_1 V_P} \tag{1.12}$$

where ψ depends on particle packing fraction and A_1 and B_1 are constants for a given composite.

$$A_1 = k_E - 1, \qquad B_1 = \frac{E_P/E_m - 1}{E_P/E_m + A}, \qquad \psi = 1 + \left[\frac{(1 - V_{Pmax})}{V_{Pmax}^2}\right] V_P \tag{1.13}$$

where k_E is the Einstein's coefficient and V_{Pmax} is the maximum volume fraction.

Cohen [76] assumed that the two components are in a state of macroscopically homogeneous stress, and that adhesion is perfect at the interface of a cubic inclusion in a cubic matrix. When a uniform stress is applied on the boundary, the elastic modulus of the composites can be given by:

$$\frac{E_c}{E_m} = 1 + \frac{1 + (\delta - 1)V_P^{\frac{2}{3}}}{1 + (\delta - 1)\left(V_P^{\frac{2}{3}} - V_P\right)} \tag{1.14}$$

where δ is the ratio between E_P and E_m.

Fu [77] proposed a simple equation based on the modified rule of mixtures to predict the elastic modulus of particulate composites:

$$E_c = \chi_P E_P V_P + E_m(1 - V_P) \tag{1.15}$$

where $0 < \chi_P < 1$ and is a particle strengthening factor.

In conclusion, the stiffness of particulate-filled composites can be effectively increased by the addition of inorganic nanoparticles and the interfacial adhesion has little effect on this property.

b. Strength

The strength of a material is defined as the maximum stress that the materials can sustain under the uniaxial tension. This parameter is also strongly connected with the particle size, volume fraction and the interfacial adhesion in the composites. It has been noted in some work [11, 12, 63] that the yield stress gradually decreased with the increasing of the particle loading in different particle sizes. However, the variation of the yield stress on the particle size is small, and the mechanical properties are mainly controlled by the volume loading rather than the particle sizes. The surface coating for the nanoparticles was carried out in that work in an attempt to achieve random dispersion of the nanoparticles. Therefore, the effect of the coated nanoparticles on the mechanical properties was compared to that of the uncoated one. For calcium carbonate industrially coated with stearin a few papers have discussed [6, 7, 11], the effect of the interfacial adhesion on the strength of final composites. Lazzeri prepared a series of HDPE composites with $CaCO_3$ nanofillers, which were coated with different stearin amounts. The addition of the pure rigid fillers can increase the yield stress firstly, but then decrease with the increasing of surface coating amount. This can be related to the effect of surface coating amount on the interfacial adhesion, which was determined to be weaker with a larger stearin coating amount. Consequently, the extensive debonding of the particle from the matrix happened before the yield point under the applied load. In principle, a strong interfacial adhesion is critical for effective stress transfer leading to high composite strength. Inversely, a weak particle/matrix interface boding will only show a relatively lower strength. In the next section, the dependence of the toughness on the interfacial adhesion will also be discussed.

The theoretical prediction of the strength of composites is difficult because this parameter is determined by the fracture behavior, which is associated with the extreme values of interface interaction, stress concentration, defect size or the particle distribution. Some proposed models are briefly summarized. Nielsen [78] calculated the strength of a filled polymer by:

$$\sigma_c = \sigma_m(1 - V_P)S \tag{1.16}$$

where σ_c and σ_m are the tensile strength of the composite and the polymer matrix, respectively, V_P is the volume fraction of filler and S accounts for the weakness in the structure resulting from a discontinuity in stress transfer and the generation of stress concentrations at the filler-polymer interface. This model is proposed for poorly-bonded particles. This equation indicated that the strength of the composites decreased linearly with the increasing of the filler loading. However, some practical tests showed a non-linear

relationship with the calculated yield stress. Therefore, there is a modified model [79, 80] such as:

$$\sigma_c = \sigma_m\left(1 - aV_P^b\right) \tag{1.17}$$

where a is related to the stress concentration or to the quality of adhesion between the polymer matrix and particles, and b is related to the geometry of the fillers. This model still predicts a decrease in strength with an increase of particle loading.

Furthermore, Pukanszky [81-83] proposed that the tensile yield strength of composites could be calculated from the following equation:

$$\sigma_c = \left[\frac{1 - V_P}{1 + 2.5V_P}\sigma_m\right] exp(BV_P) \tag{1.18}$$

where B is the interfacial adhesion between particles and polymer, which depends on the surface area of particle, particle density and interfacial bonding energy. For a poor interfacial bonding, the particle could not handle any load and B is zero. The parameter B presents the interfacial adhesion strength between particle and polymer matrix. The parameter B depends on both the thickness and the strength of the interphase:

$$B = (1 + A_P\rho_P l)\ln\frac{\sigma_{T_i}}{\sigma_{T_0}} \tag{1.19}$$

where A_P and ρ_P are the specific area and density of the filler, l is the thickness, and σ_{T_i} is the strength of the interface. This model is applied in a series of works of Pukanszky to determine the thickness of the interphase through the above equations (1.18) and (1.19) when the tensile strength of the composites is determined as a function of the volume fraction.

In summary, the strength of the particulate polymer composite also relies on the properties of each component in the blends, such as the particle size, interfacial adhesion, and particle contents. Even many theoretical models were proposed to predict the strength for a given composites, but so far there is no one single equation that can be applied to all types of filled polymer composites. However, based on that prediction from the theory background, we have the direction to tailor new composites following the requirements of the special application.

c. Fracture toughness

As mentioned above, toughness is one of the most difficult parameters to control, and the design against brittle failure in composites is of critical importance. The deformation and fracture characteristics of toughened polymers and the interrelationship between the

micro-structure or micro-morphology and the mechanical properties are the main purposes for the toughness studies. It is very important that the special region with plane stress, between the particles, be provoked allowing the material to yield. Thus, it is possible for a material to show the plastic deformation and craze formation, which are the element processes for dissipated energy.

Some experiment results of the particulate filled polymers have been recorded with the increasing of toughness. Thio [84] studied the effect of interfacial adhesion on the toughened polypropylene with glass beads with different surface treatments to either increase or decrease the interfacial interaction. The Izod impact toughness increased with the increasing of CF-silane (heptadecafluorodecyl trichlorosilane) amount used for the surface treatment of the glass particles, which showed a decreased interfacial interaction with the polypropylene. This confirms the hypothesis that a weaker interaction would lead to a higher toughness. Another study [11] of the HDPE/$CaCO_3$ composites work has demonstrated a very successful toughening behavior exhibiting dramatic toughness jumps in connection with the critical ligament size criterion of Wu [3]. Lazzeri [7] worked on the HDPE nanocomposites with the precipitated calcium carbonate filler coated with stearin. The Charpy impact in their work indicated an almost linear increasing relationship between the surface coating amount on the PCC particles and the impact strength as shown in Fig. 1.9. That is the former work of this thesis. The explanation of this increasing of impact toughness is possibly due to the effect of the surface coating amount on the interfacial adhesion. However, the discussion about the relationship between stearin surface coating on the PCC particle and the interfacial adhesion with polyethylene was not reported in that work.

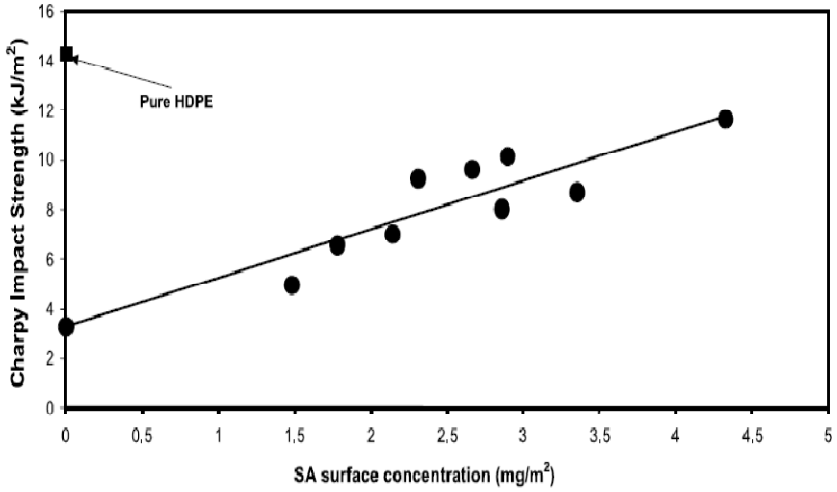

Figure 1.9 From reference [7] dependence of the impact strength of HDPE/PCC nanocomposites versus the surface coating amount of PCC

The toughness of particulate polymer composites also depends on the filler loading. Zuiderduin [60] studied the effect of $CaCO_3$ particles with a diameter of 0.7μm on the notched Izod fracture toughness of polypropylene. This is an almost linear increase of the impact strength with the increasing of particle loading and the toughness is improved four-fold with 60 wt% fillers in PP. They indicated that the stearic acid coating on the particle surface showed a large positive effect on the impact strength. However they also reported the failure of the smaller particle with an average size of 70 nm in achieving toughness improvement was attributed to the poor dispersion of the nanoparticles. In fact, this is one of the most difficult problems during the preparation of filled polymer nanocomposites. The dispersion of the particle is critical in these composites, and at high filler loadings it may become difficult to avoid aggregates, which can lead to the brittle behavior of polymer composites. In the thermoplastic field, this problem can mostly be solved through the surface coating of the nanoparticles to avoid aggregation. Ahsan [85] carried out detailed studies on the influence of the surface energy on the mineral-polymer interaction in the polyolefin composites. The ground calcium carbonate with a lower surface energy after the surface treatment showed higher resistance to impact. This work suggested the surface energy might be a key to the development of the design of the mineral filled-polymer composites.

Except the Izod or Charpy impact tests for the investigation of polymer toughness, there are two other approaches to determine the fracture toughness: the stress intensity factor K_c and the energy release rate G_c. Under certain conditions the two parameters can be connected to each other by:

$$G_c = K_c^2 / E_c \tag{1.20}$$

A widely applied method for filler-toughened polymer nanocomposites is the micro-morphological study by SEM or TEM techniques. To-date, the possible toughening mechanisms have been proposed and include: crack pinning, crack-tip blunting, particle-matrix interphase debonding, polymer matrix shear yielding, micro-cracking, micro-shear banding and fibrillation of the polymer matrix. Some of those processes can cooperate in the particulate polymer composites. The most accepted fracture mechanism is the debonding of rigid particles from the polymer matrix during the deformation process, and the most controlled factor is the interfacial adhesion between particle and polymer. In an early work of Levita and Lazzeri et al, it is reported that when the particle was very small size, the crack-pinning had no contribution to the G_c values. If the interfacial debonding dominated

in the fracture process, the smaller particle will lead to large G_c due to their higher surface area.

Evans et al [86] argued that energy dissipation processes within a dissipation zone in front of the crack were responsible for toughness enhancement by adding rigid particles to ductile polymer. They also found that the particle debonding and subsequent yielding of local polymer regions were the dominant mechanism. Bohse [87] also reported a similar work about the fracture toughness of particulate-filled plastics.

Based on the knowledge of literature and former proposed models, it is clear that the rubber toughening mainly depends on the fine dispersion of the rubber particles. However for the filler toughening system, the mechanism requires only a modest level of adhesion between the particles and polymer. In general, a poor adhesion leads to an increase in toughness. [7, 84, 88, 89] Following this principle, an important part of this work will be devoted to the surface treatment and the characterization of the nanoparticles to achieve the suitable interfacial adhesion. The basic theoretical background for the surface treatment of the nanoparticles is discussed in the following.

1.4 Surface treatment and characterization

In order to design new materials according to the requirements for the application, it is important to make surface treatments for both rubber particles and inorganic rigid particle. The microstructure of the filled-polymer will be consequently changed to facilitate the suitable deformation process during the application.

In the rubber-toughened plastics, it is well known that the elastomer particle size plays a key role in achieving the super-toughness. Some former work also studied the strategies for toughening to achieve an optimum rubber particle size. For example, it has been reported [90] that the size of the elastomer particles in the polyamide blends can be significantly decreased because of the reaction of the grafted maleic anhydride groups with the amine end group of the polyamide to form copolymers that retard the coalescence of elastomers particles.

a. Aggregation of rigid particles

In the filler-toughened plastics, the surface treatment of the rigid nanoparticles aims at two key points: particle-particle interaction and particle-polymer interaction. The first one aims to decrease the aggregation degree and take advantage of the large surface area of nanoparticles. The other purpose is to achieve a suitable interfacial adhesion for the necessary process under external loads. The aggregation of nanoparticles is connected to

their small particle size, since the balance between the separation force and the adhesion force is strongly dependent on this parameter. For smaller particles, separation forces are smaller than adhesion forces. This can result in either a large aggregation in the polymer leading to brittle behavior or debonding from the matrix or a break inside with the formation of cracks. The adhesion strength between the particles is determined by the size and surface energy for each component.

$$F_a = \frac{3}{2}\pi W_{AB} r_a \tag{1.21}$$

where F_a is the adhesive force between the particles is, W_{AB} is the reversible work of adhesion and r_a is the effective radius. A lower reversible work for adhesion was found to result in a decreased aggregation tendency. Non-reactive surface treatment invariably leads to a decrease in the surface tension and W_{AB} , thus to decreased aggregation and consequently improved mechanical properties [91, 92].

b. Surface treatment for rigid particles

The easiest way for the modification of the interfacial adhesion is the surface treatment of fillers. There are a few different types of surface coating agents according to different goals for the treatment, such as the coupling agents to increase the interfacial adhesion or the surfactant to weaken the interaction. In the industrial field, the surface treatment is quite important for solving problems of processing technology and product quality. In the filled-polymer composites, the surface treatment of nanoparticles changes not only the particle-particle interaction but also the particle-matrix interaction. Basically, there are four different types [93] of surface treatment: (1) Non–reactive treatment-surfactants, (2) Reactive treatment-coupling agents, (3) Polymer layers-inter-diffusion and (4) Soft interlayer-elastomers.

Reactive treatment assumes the chemical reaction of the coupling agent with both the particle and polymer matrix. The surface treatment of glass beads with silanes is one of successful examples. Silane coupling agents are effective in the particles, which have the reactive OH groups on the surface [94, 95]. The application of silanes was also carried out on calcium carbonate to study the interaction of coupling agents and $CaCO_3$ [96]. They found that silanes coated $CaCO_3$ showed increased strength but decreased deformability. A study of the surface treatment of montmorillonite with alkyammonium monolayer [97] found that the hydrophilic surface of clay was modified to be hydrophobic. In fact, the reactive treatment with coupling agents is more complicated because of the possible polymerization of coupling agents and the chemical bonding or physical absorbed layers.

In industry, the widest used and also the oldest method for surface treatment is the use of nonreactive surfactants, which are usually available, small molecular weight organic compounds. For the calcium carbonate particles, the most widely used surfactants [98-101] are fatty acids such as stearin, which is mainly a blend of palmitic acid and stearic acid with a little amount of other acids, due to the low cost and easy preparation. Because of both the polar group (carboxyl part) and non-polar group (aliphatic chain) in fatty acids, it is reported that a preferred adsorption process of the surfactant occurs on the nanoparticles' surface. However, the industrial method for surface coating focuses more on the coating effect of the products and little information has been disclosed about the detailed adsorption process during surface coating process that can be dry coating or in a special liquid medium. Furthermore, the study of the surface coating amount is a crucial question for optimizing the recipe for special applications. The surface characteristics of nanoparticles, such as the organic coating amount, the molecular arrangement on the surface, the specific surface area of nanoparticles and the surface energy, are all interconnected with each other and will affect the application of the nanoparticles in several polymers. For example the interfacial adhesion between nanoparticles and the polymer matrix can be expressed [102] by:

$$\gamma_{12} = \gamma_1 + \gamma_2 - 2\left(\gamma_1^d \gamma_2^d\right)^{1/2} - 2\left(\gamma_1^p \gamma_2^p\right)^{1/2} \tag{1.22}$$

where γ_i^d and γ_i^p are the dispersion and the specific components of γ_i. In fact the surface tension of the polymer and rigid particles are different for both the dispersion and specific components. The surface treatment effect on the surface free energy will be another factor for the application to polymers. In fact, the relationships between the coating amount with the surface energy change, and then the mechanical properties are discussed in detail in this thesis.

In summary, filler-toughened polymer systems can be prepared by compounding rigid particles into the polymer matrix. In order to improve the toughness of polymer nanocomposites, the surface treatment of the inorganic particles is necessary to avoid the aggregation among particles and also to weaken the particle-matrix interfacial adhesion. The high surface area of nanoparticles in the plastics and the weaker interfacial interaction make the debonding process easier, which is the initial part for the energy dissipation process. This is the basic structure of this thesis.

1.5 Outline of this thesis

In the former work of this thesis, some interesting results have been published. The application of ultra-fine calcium carbonate nanoparticles can effectively increase the

toughness of the semi-crystalline polymer such as high-density polyethylene and polypropylene. The former study of Lazzeri on the rubber-toughened polymer system gives theoretic models, the cavitation and dilatation yielding bands models, in order to predict the possibility of toughness improvement of the filler-toughened system. However, some problems were found also during the former studies. For example, calcium carbonate nanoparticles tend to easily aggregate during the compounding process with the polymer.

The former study showed that commercial PCC nanoparticles coated with stearin in the water medium had a very low aggregation degree in the HDPE polymer matrix by the melt extrusion process. The surface coating by organic materials is of critical importance to the particle distribution and the particle-polymer interaction. These two parameters are the determinant factors for the mechanical properties of the final nanocomposites. Precipitated calcium carbonate (PCC) has been widely used in the industrial field for many applications, such as automotive, household, and packaging sectors. Moreover, the enhanced toughness of filler-toughened plastics with PCC particles has been reported, especially their mechanical performance. Therefore in this thesis, the relationship between the surface coating effect of calcium carbonate nanoparticles and the properties of the final polymer nanocomposites is mainly discussed. The main research work is shown as following:

In Chapter 2, the preparation and surface treatment processes of precipitated calcium carbonate is described in detail. The techniques used for the surface characterization are shown according to the different purposes, such as the surface organic coating amount, surface molecular arrangement, and surface coating mechanism. The lab-scale melt-extrusion machine HAAKE minilab was used for the preparation of the polymer nanocomposites. The tests for the mechanical properties, crystalline behavior and the micro-morphology of polymer nanocomposites were described concerning the measurement conditions.

In Chapter 3, the surface coating process of the commercial PCC nanoparticles with stearin in the water medium is compared with that of dry coating or lab-scale solvent coating. The main surface characterizations focus on the total organic amount of surfactant and the adsorption process of the surfactants in the aqueous solution.

In Chapter 4, the surface characterization of the water-coated PCC nanoparticles is discussed on the molecular arrangement of the surfactant. The temperature dependence of the surface coating molecular crystalline is discussed according to the different thermal treatment, which is helpful in understanding the reality of the coating molecules under

different temperatures. The influence of the surface treatment on the surface free energy change is also investigated on a series of PCC nanoparticles.

In Chapter 5, the surface coated PCC nanoparticles are added to high-density polyethylene for the application as filler-toughened polymer system. The surface coating characteristics such as the coating amount or the surface free energy are investigated connected to the mechanical properties, including the tensile and impact properties. The impact fracture surface of HDPE/PCC nanocomposites is discussed for the toughness mechanism.

In Chapter 6, the stearin-coated PCC particles are also applied to a biodegradable polymer, polylactic acid (PLA), to test the capability as toughness particles. PLA is an alternative material for the fossil fuel-based traditional polymers and can be derived from renewable resources. Because the PLA has a poor toughness and the PCC is reported as toughness filler, the purpose of this Chapter is to try to understand the effect of coated PCC particles on the mechanical properties, thermal behaviors and the micro-morphology of PLA/PCC nanocomposites.

In Chapter 7, the main results in this thesis are summarized and the major points of this thesis are listed. Nevertheless, several questions remained open in this work and further research work is needed. Some on-going work will continue in the particulate field based on the results of this thesis.

Chapter 2 Materials and Experiments

2.1 Surface characterization of PCC nanoparticles

2.1.1 Materials

A series of experimental precipitated calcium carbonate (PCC) particles was supplied by Solvay Advanced Functional Minerals (Salin-de-Giraud, France). The surface treatment with a commercial stearin, Pristerene 4937 from Uniqema (now Croda Italiana S.p.A., Mortara, Italy), ranged from 0 to 13.5 % by weight (that is 0 to 135 g acid/kg PCC) and it was carried out in aqueous solution. These particles were coded from PCC1 to PCC9 in this thesis. The particle size is about 62 nm and the corresponding specific surface area is around 19 m^2/g, as shown in Table 2.1. PCC particles with full monolayer coating coverage (also with the same commercial stearin) obtained by dry coating also supplied from Solvay were used as a reference sample and coded ML2. These particles have a specific surface area of 65 m^2/g and surface coating amount of 15 wt%. Concerning the choice of the surfactant used in this work, it should be noted that industrially available calcium carbonates are coated with commercial stearin and not with pure stearic acid. The commercial stearin chosen, Pristerene 4937, contains about 48.8% stearic acid (C18, molar mass 284.5 g/mol); 49.5% palmitic acid (C16, molar mass 256.4 g/mol); and small amounts of oleic acid. In stoichiometric calculations, a molar mass of 270.4 is assumed for stearin.

For purposes of comparison, an industrially-available PCC, Socal U1, also from SOLVAY Advanced Functional Minerals, was also used [103]. The mean particle size (D50%) of Socal U1 is 0.08 µm, and the average surface area is 20 m^2/g, as reported by the supplier, and is not coated. This pure PCC was used for the preparation of a fully covered monolayer sample in solvent and coded to be ML1.

In this thesis, the term “full monolayer” is defined to be a coating level corresponding to the maximum theoretical monolayer coverage that is determined according to the specific surface area of PCC and the theoretical cross section area of stearate molecule, with the orientation of stearate molecules assumed to be vertical to the PCC surface. The term “monolayer” refers to a coating level below the maximum theoretical, which means that a part of the surface is covered by a chemisorbed layer of stearin/stearic molecules, and other part is still uncovered. Throughout this thesis, the term “stearin” is to indicate the commercial stearin Pristerene 4937 and the term “stearic acid” refers to pure acid from Aldrich.

In Table 2.1 all PCC particles used in this work are shown by the main properties of particle size, specific surface free energy (determined by the BET tests) and nominal coating amount.

Table 2.1 Specification of PCC powders used

Particle code	Specific surface area (m^2/g)	Nominal coating (*wt%*)
PCC1	19.0	0
PCC2	19.9	3
PCC3	18.0	4.5
PCC4	19.2	6.0
PCC5	18.0	7.5
PCC6	18.7	9.0
PCC7	18.9	10.5
PCC8	18.9	12.0
PCC9	18.9	13.5
ML1	20.0	4.5
ML2	65.0	15.0
SOCAL U1	20.0	0

2.1.2 Preparation of precipitated calcium carbonate

Preparation of the aqueous suspension of calcium hydroxide. 1 liter of water was first heated to 60 °C. Hydration was carried out by stirring in 100 g of granules of calcium oxide, 25-50 mm in size and a max residual CO_2 content of 3.5% was added. After the addition of calcium oxide, the temperature of the suspension was measured at 10 min intervals. Stirring was stopped when the reaction was completed, meaning that there was no further increase in temperature due to the exothermicity of the reaction. The suspension was filtered through a 500 µm sieve in order to remove unreacted material (excessively or insufficiently calcinated material) and later with a 75 µm sieve.

Preparation of precipitated calcium carbonate. A suspension of calcium hydroxide in water with the concentration of 133 g/L was prepared in a 1 L continuously-stirred tank reactor. The temperature was adjusted to 18 °C. Carbon dioxide, at a concentration of 25%, (volume of CO_2 in air), under a constant flow rate of 0.1 Nm^3/h, was bubbled into the tank and reacted with the calcium hydroxide for about 90 min to ensure completion of the carbonation reaction [104]. The temperature in the tank reaches a peak of about 60 °C and starts to decrease at the end of the reaction. The final concentration of PCC was 180 g/L.

Preparation of the stearin soap emulsion. Stearin was first dissolved by adding water at 85 °C with a concentration of 0.40 M. The mixture was stirred for 30 min before the

addition of a 30 wt% sodium hydroxide water solution, with a stearin/hydroxide mole ratio of 1:1.3.

Surface treatment with stearin. The surface coating was carried out by mixing the suspension of precipitated calcium carbonate and the stearin soap emulsion for 60 min. The PCC suspension was brought to a temperature of about 80 °C, and then it was continuously recirculated outside the reaction tank by means of an external pump at a rate of 1 L/h. The stearin soap emulsion was added to the recirculation stream until the desired coating level was reached. The addition rate was 0.5 L/min.

Drying process. The coated calcium carbonate was then separated by vacuum filtration and dried in an oven at 105° C and finally grinded [105]. The image picture of PCC particles prepared in this way was shown in Fig. 2.1.

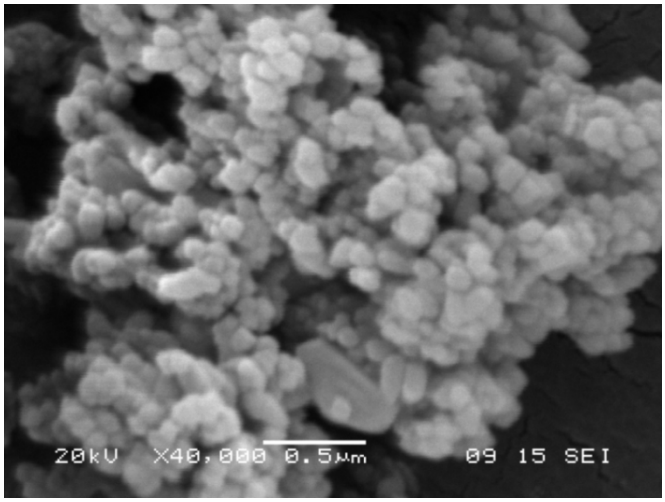

Figure 2.1 SEM picture of PCC particle used

2.1.3 FTIR

Surface organic groups on the coated PCC nanoparticles were analyzed by using a Nicolet 380 spectrometer with diffuse reflectance accessory (DRIFT) from the Thermo Electron Corporation (Thermo Scientific Instruments, Madison, WI, USA). PCC nanoparticles were mixed with potassium bromide (KBr) in proportion 4:96 in order to obtain the DRIFT spectra. During the DRIFT measurements, the spectrum of pure calcium carbonate was chosen as the background. The DRIFT spectra of PCC particles mechanically mixed with pure stearic acid and calcium stearate were also tested for comparison.

This DRIFT measurement was carried out to obtain a semi-qualitative characterization of PCC particles coated with stearin. For the calibration curve of COO^- organic groups, different amounts of calcium stearate were mixed with pure calcium carbonate as the reference sample. Then the height of COO^- group in the DRIFT spectrum was recorded and

plotted against the concentration of stearate, which was carefully controlled to be in a very low range according to the Beer-Lambert law. This calibration curve was then applied to the DRIFT spectra of all the water coated PCC particles, making it possible to obtain the semi-quantitative analysis on the COO^- amount on the PCC surface. Since the possible surface adsorbed molecules can be determined from the FTIR analysis, the relationship between reacted stearin and the nominal amount then could also be assessed.

2.1.4 BET

The specific surface area of all the PCC particles was determined by the low temperature nitrogen adsorption method using the BET technique with the Gemini V series surface area analyzer (Micromeritics Instrument Corporation, Norcross, GA, USA.) The results are shown in Table 2.1. All the investigated nanoparticles were degassed by the flowing-gas devices unit at 100 °C for three hours to remove all impurities on the surface. Then the prepared container tube was analyzed in the liquid nitrogen dewar to maintain a stable measurement condition.

2.1.5 Thermo gravimetric analysis (TGA)

TGA measurement was carried out in air at a heating rate of 5 °C/min by Rheometric Scientific TGA 1000 (TA Instruments, New castle, DE, USA) for all the series coated PCC particles together with PCC monolayer sample ML2 and the PCC mechanical mixtures with stearic acid or calcium stearate. The full temperature region ranges from room temperature to 1000 °C in order to ensure the full decomposition of the organic group on the PCC surface. Derivative thermo gravimetric analysis (DTG) was recorded for the comparison of decomposition peaks.

2.1.6 Differential scanning calorimetry (DSC)

DSC measurements were carried out for the surface characterization of coated PCC particles in aqueous medium with a TA Q200 instrument (TA Instruments, New castle, DE, USA) with nitrogen as the carrier gas and indium used for the calibration. The two main purposes of the DSC measurements are shown as following in different thermal treatment programs.

2.1.6.1 Determination of chemisorbed monolayer amount

In order to discuss the influence of water on the PCC regarding the thermal behavior of organic coating layers, DSC measurements were carried out in three different measurement conditions. In one series, the sample was put into an aluminum hermetic-type pan and

heated from 50 °C to 220 °C at a heating rate of 5 °C/min. In the second series, the same hermetic-type pan was used. After loading of the sample and sealing the pan, the lid was perforated with pinholes in order to better control the emission of free water vapors that might be removed from hydrated alkanoates during heating. The use of hermetic-type pans and lids with pinholes was suggested by the producer of the DSC instrument as being useful in vapor pressure studies (TA Thermal Applications Notes #18 – "Guide for Choosing DSC pans"; and # 5 – "Boiling Point and Vapor Pressure Measurement by Pressure DSC"). Finally, similarly perforated pans were kept at 60 °C for 3 hours and then were heated up to 220 °C at 5 °C/min to check the effects of either possible evaporation of free adsorbed water or dehydration of the monohydrate on the thermal behavior of the surfactants.

2.1.6.2 Thermal transition behavior of calcium alkanoates

The thermal transition behavior of organic coating, especially physisorbed layers on the PCC surface, was discussed by DSC tests of calcium alkanoates monohydrate to study the influence of the dry process on the coating molecular arrangement on the PCC nanoparticles.

2.1.7 Dissolution method

2.1.7.1 Gas chromatograph (GC) internal standard method

The GC internal standard method was used for the determination of stearic acid concentration in solvent. Lauric acid was chosen as the internal standard solvent because of its similar properties to stearic acid and a separate peak in the GC measurement.

Firstly, stearic acid solution and lauric acid solution were prepared in acetone to be 10 and 5 mg/mL, respectively, and were kept at 4°C in a refrigerator. Each time before the GC analysis, an aliquot of both the stearic acid and lauric acid solutions was brought back to room temperature and then was diluted to a suitable concentration in acetone. The stearic acid solution was diluted to be a series of different concentrations from 0.5 to 2.5 mg/mL, while the concentration of the lauric acid solution was kept constant at 0.5mg/mL.

Secondly, a GC measurement was carried out with the Agilent 7890A instrument equipped with a flame ionization detector (FID) (Agilent technologies Palo Alto CA, USA). Both the injector and detector temperatures were 300 °C. The capillary column HP-FFAP was programmed from 110 °C (4 min) to 240 °C at 10 °C/min. Helium gas was used as the carrier gas, and at least five 1μL splitless injections were made for each solution sample. The GC spectra of lauric acid and stearic acid are shown in Fig. 2.2, and the peak areas were calculated for obtaining the calibration curve.

The calibration curve shows the ratio of peak area of stearic acid to the peak area of lauric acid as the Y-axis and the ratio of concentration of stearic acid to the concentration of lauric acid as the X-axis. In the calibration curve, the slope of the linear line is the internal response factor and would be used in the analysis for an unknown concentration of stearic acid solution.

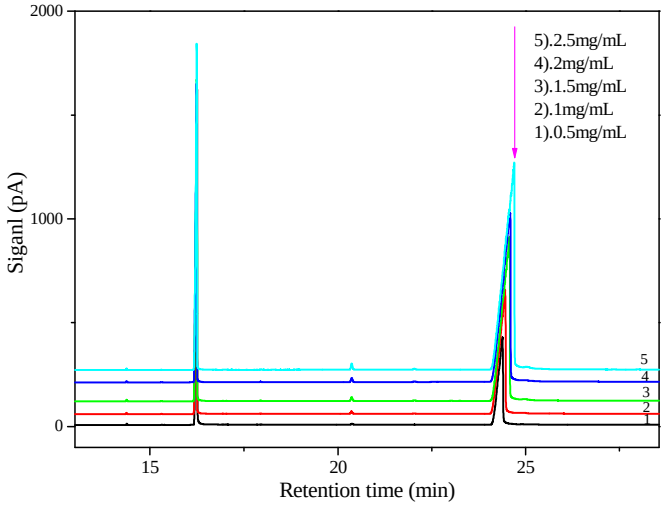

Figure 2.2 GC spectra of stearic acid with lauric acid as internal standard materials

2.1.7.2 Surface coating of PCC nanoparticles in solvent

Pure precipitated calcium carbonate particles SOCAL U1 were supplied by SOLVAY Advanced Functional Mineral Company. This pure calcium carbonate was coated with stearic acid in acetone, which is a good solvent of stearic acid. The pure nanoparticles were firstly fully wetted in the solvent. Then a stearic acid solution with a fixed coating concentration was added to the particle suspension. In order to allow sufficient time for the reaction between calcium carbonate and stearic acid, the acetone suspension was kept stirred at 80 °C for 4 hours.

Moreover, the series of PCCs nanoparticles modified with stearin in water medium were also analyzed using the dissolution method during a recoating process with stearic acid solution in acetone. All PCC particles were coated again with an excess amount of stearic acid in acetone at 80 °C. After both the pure calcium carbonate and the already surface coated PCCs reacted with stearic acid in solvent, the unknown concentration of the stearic acid solution is then determined by the GC analysis. The lauric acid solution was diluted to be 0.5 mg/mL, similar to the calibration procedure.

2.1.8 Preparation of calcium alkanoate monohydrate

Calcium alkanoate monohydrates were prepared in the laboratory following the literature method [106, 107] to discuss the thermal dependence at different temperatures.

They were prepared from three different fatty acids, stearic acid, palmitic acid, and the stearin, which in our work is the Pristerene 4937 as mentioned in 2.1.1.

The fatty acid was put into distilled hot water at 85 °C. Meanwhile, the calcium hydroxide water solution was also prepared and added to the water solution with fatty acid using a magnetic stirrer for 3 hours. Afterwards, the precipitated calcium soap was washed in the distilled water and then filtered before being air-dried at room temperature. FTIR spectra was used to determine the purity of calcium soaps.

2.1.9 X-ray diffraction (XRD)

The crystal structure of the stearate multilayer on the PCC surface was analyzed using a Siemens Kristalloflex 800 diffractometer (SIEMENS AG, Munich, Germany) with CuKα radiation. The X-ray scans were performed in the 2θ range from 1.5° to 60°. The typical patterns of calcium carboxylate were discussed and the thermal dependence of stearate polymorphism was also discussed in view of the XRD measurements. The influence of thermal treatment on the surface organic layers was compared by determining the interlayer spacing distance. Bragg d-spacing corresponding to the interlayer distance of the crystal lattice was calculated from the peaks appearing in the curves using the Bragg's law: $n\lambda = 2d \sin\theta$, where =1.5418 Å.

2.1.10 X-ray photoelectron spectroscopy (XPS)

XPS spectra were recorded using a Kratos XSAM 800 spectrometer (Kratos Analytical Instruments Ltd, Manchester, UK) operated in fixed analyzer transmission mode using MgK$\alpha_{1,2}$ (1253.6 eV) excitation. The pressure of the analysis chamber was below 10^{-7} Pa. Wide scan spectra were recorded for all samples in the 100-1300 eV kinetic energy range with 0.5 eV steps and 0.5 s dwell time. High-resolution spectra of photoelectron lines of the main constituent elements as well as the C1s region of the carbon-containing layers and contaminations were recorded by 0.1 eV steps having a minimum of 1 s dwell time. Spectra were referenced against the energy of the C1s line of the hydrocarbon type adventitious carbon (present or built up at the surface of the samples during spectra acquisition) set at 285 eV B.E. (binding energy). Quantitative analysis based on peak area intensities after the removal of the Shirley- or linear-type background was performed by the Vision 2000 and XPS MultiQuant programs [108, 109] using the experimentally determined photo-ionization cross-section data of Evans *et al.* [110] and asymmetry parameters of Reilman *et al* [111].

2.1.11 Inverse gas chromatograph

IGC is a very useful physical characterization technique in the surface free energy analysis for particles. In this work, the known gas or vapor is injected down the column at a fixed carrier gas flow rate. The retention time of the probe molecule is then recorded by the traditional GC detectors. Several literature papers reviewed the IGC technique about the application in depth [48, 85, 112-114].

In this work, both the dispersion and specific components of surface free energy were discussed, since they can be related to the surface tension and acid-base properties, respectively. The dispersion component of the surface tension of the fillers was determined by means of infinite dilution using n-alkanes with different chain lengths. The specific component of the surface energy of the fillers was measured with three polar solvents: tetrahydrofuran (THF), ethylacetate (EtAc), and chloroform (CHCl3). All solvents used were of chromatography grade.

The influence of the precondition temperature on the two components of surface energy was discussed when PCC particles were preconditioned at 140 °C and 60 °C, respectively. In order to prepare a PCC particle packed column, the fillers were first aggregated in methanol and then dried at room temperature. The ground filler was sieved and the fraction between 800 and 1000 μm was used as packing. Then those fillers were added into a stainless column of 50 cm in length and 6 mm in internal diameter, which was connected with the inlet and detected parts in the gas chromatograph instrument. The preconditioning process under different temperatures lasted for about 16 hours under the constant flow of nitrogen to ensure a stable PCC surface.

The vapor amount of both the non-polar n-alkanes and the polar probes injected into the packed column with PCC fillers changed between 5 and 20 μL: methane was used as marker and retention peaks were recorded using the flame ionization detector (FID). High purity nitrogen was used as a carrier gas and its flow rate varied between 10 and 20 mL/min. The temperature of both the injector and the FID detector was set to 200 °C. Each reported value is the result of a minimum of three parallel measurements.

2.2 Surface characterization of Polymer/PCC composites

2.2.1 Materials for polymer nanocomposites

Two different polymers were chosen as the polymer matrix. Firstly, high-density polyethylene (HDPE) Eltex®B4020 from Solvay Polyolefins (Rosignano, Italy) was used.

This high-density polyethylene is specifically intended for the injection moulding process. Its density is about 0.952 g/cm^3 and the melt index is about 1.9 g/10min (190 °C/2.16 kg).

Another polymer polylactic acid (PLA), which is commercially available and specifically designed for extrusion grade, PLA Ingeo 2002D, was purchased from Natureworks LLC, Milan, Italy. PLA 2002D has a density of 1.24 g/cm^3 and the melt index is between 5 and 7 g/10min (210 °C/2.16 kg). The D-isomer content is about 4.0% in this PLA grade (Mw = 2.53 × 10^5 g/mol).

The fillers used in this work are PCC particles with or without surface coating as mentioned in 2.1.1. The other type of inorganic fillers used were the halloysite natural tubes (HNT) supplied by Imerys Tiles Minerals Italia Reggio Emilia (RE), Italy. These halloysite nanotubes have a diameter typically smaller than 100 nm, and a length typically ranging from about 500 nm to over 1-2 μm. The HNT schematic structure is shown in Fig. 2.3.

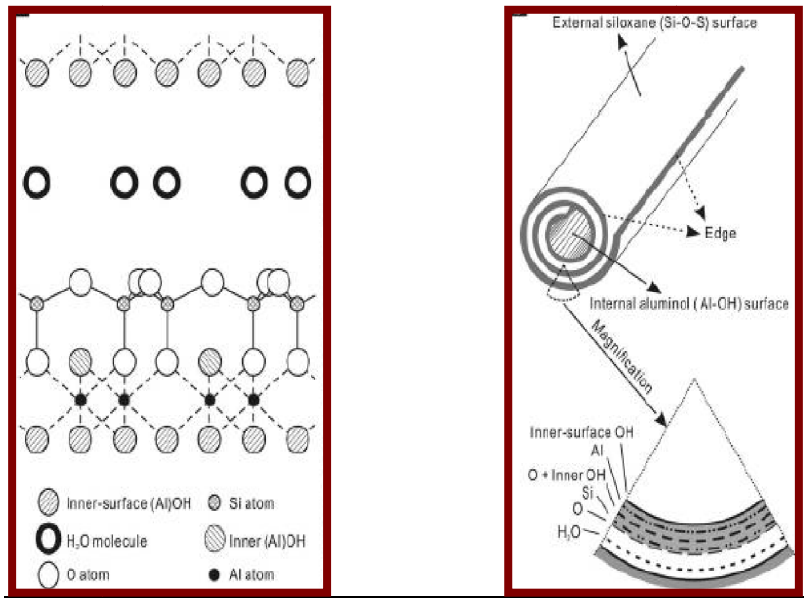

(a) (b)

Figure 2.3. From reference [115] Schematic diagrams of (a) the crystalline structure of halloysite-(10 Å), and (b) the structure of a halloysite nanotube

2.2.2 Preparation of polymer composites

The polymer nanocomposites studied in this work were prepared by melt extrusion using the MiniLab II Haake Rheomex CTW 5 conical twin-screw extruder (Thermo Scientific Haake GmbH, Karlsruhe, Germany). After extrusion, the molten materials were transferred through a preheated cylinder to the Haake MiniJet II mini injection molder (Thermo Scientific Haake GmbH, Karlsruhe, Germany) to obtain ASTM D638 V dog-bone tensile bars and impact specimens used for measurements and analysis.

HDPE nanocomposites. HDPE pellets and PCC fillers were dried at 80°C in a vacuum oven for four hours before the extrusion process. Ten percent PCC particles (in volume) with different surface coating amounts were added into HDPE for mechanical mixing and the HDPE sample code is specified in Table 2.2. The extrusion barrel was programmed to be at a temperature of 190 °C and a screw speed of 90 rpm with the cycle time of 30 seconds. The injection mold program was set: barrel: 190 °C, mold, 60 °C, injection pressure: 800 bar and cycle time: 40 seconds. The dog-bone bars for the tensile measurement were prepared with the Mould bar type 3 (557-2290 tensile bar) and the dimension mould for the impact measurement is 80*10*4 mm from the Mould Rechtech (557-2296).

Table 2.2 Specification of HDPE/PCC composites

Composites code	Composition (HDPE/PCC) *Volume %*	PCC code	PCC nominal coating (*wt%*)
PE00	100/0	----	0
PE01	90/10	PCC1	0
PE02	90/10	PCC2	3.0
PE03	90/10	PCC3	4.5
PE04	90/10	PCC4	6.0
PE05	90/10	PCC5	7.5
PE06	90/10	PCC6	9.0
PE07	90/10	PCC7	10.5
PE08	90/10	PCC8	12.0
PE09	90/10	PCC9	13.5
PES1	90/10	S2	2.75
PES2	90/10	ML1	4.5
PEML	90/10	ML2	15

PLA nanocomposites. PLA/PCC binary composites (with PCC9) were prepared with increasing filler content from 5 wt% to 25 wt%. PLA/HNT composites were prepared with the nanotubes loading from 2 wt% to 10 wt%. The compositions and codes of all the PLA nanocomposites with both PCC and HNT are shown in Table 2.3. Before the extrusion process, both the PLA pellets and nanofillers were dried in a vacuum oven at 80 °C for 4 hours. The temperature of the extruder barrel and injection chamber for PLA specimens were set to be 180 °C. The injection mould had a temperature of 50 °C and the injection time cycle was set to be 30 seconds under a high pressure of 700 bar. After molding, the specimens were placed in nylon bags with vacuum sealing to prevent moisture absorption.

Table 2.3 Specification of PLA binary and ternary composites

PLA composite code	Composition (*wt%*)		
	PLA	HNT	PCC9
Pure PLA	100	0	0
PLA/PCC05	95	0	5
PLA/PCC10	90	0	10
PLA/PCC15	85	0	15
PLA/PCC20	80	0	20
PLA/PCC25	75	0	25
PLA/HNT02	98	2	0
PLA/HNT05	95	5	0
PLA/HNT08	92	8	0
PLA/HNT10	90	10	0
PHC1	90	5	5
PHC2	85	5	10
PHC3	80	5	15
PHC4	75	5	20
PHC5	70	5	25

HDPE nanocomposites with PCC particles coated with different fatty acids. In this work, a series of fatty acids with different chain lengths were chosen as the surface coating agents for PCC particles in order to discuss the influence of surface coating thickness on the mechanical properties. The surface coating process was carried out in acetone as a solvent at 80 °C for 4 hours to allow enough time to ensure a full reaction, as mentioned in 2.1.7. After drying at 80 °C in a vacuum oven for 8 hours, the PCC particles were mixed with HDPE before melt extrusion following the same conditions for HDPE composites with the HAAKE MiniLab. The tensile and impact specimens were prepared with the HAAKE MiniJet injection moulding machine.

2.2.3 Mechanical measurements

Tensile tests. The dog-bone tensile bars of HDPE and its composites were molded by HAAKE MiniJet with the Mold form HAAKE Mold tensile bar type 3 (557-2290). Tensile tests were carried out with an Instron 14302 universal testing machine (Canton MA, USA), equipped with a 10 kN load cell and interfaced with a computer running the Testworks 4.0 software (MTS Systems Corporation, Eden Prairie MN, USA). Tensile tests were performed at room temperature following the ASTM D638 procedure at a crosshead speed of 10 mm/min. At least five samples of each material were tested at room temperature. The PLA nanocomposites were tested following the same procedure.

Charpy impact. To evaluate the impact strength of the polymer nanocomposites, impact tests were carried out according to ASTM D256, using a CEAST (Torino, I) pendulum with a striking speed of 3.5 m/s. A minimum of three specimens was tested, and the average energy was calculated for each point reported.

2.2.4 Thermal behavior

The thermal behavior of polymer nanocomposites was studied by the DSC measurement with the TA Q200 instrument.

Isothermal crystallization analysis. The crystallization behaviour of PLA composites was investigated with nitrogen as a purge gas. The isothermal program was carried out firstly from 20 °C to 190 °C at a heating rate 5 °C/min. The sample was kept at 190 °C for 5 minutes to remove any thermal history before isothermal measurement at 120 °C as the crystallization temperature in this work. The temperature was maintained at 120 °C until crystallization was completed. The Avrami equation was used for the kinetic crystallization study.

Non-isothermal analysis. All the injection molded samples of PLA composites were investigated by DSC from room temperature to 190 °C. The glass transition temperature (T_g), cold crystallization temperature (T_{cc}), melting temperature (T_m) of different PLA composites were recorded together with the enthalpies of cold crystallization and fusion.

2.2.5 Dynamic mechanical thermal analysis (DMTA)

DMTA measurement was applied to pure PLA and PLA composites prepared with PCC or HNT fillers by means of a Gabo Eplexor® 100N (Gabo Qualimeter GmbH, Ahlden, Germany). Test bars were cut from the tensile bar specimens (size: 20 x 5 x 1.5 mm) and mounted in tensile geometry. The dynamic storage and loss modulus of the investigated samples are recorded with a constant frequency of 1.00 Hz as a function of temperature from -100 °C to 150 °C at a heating rate of 2 °C/min. The tension mode is chosen for all the polymer nanocomposites.

2.2.6 Scanning electron microscopy (SEM)

HDPE/PCC composites. The morphology of HDPE/PCC composites was studied by a Jeol JSM-5600LV scanning electron microscope (Jeol Ltd, Tokyo, Japan). The fracture surface of samples after impact testing was analyzed for the deformation mechanism study.

PLA composites. The fracture surface of the tensile specimens was investigated by the SEM with the Jeol ISM-5600LV instrument. Prior to SEM analysis, all surfaces were sputtered with a thin layer of gold.

Chapter 3 Surface characterization of coated PCC particles with stearin in water medium

3.1 Introduction

As mentioned before, precipitated calcium carbonate (PCC) particles are more widely used as functional fillers in polymers because of the low cost of the nanofillers and the improvement of both stiffness and toughness [6, 7, 116, 117]. Many researchers have discussed PCC filled toughening of polyolefin plastics, which strongly depends on many factors, such as particle size [118], critical interparticle distance [3], interfacial adhesion between fillers and matrix [84, 119] and the crystalline structure of the matrix [120]. The most accepted filler toughening mechanism is the energy adsorption mechanism based on the extensive plastic deformation of the polymer matrix after the debonding between the polymer matrix and the filler, which is followed by the formation of polymer fibrils from the matrix ligaments around the microvoids. There are two element factors that are strongly affected on the debonding, which is the process that enables the attainment of a high level of plastic deformation. The first one is to have a suitable interface adhesion between nanoparticles and the polymer matrix, while the second one is to achieve a homogeneous dispersion of nanoparticles in the polymer. As the nanoparticles quite easily tend to aggregate with each other due to the high surface energy, then it is necessary that some kind of surface coating be applied to the PCC nanoparticles.

Fatty acids, usually stearic acid [121], are the most common surfactants for PCC particles due to their high availability and low cost. Industrially, PCC particles are produced by the carbonation reaction between calcium hydroxide and carbon dioxide. Then, in order to decrease the high surface energy of these hydrophilic particles, the surface modification is directly carried out with stearic acid salts in aqueous PCC suspensions before the final drying step. Nevertheless, only limited information has been reported about the adsorption processes during aqueous coating with stearic acid. Suess [122] used Carbon 14 labeled stearic acid and observed a Langmuir-type isotherm showing monolayer adsorption. He also found that a much lower adsorption level could be reached when the coating was carried out in water rather than in a solvent. The reason for this result was not clear, and it was postulated to be due to the adsorption of a hydrated calcium bicarbonate complex.

In the literature, some papers have been published on the characterization of stearic acid coated PCCs, but only in either dry conditions by means of a high speed internal mixer or in a solution of a good solvent for stearic acid (for example toluene). However, there are

different opinions in the scientific literature about the structure and properties of the organic coating layer on the surface of fatty acid coated calcium carbonate. It is generally accepted that the chemical reaction between stearic acid and calcium carbonate results in calcium stearate ($CaSt_2$) on the surface during dry or solvent coating [123, 124]. Other researchers [100] suggested that only one stearic acid molecule was attached to each Ca^{2+} cation to result in calcium stearate bicarbonate, $Ca(HCO_3)OOCC_{17}H_{35}$. Similarly, Fekete *et al.* [99] suggested, on the basis of XPS technology, that only one molecule of stearic acid reacted with each Ca^{2+}, accompanied by hydrolytic degradation during the reaction of stearic acid with calcium carbonate. Packed vertical arrangement of the surfactant molecules indicated that the dry coating process produced a similar monolayer compared to the solvent process.

The optimum coating amount for PCC nanoparticles is another critical factor during the application in the polymer nanocomposites with enhanced toughness performance. This depends on the type of surface modification, the chemical reaction, and the arrangement of the surfactant molecules on the surface. Osman and co-workers[46] found that an excessive amount of stearic acid, in dry coating, led to processing problems and inferior mechanical properties, of the final composites, apart from stiffness. Surface coating of PCCs with stearic acid effectively reduces the dispersive component of surface tension from 45.1 to 18 mJ/m^2 [93], which results in a better dispersion of rigid particles and decreases the adhesion between fillers and polymer matrix.

From the current literature it seems that two types of stearate salts can be possibly present on the surface of calcium carbonate particles: a stearate monolayer (CSM) and calcium stearate, $CaSt_2$, adsorbed to the surface. The reaction leading to the formation of the chemisorbed monolayer may be schematized as follows [125]:

$$> Ca\text{–}OH + HOOC\text{–}R \rightarrow > Ca\text{–}OOC\text{–}R + H_2O \qquad (3.1)$$

where $> Ca$ denotes a surface calcium site, and R indicates the hydrocarbon chain of the stearate molecule.

The main purpose of this section is to discuss the molecular structure of the organic coating of calcium carbonate particles prepared in aqueous medium, which is definitely the most used industrial process as mentioned in Chapter 2.1.2. A series of experimental PCC nanoparticles coated with stearic acid in aqueous medium as shown in Table 2.1 was characterized. The surface characterization of stearic acid coated PCCs was carried out in order to distinguish the chemically and physically adsorbed surface organic structure present

on the surface of the particles and the degree of surface coating. The coating processed in different mediums was also discussed regarding the surfactant adsorption mechanism.

3.2 Surface organic molecular structure

3.2.1 FTIR

The organic group on the PCC surface after coating can be analyzed by the FTIR measurements. According to the literature, the organic group of COO^- is present in either the calcium stearate or carbon stearate bicarbonate as a possible organic group on the coated PCC surface, while there is a record of the C=O group in the free acid that appeared when the coating amount is in excess. Therefore, the FTIR spectra of pure PCC, calcium carbonate, and free acid were characterized for comparing characteristic peaks as shown in Fig. 3.1, and the main peaks in the spectra for three different materials is shown in Table 3.1. In the FTIR peak of pure calcium carbonate, there is one peak of a CO_3^{2-} combination peak at about 1795 cm^{-1} and a large peak from about 1700 to 1250 cm^{-1} that is attributed to the stretching vibrations. The second large peak can overlay the effect of the surface organic group of COO^-. Subsequently, the diffused reflectance infrared technology (DRIFT) is used for separating the organic groups when the spectrum of pure calcium carbonate is chosen as the background.

Table 3.1 IR wave number (cm^{-1}) for stearic acid, calcium carbonate and calcium stearate [126]

Stearic acid	Calcium carbonate	Calcium stearate	Assignment
	2980		CO_3 asym str
	2960		CO_3^{2-} asym str
2954		2958	CH_3 asym str
2916		2918	CH_2 asym str
	2873		CO_3^{2-} asym str
2870			CH_3 sym str
2849		2850	CH_2 sym str
	1795		CO_3^{2-} combination band
1697			C=O str
		1575	C=O str for COO^-
	~1486		
1471			CH_3 scissors def
1464			CH_2 scissors def
1431			C-O str + OH def
1150-1350			CH_2 wagging & twisting
	876		CO_3^{2-} out of plane bend
	713		CO_3^{2-} degenerate bend

The subscripts: *str* presents stretching, *sym* presents symmetric and *asym* presents antisymmetric.

The DRIFT method was also used for the semi-quantitatively calculation of the organic group in the coated PCC particles with different nominal coating amounts. The DRIFT spectrum of coated PCC particles is compared to that of the PCC mechanical mixture with pure calcium stearate and stearic acid as shown in Fig. 3.2. The spectrum of PCC6 is also reported as an example in Fig 3.2. It is evident from this qualitative analysis that only the COO^- peak appeared on the spectra of PCC6, indicating that there is no free stearic acid on the surface after the coating process, only its salts. However, this technique cannot distinguish between calcium stearate ($CaSt_2$) and a stearate monolayer (CSM) in Formula 3.1, and their analogues calcium palmitate ($CaPm_2$) and chemisorbed palmitate monolayer (CPM), as a consequence of the reaction of stearin with calcium carbonate.

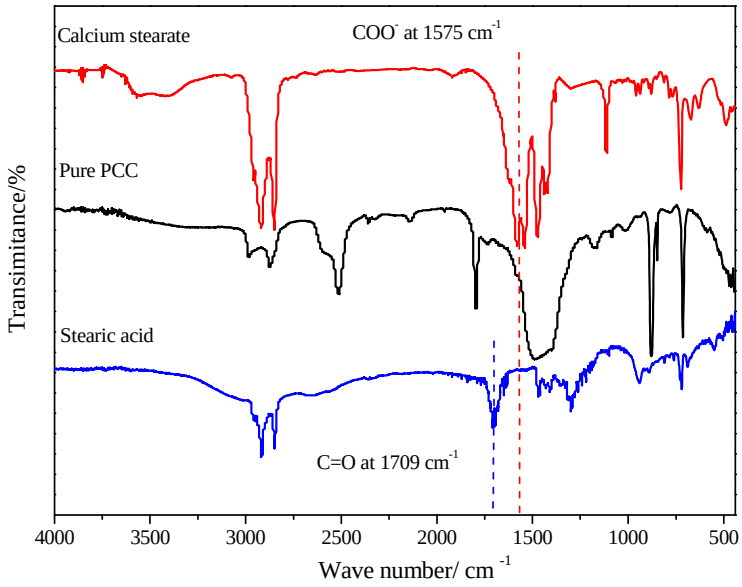

Figure 3.1 IR spectra of pure calcium carbonate, stearic acid and calcium stearate

Nonetheless, the evidence of the peak corresponding to the COO^- group on the coated PCC surface means that the stearate is present on the PCC surface in either a chemisorbed or physisorbed form. The adsorbed amount of COO^- on the PCC surface was determined in semi-quantitative calculation using a series of DRIFT spectra. As mentioned in experimental part 2.1.3, the calibration curve for organic COO^- group is obtained from the characteristic peak at 1575 cm^{-1} in the DRIFT spectra of pure PCC mixture with different concentration calcium stearates following the Beer-Lambert Law. Then, the height of the COO^- group on the coated PCC particles was chosen to calculate the amount of adsorbed coating agents. Fig. 3.3 shows the relationship between the adsorbed coating agents and the original amount present in the aqueous solution. This semi-quantitative analysis indicates that there is a kind of linear correlation between the amount of coating agents adsorbed on

the PCC surface and its concentration in the water solution. The adsorbed amount is determined in terms of g acid/ kg PCC following the industrial match, and this unit is equivalent to the 0.1 wt% unit that is used in this thesis as the main one. This linear relationship between the adsorbed organic amount and the fixed coating amount in the water medium is very interesting, which is different from previous reports for solvent coating [99] that note when once the monolayer coating is obtained, the adsorbed coating amount does not change further.

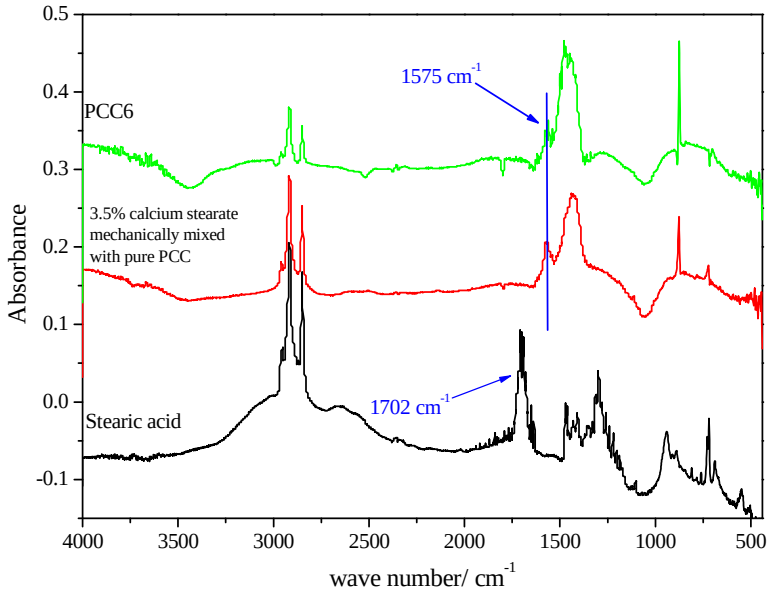

Figure 3.2 DRIFT spectra of PCC6, 3.5 %wt calcium stearate mechanically mixed with pure PCC and stearic acid when pure calcium carbonate was chosen as the background

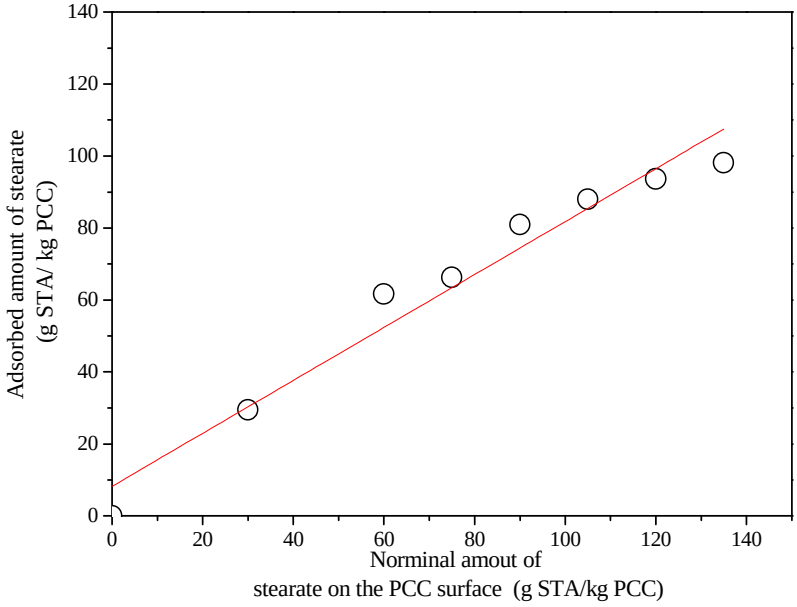

Figure 3.3 DRIFT semi-quantitative analysis of adsorbed stearate amount versus the nominal amount of stearate during the coating process

In fact, the FTIR analysis can only detect COO^- groups, which can be present either in the $CaSt_2$ or in the CSM forms. The molecular structure of coating agents needs to be discovered using other methods. Moreover, the surface coating amount requires a more precise determination besides the semi-quantitative DRIFT discussion. Therefore, the TGA analysis was carried out to clarify the chemical structure of the surfactant, which is the relative proportions of the two salts on the surface of PCC particles coated in water medium.

3.2.2 TGA

TGA is a useful technology used to determine the organic surface amount on the surface of the PCC particles. All the TGA traces of precipitated calcium carbonate samples show two main decomposition stages in Fig 3.4. The first weight loss is attributed to be the decomposition of surface organic coating agents, and the second one can be associated to the decomposition of calcium carbonate. The amount of organic coating on the PCC surface is recorded in Table 3.2, where it is clearly evident that almost all of the surfactant added to the solution is adsorbed on the PCC particles in the form of salts with the COO^- group.

As we mentioned in the FTIR section, the maximum monolayer amount is strongly related to the cross sectional area of surfactant molecules. In the literature, the exact determination of the surface area covered by one molecule of the fatty acid at the equilibrium has been carefully considered [127]. Some researchers have indicated that this parameter depends also on the morphology of the calcium carbonate particles. For example, the cross sectional area of one stearate molecule was calculated as 0.21 nm^2 for rhombohedral {104} calcite planes and 0.31 nm^2 for scalenohedral {211} planes in non-stoichiometric calcites [128]. Another influencing factor on fatty acid adsorption on the nanoparticles surface is reported to be the arrangement of the stearate molecules. Wright and Pratt [129] suggested the value of 0.22-0.26 nm^2 for a perpendicular orientation of stearic acid on the calcite surface and about 0.51 nm^2 for a parallel orientation. If the cross sectional area of stearate is assumed to be 0.205 nm^2, which corresponds to the surface area for one stearate molecule in a perpendicular orientation [99], for the mean surface areas of PCCs used in this work (19 m^2/g), the theoretical full monolayer coverage is about 4.26 wt% for SA coating and 4.17 wt% for stearin coating. However, during the coating process in aqueous medium, the amount of adsorbed stearin increases even beyond the theoretical monolayer coverage, as shown in Table 3.2. In other words, the stearate formed on the PCC surface must probably exist in a multilayer form instead of a single monolayer form, with the number of layers increasing as the adsorbed organic amount of stearin increases.

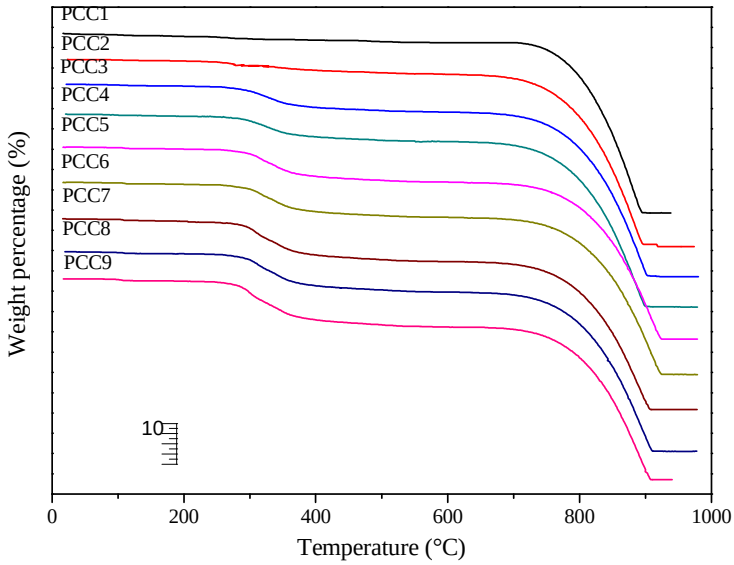

Figure 3.4 TGA trace of all the coated PCC particles in aqueous medium

Recently, some researchers [100, 101, 124] used TGA to differentiate the chemisorbed and physisorbed molecular structure on the coated PCCs, which were prepared in solvent medium. Fig. 3.5 shows the DTG traces of the water coated PCCs prepared with stearin, together with mechanical mixtures of uncoated PCC1 with 10 wt% stearic acid or 10 wt% $CaSt_2$, respectively. All of the coated PCCs showed the same wide decomposition temperature with that of the 10 wt% $CaSt_2$ mixture with pure PCC, from about 240 °C to 400 °C. However, the decomposition peak of stearic acid, which is shown in Fig. 3.5 at around 220 °C, was not observed for this series of PCCs. This observation confirms the DRIFT results that no stearic acid exists on the PCC surface when the surface coating amount exceeds the nominal full monolayer coverage.

Table 3.2 Surface organic amount on the coated PCC surface by TGA technique

Sample code	Nominal coating content (*wt%*)	TGA Coating amount (*wt%*)
PCC1	0	----
PCC2	3	3.16
PCC3	4.5	6.58
PCC4	6	6.54
PCC5	7.5	8.09
PCC6	9	8.89
PCC7	10.5	10.33
PCC8	12	11.54
PCC9	13.5	12.92
ML	15	15.28
SOCAL U1	0	----

Another interesting result from the DTG curves in Fig. 3.5 is that the two peaks, ranging between 240 °C and 400 °C, separate more and more clearly upon increasing the adsorbed amount of stearin. Those two peaks indicate that two different types of stearate exist together on the coated PCC surface. The higher temperature peak probably corresponds to a much stronger interaction with the surface, while the other may be related to layers that are only physically adsorbed. In order to identify these two different types of stearate, the ML2 sample was also analyzed by DTG as a reference. The comparison of the decomposition peak of the chemisorbed stearate in the ML sample with those found in PCC particles enabled us to identify the peak corresponding to the decomposition of the chemisorbed stearate. As it may be easily anticipated, the decomposition of the chemisorbed CSM occurs at a higher temperature with respect to that of the physisorbed $CaSt_2$ because the chemisorbed monolayer is chemically reacted with the free active sites of calcium carbonate nanoparticles.

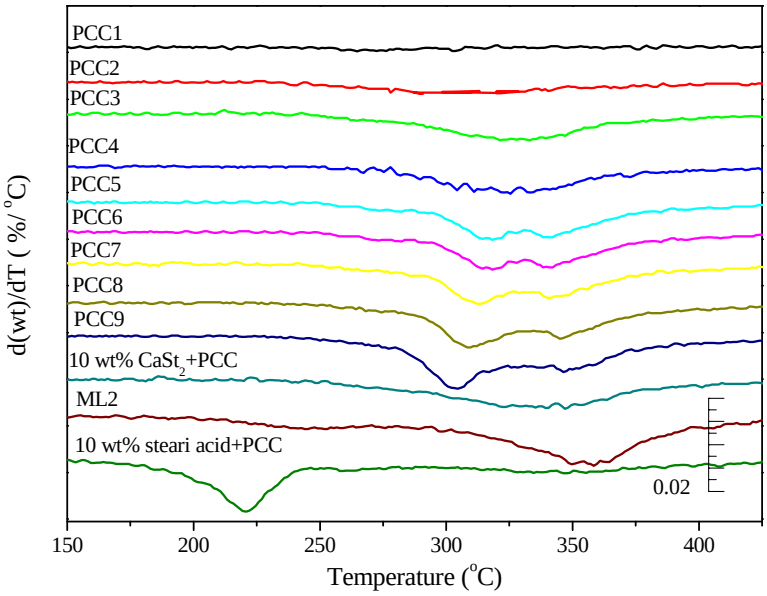

Figure 3.5 DTG traces of the coated PCCs, ML sample, compared to those of PCC mechanical mixtures with 10 wt% stearic acid and calcium stearate ($CaSt_2$)

Moreover, the decomposition peak at lower temperature is attributed to the presence of salts on the coating layer and may be explained by considering that during the surface treatment process with the stearin soap, calcium stearate and palmitate precipitate from the solution as the result of the salt exchange reaction between dissociated Na^+ and Ca^{2+} ions in the water suspension due to the low solubility of $CaSt_2$ and $CaPm_2$ in water [125].

$$Na^+(aq.) + CH_3\text{-}(CH_2)_n\text{-}COO^-(aq.) + Ca^{2+}(aq.) \rightarrow Ca\left(CH_3\text{-}(CH_2)_n\text{-}COO\right)_2\downarrow(s) + Na^+(aq.) \quad (3.2)$$

where *n* is 16 for stearic acid and 14 for palmitic acid. Following the precipitation of each molecule of salt, new Ca^{2+} ions are dissolved from the surface of PCC particles to restore the equilibrium, and the process continues until all of the sodium soap is transformed into the calcium stearate. In conclusion, the PCC particles coated with stearate in water medium resulted in two different types of layers: one chemisorbed monolayer with a strong bond directly on the PCC surface, and a stearate physisorbed multilayer with a relative lower decomposition peak. The organic structure on the PCC surface after the water coating process is compared to dry or solvent coating, where only a monolayer and excess free acid molecules are reported to be present.

3.3 Surface coating composition

3.3.1 DSC measurements

The determination of the surface coating amount of PCC fillers is a critical factor for their application in the field of polymer composites. Based on the TGA measurements, calcium alkanoate species formed on the surface of the PCC surface during coating with stearin soap from aqueous solution when prepared from water precipitation. It is known that calcium stearate ($CaSt_2$) forms a stoichiometric hydrate, calcium stearate monohydrate ($CaSt_2 \cdot H_2O$ or CSH), which shows a complex calorimetric behavior [106, 130]. A sample of calcium stearate monohydrate was prepared in our laboratory for comparison according to a procedure reported in the literature [131, 132]. The DSC trace recorded during the heating of this compound is shown in Fig. 3.6. A dehydration peak of monohydrate (115 °C) and three other peaks corresponding to the transition from the crystalline C2 to the smectic phase (orthorhombic C-face centered lattice) (130 °C), from the orthorhombic to the pseudo-lamellar liquid crystal phase (160 °C, slightly noticeable), and from the pseudo-lamellar to the hexagonal columnar liquid phase (192 °C) appear in the DSC trace of calcium stearate monohydrate, that is very similar to those reported in the literature [133].

The DSC thermal transition behavior of the coated PCC particles is discussed with different measurement conditions as shown in 2.1.6. Moreover, it is quite important to clarify if there is any possible sodium stearate also physisorbed on the coated PCC surface, because the industrial water coating method is processed by adding a water solution of sodium stearate into the suspension of precipitated calcium carbonate. The DSC method is useful to specify the different thermal behaviors of calcium stearate and sodium stearate in the appearance of different thermal transition peaks as shown in Fig. 3.7 together with that of pure stearic acid and calcium palmitate. It is evident that the sodium stearate has different

thermal transition characteristic peaks with the calcium stearate, more specifically, the smectic-to-isotropic phase transition at about 280-290 °C [134]. This DSC curve rules out the possibility that the physically adsorbed stearate is, at least in part, sodium stearate instead of calcium stearate. Meanwhile, the possibility of there being any free fatty acid also can be confirmed by the DSC curves comparison in Fig. 3.7, which matches well with the FTIR and TGA results.

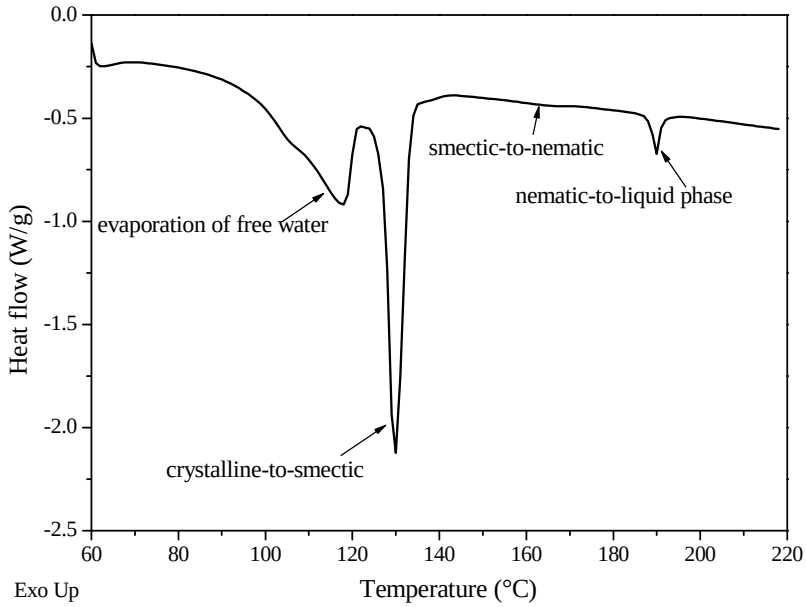

Figure 3.6 DSC trace of calcium stearate monohydrate

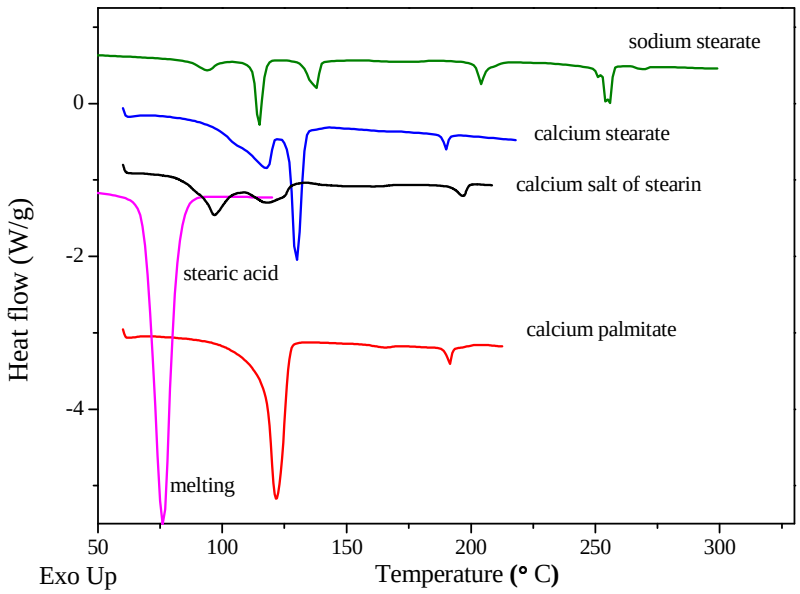

Figure 3.7 DSC traces of calcium stearate, sodium stearate, stearic acid, calcium palmitate and calcium salt of stearin measured in the perforated pan

DSC traces were recorded for all PCC samples with different surface coatings in three different conditions, their traces being shown in Fig. 3.8. A sample with a full monolayer

coating (ML2) prepared by dry-coating is also shown as a reference and was tested in the second measurement condition as shown in Fig. 3.8 (b). As only chemically adsorbed alkanoates are present, no specific peaks appear on its DSC trace because of the strong interaction of the stearate ions with the PCC surface. The only process observed during heating for ML2 is the evaporation of free water adsorbed on the surface during storage. The conclusion that both chemisorbed and physisorbed alkanoates exist on the surface of PCC coated in aqueous solution is further supported by the fact that endothermic peaks related to the transition of physisorbed calcium stearate can be detected in the DSC traces of all of the PCCs studied. However, the peak of the crystalline C2-to-smectic phase transition appears at about 120 °C, that is almost 10 °C lower than the corresponding peak of neat calcium stearate monohydrate in Fig. 3.6. This result can be explained by the eutectic melting of the calcium salts formed from the stearin used in our case which is a mixture of palmitic and stearic acid [135] or by the formation of mixed crystals of calcium stearate and palmitate[136]. The DSC curves of calcium stearate, calcium palmitate and calcium salt from stearin are also compared in Fig. 3.7 to explain the eutectic effect. All of the calcium soaps were prepared in the laboratory and measured in the perforated hermetic pan. In fact, the main thermal transition peak of the calcium salt of stearin (Pristerene 4937), which was used for the PCC surface coating agents during industrial water production, is about 10 °C lower than that of the pure calcium stearate. The main peak of calcium palmitate is even lower and in Fig. 3.7 only one unsymmetrical peak is available. This can be explained by the fact that the closed dehydration peak of monohydrate and the main thermal transition peak could not be separated clearly and overlap each other.

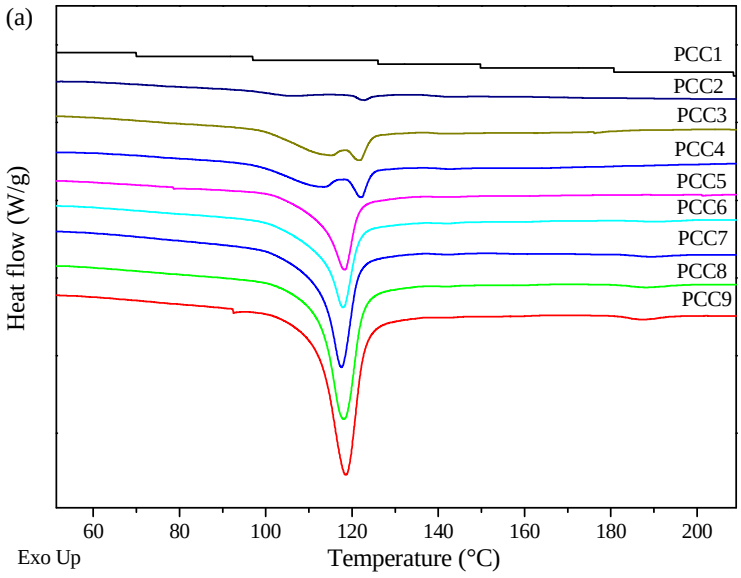

Figure 3.8 (to be continued)

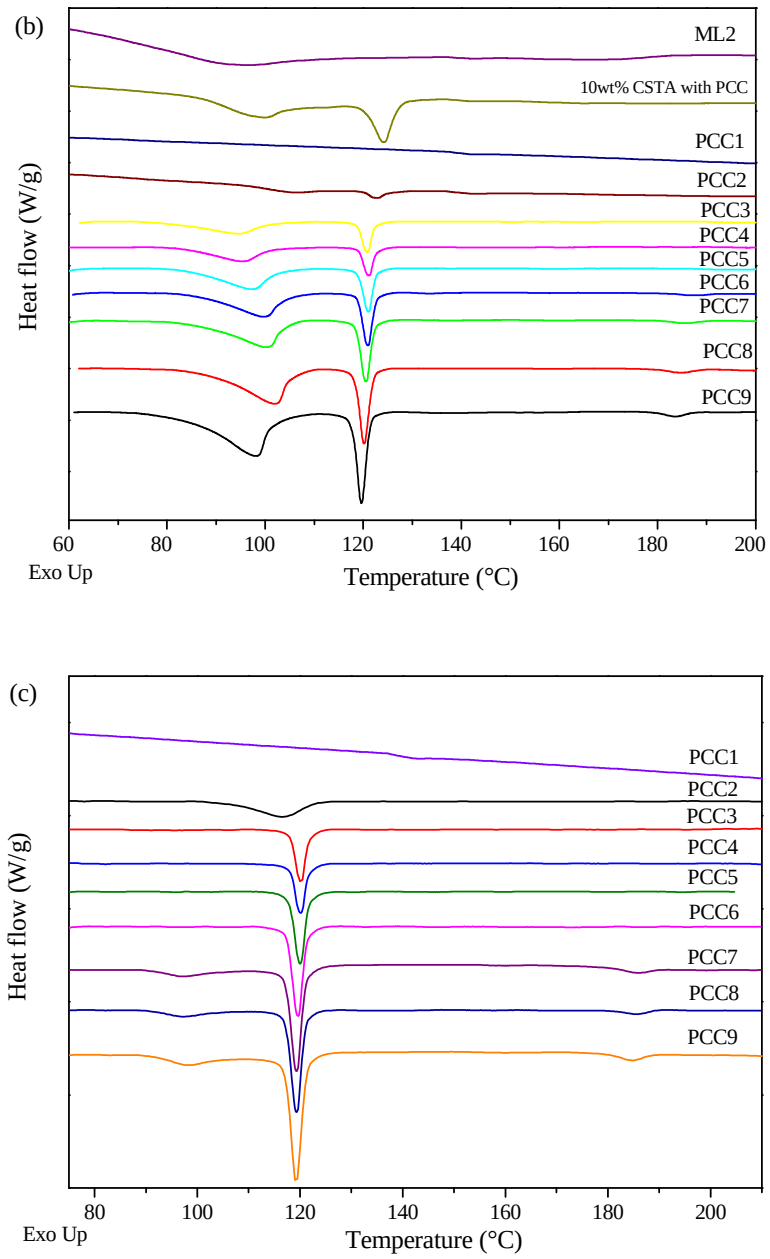

Figure 3.8 DSC traces of water-coated PCCs in different measurement conditions:
(a) standard pan; (b) perforated pan; (c) perforated pan with preconditioning at 60 °C for 3 hours

The influence of water adsorbed on the surface of PCC particles was also studied by DSC different testing conditions as described in the experimental part. It is apparent in Fig. 3.8 that different conditions result in different DSC traces. The peak associated with the evaporation of water adsorbed on the surface of PCC merges with the main transition of the calcium soap of stearin (crystalline C2-to-smectic) in the crimped pan, and only one large asymmetric peak (a peak with a big shoulder) appears on the DSC trace in Fig. 3.8 (a). However, the hermetic-type pan perforated with pinholes allows for a more controlled volatilization of moisture from the surface, which results in two separate peaks in Fig. 3.8 (b)

corresponding to the elimination of free water and to the crystalline C2-to-smectic phase transition, respectively. The preconditioning of the sample at 60 °C for three hours in an open pan, under the continuous flow of nitrogen, can efficiently eliminate water from the surface, and only one main melting peak appears in Fig. 3.8 (c). This shows that the evaporation process is related to physically adsorbed water present on the surface of PCC particles and not crystallization water as in $CaSt_2 \cdot H_2O$. It is known, for example, that anhydrous calcium stearate adsorbs about 0.3% moisture upon exposure to air at room temperature. Moreover, it does not recrystallize to the hydrate form even when suspended in water for many hours [137].

The amount of chemisorbed stearin alkanoates can be calculated from the correlation between peak enthalpy and the amount of stearin used for coating determined by the TGA tests. The enthalpy of the two processes occurring during heating, i.e. volatilization of free water and crystalline-to-smectic transition, was determined from the DSC traces and is plotted against the adsorbed amount of stearin used for coating in Fig. 3.9. The two processes appear simultaneously in the closed pan, while volatilization of free water is absent after preconditioning. Both transition peaks appear, and their enthalpy can be determined in the perforated pan. The enthalpy of each peak increases linearly with the amount of stearin used, indicating that the amount of both the free water and the physisorbed stearin alkanoates are proportional to the total organic content of the surface, as shown in Fig. 3.9. In other words, the amount of chemisorbed stearate is constant on the surface of PCC and corresponds to the intercept with the *x*-axis. The four lines in Fig. 3.9 have almost the same intercept with the *x*-axis that ranges from 3.01 to 3.29 wt% with a slight variation probably due to experimental error. As the surface coating layers separate into an inner chemisorbed monolayer and outer physisorbed multilayer, we can estimate the amount of chemisorbed monolayer from the peak assigned to the crystalline C2-to-smectic phase transition or from the volatilization of free water peak. The DSC data show that this physically adsorbed water on PCC particles is proportional to their organic content, so it seems related to the physisorbed calcium soap of stearin and not to the fraction of the surface of calcium carbonate that remains uncoated during the water treatment.

The analysis of the results obtained in the perforated pan both with and without preconditioning yielded a maximum coating level of about 3.0 wt% for the chemisorbed monolayer. The degree of coverage with the chemisorbed monolayer is one of the most important questions, since it has been reported that the best mechanical performance of polymer nanocomposites was achieved at full monolayer coverage [89]. The theoretical

monolayer coverage of PCC with stearic acid has been discussed extensively in the work of Ukrainczyk *et al* [128]. As already mentioned, the theoretical maximum monolayer coverage is about 4.17 wt% for the average surface area of PCC used in this work (19 m^2/g). In comparing this number to the amount of chemisorbed layer of about 3.0 wt% determined by DSC, the maximum fractional surface coverage is estimated to be about 0.72 for this series of water-coated products. In other words, 72% of the total calcium carbonate surface is covered by a chemisorbed monolayer, and the other remaining stearate/palmitate molecules form physisorbed layers on the monolayer. From the slopes of the fitting lines in Fig. 3.9, we can estimate the melting and dehydration enthalpies for the physisorbed CaSt2 layer in 55 J/g and 109 J/g, respectively. For a comparison with literature data, a value of 75.9 J/g was reported by Vold et al. for the melting enthalpy of anhydrous calcium stearate, although with a different calorimetric technique [137].

The incomplete chemisorbed monolayer on the PCC surface by water coating is totally different from that of the solvent or dry coating method. The presence of free active sites on the PCC surface are strongly related to the water coated particles, which had an important effect on the interfacial adhesion when applied on polymer nanocomposites. In order to confirm the presence of free sites on the PCC surface, the possible reaction between coated PCC and the free stearic acid is investigated by using the dissolution method.

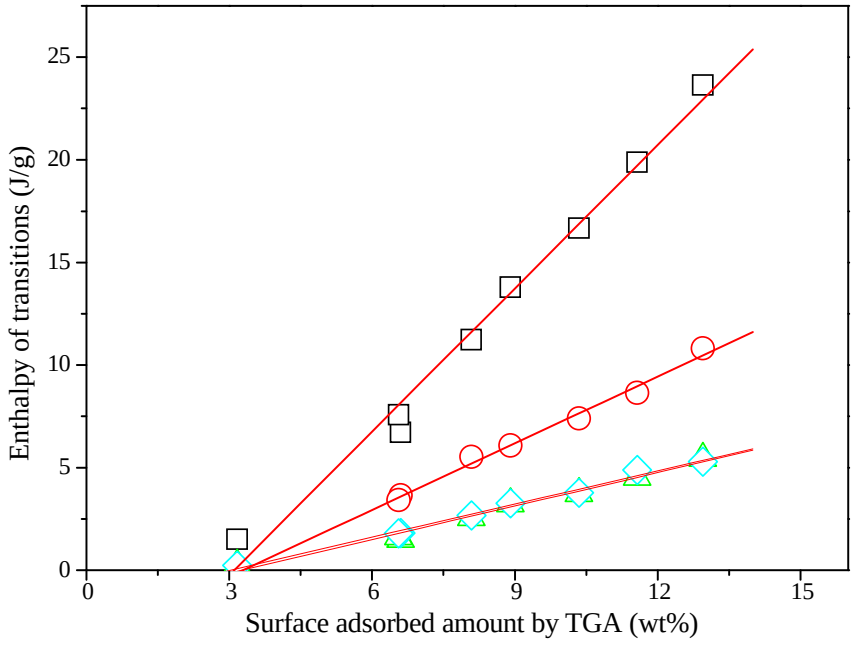

Figure 3.9 Correlation between the enthalpy of transitions and the adsorbed amount of stearin in aqueous medium: standard pan (□): simultaneous volatilization of free water and crystalline-to-smectic transition; perforated pan: separate volatilization of free water (○) and crystalline-to-smectic transition (◊); perforated pan with preconditioning (Δ): only crystalline-to-smectic transition

3.3.2 Dissolution method

3.3.2.1 GC internal standard method

In order to determine the concentration of stearic acid in solvent, the GC internal standard method was carried out to first determine the calibration curve of stearic acid, with lauric acid chosen as the internal standard. The concentration of lauric acid was fixed to 0.5 mg/ml in acetone, while the concentration of stearic acid varied from 0.5 to 2.5 mg/ml. The relationship between the GC peak area ratio between stearic acid and lauric acid and the concentration ratio between stearic acid and lauric acid is plotted in Fig. 3.10. A straight line with a slope of 0.9442 gives an excellent fit through the data and is used for the determination of stearic acid concentration in acetone during the coating process.

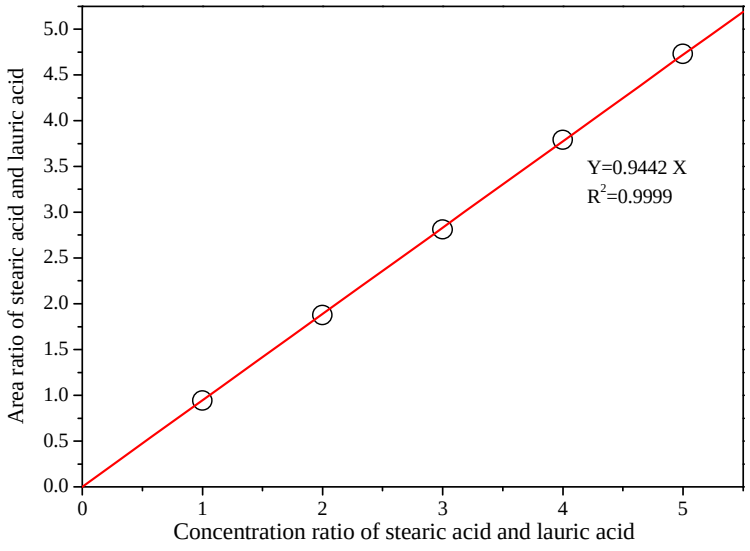

Figure 3.10 Calibration curve of stearic acid concentration in acetone by the GC internal standard method

3.3.2.2 PCC Solvent coating process

The solvent coating process of pure calcium carbonate particles was studied by using the dissolution method, which can record the amount of stearic acid adsorbed on the PCC surface. The initial and final quantity of stearic acid in acetone solution is determined by the GC internal method according to the calibration line.

The pure SOCAL U1 PCC particles were coated with acetone solutions of pure stearic acid with concentrations ranging from 1 to 10 wt%. The adsorbed amount of stearic acid bonded on the surface of the SOCAL U1 first increases linearly until it reaches a constant plateau value as shown in Fig. 3.11. This can be explained as follows: when the amount of stearic acid is small, almost all of the stearic acid molecules have the possibility of reacting with the active sites on the surface of the PCC particles. Then, when the quantity of stearic

acid further increases above the theoretical full monolayer content as defined above, no more free space is available on the PCC surface to react with the extra amount of stearic acid. For the uncoated PCC SOCAL particles used in this work, the maximum amount of chemically-bonded SA thus results in 4.22 wt%, which matches very close (within the experimental limitations due to the GC technique used) with the theoretical full monolayer content, estimated as 4.26 wt% for pure stearic acid. For calcium carbonate, as reported in the scientific literature [138], the surface is positively charged and will easily attract negatively charged molecules like the anionic form of the fatty acid. The dissolution curve for the solvent coating process of pure calcium carbonate particles shown in Fig. 3.11 agrees well with the consideration [99] that a densely packed arrangement of the surfactant molecules can be produced through ionic bonding, which is chemisorbed on the surface of calcite and cannot be washed by normal solvents of fatty acids, like heptanes, toluene and acetone. A further chemical reaction between calcium carbonate and stearic acid in the solvent is unfeasible because of the presence of a full monolayer on the PCC surface. In principle, stearic acid molecules could also physically adsorb to the chemically bonded layer (CSM). To test this possibility, an additional GC measurement has been carried out on the solution obtained after washing the 10 wt% coated PCC with acetone for four hours. No stearic acid peak appeared on the GC spectra reported in Fig. 3.12. This result can be explained by the high solubility of stearic acid in acetone. However, it will be possible for particles treated by the dry coating process to show some free acid molecules in tail-to-tail with the internal chemisorbed monolayer as it has been reported in the literature [99, 139].

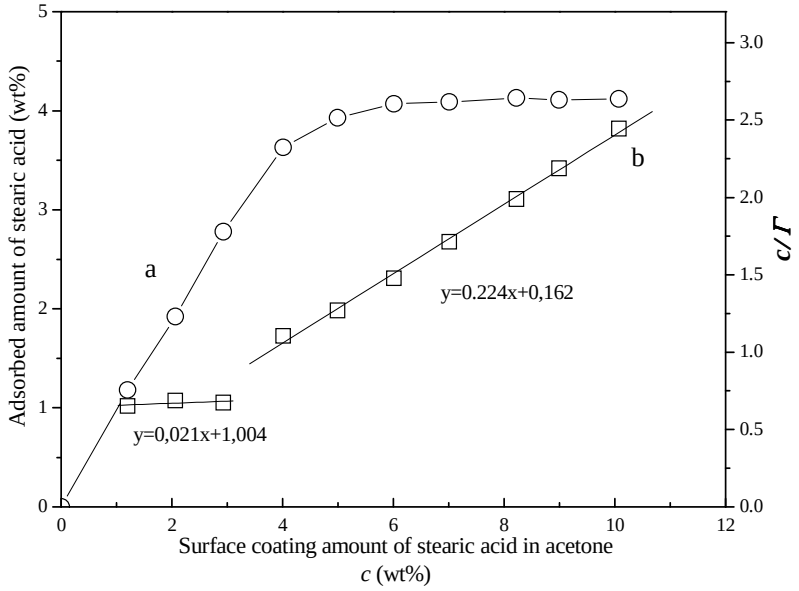

Figure 3.11 Dissolution curves for solvent coating of pure PCC with stearic acid,
(a) Adsorbed amount of stearic acid against the nominal coating amount of pure stearic acid
(b)Langmuir isotherm plot of (c/Γ) versus (c)

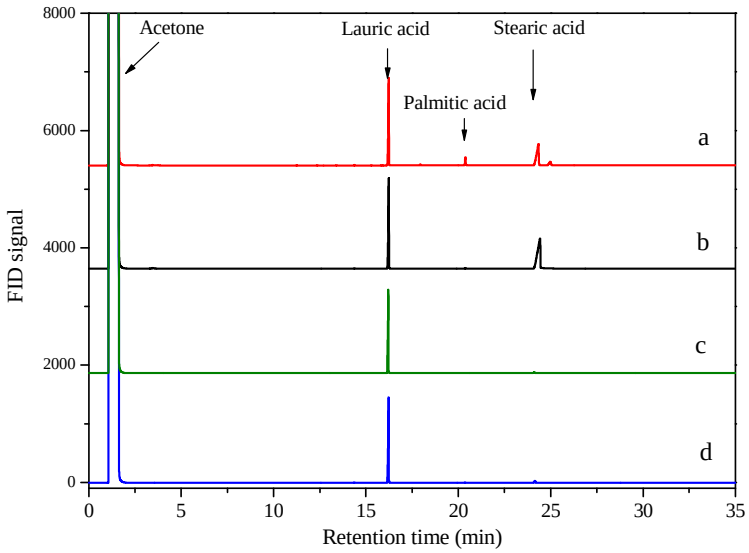

Figure 3.12 GC spectra of acetone solution (a) after the recoating with pure stearic acid for already water coated PCCs (b) after the solvent coating for uncoated PCCs (c) after washing solvent coated PCCs (10w% as example) (d) after washing PCC7 as example

The solvent coating of PCC particles with pure stearic acid follows the Langmuir type isotherm and may be fitted with the following equation:

$$\theta = \frac{\Gamma}{\Gamma_{max}} = \frac{cK}{1 + cK} \tag{3.3}$$

where is θ the surface fractional coverage, which in this study is the ratio between Γ, that is, the number of Ca^{2+} cations that have reacted with the stearate ions and Γ_{max} , i.e. the total of all the potentially available Ca^{2+} sites on the surface; c is the concentration of absorbate in the solution (in our case it is the concentration of stearate ions in the medium); and K is the Langmuir adsorption constant for the equilibrium between the adsorption and desorption processes. Similar Langmuir isotherm results for the adsorption of stearic acid on calcite in water were reported by Suess [122]. Additionally, we used the following rearrangement of the Langmuir equation for the linear fitting of the dissolution data:

$$\frac{c}{\Gamma} = \frac{1}{K\Gamma_{max}} + \frac{c}{\Gamma_{max}} \tag{3.4}$$

A plot of (c/Γ) versus (c) yields a slope as $1/\Gamma max$ and an intercept as $1/(K\Gamma_{max})$, which is shown in Fig. 3.11(b). It is clear from this figure that the data cannot be fitted with a single regression line, but there are two distinct regions where the data points can be fitted with two lines: one with a lower slope at low concentration, and another one with a higher slope at high concentration. Ontko and Angelici [140] also found that there were two different Langmuir adsorption regimes for the chemisorption of the alkyl isocyanides on Au

powder due to the different adsorbed binding mechanisms in different ranges of surface coverage.

3.3.2.3 Recoating process for PCC with incomplete monolayer

The re-coating experiment for already water coated PCCs indicates that the quantity of stearic acid necessary for a full monolayer coating of PCC1 is about 4.22 wt% as shown in Fig. 3.13. This value is consistent with the maximum theoretic monolayer amount and also similar to the experimental value for the pure calcium carbonate particles. However, the adsorbed quantity of stearic acid for all of the water coated PCC nanoparticles is almost a constant value of about 1.18 wt%, except that PCC2 had a much larger value of 2 wt%. The difference between those two values gives the amount already covered by stearin during the water coating process, which is about 3.04 wt%. Again, the free space on the already water coated PCC surface is confirmed to be present and to be a constant value for all of the coated PCC particles with the only exception of PCC2. The amount of the CSM layer from the DSC technique and dissolution method is slight different because of the experiment inaccuracies.

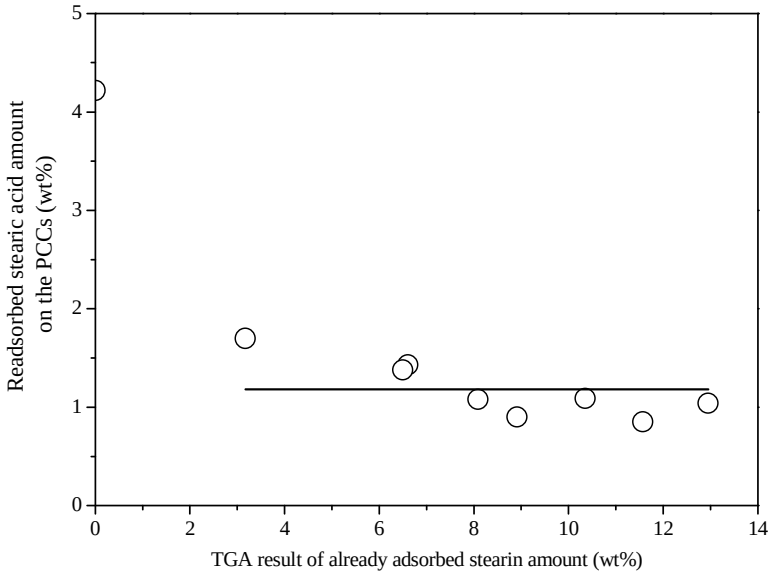

Figure 3.13 Reabsorbed amount of stearic acid on the coated PCC2 to PCC9 in acetone

During the GC measurement for the already water coated PCC particles, as shown in Fig. 3.12 (a), a peak corresponding to palmitic acid appears in the GC spectrum. This can be explained by considering that, for the water coated PCCs we used stearin, which is, a mixture of stearic acid and palmitic acid. After neutralization with sodium hydroxide and the reaction with calcium carbonate, the corresponding calcium stearate and calcium palmitate form as a physically adsorbed layer on the PCC particles. Since an equilibrium

exists in a solution between salts and a pure acid, and the solubility of the two acids (stearic and palmitic) is similar, the occurrence of a peak for palmitic acid can be easily explained. Thus, for the water coated PCCs, pure stearic acid is consumed during two separate reactions, i.e. a part is used for the surface reaction with the Ca sites remaining unreacted after the water coating process, and the other part is for the salt exchange reaction between stearic acid and the calcium palmitate that is physically bonded to the PCC surface. In order to evaluate the amount of stearic acid consumed in the first reaction, we need to also estimate the amount consumed in the second reaction. In this way, the exact amount of stearic acid needed for the reaction with the free Ca sites still available on the PCC surface, in order to reach the full monolayer condition, is given by the difference between the total amount of stearic acid consumed in the dissolution experiment and the quantity used for the salt exchange reaction. The calibration curve for palmitic acid is determined in acetone with lauric acid as an internal standard material.

3.4 Adsorption process of stearate on the PCC surface

Based on the qualitative and quantitative analysis of FTIR, TGA and DSC techniques on the calcium carbonate particles coated with stearin in aqueous medium and the dissolution results on the solvent coating process, the adsorption process of self-assembled stearate molecules on calcium carbonate surface from different solution is discussed in the following section.

According to the data in experimental section 2.1.2 concerning the preparation of sodium stearate, the sodium stearate concentration in water is 399 mM (10.8 wt%) at 80° C as the preparation temperature. According to the Krafft solubility boundary for sodium stearate, the Krafft temperature for this concentration is about 73 °C, and the critical micelle concentration (CMC) is reported to be 85×10^{-6} (mole fraction) or 4.7 mM at 95 °C[141]. Thus, in this work, the sodium stearate in water is above the Krafft boundary, and a homogeneous micelle phase exists like in Scheme 3.1 (a). The aggregation number of molecules is calculated to be 106 according to a soap solubility model [141].

After the addition of sodium stearate aqueous solution into the PCC suspension, micelle adsorption in Scheme 3.1 (b) is supposed to be the dominating mechanism in the surface coating for calcium carbonate in aqueous medium. Amphiphilic molecules used as surface coating agents like sodium stearate are known to form ordered molecular structures. In hydrophilic polar solvents, surfactants like calcium stearate adsorb on the surface of calcium carbonate in two steps. The surfactant molecules first absorb to form a layer with the hydrophilic head group bonded to the surface lining up with one another with the tails

perpendicular to the surface. Then on the top of this first layer, other stearate molecules can absorb in tail-to-tail arrangement to form a hemimicelle or bilayer structure [139]. This is the basic framework when the sodium stearate micelle solution is added into the suspension of the precipitated calcium carbonate. In the water coating process, a large number of stearate micelles are present in the system and are responsible for the formation of both the CSM layer and $CaSt_2$ layers. The micelles will deform during the adsorption process on the high positively charged sites of the PCC surface without opening up. In fact, one half of the stearate molecules in a single micelle will be chemisorbed to the surface; the rest will be physically adsorbed with a weak interface link in a tail-to-tail arrangement [100], as shown in Scheme 3.1(c). When other micelles approach the PCC surface already covered by a first stratum of micelles, they can only connect to the already deposited layer. As mentioned above, a salt exchange reaction between sodium ions with the calcium ions, dissolved in the water suspension of PCCs, leads to the precipitation of micelles of calcium stearate ($CaSt_2$). The process can continue until exhaustion of all of the micelles present in the water medium. It is apparent from Scheme 3.1 (c) that this results in the formation of a chemisorbed monolayer and one or more layers of physically adsorbed $CaSt_2$, controlled only by the van de Waals attraction. The deposition of $CaSt_2$ physically adsorbed on the monolayer surface resembles a sort of epitaxial growth; nevertheless, the monolayer provides a surface that acts as a nucleus for the precipitation of calcium stearate monohydrate. $CaSt_2 \cdot H_2O$ is reported to exist in several crystalline forms, both in the form of disks and lamellas, so the proposed deposition mechanism allows for the continued increase of precipitated stearate molecules on the PCC surface as the original concentration of stearin increases.

Based on the proposed micelle adsorption mechanism for the water coating process, commercially-available, water-coated PCC particles with a stearin content of about 3% such as PCC2 may show a much lower degree of surface coverage. In fact, the aforementioned maximum monolayer coating roughly corresponds to 3.0 wt% stearin for the particle size considered in this work. Because of the micelle precipitation mechanism, in the case of PCC2, only one half of the stearin (corresponding to an organic content of 1.5% with respect to the PCC particles) will be associated to the lower, disk-shape monolayer chemisorbed on the PCC surface, and the rest will be found in the upper, physically adsorbed, disk-layer. This corresponds to a degree of coverage of about 36%, much below the achievable maximum, which can be obtained only above stearin contents above 6 wt% (from PCC4 outwards). This proposed micelle adsorption confirmed our dissolution result

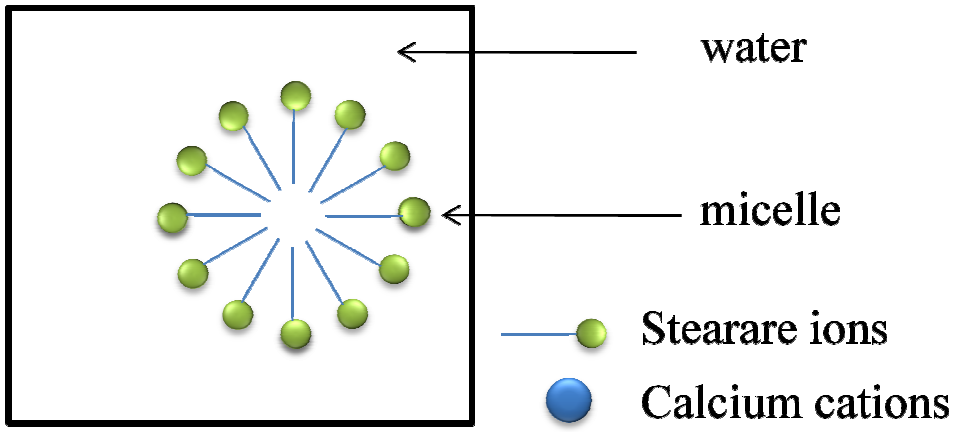

(a)

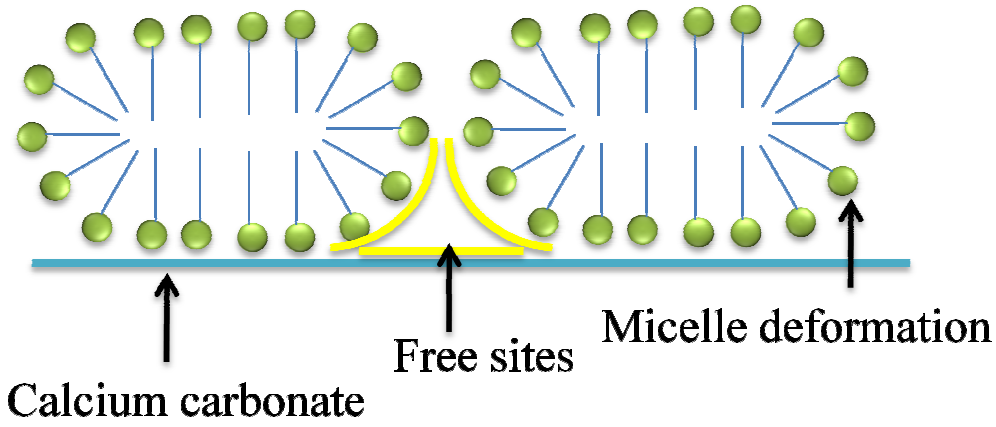

(b)

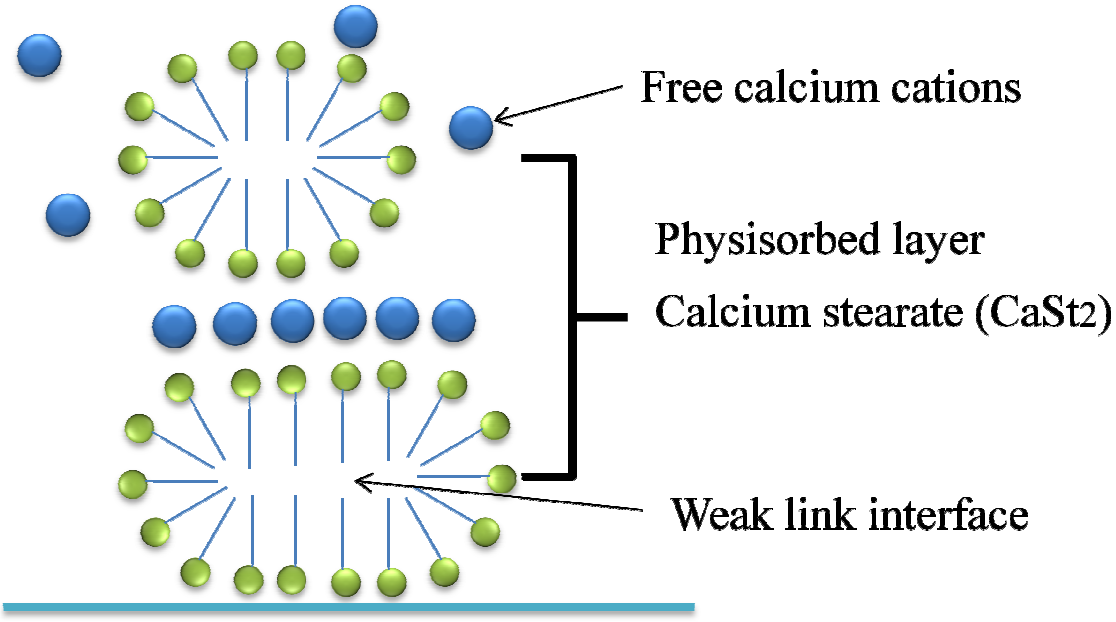

(c)

Scheme 3.1 Micelle adsorption mechanism

of recoating process for the already coated PCC particles, which determined that the free sites on the PCC2 surface are much larger than the other nanoparticles from PCC3 to PCC9 as shown in Fig. 3.13. It should be noted that at a high level of coating, i.e. higher than 6 wt%, the surface will be covered by an array of disk-shaped lamellar micelles, each of which are formed by a chemisorbed lower disk and an upper disk-layer that is physically adsorbed in a tail-to-tail arrangement with the chemisorbed monolayer.

Another important consequence is that the chemisorbed CSM layer on the PCC surface is quite different from the deposited $CaSt_2$ in terms of physical properties, such as, for example, the crystalline-to-smectic transition temperature. The physically adsorbed $CaSt_2$, shows this transition at around 120 °C, while the chemisorbed CSM layer does not show this transition at all. In fact, the DSC measurement as shown in Fig. 3.8 also showed no other peaks associated with the chemisorbed monolayer, but only peaks similar to those previously reported in the literature for both the dehydration and melting peaks of $CaSt_2$ in the form of a monohydrate ($CaSt_2 \cdot H_2O$) [106, 136]. One of the most relevant differences is the decomposition peak of the chemisorbed part, which is higher than that measured for the physisorbed one as shown in Fig. 3.5. This can be explained considering that the chemical bonding for the chemisorbed CSM layer is due to ionic forces, while only weak Van der Waals forces are probably present between the CSM and the physisorbed $CaSt_2$ layer.

The different adsorption processes of fatty acids on the PCC surface by water and solvent coating can be explained by the Langmuir equation. A similar work by Chen and Frank [139] used the Langmuir equation to discuss the adsorption process of stearate molecules on amorphous silica surfaces from a hexadecane solvent. For the adsorption of the stearate molecules from aqueous medium on the PCC surface in Scheme 3.1, the micelle mechanism leads to a bilayer formation, so the Langmuir equation can only be applied to the first CSM layer. The above Equation (3.3) discusses the relationship between the surface fractional coverage and the concentration of absorbent, and the equilibrium constant of the adsorption and desorption reaction. From the Langmuir adsorption equation, the concentration of stearate ions in different media will be the dominating parameter, which determines the coating coverage of the surface of PCC particles bonded with the stearate ions. It is clear that if the $K \cdot c$ product is too small, the surface fractional coverage will be smaller than 1, which is the situation of an incomplete monolayer. In the aqueous coating, since the stearate has only a partial solubility in water [142], the concentration of the stearate is limited to a constant value because of the micelle formation corresponding to the CMC at the coating temperature. This lower value indicates that a full monolayer cannot be

achieved, as confirmed by the TGA and DSC results that show that the chemisorbed fractional coverage is kept constant at a value of about 72%.

However, if the adsorption of stearic acid on PCC occurs in a good solvent for the acid, for example, in acetone as in the present work, the solubility of stearic acid is much larger than in water, and can be estimated to about 37.6×10^{-3} (mole fraction), or 3.5 M at 50° C [143], so a full monolayer can be achieved. In fact, as the concentration of stearic acid increases, the surface fractional coverage increases until close to 1 as shown in Fig. 3.11. It will be interesting to investigate different adsorption mechanisms by changing the medium, for example, the use of water and acetone as co-solvents. This will be left to some future work.

The adsorption of stearic acid on the PCC surface in acetone follows the Langmuir isotherm, although two different regimes have been observed as described above. In fact, at low and high concentrations, data can be fitted with two separated regression lines with different slopes and, as a consequence, different adsorption constants and maximum adsorption amounts. In particular, from the high concentration region of the Langmuir plot shown in Fig. 3.11, the maximum adsorption amount of stearic acid Γ_{max} on the PCC surface by the Langmuir isothermal equation is calculated to be 4.46 wt%, which matches well with the theoretical full monolayer coverage estimated above for SOCAL U1. In the literature we found other examples of systems showing different adsorption regions in Langmuir plots, where two fitting lines with different slopes have been observed for heterogeneous absorbents [144]. In analogy to that found in these papers, we suggest that the two different adsorption regimes can be explained with the diverse arrangements of the long hydrocarbon chains of the stearate ions on the surface of PCC particles at low and high concentrations. In fact, at low concentrations of absorbent, the long chains are probably arranged randomly on the surface while at high concentration, the arrangement is predominantly vertical to the surface of the PCC particles.

In fact, the degree of surface fractional coverage will also depend on the level of deformation of the initially spherical micelles, under the action of the chemical attraction forces between the calcium cations and the hydrophilic head group of stearate ions. During the bonding between micelles with the PCC surface, the different micelle shapes (flat-disks or hexagonal shape) will influence the surface fractional coverage. A simple geometrical consideration in Scheme 3.2 allows us to predict that partially covered flat surface can be covered by disks of the same diameter, and this proposed micelle deformation model explains why the calcium carbonate surface can only be partially covered with stearate from

aqueous medium. Assuming a cubic arrangement of the flat disks on the surface, the maximum surface fractional coverage that can be reached with disks of the same diameter is 0.78, while for a hexagonal array, Γ_{max} is 0.91.

A simple equation can be derived as the following, for a cubic array in Scheme 3.2 (a):

$$\theta = \frac{\pi D^2}{4 \cdot (2x + D)^2} \leq 0.79 \tag{3.5}$$

where θ is the surface coverage, D is the diameter of micelles, and x is the distance between two micelles because of their deformation. For a hexagonal array the model shown in Scheme 3.2 (b) gives:

$$\theta = \frac{\pi D^2}{2\sqrt{3} \cdot (2x + D)^2} \leq 0.91 \tag{3.6}$$

Based on the fact the calcium soaps can crystallize in cubic arrays of flat disks [145], we believe that this arrangement is more likely to occur than the hexagonal. In any case, because of the curvature among micelles and the flat PCC surface (see the yellow part in Scheme 3.1 (b)), the surface coverage will be lower than 0.79 for the cubic array (and lower than 0.91 for the hexagonal array). This model again confirms the DSC result for the chemisorbed amount of stearate and the fact that a partially covered PCC surface results from the water coating process.

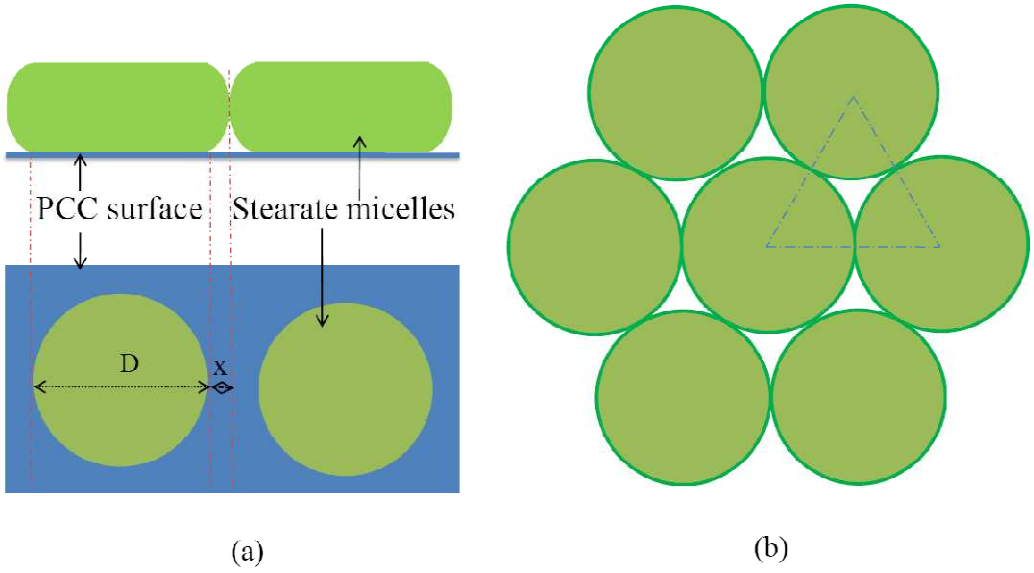

Scheme 3.2 Surface fractional model for micelle adsorption if the arrangement of micelle on the PCC surface (a) in cubic array (b) in hexagonal array

After the water coating process, PCC nanoparticles are covered with two types of stearate layers. The most interesting incomplete monolayer and the physisorbed multilayer outside would strongly affect the surface free energy, which is the dominating and critical

factor regarding the coating result. The physisorbed calcium stearate multilayer produced by the water coating process is totally different from the pure calcium stearate added to the inorganic rigid fillers by mechanical mixing. The first case can achieve a uniform mask on each PCC particle, while the latter results in a random mechanical mixture.

3.5 Conclusion

The industrial process of water coating PCC nanoparticles with stearin was investigated based on different surface characterization techniques. In water medium, micelle adsorption is the dominating process for stearate molecules on the PCC surface. The multilayer produced can be separated into two different types of stearate. One is chemically reacted with the free sites on the PCC surface but only partially covering its surface. The other one is the precipitated calcium stearate layers due to the salt exchange reaction between calcium ions and the sodium stearate in solution. Because of the different chemical-physical properties of the two stearate layers, the thermal transition and the decomposition peaks are very different. The comparison of the water coating and solvent coating process demonstrated that the solubility of stearate in the medium was an important parameter to determine the surface coating result. The chemisorbed monolayer in both cases follows the Langmuir isothermal adsorption process. The structure of the physisorbed stearate multilayer is strongly related to the coating process, which is effected by the molecular arrangement. However, calcium carboxylates present a complicated, thermal transition behavior and polymorphism strongly related to the thermal treatment. Therefore, the PCC samples coated with a stearate multilayer are further investigated regarding the molecule arrangement at different thermal conditions, molecular orientation, and surface free energy change in the next chapter.

Chapter 4 Surface coating molecular arrangement and surface free energy determination

4.1 Introduction

The aim of the surface coating of precipitated calcium carbonate (PCC) nanoparticles is to achieve good dispersion in a polymer matrix necessary for obtaining good composite toughness. The most widely used surfactants are fatty acids, and industrial coating is done in water because of the low cost and simplicity of the process. Previous studies discussed in detail about the effect of the amount of surface coating on the final properties of polymer nanocomposites. The optimum level of surface coating was found to correspond to the minimum of surface tension [114, 146, 147], which is reached at complete monolayer coverage, or rather, when all active sites on the surface of calcium carbonate react with stearic acid molecules. Surface coating of PCC with stearic acid considerably reduces its surface tension from about 210 to 40-60 mJ/m^2 [93]. Some researchers found processing problems during the preparation of HDPE-based composites filled with dry coated PCC particles with stearic acid content in excess with respect to the stoichiometric amount required to reach a full monolayer. Moreover, an inferior tensile strength, together with a higher Young's modulus, was reported for the materials that were filled with PCC particles dry-coated with excess stearic acid, compared to composites that were filled with similar PCC particles dry-coated with the stoichiometric amount necessary to reach the condition of a fully-chemisorbed monolayer [46].

However, those former studies on the surface characterization of PCCs coated with stearic acid have been carried out almost exclusively in either dry conditions, using a high speed mixer (dry-blending or dry-coating), or in the solution of a good solvent of stearic acid (e.g. toluene). Based on our knowledge, limited information is available on the adsorption of stearic acid onto the surface of PCC in aqueous medium, although this is the usual method in the industry for the coating of such fillers. The surface characterization of PCC nanofillers by the water coating process in Chapter 3 yielded interesting results, the micelle adsorption mechanism of which differs from that occurring in dry or solution coating. We can demonstrate that calcium alkanoate molecules form two types of coating layers with different physic-chemical characteristics: a chemisorbed monolayer with the acid groups in the carboxylated form, interacting with a basic surface site (that is the coating is in the form of a partial or half salt, >Ca COOR, where R represents the aliphatic tail, and

the symbol > the surface site) and one or more physisorbed calcium alkanoate (mainly calcium stearate, $CaSt_2$, and calcium palmitate $CaPm_2$) multilayers. These fatty acid salts are not associated with the filler surface and are only weakly attached to the surface monolayer. More interestingly, the PCC surface is covered only partially with the chemisorbed monolayer, while a significant part of it remains free. This experimental observation was tentatively explained by a micelle adsorption mechanism that results in an incomplete chemisorbed layer.

Even if the mechanism of surface coating has been elucidated as discussed in Chapter 3, the structure obtained in such a process is not fully clear. Calcium stearate and calcium palmitate are typical soaps (salts of fatty acids) made of amphiphilic molecules consisting of a long hydrocarbon (or paraffinic) chain attached to a polar carboxyl group. Each molecule thus consists of two parts with physical and clear differential chemical properties: the paraffinic chains are hydrophobic and tend to aggregate together by effect of molecular interactions like Van der Waals, the carboxyl groups are essentially soluble in water and associated by dipole interactions. Both parts are in perpetual competition, and the crystal structures of these amphiphilic compounds are severely constrained by the presence of aliphatic chains in the crystalline state. These molecules will thus able to arrange in different ways and exist in different crystalline forms. The study of the surface coating stearate molecule on the molecular polymorphism and orientation is quite important since it will help us to better understand the influence of organic coating on the surface free energy change for PCC particles and will give a theoretical prediction of the interfacial adhesion when PCC fillers are added into polymers.

In the literature, the thermal behavior and the polymorphism of crystalline phases of calcium stearate have been described in detail by Vold *et al* [136, 137], Bérar *et al.* [130] and Montmitonnet *et al.*[106], using experimental techniques such as X-ray diffraction, thermogravimetry and differential scanning calorimetry. It has been shown that the room temperature structure is extremely sensitive to the presence of impurities, like water or glycerol, and thermal treatments. Also the manufacture method, especially the maximum processing temperature, and aging can affect the final structure obtained. From room temperature to about 123 °C, the chains and carboxyl groups are perfectly rigid and fully crystallized, although two distinct lamellar crystalline phases are encountered: one that is stable up to 104 °C, and the other between 104 °C and 123 °C, respectively termed C1 and C2 [106]. The molecules of calcium stearate are arranged, in the C2 phase, into a hexagonal lattice, a less organized structure in which the paraffin chains attain a certain freedom of

rotation about their main axis [142].

Below 104 °C, in the C1 phase range, calcium stearate exhibits one monohydrate monoclinic α phase (corresponding to the stacking of four molecular layers), and two anhydrous forms: orthorhombic β phase and γ (undetermined structure) [106, 130]. Within these groups, thermotropic phase transitions have been revealed: two in the α group at about -63 °C (from α_2 to α_1) and -3 °C (from α_1 to α_0, one in the γ group at 65 °C (from γ_0 to γ_1). Moreover, dehydration of α leads to a mixture of β and γ, the proportion of which depends on the dehydration temperature and probably on sample heterogeneities. In particular, it was reported that, at 104 °C, both the monohydrate α and the anhydrous β phases undergo a transition towards to the C2 phase [106]. Then on cooling back to room temperature, the C2 is stable down to 65 °C. Then the orthorhombic β' phase (a poorly crystallized β phase) appears, whatever was the initial state, either α or β. The interlayer distance *d* of the β' phase was reported to be about 5.037 nm, which is slightly lower than that of β phase (5.048 nm) due to the poorer in-plane order. Fig. 4.1 shows the main transition of calcium stearate at a relatively lower temperature.

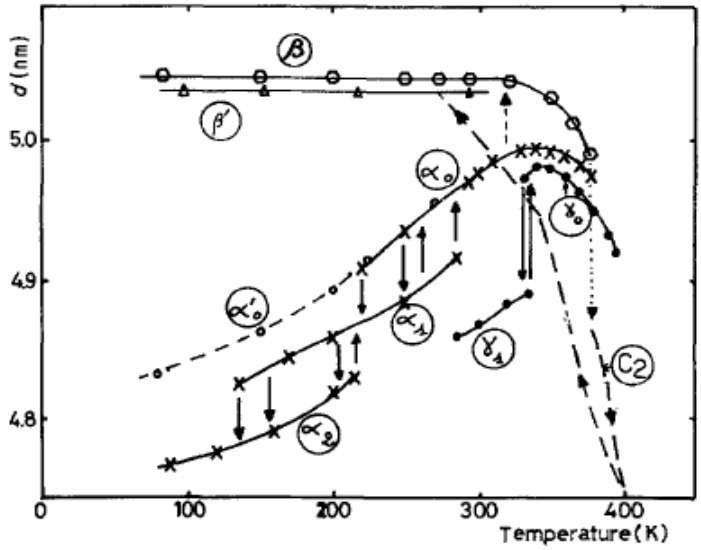

Figure 4.1 From reference [106]. Diagram of low temperature transitions of calcium stearate determined by X-ray measurement of interlayer spacing *d* :
(↑↓) arrows indicate heating or cooling,→ effect of thermal treatment.

For all these crystalline phases, at 70 °C, temperature corresponding to the melting of stearic acid, the conformational disorder of the chains suddenly increases, leading to a poorer in-plane order much before the C1 → C2 transition, and above 120 °C, three mesomorphic phases follow. This condition corresponds to a liquid-crystal state, a state of matter where the molecules have orientational ordering, but are in dynamic motion. The

agitation of paraffinic chains causes the dislocation of sheets and the location of polar groups in limited size discs [142]. In the temperature range 120-160 °C, these discs are first assembled as an orthorhombic C-face centered lattice. However, as the temperature rises further, the correlation between discs diminishes, and the orthorhombic network collapses giving way to a less ordered pseudo-lamellar assembly, where the discs are arranged into layers.

Finally, around 180 °C, the polar groups undergo an allotropic transformation to a hexagonal columnar phase where the discs rearrange themselves into cylinders. The cylinders are formed by the carboxylate groups and are surrounded by alkyl chains that are in a molten state. This cylindrical structure of the polar groups of calcium stearate is stable until the transition to isotropic liquid at 350 °C [137, 142]. The transition temperatures and transition heats of calcium palmitate and stearate are almost identical [136], so the phase behavior of the two alkanoates can be considered as similar.

The goal of the present study is to obtain more information about the water coating process of PCC nanoparticles with fatty acids with particular interest paid to the molecular **s**tructure of stearate/palmitate surface coatings, which is very significant in relation to the state of aggregation of the particles and the level of dispersion which can be achieved during melt blending with industrially relevant polymers. DSC and XRD techniques were used for the phase transition investigation. The thickness of the coating was estimated by XPS island-on-sphere model calculations. Additionally, the surface free energy of PCC particles was also determined by IGC in this study in order to estimate the strength of interfacial interactions in polymer composites.

4.2 Phase transition

After the water coating process, similar to the current industrial procedure, it is known that calcium stearate forms stoichiometric hydrates (α_0 phase) on precipitation from aqueous solutions, which can decompose to some extent to give a partially dehydrated structure with the same crystal lattice (α_0' phase), or instead transform to a different crystal structure (β' phase) which does not return to the original crystal structure upon absorbing water from the environment. In order to specify what is the exact structure of stearate after drying at 105 °C, both DSC and XRD measurements were carried out for the freshly precipitated calcium stearate monohydrate, prepared in our laboratory, which is surely in the α phase. The influence of the drying process on the molecular arrangement is studied in depth in the following section.

4.2.1 DSC measurement

Calcium soaps, which have been heated through different thermal transitions, may undergo the following possibilities on quenching [137]: (1) pass back reversibly through all of the intermediate forms and return to the most stable phase structure at room temperature; (2) go through some transitions, to end with a stable form of one phase stable at some intermediate temperature; (3) the high temperature phase (reached during the heating stage) may be undercooled to room temperature. Fig. 4.2 shows the DSC traces, for different heating-cooling-reheating thermal cycles, for calcium stearate monohydrate freshly prepared in our laboratory. According to the literature [106], the transition from α or β to C2 phase is found at the critical temperature of 104 °C. Therefore, three different temperatures, 80 °C, 110 °C and 120 °C, were chosen for the isothermal conditioning for 3 hours before the cooling-reheating thermal program. It is evident in Fig. 4.2 that there is a sharp endothermic peak during the first heating before isothermal at 110 °C and 120 °C for three hours, followed by another phase transition peak during the cooling process. This wide exothermic peak appeared at about 86 °C during the cooling, confirming the C2 to β' phase transition. Also the measured enthalpy of about 12 J/g matches well with the results of Garnier *et al* [106]. However, the curve corresponding to the preconditioning at 80 °C does not show the phase transition from the α to the C2 phase and correspondingly, no phase transition peak appears during cooling. Besides, the second heating process also shows four thermal transition peaks similar to those shown in Fig. 3.6 with the exception of the first peak at about 100 °C. In the case of preconditioning at 80 °C, the calcium stearate monohydrate still presents the α to C2 phase transition (dehydration of monohydrate) in the second heating process, while the β' to C2 phase transition occurs with a much smaller enthalpy in the case of preconditioning at 110 or 120 °C. In other words, the transition from the α to C2 phase is irreversible while that from C2 to β' phase is reversible.

To better clarify this finding, a further study on the thermal phase transition of the calcium stearate monohydrate sample was carried out. In fact, the thermal treatment at a temperature range below 125 °C (the main phase transition temperature) results in the reversible phase transition from β' to C2 phase. However, higher temperature treatments seem to also affect the molecular arrangement. In Fig. 4.3, the calcium stearate monohydrate undergoes five different processes with both heating and cooling speeds of 5 °C/min. After the heating process from 20 °C to 220 °C with the full transition to liquid crystal phase in Fig. 4.3(3), two small peaks appear at 170 °C and 50 °C during cooling in Fig. 4.3(4). Those two dramatic phase transitions indicated that there would be another main molecular

arrangement of calcium stearate after thermal treatment at a high temperature beyond 125 °C. The comparison of thermal treatments at both lower temperature and higher temperatures results in the different molecular arrangement. The molecular transformations at lower temperatures are presumed to involve the alkyl chains, while that at higher temperatures is presumed to involve the polar heads.

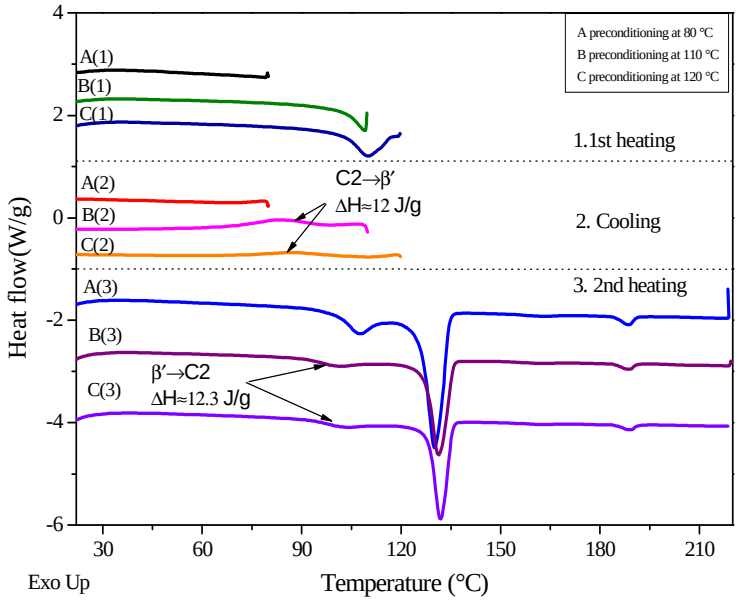

Figure 4.2 Calorimetric evidence of the phase transition of calcium stearate monohydrate

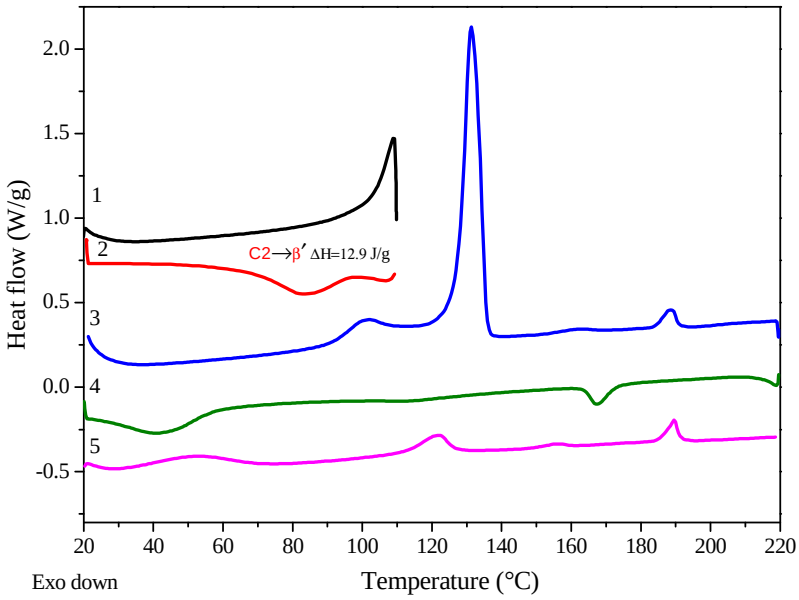

Figure 4.3 DSC traces of calcium carbonate monohydrate under different thermal treatments: 1st heating from 20 °C to 110 °C (isothermal for three hours); 2nd cooling from 110 °C to 20 °C; 3rd reheating from 20 °C to 220 °C; 4th cooling back to room temperature; 5th full scanning in the temperature range

Thus, it is reasonable to assume that the drying process at 105 °C for the PCCs coated

with stearin in aqueous medium may cause a phase transition of the physisorbed calcium alkanoates formed on the PCCs surface from the monohydrate α phase to the anhydrous C2 phase. As a result, a transition from the C2 to the β' phase should take place upon the cooling of the PCC powders back to room temperature before storage. In other words, the drying process of water-coated PCC particles is accompanied by a molecular rearrangement of the alkanoates on the PCC surface. This thermal study helps to better understand the molecular arrangements occurring at different temperatures, which have a strong effect on the surface free energy of organic coating and then on the PCC surface energy.

4.2.2 XRD measurement

X-ray diffraction is a powerful method for the determination of crystal structures. Previous studies on calcium stearate have shown that the anhydrous phases (γ_0, γ_1, β, β', C2) have a poor crystalline quality, except in the lamellar direction as evidenced by a series of sharp and equidistant peaks in the region of the low Bragg's angles. On the contrary, the monohydrate α phases (α_0, α_1, α_2) show a more complex diffraction pattern. In fact, those structures present peaks not only in the low angle region (i.e., for spacings d > 10 Å) attributed to a lamellar structure, but also with a series of diffuse bands (d ≈ 3-5 Å) due to the short-range order of these molecules, which indicates that the carboxyl groups and paraffinic chains are assembled in a periodic and regular manner according to a tridimensional crystal lattice [137, 142]. In this part, an XRD analysis has been carried out in order to identify the crystal structure of the physisorbed calcium alkanoate present on the as-received PCC particles, which is related to the precipitation conditions but also on the type of drying process used during the preparation of the particles, particularly on the drying temperature.

First, the XRD patterns of calcium stearate, calcium palmitate and calcium salts of stearin, at room temperature or preconditioned at temperatures above 105 °C, are analyzed in Fig. 4.4. Those calcium soaps have typical diffraction patterns, which show a series of sharp peaks in the low angle region from 1.5° to 10°, then a second group of peaks between 20° and 30°, and a number of unclear peaks in the 2θ region up to 60°. The peaks at small angles can thus be associated to the diffraction of X-rays by planes of atoms whose separation is proportional to the length of the calcium alkanoate molecules. The long spacing values of calcium soaps were calculated from the low 2θ angle in the XRD patterns by using the Bragg equation. For example, five orders of this distance appear as peaks in the low angle diffraction pattern of $CaSt_2 \cdot H_2O$ (d/1, d/2, d/3, d/4, d/5), at about 1.8°, 3.6°, 5.3°,

7.1° and 8.8°. From these values of 2θ, the *d*-spacing for stearate on freshly precipitated calcium stearate monohydrate is estimated to be 49.5 Å as indicated in Table 4.1 for all of the calcium salts considered in this work. The measured value of the distance between crystalline planes of calcium stearate monohydrate, 49.5167 Å, is equal to about twice the length of the fatty acid. This long spacing value matches very well the results from Vold *et al* [137]. Similarly, the long spacing value for calcium palmitate is about 44.4366 Å, which is about 5 Å shorter than that of stearate. Also the calcium salt prepared from stearin, which is a mixture of the calcium stearate and calcium palmitate, show similar XRD patterns with the calcium stearate but in different 2θ angles. In fact, the calculated value for the calcium salt of stearin is about 46.902 Å, which is perfectly the average value between 44.4366 Å (palmitate) and 49.5167 Å (stearate). All of the calcium soaps of fatty acid have analogous XRD patterns and the difference can be explained by the varying chain length of those fatty acids.

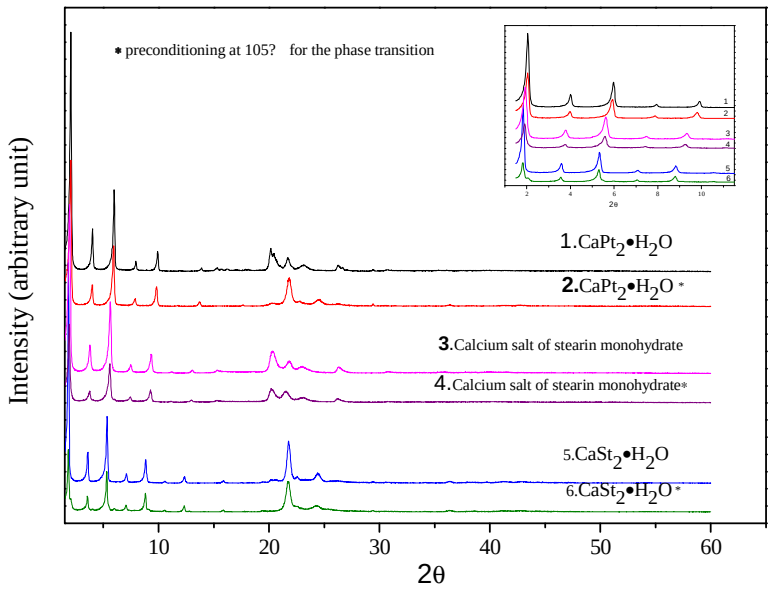

Figure 4.4 XRD spectra of calcium stearate, calcium palmitate and calcium salt of stearin at room temperature and after preconditioning at 105 °C

The occurrence of the molecular rearrangement transition of calcium soaps can also be clarified by the XRD technique by determining the interlayer spacing. The freshly prepared stearate and palmitate calcium soaps dried at 105 °C and then cooled back to room temperature before XRD examination show a small increase in the long spacing distance, for example from 49.5167 to 49.8514 Å for calcium stearate monohydrate, which is consistent with our interpretation that a transition from the hydrate α form to the anhydrous β' phase occurs in the drying-cooling stage, passing through a transient C2 phase at 104 °C, as indicated also by the results obtained with the DSC technique. The calcium monohydrate

salt of stearin was also freshly prepared in our laboratory for comparison to the pure calcium stearate and palmitate. Both the values of the long spacing distance of the α phase (freshly prepared sample) and the β' phase (after drying and subsequent cooling cycle) are intermediate between those of the pure calcium stearate and palmitate salts.

Table 4.1 X-Ray diffraction patterns of calcium stearate monohydrate, calcium salt monohydrate of stearin, calcium palmitate and physisorbed stearate on the PCC surfaces

	Long *d*-spacing *(Å)*					**Average**
Orders	1	2	3	4	5	***(Å)***
$CaSt_2$•H_2O	48.2561	24.7566	16.5962	12.4805	10.0207	49.5167
$CaSt_2$•H_2O*	48.9241	24.9044	16.7046	12.5429	10.0477	49.8514
$CaPm_2$•H_2O	43.5194	22.0753	14.8212	11.3592	8.9225	44.4366
$CaPm_2$•H_2O*	43.6030	22.2043	14.9354	11.2443	9.0176	44.5766
†Stearin salt	45.8877	23.3786	15.7356	11.8220	9.4743	46.902
†Stearin salt*	46.7739	23.5736	15.8456	11.9090	9.5502	47.3690
PCC2	----	----	----	----	----	----
PCC3	46.9754	----	15.5902	----	9.4051	46.9239
PCC4	46.1456	----	15.6322	----	----	46.5211
PCC5	45.3753	----	15.5316	----	9.378	46.7423
PCC6	45.9571	----	15.6834	----	----	47.0503
PCC7	45.4714	23.0997	15.5621	----	9.4408	46.3903
PCC8	45.9571	23.3560	15.6427	----	9.4476	46.7088
PCC9	45.7830	23.3508	15.6168	11.7777	9.4299	46.7191

*Monohydrate after precondition at 105 °C for phase transition

†Stearin 4973 used for the preparation of the calcium salt is not the same batch with that used for the PCCs surface coating.

Both the DSC and XRD measurements of calcium alkanoates indicated that the drying process cause a molecular arrangement of the surface coating. This transition was simulated on the laboratory-prepared calcium monohydrate soaps. It was confirmed that the heating program at 105 °C effectively causes a phase transition from the monohydrate α phase to the C2 phase. However, this thermal transition is proved to be irreversible and the C2 phase changed to β phase during cooling program. In fact, the coating on the PCC surface is strongly dependent on the thermal treatment and, therefore also the surface energy will change according to the amphipathic nature of soap molecules containing both strong non-polar and polar portions.

4.3 Coating molecular arrangement

4.3.1 Interlayer distance of coating molecules on PCC

Based on the XRD results of calcium alkanoate monohydrates, we concluded that the calcium stearate present as a coating of PCC particles is present at room temperature in the β′ crystal phase, which displays a regular Bragg spacing corresponding approximately to double the length of a stearate chain. Furthermore, the examination of the diffraction patterns of the coated PCC, shown in Fig. 4.5, provides useful information not only on the crystal form of calcium carbonate (calcite, vaterite or aragonite) (for angles in the range $2\theta>20°$) but also on the structure of its organic coating ($2\theta<20°$). The diffraction spectra for PCC1 as shown in Fig. 4.5, together with other PCCs, is that typical of a pure calcite crystal [148]. No peaks can be observed for diffraction angles $2\theta < 10°$ for PCC1 as well as for ML2, which means that no peaks resulting from the chemisorbed alkanoates are present on the PCC surface in the XRD spectra. This result is similar to the DSC results that showed no endothermic peak for the chemisorbed monolayer on the PCC surface. On the contrary, the other coated PCCs like PCC9 show 5 diffraction peaks in the low angle region (Fig. 4.5, inset). These peaks can thus be associated to the diffraction of x-rays by planes of atoms whose separation is proportional to the length of the calcium alkanoate molecules. From these 2θ values, the *d*-spacing for the organic coating on PCC9 is estimated to be 46.7191 Å, as also reported in Table 4.1. Meanwhile, the *d*-spacing values calculated for the other coated PCCs are shown in Table 4.1. Some order patterns of the calcium alkanoates on the surface are not clear enough for the calculation due to the small amount of physisorbed layer on the PCCs, as in the case of PCC2 and PCC3. However, all of the long *d*-spacing values are similar for all powders with an average value of about 46.7 Å, which confirms that the physisorbed organic coating on the PCC surface has the same crystal phase, and this value is in reasonable agreement with that of calcium salt of stearin, within experimental error.

Taking into consideration that the calcium soap of stearin is approximately a 50:50 blend of calcium palmitate and calcium stearate, this value compares well with the calculated values of the interlayer distance *d* for both calcium palmitate, 44.6 Å, and calcium stearate, 49.8 Å, which corresponds to extended chains oriented normal to the planes containing the ionic groups [142]. The average of these *d*-spacings is 47.3 Å, which is slightly higher than the value estimated from the diffraction pattern of PCC9 (46.7 Å). This can be explained by the presence of small amounts of calcium oleate that may cause packing defects and that may lead to a less orderly molecular arrangement, or to a slight

tilting of the paraffinic chains. Comparing the diffraction spectra of the two powders, in the intermediate angle range, at 20.4°, we also note a peak for PCC9 which is not present for PCC1. This peak arises from the diffraction of planes of atoms separated by much smaller distances of the calcium soap of stearin than those just described, and thus referred to as short spacing. A numerical value of 4.35 Å can be estimated from this diffraction angle and can be interpreted as the side spacing between one molecule and the next in the crystal phase.

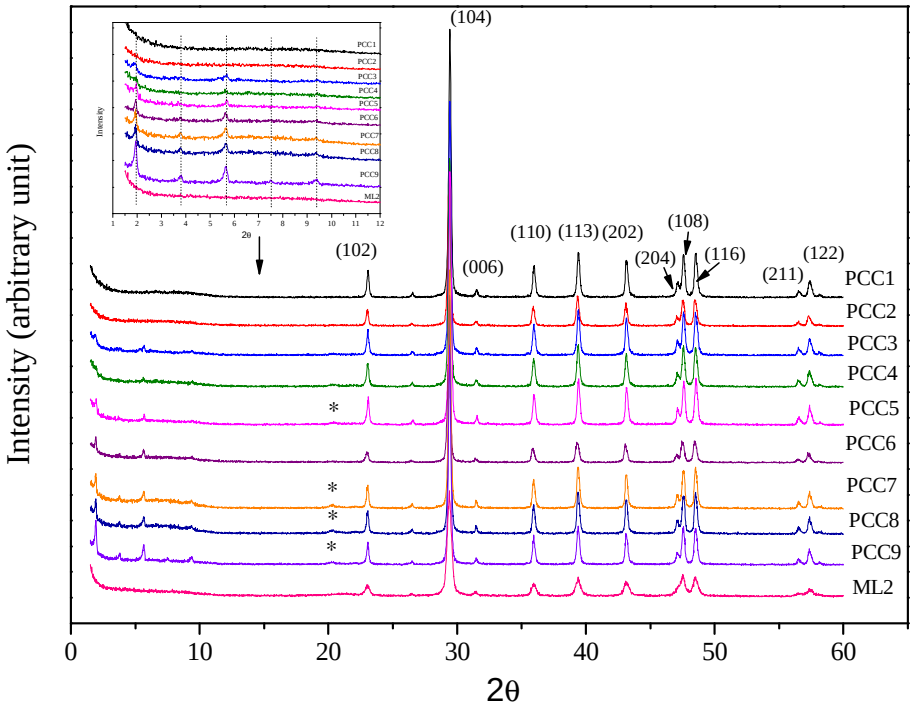

Figure 4.5 X-ray diffraction patterns of PCCs and ML2

4.3.2 Layer thickness determination of coating molecules

X-ray photoelectron spectroscopy (XPS) has been widely used for the qualitative and quantitative analysis of material surfaces up to a depth of about 10 nm. Fekete and co-workers [99] had successfully used XPS to analyze the chemical reaction between calcium carbonate and stearic acid to calculate the thickness of the stearate layer created by dry-coating. They found that the thickness of the monolayer matched well with the theoretical length of the stearic acid molecules. Similarly, Gilbert *et al* [121] estimated the thickness of a stearic acid layer on the surface of magnesium hydroxide. The thickness increased with the coating level with a change in slope at around 1.2 wt%, which corresponded to monolayer coverage for that particular filler. In this work, XPS is used for the determination of the density of the main surface elements and for the calculation of the layer thickness of the coating using the island-on-sphere model.

The wide-scan XPS spectrum contains exclusively the characteristic electron-lines and Auger-transitions of the elements constituting the PCC samples and the coatings; the most intense lines, Ca2p, Ca2s, CaLMM, C1s, CKLL, O1s, and OKLL are indicated on the spectrum in Fig. 4.6.

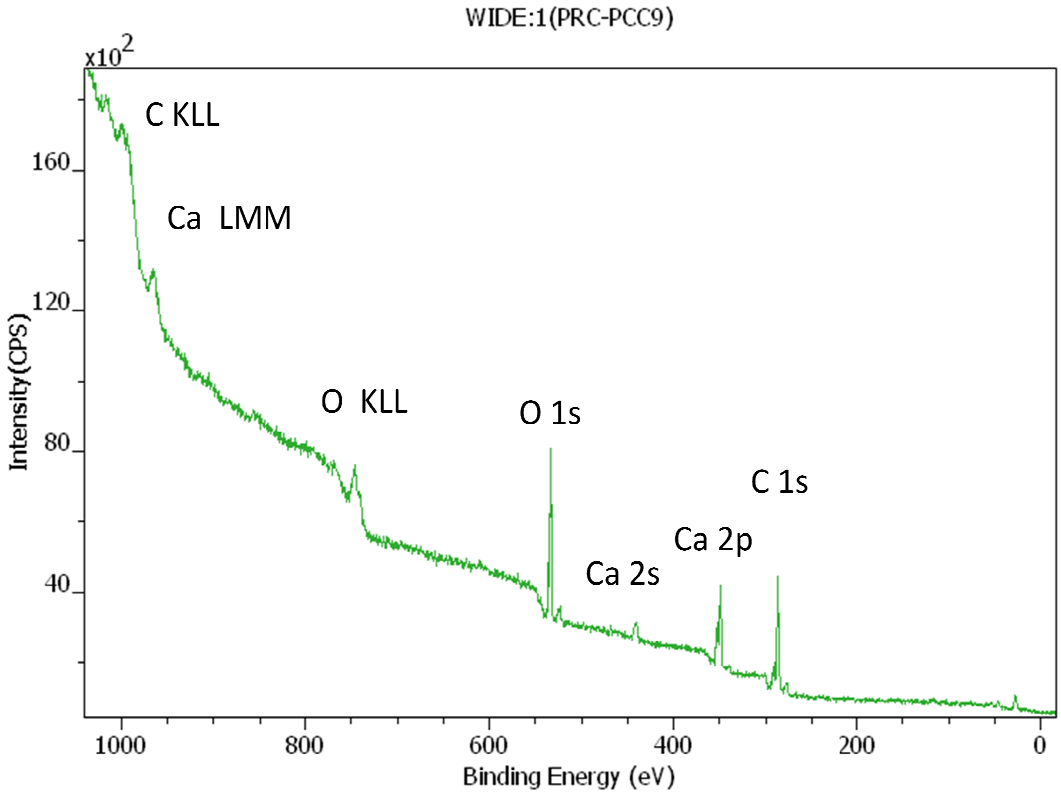

Figure 4.6 XPS survey spectrum of PCC9

The high-resolution spectra of the O1s, Ca2p and C1s regions were used for the analyses as shown in Fig. 4.7(a), (b) and (c) respectively. These lines are relatively narrow, with half-widths of 1.75-1.95 eV, representing well-defined chemical states. The O1s line recorded at 531.6 eV for the carbonate seems to overlap with that of the carboxyl. The more intense 3/2 component of the Ca2p doublet was found at 350.9 eV. The major C1s component at 285.0 eV was chosen as a reference for the hydrocarbon chains of the coating, (and also the carbonaceous contamination on the untreated sample), while the peak at 289.7 eV corresponds to the carbon in the carbonate. The carbon of the carboxyl group should appear at about 288.5 eV, but due to its small intensity, it could not be evaluated separately with confidence. This is why it was integrated to one peak of the carbonate. The peak area of each relevant element was calculated by deconvolution and the results are listed in Table 4.2. The CH/CO_3 ratio increases with an increase in the surface coating amount, which confirms the continuous precipitation of calcium stearate layers on the PCC surface.

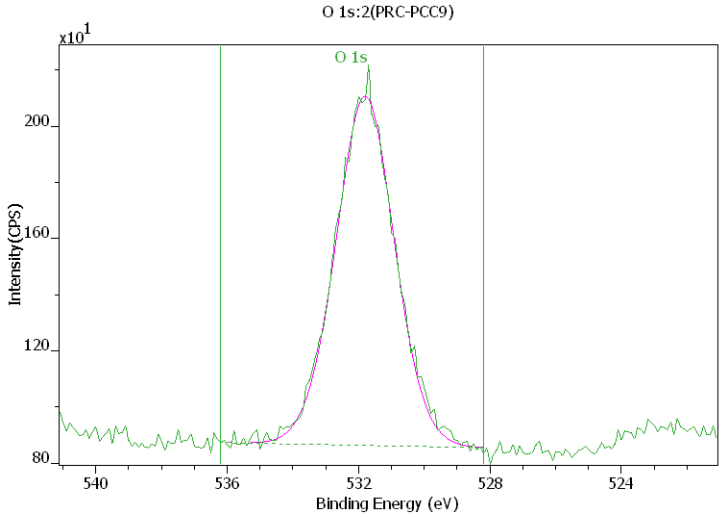

(a)

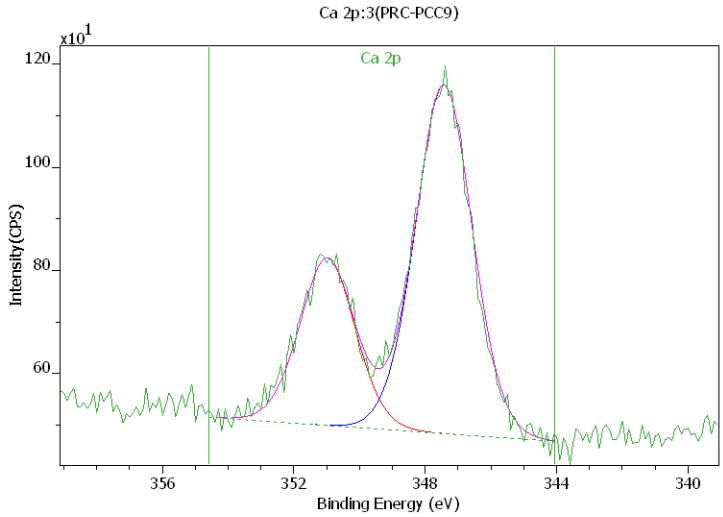

(b)

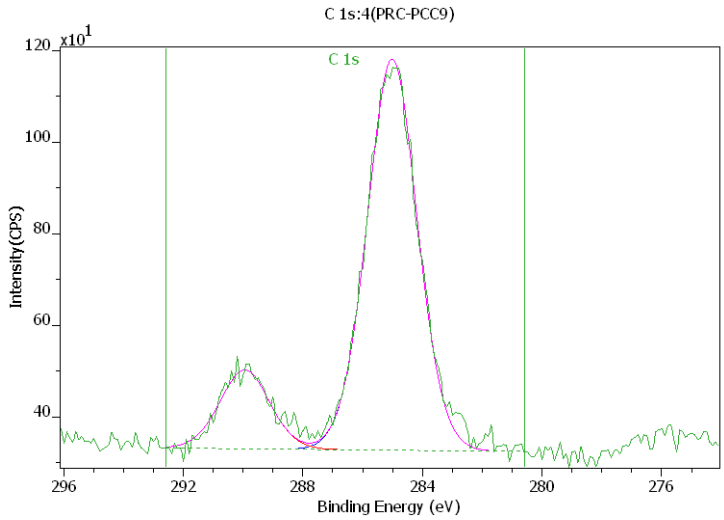

(c)

Figure 4.7 XPS spectra for the main element (a) O 1s, (b) Ca 2p and (c)C 1s

The element density in Table 4.2 was used for the surface coating layer determination with the MultiQuant software [108, 109, 149]. When the surface of the sample is covered by one or more thin overlayers (the whole structure should be thinner than the information depth of the XPS measurement) and the compositions of these layers are known, the thickness of the layers can be estimated from the photoelectron intensity. In this thesis, all of the calculated element densities of different PCC particles from the peak area as shown in Table 4.2 were used for the layer thickness calculation with the MultiQuant software based on the island-on-sphere model. This model is available for the determination of coating layer thickness even for the multilayer's coating. However, there is one limitation that the coating layers must have the same surface coating coverage. Considering the former results by TGA measurements and the micelle adsorption mechanism, only PCC6, with a coating level of about 9 wt%, is believed to show a coverage of 72 % for both the chemisorbed monolayer and the physisorbed bilayer.

Table 4.2 XPS elements density determination and layer thickness calculation

Name	**Amount adsorbed**	**Intensity**					**Thickness**	
	(mass %)	**O**	**Ca**	**C CH**	**C CO3**	**CH/CO_3**	***(Å)***	**Coverage**
PCC1	0.00	11726	7191	733	1355	0.54	-----	-----
PCC2	3.17	8132	5316	2003	978	2.05	-----	-----
PCC3	6.60	7136	4764	2807	924	3.04	-----	-----
PCC4	6.50	6048	4290	2589	794	3.26	-----	-----
PCC5	8.09	6599	4673	2969	881	3.37	-----	-----
PCC6	8.91	3176	2235	1705	361	4.72	**65.41**	**72%**
PCC7	10.35	5954	4126	3324	768	4.33	-----	-----
PCC8	11.57	6202	4217	3450	817	4.22	-----	-----
PCC9	12.95	2933	2159	1783	360	4.95	-----	-----
ML1	15.00	4371	2917	2948	555	5.31	**25.0**	**100%**
ML2	4.22	4494	3322	2812	603	4.66	**23.6**	**100%**

The thickness of the fully chemisorbed monolayer reference samples prepared with solvent and dry coating, i.e. ML1 and ML2 respectively, was estimated first. The calculations yielded layer thicknesses of 25.0 Å for ML1 and 23.6 Å for ML2. If we compare these values with the theoretical length of the stearate molecule that is 24 Å [125], we may conclude that the stearate molecules in the monolayer present on the ML1 sample are oriented perpendicularly to the surface. ML2 was prepared by dry-coating with stearin and not with pure stearic acid that might explain the slightly thinner coating. In fact, as mentioned above, stearin is practically a 1:1 blend of stearic and palmitic acids, so we can

assume that the stearin is a virtual fatty acid comprised of 17 CH_2 groups, with a theoretical length of about 21.08 Å. Adding the COOH head group, which is about 1.5 Å, the calculated monolayer thickness is about 22.6 Å, which is not far, within experimental error, from the value of 23.6 Å as estimated from XPS data. For PCC6, a surface coating layer thickness of 65.4 Å is calculated which is close, within the limits of these types of calculations, to the sum of the length of one molecule of stearin (22 Å) plus an interlayer distance corresponding to one stearate/palmitate double layer in the orthorhombic β' phase, which we estimated to be 46.7 Å. The calculated value is slightly lower than the theoretical one, which can be attributed to the fact that the surface coating amount of PCC6 of about 8.91 % is slightly lower than 9 wt%, which resulted in then a lower surface element density and then a lower layer thickness. From the layer thickness of both the monolayer and the multilayer coating, we can assume that two different types of stearate molecules are in a vertical arrangement on the PCC surface.

4.4 Surface free energy

It is very well known that a lower surface energy of the inorganic rigid fillers is necessary in the industrial applications in order to achieve a homogeneous dispersion of nanoparticles as well as to have a weaker interfacial adhesion between coated fillers and the polymer matrix. Those two factors are very important for toughness improvement in polymer nanocomposites. In fact, this is also the purpose of this thesis. The interfacial adhesion between nanoparticles and the polymer matrix is strongly dependent upon the thermodynamic nature of both components. Pure calcium carbonate nanoparticles have high hydrophilicity and are usually modified by organic materials to increase the compatibility with hydrophobic polymers and to prevent aggregation of nanoparticles. In the literature, the surface energy characterization can be carried out by the inverse gas chromatography (IGC) technique. However, the surface energy determination of calcium carbonate is not so easy because of free water adsorption on the surface. In our work, the PCC particles are coated with stearin following the typical industrial procedure in aqueous medium, and the most interesting result is that some free space is left on the PCC surface due to the micelle adsorption mechanism. Additionally, XPS and XRD results have indicated the surface coating of PCC particles is a component of a chemisorbed monolayer and physisorbed layers, where alkanoate molecules are disposed vertically to the surface with the alkyl chains directed outwards.

Therefore in this thesis, the PCC nanoparticles with different surface coating amounts are investigated by using the IGC techniques to analyze the dependence of PCC surface free

energy on the preconditioning and on the measurement temperatures. The influence of the surface organic coating amount on the surface free energy of nanoparticles is also discussed, which is strongly related to interfacial adhesion during the application of PCC nanoparticles in the polymer. Both the dispersion and the specific components of surface free energy are discussed in the following.

4.4.1 IGC theory background

The thermodynamic work of adhesion is related to the intermolecular interactions, these being the sum of the contribution of London-Lifshitz-Van. der Waals (LW) dispersion forces and of the Lewis acid-base forces (AB or electron donor-acceptor), according to following (4.1):

$$W_A = W_A^d + W_A^{ab} \tag{4.1}$$

where W_A is the energy of adhesion; W_A^d is the dispersion component or London component and W_A^{ab} is the electron donor-acceptor interaction.

Dispersion component of surface tension:

When non-polar probe molecules like alkanes are chosen as adsorbates, the adhesion between the probe and the solid surface only involves the dispersion interaction. So the second part of equation (1) will be equal to zero and W_A can be simply written by equation (4.2):

$$W_A = W_A^d = 2 \cdot \left(\gamma_1^d \gamma_2^d\right)^2 \tag{4.2}$$

The free energy of adsorption, ΔG_a, per mole of vapor probe is related to the work of adhesion W_A between the vapor probe and the solid stationary phase per unit surface area, in the following form [150]:

$$-\Delta G_a = N \cdot \alpha_{LV} \cdot W_A \tag{4.3}$$

where N is the Avogadro's number and α_{LV} is the molecular surface area of the absorbate. ΔG_a is also related with V_n by equation 4.4:

$$\Delta G_a = -RT \, ln \, V_n + K \tag{4.4}$$

In an infinite dilution when W_A^{ab} is equal to zero, the dispersion component of the surface tension of the stationary phase can be obtained from the cross-sectional area of n-alkane of different chain length.

A combination of equations (4.2), (4.3) and (4.4) leads to the statement:

$$RT\ ln\ V_n = 2N(\gamma_s^d)^{\frac{1}{2}}\alpha_{LV}\left(\gamma_{LV}^d\right)^{\frac{1}{2}} + C \tag{4.5}$$

where γ_s^d is the non-specific or the dispersive component of surface energy, and γ_{LV}^d is the surface tension of the probe.

Dorris and Gray [151] proposed a more simple approach to the determination of γ_s^d. They considered the contribution of a methylene (-CH_2-) group in the alkane series to the free energy of adsorption $\Delta G_{CH_2}^0$, defined by:

$$-RTln\frac{V_n}{V_{n+1}} = 2N(\gamma_s^d)^{\frac{1}{2}} \cdot \alpha_{CH_2} \cdot \left(\gamma_{CH_2}^d\right)^{\frac{1}{2}} \tag{4.6}$$

$$\gamma_s^d = \frac{(RTLn\,(V_{n+1}/V_n))^2}{4 \cdot N^2 \cdot {\alpha_{CH_2}}^2 \cdot \gamma_{CH_2}^d} \tag{4.7}$$

where V_n and V_{n+1} are the retention volumes of n-alkanes with *n* and *n+1* carbon atoms, respectively, and α_{CH_2} is the surface area occupied by –CH_2– groups, estimated to be about 0.06 nm^2. Fig. 4.8 gives an example for the calculation of γ_s^d for PCC9 chosen as an example in this figure. The term $\gamma_{CH_2}^d$ is the surface tension of a hypothetical surface containing only methylene groups, which can be calculated by the following equation:

$$\gamma_{CH_2}^d = 35.6 + 0.058 \times (293.13 - T) \tag{4.8}$$

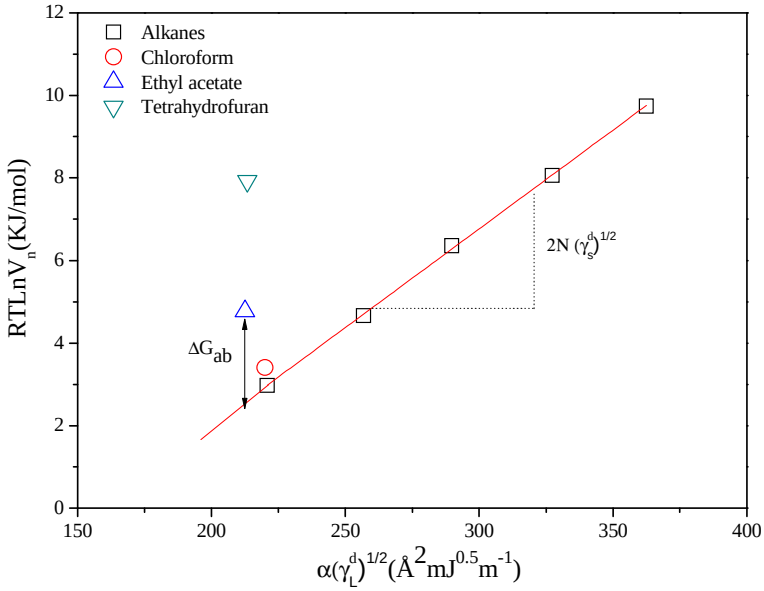

Figure 4.8 Determination of the dispersion and specific component of surface free energy of particles (PCC9 is chosen as an example under preconditioning at 140°C and measured at 140°C)

Acid-Base interaction

When polar adsorbates are used in the IGC experiments, both the LW and AB interactions are present between the adsorbate and the adsorbent.

$$\Delta G_A = \Delta G_A^d + \Delta G_A^{ab} \quad (4.9)$$

In this case, the component of acid-base interaction is related to the retention volume of the polar probes in the following way:

$$\Delta G_A^{ab} = -[(RT\ ln\ V) + C] - [RT\ ln\ V^{ref} + C] = -RT \ln\left(\frac{V}{V^{ref}}\right) \quad (4.10)$$

where V is the net retention volume of the polar probe and V^{ref} is the retention volume that is determined by the n-alkanes reference line. The baseline is the straight line of $-RT\ ln\ V$ against the dispersive potential of n-alkanes, and ΔG_{ab} is given by the distance of the $-RT\ ln\ V$ value obtained from the polar solvent and the baseline. In our case, the physicochemical quantity used to determine the value of $\Delta G_{ab}$is $\alpha\gamma^{1/2}$ of the chosen solvent as shown in Fig. 4.8.

The enthalpy of acid-base interaction (ΔH_A^{ab}) can also be calculated from the value of ΔG_{ab} calculated at different temperatures, because there is the following relationship between those two parameters by equation 4.11:

$$\Delta G_A^{ab} = \Delta H_A^{ab} - T\Delta S_A^{ab} \quad (4.11)$$

So the curve plotting $\Delta G_A^{ab}/T$ against $1/T$ yields a straight line with the slope of ΔH_A^{ab}.

Acid-base interaction parameters

Quantitative evaluation of acid-base interaction parameters for surfaces of the stationary phase is based on the use of ΔH_A^{ab}. Adopting the Gutmann [152] terminology in this work, those selected probes are categorized by their electron acceptor and electron donor numbers, AN^* and DN, respectively, as shown in Table 4.3. If the solid adsorbent has the ability to accept or to donate electrons, then the analogous parameter of acidity and basicity can be determined for the solid.

Table 4.3 Acceptor AN and donor DN parameters of solvent in the reference [152, 153]

AN DN parameters	AN	AN*	AN**	DN	DN *	DN**
alkane	0	0	0	0	0	0
THF	8	0.5	3.2	20	50	1.9
Cloroform	23.1	5.4	9.24	0	0	18.7
ethyl acetate	9.3	1.5	3.72	17.1	42.8	5.3

The value of the Lewis acidity constant, K_a and of the Lewis basicity constant K_b is calculated by using the following equation [154, 155]:

$$-\Delta H_A^{ab} = K_a \cdot DN + K_b \cdot AN^* \quad (4.12)$$

Although the acid-base characteristic of the particles should be obtained from the ΔH_A^{ab}, some researchers [156-158] also decided the values from ΔG_{ab}. Gutmann [152] and others [159] defined and modified the polar probes by their electron acceptor DN and electron donor numbers AN^*.

Rearranging the above Equ. 4.12, when $-\Delta G_{ab}/AN^*$ is plotted versus DN/AN^* of polar probes, there will be a straight line. The slope K_a is related to the acidity of the solid, and the intercept K_b reflecting the electron donor ability.

4.4.2 Influence of surface coating amount on the surface free energy

The surface free energy of PCC nanoparticles strongly depends on the surface coating molecules, such as crystal phase of surface molecules, the coating amount of stearate on the PCC, the molecular arrangement and the coating-layer thickness. Based on the DSC and XRD studies about the water coated PCC particles, it has been concluded that a phase transition during the drying process and the physisorbed calcium stearate shows a polymorphism that is strongly related to thermal treatments. In this section, we only discuss the influence of the surface coating amount on the PCC surface free energy when this series of water-coated PCC particles were preconditioned at 140 °C, since the stable phase of alkanoate species present on the PCC particles is the same when these particles are added to the polymers during melt processing.

Firstly, the dispersion component of the surface energy of the series of water-coated PCC particles studied in this thesis is presented in Fig. 4.9 as a function of the amount of stearin used for coating. The dispersion component value for the neat PCC is about 53.0 mJ/m^2 that agrees well with the number published by Papirer (54 mJ/m^2) [113]. The Surface tension decreases steeply with surface coverage down to a minimum value of 24.3 mJ/m^2. In spite of the fact that the micelle adsorption mechanism of the water coating process results in an inhomogeneous surface, our results are similar to those reported by other researchers [114] about PCC particles surface modified by the dry and solvent coating methods. Further increases in coating amount do not lead to any significant change in the dispersion component of surface energy, and the final value is about 24-25 mJ/m^2. The surface tension of a surface covered by –CH_3 groups was found to be about 22-24 mJ/m^2 [160]. The good agreement with our result indicates that the alkyl chains of calcium stearate/palmitate are oriented towards the outside surface of the coated particles, and the multilayer is arranged tail-to-tail with the inside monolayer. The surface tension of the ML1 sample (organic content 4.22 wt %) coated from solution is also plotted in Fig. 4.9 (star symbol). The γ_s^d value of the sample perfectly fits the correlation obtained for the water-coated PCC

particles. Physisorbed stearate multilayers have the same effect on the dispersion component of surface energy as the chemisorbed monolayer (sample ML1). Here we want to specify the influence of the preconditioning temperature on the final surface free energy of nanoparticles, as the stearate/palmitate on the PCC surface has a complicated thermal transition behavior discussed in the DSC measurements. In fact, the preconditioning at 140 °C brings organic coating molecules to one type of liquid crystal phase, probably similar to what happens when the PCC particles are blended with a polymer during an extrusion process. Some IGC measurements of the surface free energy of PCCs preconditioned at 60 °C, which was enough to eliminate the free adsorbed water on the surface without any phase transition occurring, will be also discussed in the next part.

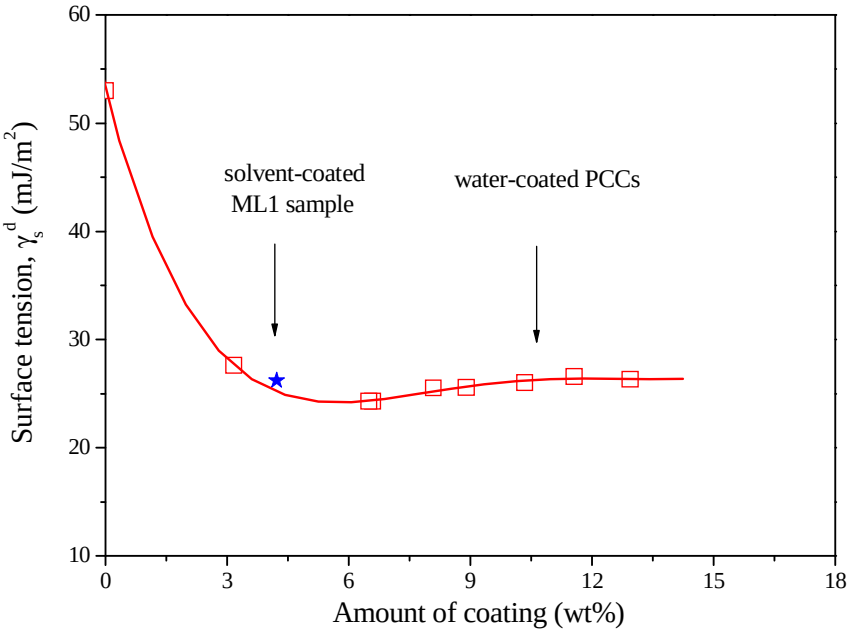

Figure 4.9 Effect of surface coating amount on the dispersion component of the surface free energy for the water-coated PCC nanoparticles

Moreover, three different polar solvents (tetrahydrofuran (THF), ethylacetate (EtAc) and chloroform ($CHCl_3$)) are chosen for the determination of specific components for those coated PCC particles with different surface coating amounts. However, some polar probes adsorbed strongly on the pure PCC surface or even the coated PCC surface with stearate because of their high polarity. The determination of specific component is only available in the case when the particles column is preconditioning at 140 °C, which made the surface stearate molecules undergo the phase transition into liquid crystal and have enhanced active mobility. Fig. 4.10 shows the relationship of surface free enthalpy ΔG_{ab} versus the PCC surface coating amount obtained by using three different polar solvents, measured at 140 °C. The interaction between chloroform and the coated PCCs is much weaker than that between

the filler and the other two polar solvents. Ethyl acetate and tetrahydrofuran enter into much stronger interaction with the active sites of the coated PCC surface than $CHCl_3$. The specific component of surface energy decreases with different slopes below and above a 9 wt% stearin content which indicates that polar probes may have higher access to the active sites of the surface below this coating level. The ΔG_{ab} value of the ML1 reference sample is also plotted in Fig. 4.10 and fits the general tendency of water coated particles. The results obtained in the IGC experiments and presented above agree well with those derived from other methods and strongly support the tentative explanation given for the multilayered structure of the stearate coating on PCC formed in water. In fact, incomplete coverage due to the micelle adsorption mechanism results in relatively strong acid-base interactions of the surface with two of the polar probes. Incomplete coverage allows access to the surface, while a strong interaction is the driving force aiding diffusion. With increasing surface coverage, access to the surface becomes more limited, leading to a decrease in the specific component of surface energy. The presence of additional molecules in the physisorbed stearate multilayer completely closes the surface and hinders the diffusion of polar probes to the filler surface. The changing slope at around a 9.0 wt% coating level indicates the attainment of the maximum coverage of the first physisorbed stearate layer, which matches very well with our XRD and XPS results in the sections 4.2 and 4.3. The rather specific structure of the coating forming in the water coating process may lead to interesting properties in composites.

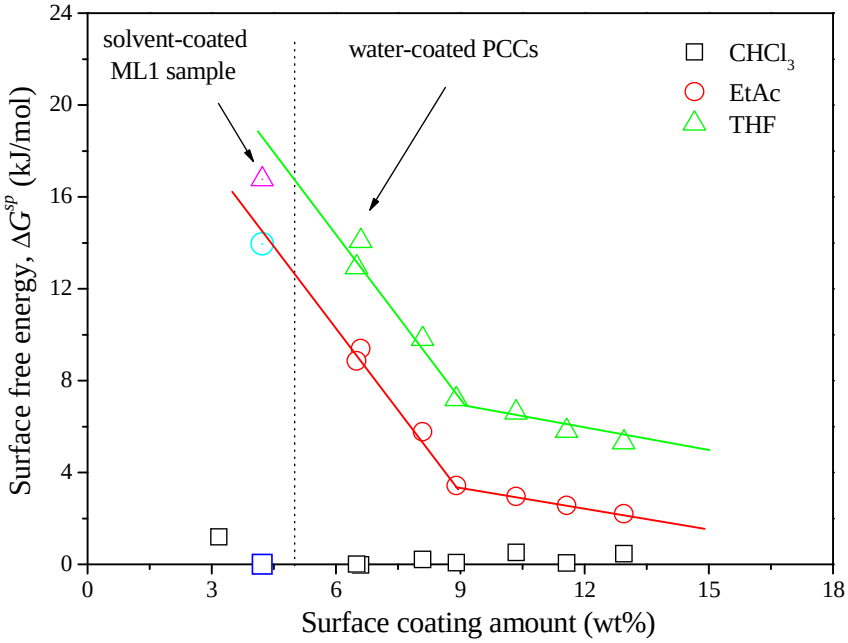

Figure 4.10 Effect of surface coating amount on the specific component of the surface free energy of water-coated PCC

From the IGC results, both the dispersion and specific components of PCC surface free energy calculated by non-polar alkanes and polar solvents show the decreasing tendency when the surface coating amount increases, especially the specific component depends significantly on the coating amount. The comparison with surface free energy of full monolayer covered PCC particles indicated that the physisorbed multilayer had a similar effect on the decreasing of surface free energy, and the specific component was even lower than that of the ML PCC sample. In fact, the surface free energy amount is an important parameter for the surface coating effect rather than the coating amount. By using the water coating process, it seems that the physisorbed calcium stearate multilayer strongly affects the surface free energy.

4.4.2 Dependence of surface free energy on preconditioning temperature

All of the PCC nanoparticles coated with stearin in the aqueous medium have the physisorbed calcium carboxylate multilayer on the surface with a fixed incomplete chemisorbed monolayer. As mentioned earlier, the thermal properties of calcium carboxylate are discussed in depth by the DSC and XRD techniques. It has been concluded that those PCC nanoparticles had already undergone a molecular rearrangement during the drying process after the coating in the water medium. The physisorbed calcium carboxylate molecules reorganized as a consequence of the crystalline phase transition from the monohydrate α type to the anhydrous β' phase. Additionally, several typical thermal transitions were observed on increasing the temperature: evaporation of the free adsorbed water (around 100 °C), β' to the C2 phase or the smectic phase (around 125 °C), smectic-to-nematic phase (around 165 °C), and the nematic-to the liquid-crystal phase transition (around 190 °C). The free water on the PCC surface can be easily removed by the preconditioning process even at a lower temperature such as 60 °C, which was confirmed by the DSC measurement. However, if the preconditioning temperature is higher or similar to the first main phase transition around 125 °C, the surface coating molecules will be in a different structure with an orientational order but in dynamic motion. Meanwhile, considering the prepared process for polymer nanocomposites with PCC particles by the melt extrusion at a high temperature, two different preconditioning temperatures are chosen: 60 °C and 140 °C. The first conditioning temperature is enough to remove the free water on the surface without any phase transition occurring. The latter is high enough for the physisorbed layers to undergo the main phase transition and is closer to the compounding temperature for polymers during melt extrusion. The value of 140 °C was also chosen for comparison with literature values.

Fig. 4.11 shows the dispersion component of surface free energy of this series of PCC particles, which are measured at 100 °C after preconditioning at two different temperatures. The pure PCC particles have a value of 55 mJ/m^2 in the two cases and a similar decreasing tendency was found in both cases with increasing surface coating amount. However, it is to be noted that PCC2 particles are coated with a minimum amount of chemisorbed stearate, which is lower than maximum chemisorbed amount (3.0 wt%) that can be achieved in water coating as discussed in Chapter 3. The preconditioning temperature clearly effected the surface dispersion component of PCC2, which resulted to be 40 mJ/m^2 for a preconditioning at 60 °C and 28 mJ/m^2 with a preconditioning at 140 °C. These results can be explained by considering that the higher temperature preconditioning resulted in a lower accessibility of PCC free sites due to the dynamic motion of the physisorbed stearate molecules. Further increase in coverage (from PCC3 to PCC9) does not lead to a significant change in the dispersion component of surface energy and the final value is about 24-25 mJ/m^2 in both cases with different preconditioning temperatures. In other words, even the stearate molecules are in a kind of dynamic motion at higher temperatures, but the molecular orientation is still in order. The preconditioning temperatures show little effect on the dispersion component of surface free energy.

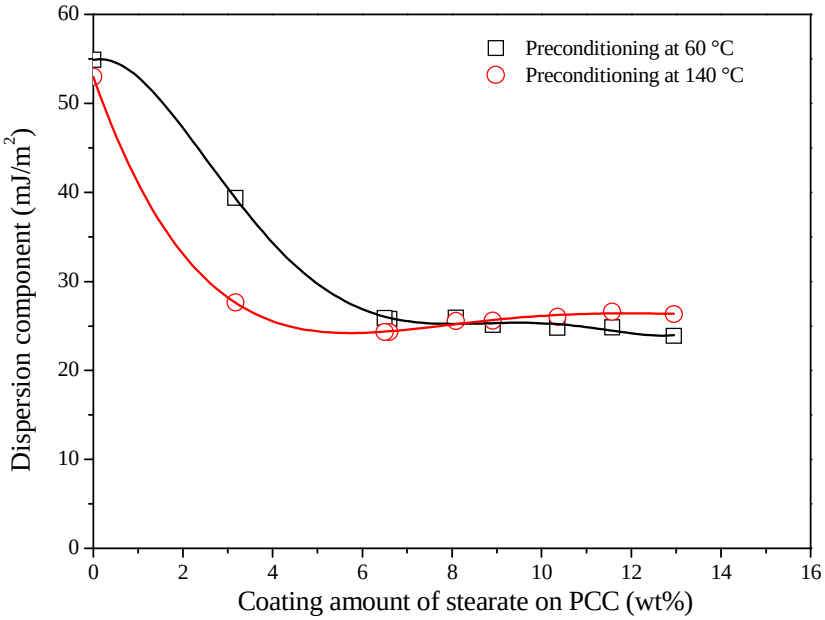

Figure 4.11 Dispersion component of surface free energy for coated PCC particles against the surface stearate coating amount at different preconditioning temperatures

The specific component of PCC surface free energy is shown in Fig. 4.12 with two different preconditioning temperatures, while the measurement temperature is the same (100 °C) and the polar solvent is chosen to be chloroform. In both cases, the ΔG_{ab} values

decreased continually with the increasing of surface stearate coating amount. However, there are different decreasing rates. When coated PCC nanoparticles are preconditioned at 60 °C, no phase transition of stearate molecules occurred, and the interaction between polar solvent (chloroform in this work) are related only to the coating layers. However, the preconditioning at 140 °C would result in a more active mobility of the stearate layers on the PCC surface because of the transition to a liquid-crystal phase (see Chapter 3) and can effectively decrease the adsorption of chloroform on the PCC surface. Beyond a surface coating amount of 6 wt% (PCC3), the ΔG_{ab}values are close to 0 and remain almost constant, which indicates that the stearate coated PCC particles are now completely hydrophobic. From this comparison, it has been concluded that the specific component of surface free energy is strongly dependent on both the surface coating amount and the crystal phases present at different temperatures.

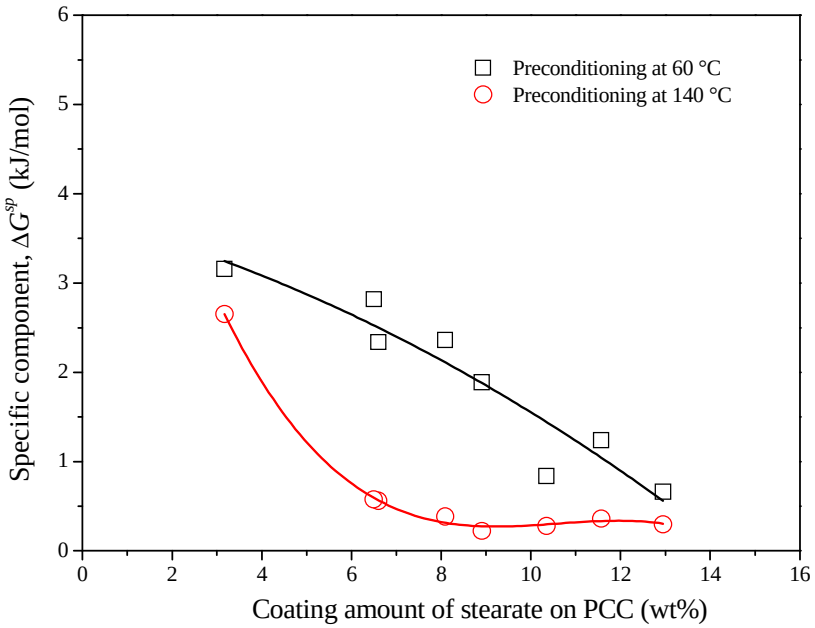

Figure 4.12 Specific component of PCC particles surface free energy against the surface stearate coating amount at different preconditioning temperatures (Chloroform)

4.4.3 Dependence of the surface free energy on measurement temperature

The influence of the measurement temperatures on the surface free energy is also investigated in this work and is shown in Fig. 4.13. The most interesting result is relative to the surface tension of pure calcium carbonate. Fig. 4.13 (a) shows that the dispersion component of pure calcium carbonate measured at 60 °C is about 107 mJ/m^2. Then this value is significantly decreased to be 54 mJ/m^2 measured at 80 °C and keeps at the same level following a further increase in measurement temperature. The non-polar alkanes are used for the calculation of surface tension by using the IGC technique according to the

recorded retention time from the inlet part to the detect FID signal, which is strongly dependent on the adsorption and then desorption equilibrium process in the PCC column. We believe that the mobility of non-polar probes is increased when the measurement temperature increases but below 125 °C without any phase transition of the surface stearate molecules. For each PCC particle, the surface tension decreases with the increasing of the measurement temperature, and no big change occurs when the measurement temperature is higher than 100 °C. At different measurement temperatures, the relationship between the surface tension and the surface coating amount shows a similar trend, first decreasing to reach a minimum value of 24 mJ/m^2 and then staying at this plateau value.

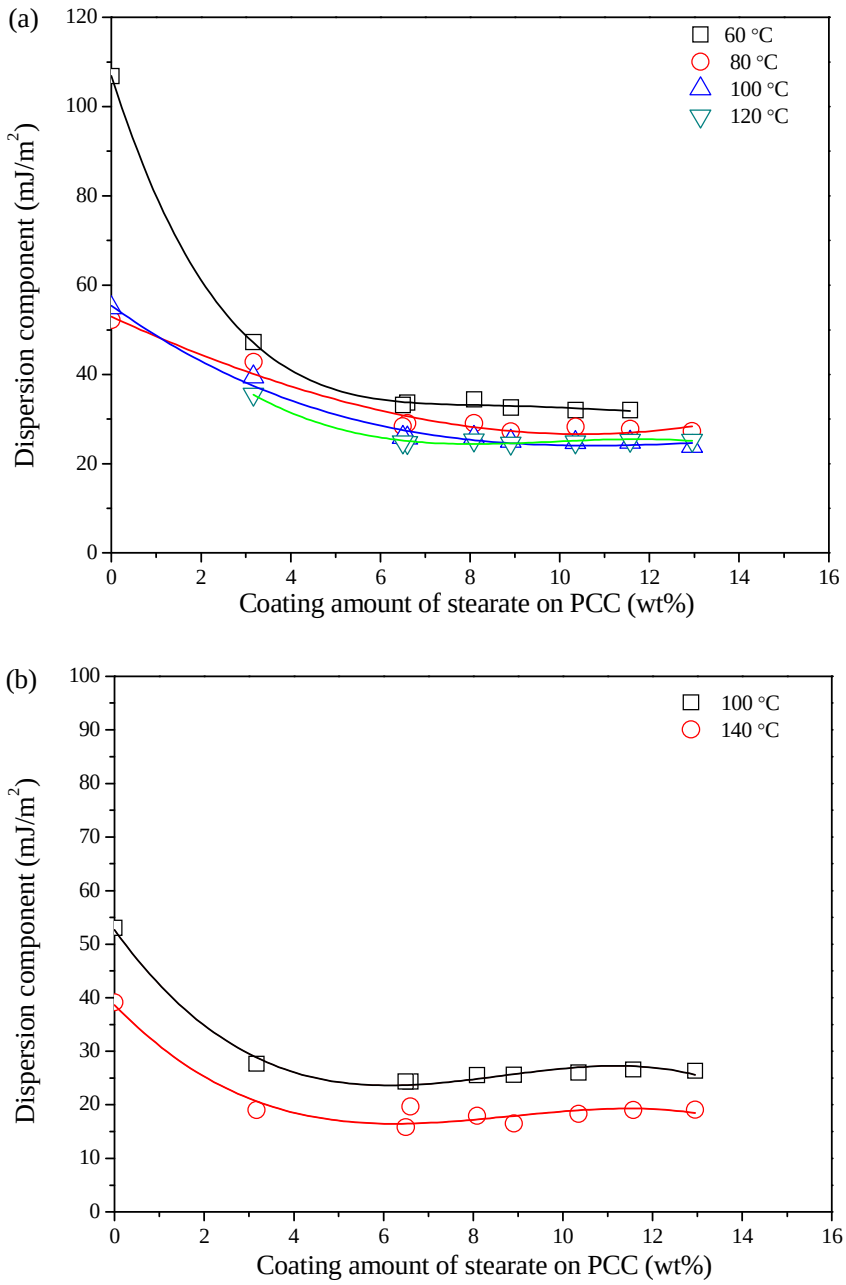

Figure 4.13 Dependence of the surface tension of PCC particles on the measurement temperature: (a) Preconditioning at 60 °C and (b) Preconditioning at 140 °C

Fig. 4.13 (b) shows the results of the surface tension at two measurement temperatures on a series of particles preconditioned at 140 °C for 16 hours. They show exactly the same decreasing tendency with an increase of surface coating amount. However, we want to emphasise that the measurement temperature at 140 °C not only increases the mobility of the detected probes but also leads to a main phase transition of the stearate layers on the PCC surface from C2 to liquid crystalline phase. This is the explanation for the much lower surface tension (around 17 mJ/m^2) for the multilayer coated PCC particles. This situation is closer to the conditions of extrusion when PCC particles are added into polymers.

When this series of PCC particles were preconditioned at 60 °C, the calculated ΔG_{ab} values progressively decreased with the increasing of the surface coating amount at all of the measurement temperatures as shown in Fig. 4.14 (a). This influence of measurement temperatures can be explained by the high adsorption and desorption equilibrium rate for chloroform as the polar probe with increasing temperatures. The calculated ΔG_{ab} measured at 60 °C is about 5.5 kJ/mol, and this high value confirmed that there is still some active sites available on the PCC2 surface with the incomplete monolayer. However, the possibility for the $CHCl_3$ to reach the free PCC sites decreases with the coating amount increases.

Similar to surface tension, the preconditioning at 140 °C resulted in a relatively lower value of ΔG_{ab}, and this can be explained by the more dynamic motion of stearate molecules to mask the available PCC active surface sites.

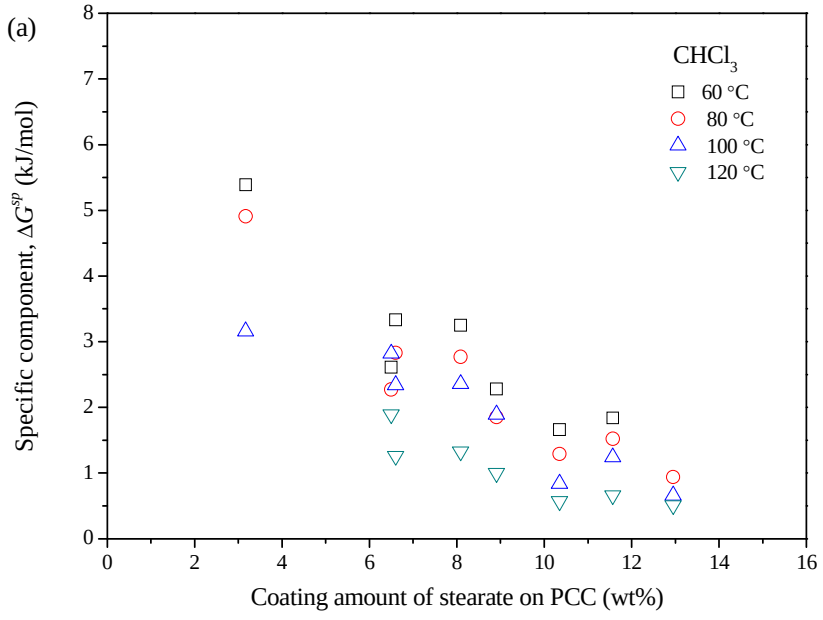

Figure 4.14 (to be continued)

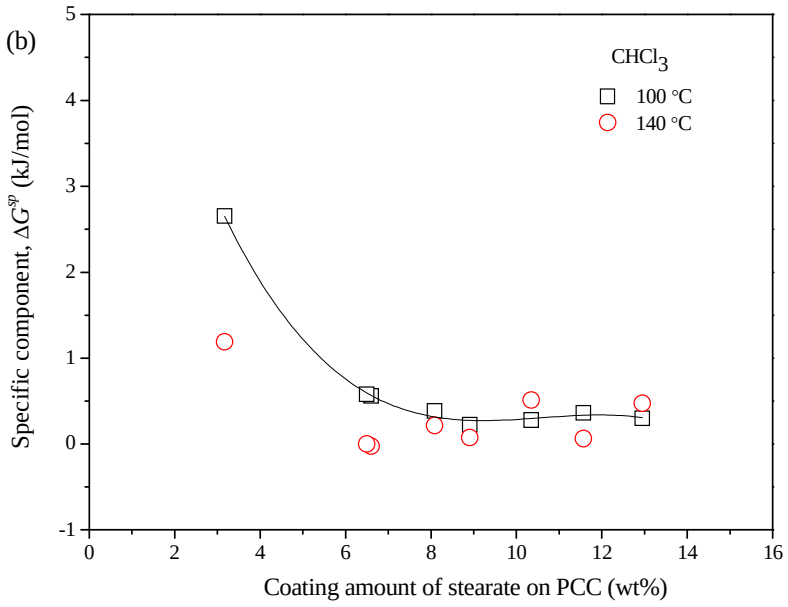

Figure 4.14 Dependence of specific component of PCC surface free energy on the measurement temperature: (a) Preconditioning at 60 °C and (b) Preconditioning at 140 °C

4.4.4 Acid-base interaction parameter

One important aspect of investigating different measurement temperatures is the determination of acid-base parameters of PCC particles before and after coating with stearin. According to Equ. 4.11, the curve plotting $\Delta G_A^{ab}/T$ against $1/T$ should yields a straight line with the slope ΔH_A^{ab}. Fig. 4.15 shows regression straight fitting lines for all of the coated PCC particles according to the free enthalpy ΔG_A^{ab} of the same series of particles as shown in Fig. 4.14 (a). From those fitting lines for PCC particles (from PCC2 to PCC9), those slopes ΔH_A^{ab} seems to decreased first then almost stay as parallel lines. In other words, the adsorption enthalpy of Lewis acid-base interaction ΔH_A^{ab} of the water-coated PCC particles becomes smaller when the coating amount increases. This result is similar to the relationship found between the dispersion component of surface energy and surface coating amount. The PCC surface characteristic is changed to be hydrophobic due to the stearin coating.

However, in our work, only chloroform is available to show some retention peaks at different temperatures when passing through the column packed with PCC particles. This is the experimental limitation to obtain more results from other polar probes. As mentioned in the section on theory background, the acid-base interaction parameters of this series of fillers can be calculated not only from the specific component of adsorption enthalpy ΔH_A^{ab}, but also can be determined directly from free enthalpy ΔG_A^{ab} using the *AN** and *DN* numbers listed in Table 4.3. From Euq. 4.12, K_a and K_b can be calculated from the fitting

line when $\Delta G_{ab}/AN^*$ is plotted versus DN/AN^* of polar probes. The slope of the fitting line K_a is related to the acidity of the solid and the intercept K_b reflects the electron donor ability.

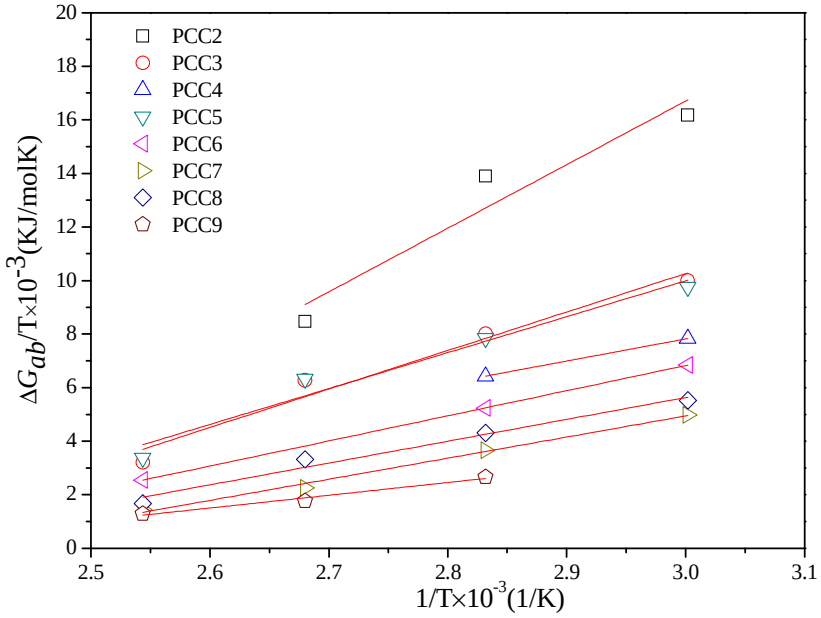

Figure 4.15 Determination of the enthalpy of acid base interaction according equation 4.11

Three polar probes THF, EtAc and $CHCl_3$ were used in this work for the determination of acid-base interaction parameters and their ΔG_{ab} values are shown in Fig. 4.10, which were determined after the PCC particles were preconditioned and measured at 140 °C. It is quite clear that the slopes of those fitting lines as shown in Fig. 4.16 decreased following the increase of coating amount from PCC3 to PCC9. In other words, this means that the relative acidity of the coated PCC particles significantly related to the stearate coating amount.

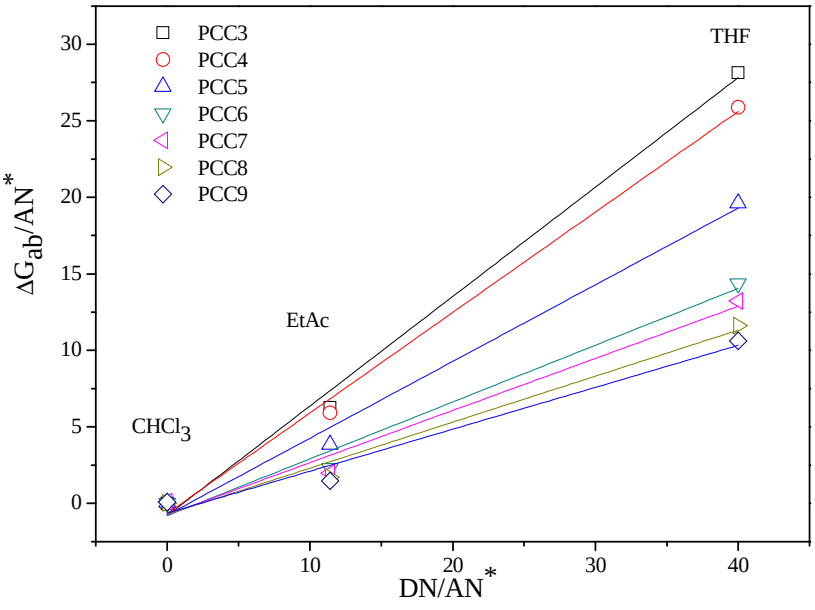

Figure 4.16 Determination of the acid-base parameters of coated PCC particles

Moreover, Fig. 4.17 shows the relationship between the acidity parameter K_a and the stearate coating amount on PCC surface. It is apparent that two straight lines can be traced through the experimental points with a transition point corresponding to PCC6, which is consistent with the former discussion about the molecular arrangement and presence of a second physisorbed stearate layer present on the surface.

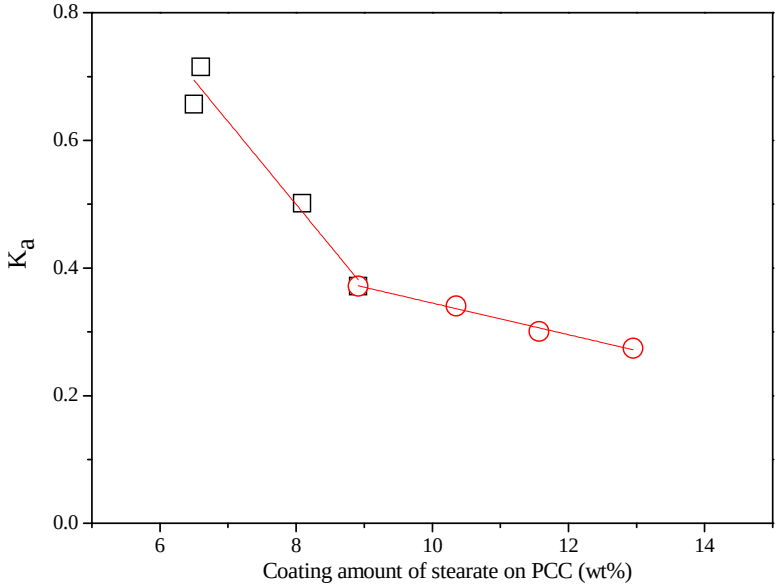

Figure 4.17 Relationship between the acidity parameter with the stearate coating amount

4.4.5 Filler/polymer matrix interaction

In filler toughening of plastics, the interfacial adhesion between the polymer matrix and the fillers is strongly related to the surface chemical and physical properties of the two components. It is reported that the interaction between two surfaces in contact with each other can be created by primary or secondary bonds. The most important primary forces are the ionic, covalent and metallic bonds, and the secondary bonds are created by the van der Waals forces, such as the dipole-dipole, induced dipole and dispersion interactions. The first one is very strong while the others are relatively weak. Also an H-bond can also form between the two phases. There are many available theories that have tried to explain the complicated phenomenon of adhesion. Fowkers [161, 162] suggested the following relation:

$$\gamma_{12} = \gamma_1 + \gamma_2 - 2\left(\gamma_1^d \gamma_2^d\right)^{\frac{1}{2}} \tag{4.13}$$

where γ_i^d is the dispersion component of γ_i. This theory is valid only for the special case without polar interaction. However, most polymers are polar to various degrees. Thus, the polar interaction is the main parameter that determines the interfacial tension with the second phase. We have already elucidated that the influence of the surface coating amount is more significant in the specific component of the coated PCC particles.

Several theoretical equations have been obtained relating the interfacial tension to the polarity and the surface tension of individual phases. The three most used equations are the following [102]:

a. Harmonic-mean equation:

$$\gamma_{12} = \gamma_1 + \gamma_2 - \frac{4\gamma_1^d \gamma_2^d}{\gamma_1^d + \gamma_2^d} - \frac{4\gamma_1^p \gamma_2^p}{\gamma_1^p + \gamma_2^p} \tag{4.14}$$

b. Geometric- harmonic-mean equation:

$$\gamma_{12} = \gamma_1 + \gamma_2 - 2\left(\gamma_1^d \gamma_2^d\right)^{1/2} - \frac{4\gamma_1^p \gamma_2^p}{\gamma_1^p + \gamma_2^p} \tag{4.15}$$

c. Geometric-mean equation:

$$\gamma_{12} = \gamma_1 + \gamma_2 - 2\left(\gamma_1^d \gamma_2^d\right)^{1/2} - 2\left(\gamma_1^p \gamma_2^p\right)^{1/2} \tag{4.16}$$

Combining with our IGC results and those theoretical equations, it can be concluded that when the polymer matrix is fixed, the interfacial adhesion depends not only on the dispersion component of free surface energy, but is specifically related to the specific component of the PCC surface free energy. In the particulate filled polymers, the dependence of composite strength on the interfacial interaction was reported [84, 163] to support this statement. Besides, the debonding induced by a weak interfacial adhesion is the main accepted dominating micromechanical process in the polymer composites toughened with fillers. The IGC results predict that the PCC surface coating with stearin will show a weaker interfacial adhesion with a polymer matrix.

4.5 Discussion and conclusion

The experimental results from the DSC, XRD, XPS and IGC experiments lead us to a number of results that can be summarized as follows:

- The physisorbed calcium stearate/palmitate multilayer in PCC particles, prepared by the water coating process, shows a complicated thermal behavior, indicating a peak corresponding to volatilization of free water, a crystalline-to-smectic peak, a smectic-to-nematic peak, and finally a nematic-to-liquid peak. This means that the physisorbed layer, present on the coated PCC particles considered in this work, is crystalline at room temperature.
- Additionally, the exact crystal phase of the stearate on the PCC surface after drying has been determined by the DSC and XRD techniques. It has been concluded that there is a thermal transition from the monohydrate α phase formed from the aqueous medium to the anhydrous β' phase after drying at 105 °C. Thus, the physisorbed stearate has lost its water

of crystallization and only free water is present on the surface.

- Beyond 3.17 wt% coating, no major change in the dispersion component of surface energy with stearin content is noted. Our interpretation is that the surface is similar to that of solvent or dry-coated samples, that is the organic tails are oriented outwards from the surface.
- The specific component of the surface energy shows a change in trend at 9%, which should be a transition point of the molecular arrangement of the surface physisorbed stearate.
- The first monolayer, which is chemisorbed on the PCC surface, is an incomplete monolayer with a maximum surface coverage of about 72 %. All of the coated PCC particles have a similar chemisorbed monolayer due to the water micelle adsorption mechanism.
- The layer thickness for the two fully covered monolayer samples calculated by the XPS MultiQuant software, shows that the chemisorbed monolayer is vertical to the PCC surface.

All of this information enables us to depict a model of the structure of stearin water-based coatings on calcium carbonate nanoparticles.

As shown in Scheme 4.1 (a), we propose the molecular arrangement that in water the micelle mechanism leads to the formation of a chemisorbed monolayer at the surface of the particles and to a physisorbed calcium stearate layer. The physisorbed layers are in a hydrated α phase with the polar head groups directed towards the water phase, and bonded to some water molecules, while the two organic tails of each calcium di-stearate molecules are parallel to each other forming a single layer, in a tail-to-tail arrangement to the chemisorbed molecules. This structure is in a stable form since the carboxyl groups and the calcium ions are surrounded by polar water molecules. At this stage, the two layers (the chemisorbed monolayer and that formed by the alkyl chains of the physisorbed $CaSt_2$) are still reminiscent of the relative positions of the molecules in the original micelle from which they are precipitated from the water phase. The degree of coverage for the two layers is identical. For example, for PCC4 (6 wt%) both the monolayer and the $CaSt_2$ layer have a surface coverage of 72% at this stage due to the deformation of micelles. The picture for samples with larger stearin contents is somewhat similar to this and the only difference is that more $CaSt_2$ layers will be present since the maximum coverage that can be reached with the micelle mechanism of coating is just 72%.

After drying at 105° C, a critical temperature just above the transition to the C2 phase,

the water molecules are lost and the stearate (or palmitate) molecules may rearrange as shown in Scheme 4.1 (b). In the new layer of anhydrous $CaSt_2$, the organic tails of calcium di-stearate are arranged on opposite sides with respect to the central calcium ion, although they are still vertical to the calcium carbonate particle. In this way, on the outer surface of the particle, only the terminal non polar CH_3 groups of the alkyl chains will be present, in agreement with the observation that the dispersion component of surface energy of the coated particles does not appreciably change with stearin content above 3%. In fact this physisorbed $CaSt_2$ (and $CaPm_2$) layer could be better described as a double layer of long chain aliphatic carbon tails separated by a stratum of calcium ions, whose electric charge is equilibrated by the carboxyl head groups of the stearate ions. This structure is related to the orthorhombic β' phase of calcium di-stearate. In order to reach this configuration, it is necessary that one half of the aliphatic chains of the calcium di-stearate rotate 180° as shown in Scheme 4.1 (c). For temperatures beyond 120 °C, the stearate/palmitate layer will undergo a phase transition from crystalline to the liquid-crystal state, which will result in a more disordered arrangement like that depicted in Scheme 4.1 (c). This phase transition related to the thermal treatment explains very well that the preconditioning temperature at 140 °C results in a lower value of the PCC surface energy compared to that of 60 °C.

This proposed mechanism for rearrangement after drying means that the surface coverage of the double layer formed after this reorganization will be one half that of the original physisorbed layer. With a further increase of the surface coating amount, the orthorhombic double layer of calcium stearate/palmitate molecules continue to reorganize until reaching the maximum coverage of 72 %. PCC 6 was coated with about 8.91 wt% stearate molecules, which is close to the situation that both the chemisorbed and physisorbed layer have the maximum surface coverage. This proposed model can be verified by calculating the layer thickness from the XPS data. This is possible using the island-on-sphere model with the MultiQuant software. This model has the limitation that the two layers in the island type must have the same surface coverage. This is the case of the single sample PCC6 in the series considered in this work. For PCC6, a thickness of 65.4 Å is calculated which is close, within the limits of these type of calculations, to the sum of the length of one molecule of stearin (22 Å) plus an interlayer distance corresponding to one stearate/palmitate double layer in the orthorhombic β' phase, which we estimated to be about 46.7 Å.

This confirms the proposed scheme for the surface physisorbed stearate molecules. Considering the monolayer sample with vertical chemisorbed molecules on the surface, the

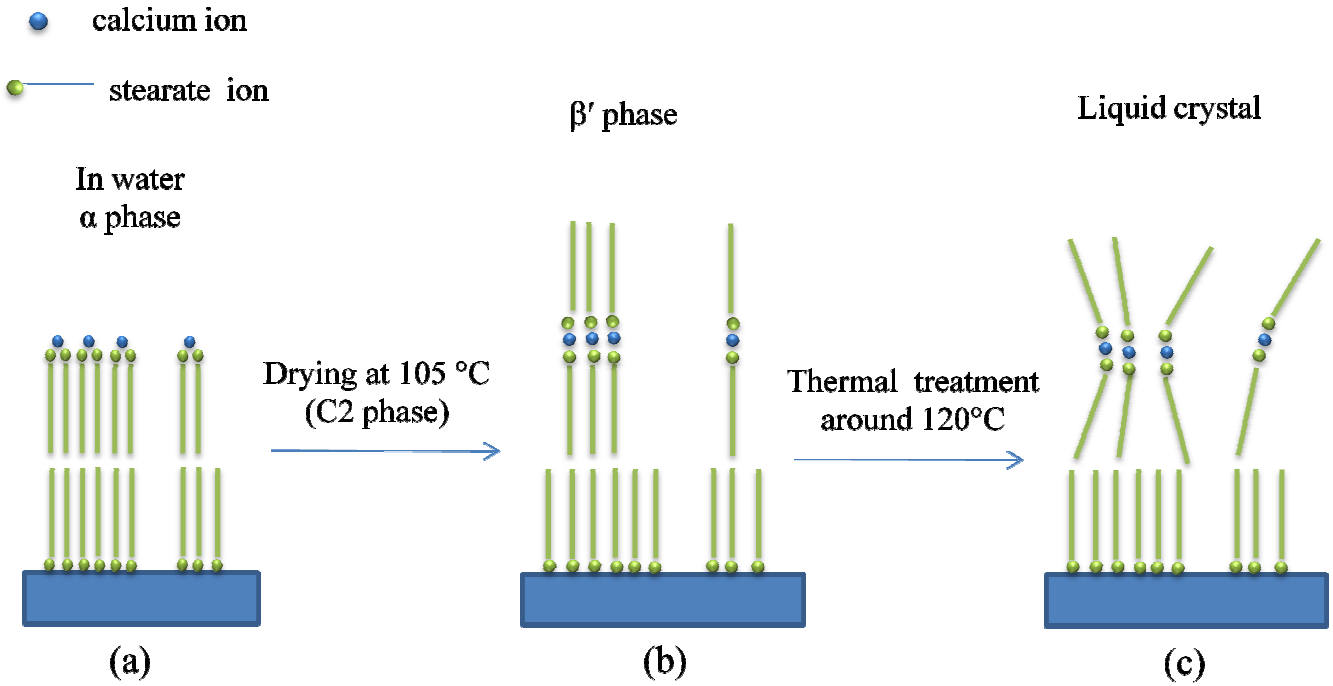

Scheme 4.1 Arrangement of stearate molecules on the surface of PCCs coated in aqueous medium.

Effect of thermal treatment during drying and the IGC measurements on molecular structure.

stearate molecular orientation on the water-coated PCC is proposed in Scheme 4.2 (b) together with dry or solvent-coated ML samples in Scheme 4.2 (a). This model helps us in explaining why the dispersion component above monolayer coverage is practically constant with the organic content of the coating, since both the monolayer and the double layers show only CH_3 groups on the outer surface of the particles.

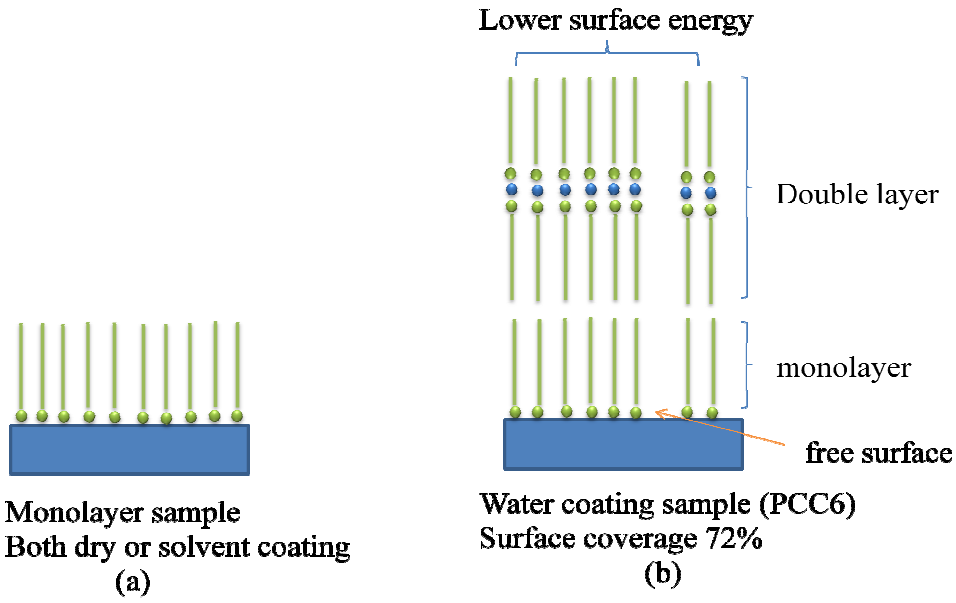

Scheme 4.2 Model for the structure of the stearate multilayer on the surface of PCC

The results obtained in the IGC experiments and presented above agree well with those derived from other methods and strongly support the tentative explanation given for the multilayered structure of the stearate coating on PCC formed in water. In fact, incomplete coverage due to the micelle adsorption mechanism results in relatively strong acid-base interactions of the surface with two of the polar probes. Incomplete coverage allows access to the surface, while a strong interaction is the driving force aiding diffusion. With increasing surface coverage, access to the surface becomes more limited leading to a decrease in the specific component of surface energy. The presence of additional molecules in the second double layer of stearate completely closes the surface and hinders the diffusion of polar probes to the filler surface. The changing slope in the dispersive component and the acid-base interaction parameters figures at around a 9.0 wt% coating level indicates the attainment of the maximum coverage of the first physisorbed double layer of stearate. The rather specific structure of the coating forming in the water coating process may lead to interesting properties in composites.

Chapter 5 HDPE/PCC nanocomposites

5.1 Introduction

Nanocomposites with quasi-spherical particles have received increasing attention in the area of "filler toughening" for their potential to improve both the toughness and stiffness when compared to traditional composites loaded with mineral fillers. Precipitated calcium carbonate particles are mostly used as nanofillers in polymeric applications mainly due to their low cost and simple processing. Many researchers have reported the possibility of increasing the toughness of PCC-filled polyolefin composites [7, 12, 40, 89]. Bartczak et al [11] found that the toughness of $CaCO_3$-filler materials increased dramatically when the mean interparticle ligament thickness of the matrix polyethylene dropped to values below 0.6 μm, which showed the same manner of the brittle-to-ductile transition as exhibited by the rubber particle-modified composition of Nylon 6,6 by Wu [3]. A former work of Lazzeri [7] indicated that progressively adding stearic acid on the coated PCCs led to a continuous increase in toughness of HDPE/PCC nanocomposites. Thio [12] also reported the improved Izod impact energy up to four times that of the pure polypropylene with the addition of $CaCO_3$ particles with an average diameter of 0.7 μm.

Toughness of a material in general reflects the degree of energy absorption from the beginning of the mechanical load to the final fracture. However, toughness is one of the most complex properties to control because it is generally influenced by many morphological and micromechanical parameters, such as particle size [63], critical interpatricle distance [14], interfacial adhesion between filler and polymer matrix [84, 93] and crystalline structure of the polymer [120]. Moreover, around the nanofillers in the polymer, or in the interphase region between the polymer and the nanofillers, it was reported that transcrystalline layers of the polymer matrix may form along with a lamella rearrangement of the polymer [4, 70]. The typical transcrystalline regions around rigid fillers are related to the effect of nanoparticles as heterogeneous nucleating agents to initiate crystallization along the interface. However, the exact mechanism of the transcrystalline growth and the influence of the transcrystalline layer or the ligament region on the mechanical properties of polymer nanocomposites are still not clear.

In filler toughening studies, one of the most accepted mechanisms for improving impact resistance is microvoid formation. Thus a weaker interfacial adhesion is required to promote the debonding between fillers and the matrix, allowing for the formation of microvoids around the fillers that then trigger the plastic deformation of the interparticle

ligaments [34, 35, 88]. Even if the debonding process plays a little role in terms of absorbing energy, the process plays an important role in initiating the toughening mechanism, which facilitates the energy absorption by shear yielding, plastic deformation and fibrillation of the polymer [34]. Therefore, in order to improve the toughness of polymer nanocomposites, it is necessary to achieve a low particle matrix adhesion. However, it is also well known that nanoparticles have the tendency to aggregate during compounding with the polymer matrix. The key point here is how to promote a uniform dispersion of the very fine nanoparticles, while, in the meantime, keeping a weaker interfacial adhesion between the polymer and nanoparticles. In other words, a suitable surfactant for the surface treatment for PCCs is necessary for solving these two problems. As we discussed in Chapters 3 and 4, the industrial approach to decrease the surface energy of nanoparticles is to prepare a surface coating with stearic acid due to its low cost. Moreover, the surface treatment of stearin on the PCC surface results in multilayers of stearate, which was determined by different surface characterization methods. The commercially available PCC nanoparticles, coated in aqueous medium, were also found to show different surface properties with respect to particles treated by the dry or solvent coating.

The main purpose of this chapter is to apply PCC nanoparticles into high-density polyethylene (HDPE) for the preparation of nanocomposites. HDPE is an important semi-crystalline polymer because of its low cost, availability and ease of processing [164-166]. Mainly, the mechanical properties such as the tensile tests and the impact toughness are investigated, and the micro-morphology of HDPE/PCC nanocomposites is also studied using SEM tests, which were also carried out for the fracture process study. The study of HDPE/PCC nanocomposites attempts to clarify the influence of surface coating on the PCC nanoparticles on the mechanical properties of polymer nanocomposites.

5.2 Tensile properties

As discussed in depth in Chapters 3 and 4 concerning the surface coating of industrial PCC nanoparticles, the stearate molecular layers on the PCC surface significantly decrease the surface free energy, which is primarily necessary for the good dispersion of nanoparticles in the polymer and also for a decreased interfacial adhesion. The dependence of the tensile properties on the surface organic coating amount of HDPE/ 10 vol% PCC nanocomposites is shown in Fig. 5.1 and in Table 5.1. Meanwhile, the PCC nanoparticles with a full covered monolayer (code ML1 and ML2) were also added to polyethylene by the

melt extrusion process for comparison. During the tension tests, the specimens of pure HDPE and HDPE/PCC nanocomposites showed similar whitening, yielding (at maximum stress), necking and then deformation until fracture occurred. In fact, the addition of coated PCC nanoparticles did not change the mechanical properties.

Table 5.1 Mechanical properties of HDPE/PCC nanocomposites

Code	PCC surface coating (*wt%*)	Yield stress (*MPa*)	Young' modulus (*GPa*)	Charpy impact strength (kJ/m^2)	
PE00	0	31.95	1.178	21.03	7.90[§]
PE01	0	45.55	1.948	10.09	
PE02	3.0	48.401	1.887	9.63	
PE03	4.5	48.04	1.75	10.60	
PE04	6.0	43.86	1.864		5.77[§]
PE05	7.5	44.75	2.005		5.91[§]
PE06	9.0	41.3	1.828		7.38[§]
PE07	10.5	45.03	1.785	8.73	7.60[§]
PE08	12.0	43.53	2.013		
PE09	13.5	46.14	2.035	10.21	7.88[§]
PES1	2.75	37.3	1.608	5.64	
PES2	4.5	45.6	1.642	9.01	
PEML2	15	44.52	1.67		6.85[§]

[§] Charpy impact tests were carried out for the specimens with sharp crack about 5 mm.

Fig. 5.1 presents the relationship between the yield stress of HDPE/10 vol% PCC nanocomposites and the surface organic coating amount on the PCC fillers. It is clear that the addition of 10 vol% pure PCC nanoparticles significantly increases the yield stress from about 32 to 46 MPa. With progressively increasing surface coating amount of stearate layers on the PCC particles, the yield stress of polyethylene nanocomposites shows a slight decrease. This can be interpreted as a result of the decreased interfacial adhesion between PCC and HDPE, due to the decreased surface free energy by the increasing the quantity of coating on PCC surface as determined in our former work. For the pure PCC particles, it is possible that the HDPE molecules arranged around the PCC particles, leading to a rigid interphase. Inversely, the organic coating on the PCC surface reduces the stress transfer ability of the interphase, leading to a kind of weaker interphase. The yield strain of HDPE/PCC nanocomposites filled with this series of stearin-coated PCC fillers is shown in Fig. 5.2. Yielding occurs earlier in HDPE nanocomposites with respect to the pure HDPE,

further increasing the coating amount produces smaller yield strain. This result confirmed the weaker interfacial adhesion between PCC particles and HDPE matrix, resulting in the earlier occurrence of debonding.

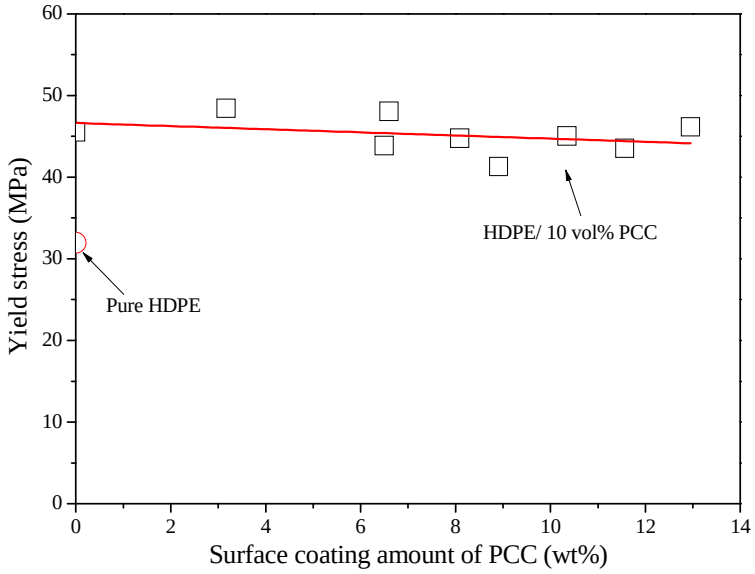

Figure 5.1 Dependency of yield stress of HDPE/PCC nanocomposites on the surface coating amount of PCC

During the tensile measurements, all the specimens of HDPE/PCC nanoparticles showed very strong whitening under the external applied loading. This phenomenon is attributed to the extensive debonding of the particles from the matrix, which is suggested to occur near or a little before the yield point by Lazzeri [7, 63]. It also confirms the suggested state of low interfacial adhesion between two components in the nanocomposites after the PCC surface coating with the stearin. Some experimental work was also carried out by Lazzeri's group based on the volume strain determination on pure HDPE and HDPE/PCC nanocomposites [7]. Volumetric strain is a quantity critical for completely understanding polymer behavior. For example, in the semi-crystalline homopolymer, it is a sign of crystal fragmentation, while in the particulate polymer, it is also a symptom of particle debonding from polymer or particle cavitations. In the former work of Lazzeri, the pure HDPE presented a decrease of volume strain with the deformation under tensile testing, which was due to the stretching of non-crystalline rubbery phases leading to the orientation of the amorphous chains parallel to each other in order to form a kind of mesomorphic structure and then producing a decrease in volume strain. In contrast to this, the presence of PCC particles indicated an increase in volume strain as in Fig 5 of reference [7] attributed to the debonding effect and then the formation and growth of microvoids. A similar work on the three dimensional large-strain deformation of HDPE/$CaCO_3$ composites was carried by the

Parsons [167] using an optical method for simultaneously measuring strains in all three dimensions during a uniaxial tension test. They found that the volume strain of HDPE composites, which was determined by the true stress-true strain data, increased with increasing the particle content in the polymer. This result is strong evidence of the debonding occurring between the fillers and the polymer followed by the formation of elongated cavities around the particles.

The debonding process occurring during the tensile tests is related to the interphase region, which consists of mainly three parts: nanoparticle surface, the organic coating layer on the PCC surface and the oriented layers of polymer matrix, and the polymer matrix outside the preferred layers [5, 11]. In this thesis, nanoparticles are applied to HDPE to balance its toughness and stiffness. The lower tensile stress of the investigated HDPE/PCC composites with increasing surface coating materials suggested lower interfacial adhesion. This factor is critical for toughness improvement and will be discussed in the following section on impact response.

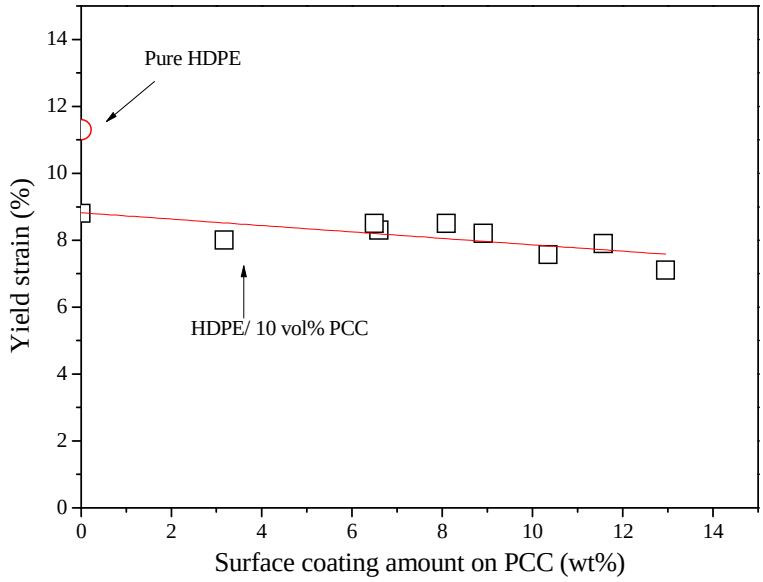

Figure 5.2 Dependence of Yield strain of HDPE/PCC nanocomposites on the surface coating amount of PCC

Young's modulus of HDPE/PCC nanocomposites is shown in Fig 5.3 against the surface coating amount of PCC fillers. As it can be seen, the addition of 10 vol% uncoated PCC causes an increase of Young's modulus by about 65% compared to pure HDPE. However, the PCC surface coating amount shows no influence on Young's modulus. It was also reported by Bartczak [11] that Young's modulus increases with an increasing concentration of PCC fillers, while the yield stress gradually decreased with increasing PCC

content. Therefore, we can conclude that Young's modulus of polymer nanocomposites is related to the amount of nanofillers, but not affected by the PCC surface coating.

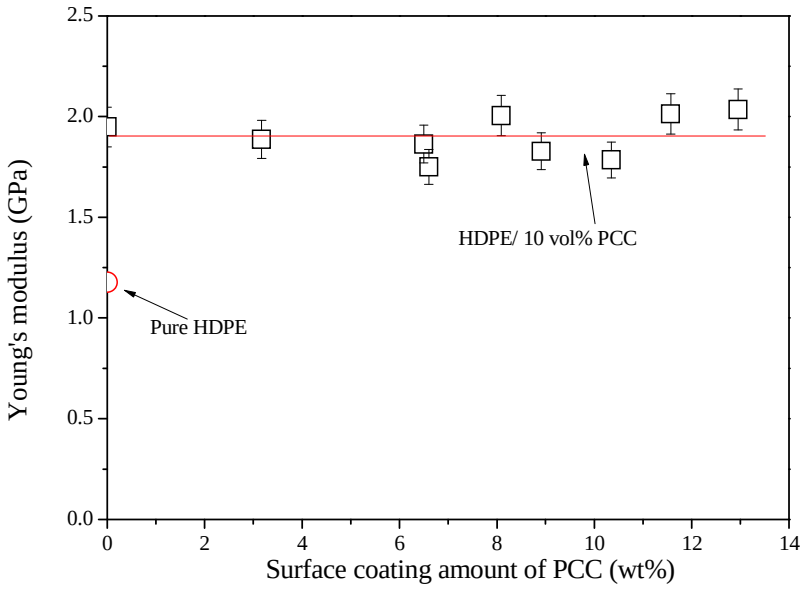

Figure 5.3 Dependence of Young's modulus of HDPE/PCC nanocomposites on the surface coating amount of PCC

5.3 Impact response

In this thesis, Charpy impact tests were carried out for determining the energy absorbed during the fracture for HDPE/PCC nanocomposites. The absorbed energy is a measure of the toughness of materials. Fig. 5.4 shows the relationship between the Charpy impact strength of HDPE composites and the surface organic coating amount of PCC fillers. It is clear that the impact strength of pure HDPE shows a value of about 8 kJ/m^2. The selected HDPE/PCC nanocomposites, for example, PE04 has a much lower value (5.7 kJ/m^2) of impact strength. However, the impact strength of nanocomposites increases with the further addition of surface coating agents to the PCC particles. When PCC9 was melt blended with HDPE, the Charpy impact strength reached almost the same value of pure HDPE. It appears that the impact strength increased linearly with the surface coating amount.

As we discussed in Chapter 4 related to the PCC surface energy determination by the IGC technique, the acid-base parameter of coated PCC particles was also determined. The coated PCC surface showed a decreasing surface free energy in both dispersion and specific components with an increase in the amount of organic coating. Moreover, the acidity of coated PCC was also reduced at high levels of surface coating. In Fig. 5.5 the relationship between the acidity of coated PCC particles and the Charpy impact strength of HDPE/PCC

nanocomposites is shown. There is a decreasing tendency of the impact strength with an increase in the PCC surface acidity. In other words, the acid-base properties of the coated surface play an important role in the interfacial adhesion. Pukanszky and Moczo [147] reported that the coated calcium carbonate particles led to a decrease in the interaction strength due to the neutral character of the filler surface, which was similar to our results. As shown in Chapter 4, the surface energy of coated PCC particles decreased with the addition of coating layers, which then led to a change in the interfacial interactions and even in the interphase thickness.

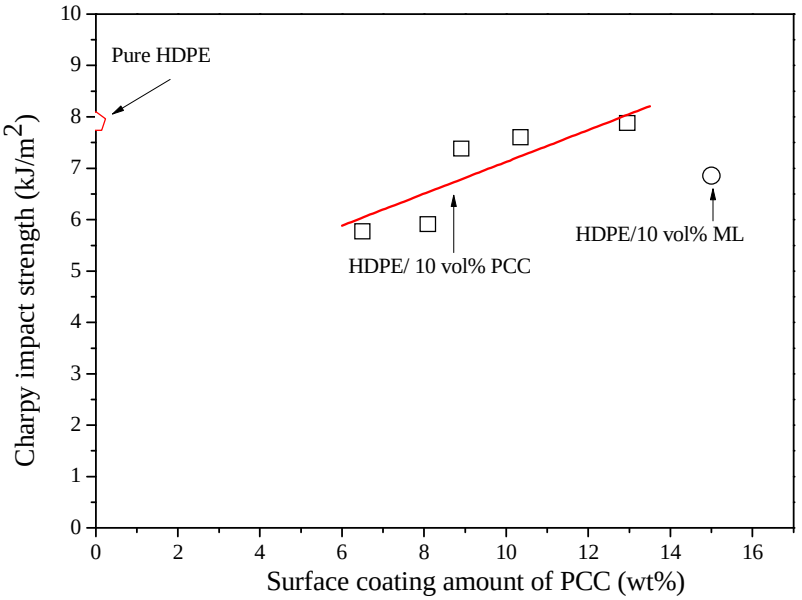

Figure 5.4 Dependency of Charpy impact strength on the surface coating amount of PCC

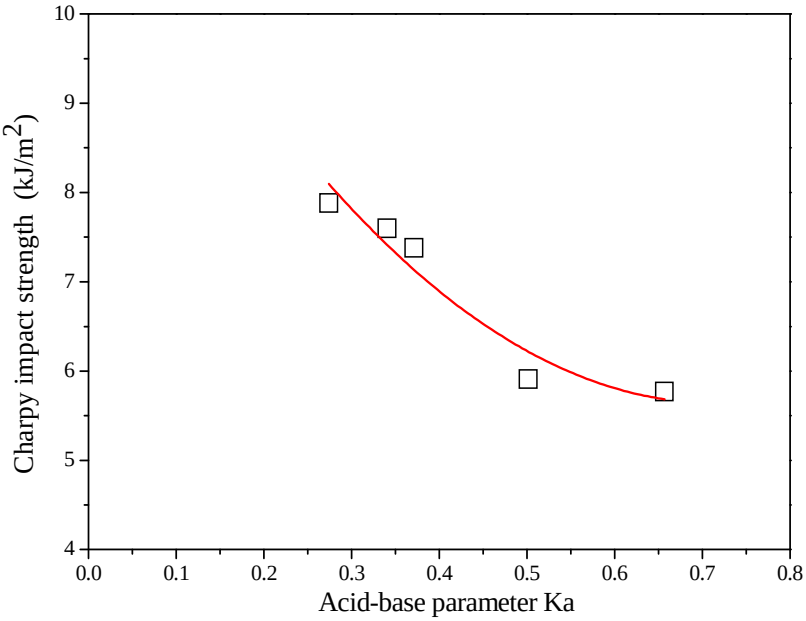

Figure 5.5 Relationship between the acid-base parameter of coated PCC and the related Charpy impact strength

5.4 Morphology of the fracture surface and analysis of the deformation process

The examination of the fracture surface of pure HDPE and HDPE/PCC nanocomposites with the SEM technique gives detailed information on the crack initiation and crack propagation processes occurring during the impact tests. This study on the microscopic fracture surface, which mainly investigates how a crack is initiated and accompanied by large energy consumption, is quite important in understanding the fracture and toughening mechanisms. Usually, there are two primary zones in the fracture surface related to the crack initiation and crack propagation steps respectively as shown in Fig. 5.6, as an example, without considering the dimension ratio, which depends on the measurement temperature [168].

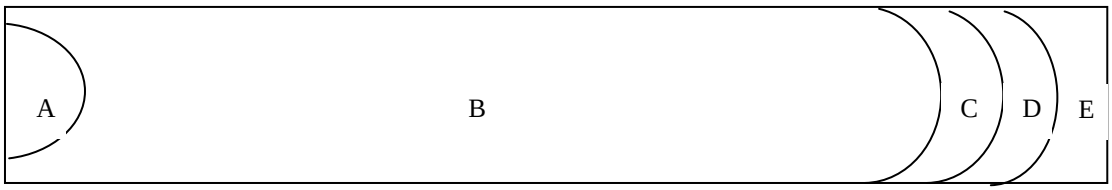

Figure 5.6 Schematic of the fracture surface after Charpy impact test

5.4.1 Fracture surface of pure HDPE

First, the fracture surface of pure HDPE is presented in figures Fig.5.7, Fig. 5.8 and Fig. 5.9 to show different parts of the fracture surface starting from the notch. In this thesis, the pure HDPE is marked with the symbol 1, while the HDPE/PCC nanocomposites are marked as 2 in order to simplify the labels in the SEM graphs and to better compare the different morphology in the two cases. The different parts of the impact fracture surface are named as A, B, C, D, E following the crack direction starting from the notch. The crack initiation zone is labeled as 1A in Fig. 5.7 (a) of a low magnification and 1Am in Fig. 5.7 (c) of a high magnification. This part can be named craze-like part. Following the crack propagation, the different parts B, C, D, E are present on the surface with a noticeable boundary as shown in Fig. 5.6. The crack propagation region in pure HDPE is obviously separated into different parts labeled as B, C, D, E in Fig. 5.8 (a) and Fig. 5.9 (a). Part B, at both low [Fig. 5.8 (a)] and high magnifications [Fig. 5.8 (c)], is a brittle-like zone. This region is located just after the crack initiation part and is caused by the burst of energy following the breakdown of the craze zone. Then the craze propagates at a progressively higher rate because the materials do not have enough time to dissipate the excess energy, leading to a brittle surface. This zone B shows a similar craze-like region as zone A including some tearing of the material and the presence of vein-type features.

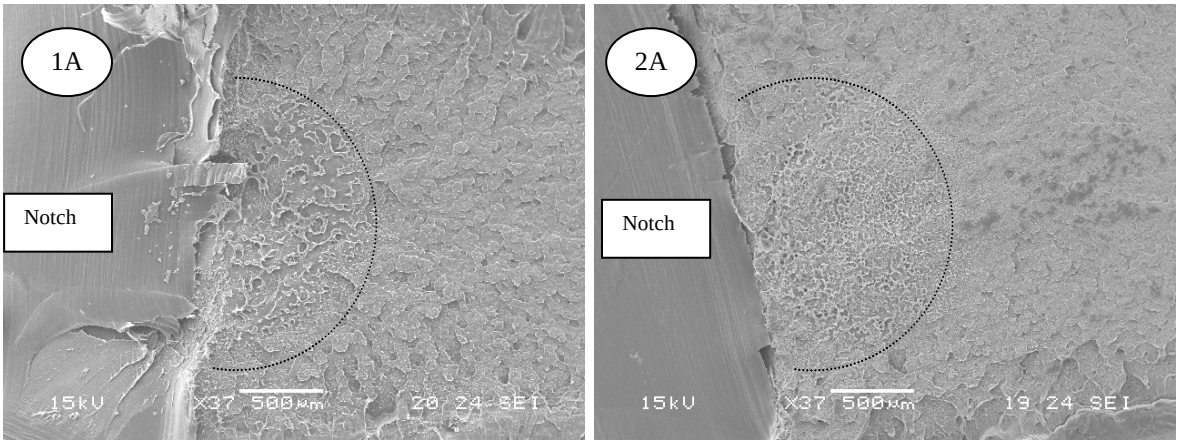

(a) **(b)**

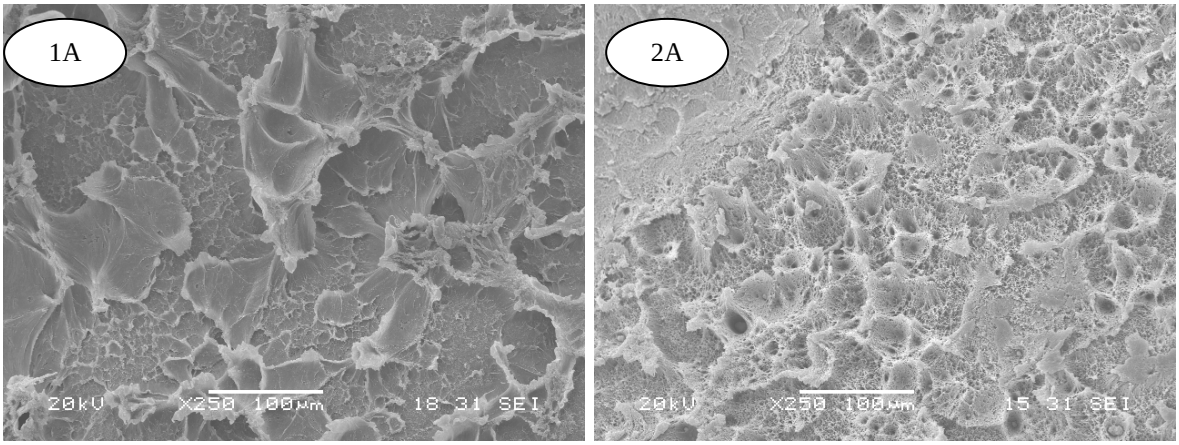

(c) **(d)**

Figure 5.7 SEM micrographs of carck iniziation region on the fracture surface

(1) pure HDPE, (2) HDPE/10 vol% PCC9

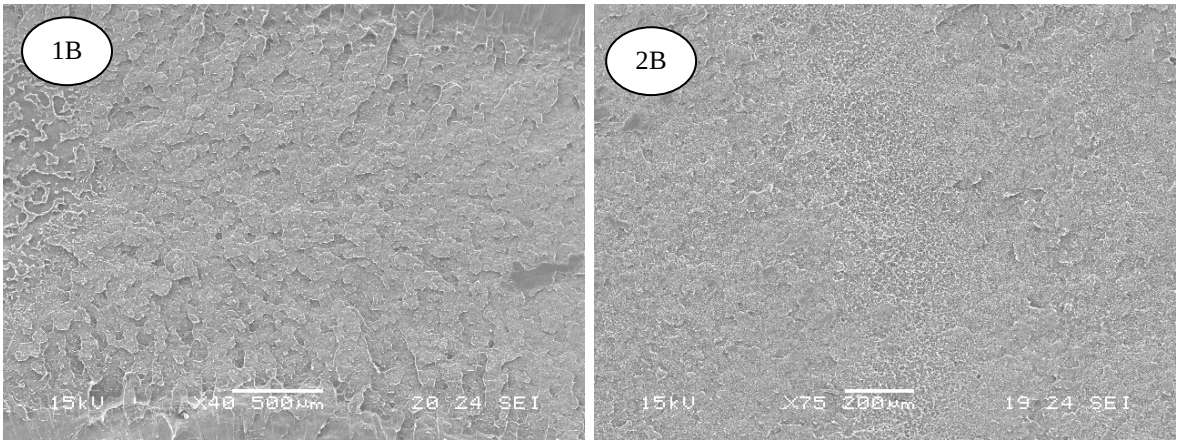

(a) **(b)**

Figure 5.8 SEM micrographs of crack propagation region on the fracture surface

(to be continued)

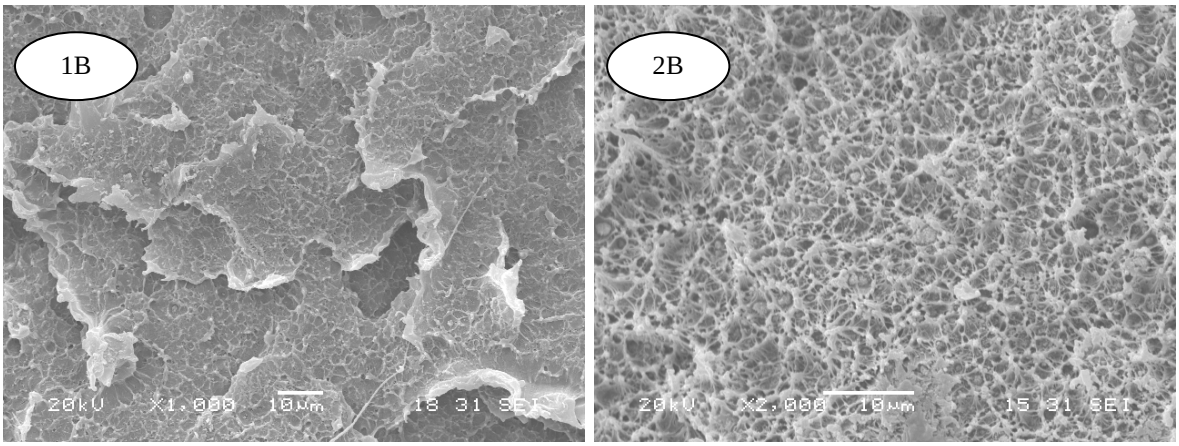

(c) **(d)**

Figure 5.8 SEM micrographs of crack propagation region on the fracture surface
(1) pure HDPE, (2) HDPE/10 vol% PCC9

As it can be seen in Fig. 5.9 (a), zone C is a relatively small part with macroscopically visible curved markings on the fracture surface. The boundary between regions C and D in Fig 5.9 (e) shows larger tearing features, typical of a zone with a transient decrease in the crack propagation rate. In other words, this surface is similar to the blunted part of an initially sharp crack. The fracture surface corresponding to a decrease in crack propagation shows a large deformation of polyethylene and also a few fibrils of the polymer matrix.

In our experiments, the samples were not fully broken at the end of the impact test. This means that the strain energy release rate has fallen below a critical value, insufficient for further crack growth. The fraction of the fracture surface corresponding to the transition from zone D to zone E shows an interesting new pattern with feather-like or parabolic markings, visible in Fig. 5.9 (f), resembling those that can be observed at the root of a notch, on the fracture surface of samples tested in impact. Our interpretation is that this corresponds to the nucleation of many secondary cracks overlapping each other. These cracks grow larger and larger in size, merging with one another, following the crack direction. However, those parabolic markings appear only in a small region, which is followed by wider zone E. In Fig. 5.9 (a) (marked as E) the crack propagation stops. The final part shows evidence of the regular striations perpendicular to the crack propagation. The detailed view of the morphology is shown in Fig. 5.9 (i) at larger magnification. This micrograph shows that these striations are associated with plastically-deformed fibrils of pure HDPE. Those slightly deformed fibrils are following the fracture direction.

In the literature, many studies have been carried out to discuss the behavior of polymer or polymer nanocomposites under tensile loading conditions. Chan and Wu [89] reported increased toughness of annealed polypropylene nanocomposites with calcium carbonate fillers. Their study of the Izod impact fracture surface suggested that the plastic deformation zone formed in the crack-initiation stage was responsible for the high impact toughness of the annealed nanocomposites. In our work for HDPE/10 vol% PCC nanocomposites, the Charpy impact strength is found to increase with the increasing amount of PCC surface organic coating. In order to study the toughness mechanism of the HDPE nanocomposites with coated PCC particles, we firstly chose the PE09 specimen as an example for the nanocomposites and the impact fracture surface is discussed below.

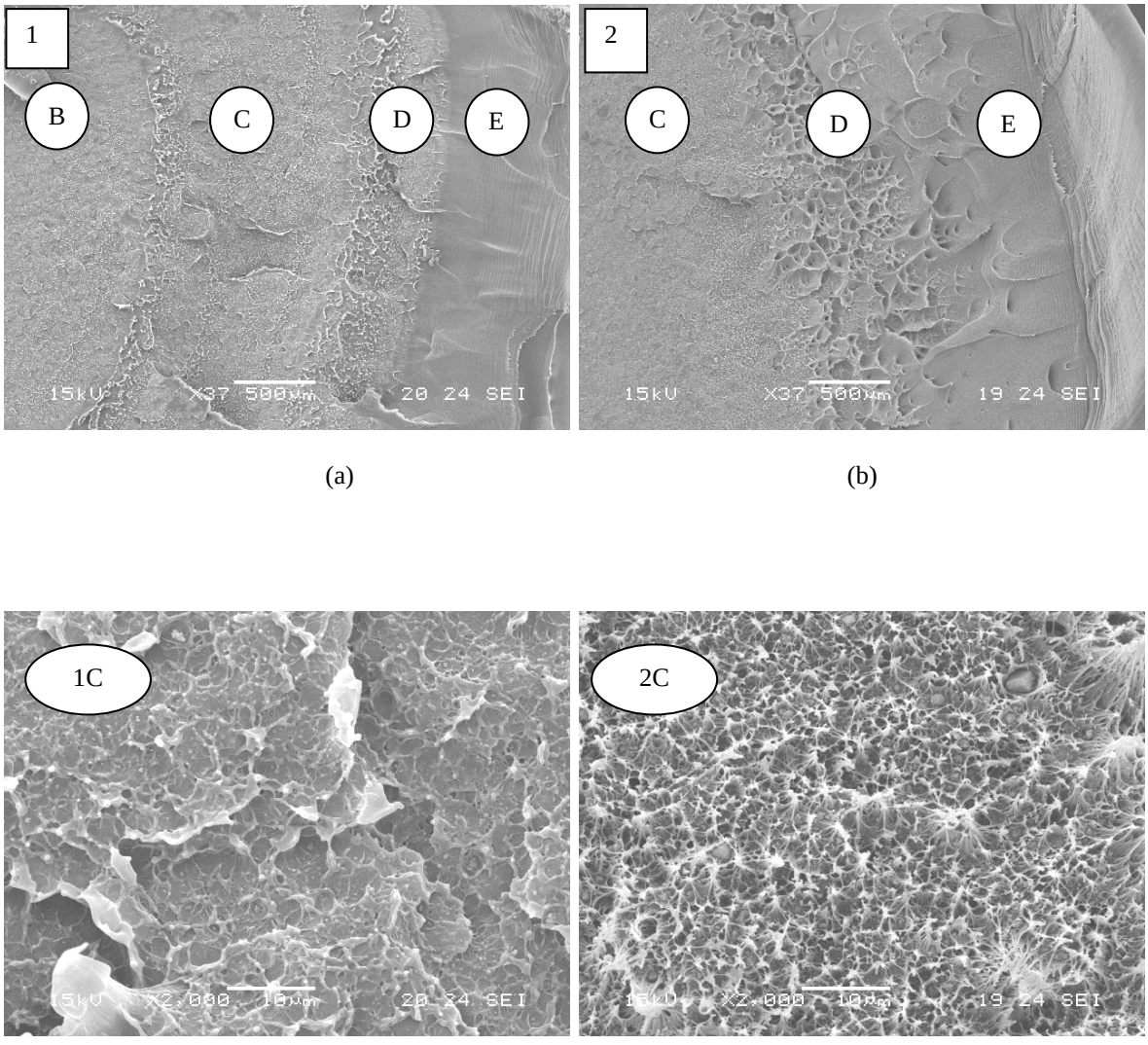

(a) (b)

(c) (d)

Figure 5.9 SEM micrographs of the impact fracture surface of pure HDPE and HDPE/PCC nanocomposites

(to be continued)

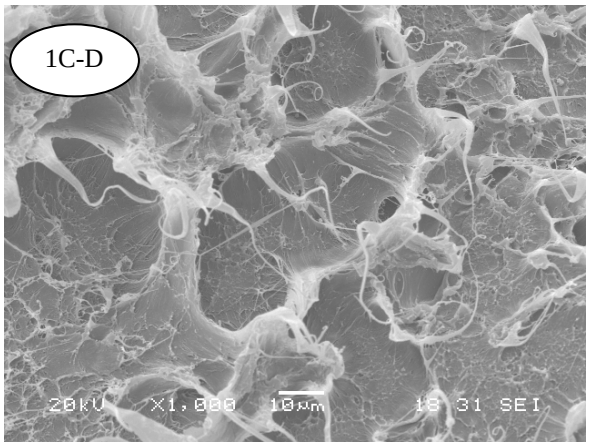

(e)

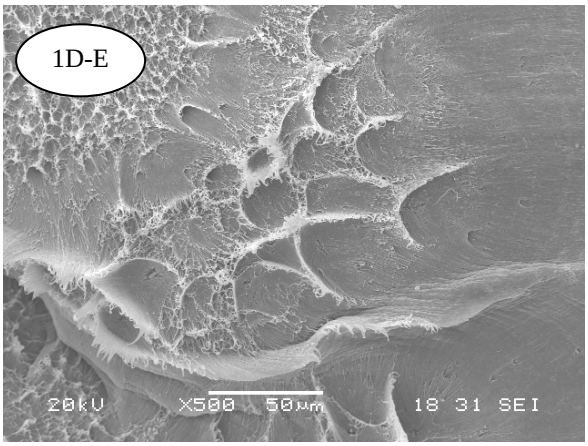

(f)

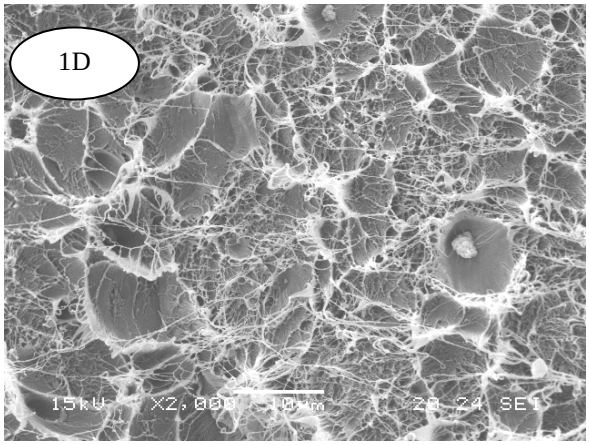

(g)

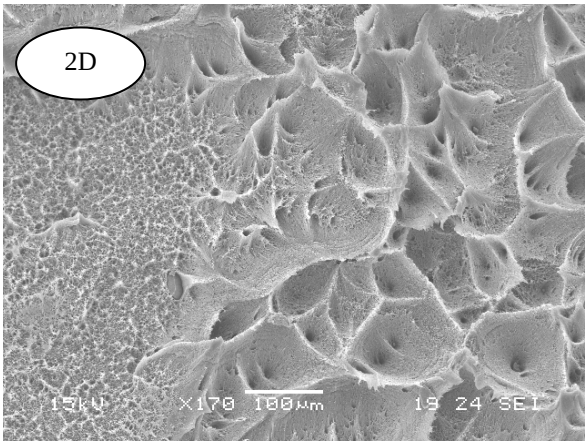

(h)

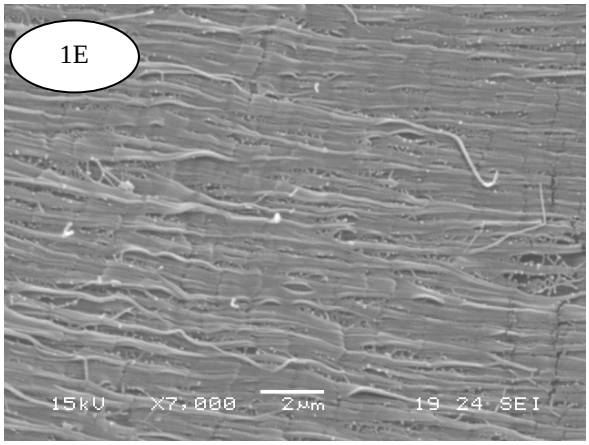

(i)

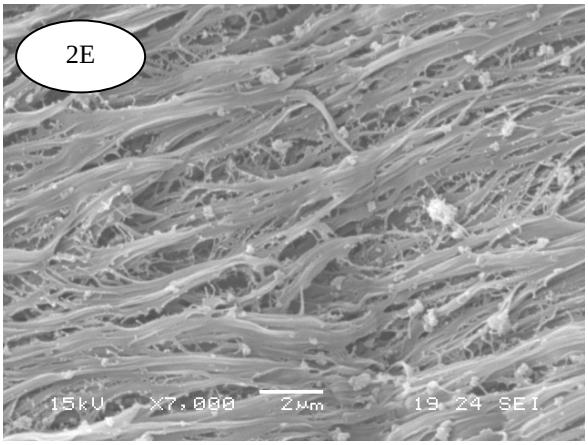

(j)

Figure 5.9 SEM micrographs of the impact fracture surface of pure HDPE and HDPE/PCC nanocomposites

5.4.2 Fracture surface of HDPE/PCC nanocomposites

The SEM micrographs of HDPE nanocomposite with coated PCC particles were shown in figures Fig. 5.7, Fig. 5.8 and Fig. 5.9 with the pictures marked with number 2. Similar to that of pure polyethylene, the impact fracture surface can be separated into two main zones, crack iniziation and propagation, respectively.

Firstly, the crack initiation part in Fig. 5.7 (b) and (d) seems to be larger in size with respect to that of pure HDPE. The micrograph of the crack initiation part of the nanocomposites sample shows large-size dimples at high magnification. This is probably associated to a high rate of energy dissipation. Moreover, the area corresponding to the following crack growth is obviously very different from that of pure HDPE. Especially in the micrographs at high magnification shown in Fig. 5.8 (d), the combined presence of secondary microvoids nucleated around the coated PCC particles and the fibrillation of the HDPE matrix between those microvoids is evident. In fact, the polymer matrix shows enhanced plastic deformation around those microvoids compared to what can be observed on the fracture surface of samples of pure HDPE at the same distance from the notch tip. Microvoid formation requires both nucleation and growth to occur during the timeframe of the fracture process. In other words, nucleation is the critical step, necessary for the growth of microvoids by the plastic flow of the matrix around them. In fact, plastic deformation of the ligaments between microvoids is much easier than in a bulk polymer because the presence of free surfaces, supplied by the walls of the cavities enclosing the nanoparticles, ensures that the mechanical stress is zero in the direction perpendicular to the cavity walls. Due to the limited thickness of the ligaments connecting two neighboring microvoids, this condition leads to a very low component of hydrostatic stress, thus triggering plastic deformation in the matrix material. This requires nanoparticles well dispersed in the polymer matrix acting as nucleating sites for microvoids. In fact, the micrographs of HDPE/PCC nanocomposites show a very good homogenous distribution of nanoparticles with very slight aggregation, which is related to the surface coating of the particles. As a consequence, intense microvoid formation leads to toughness enhancement.

Examining new areas of the fracture surface further away from the notch tip in the direction of crack propagation, zones C, D, E are shown in Fig. 5.9 (b) at a low magnification. Comparing the fracture surface of PCC/HDPE with that of pure HDPE, it is apparent that the boundary between Zones C and D is not so clearly defined for the nanocomposites, while Zone D is much larger in size and shows visible parabolas even at

lower magnification. A more detailed view of each zone is shown in Fig. 5.9 (d), (h) and (j) in order to compare the appearance of zones in pure HDPE, at similar distance from the notch. Similar to Zone B, the fracture surface of nanocomposites in Zone C also shows the combination of microvoids and fibrillation. However, there are few big agglomerates of the nanoparticles. The fracture surface area D shows an obvious difference with that of pure HDPE. Some secondary nucleating cracks are present in this zone overlapping each other. The typical micrograph of the secondary crack in Zone D is shown in Fig. 5.10 at higher magnification.

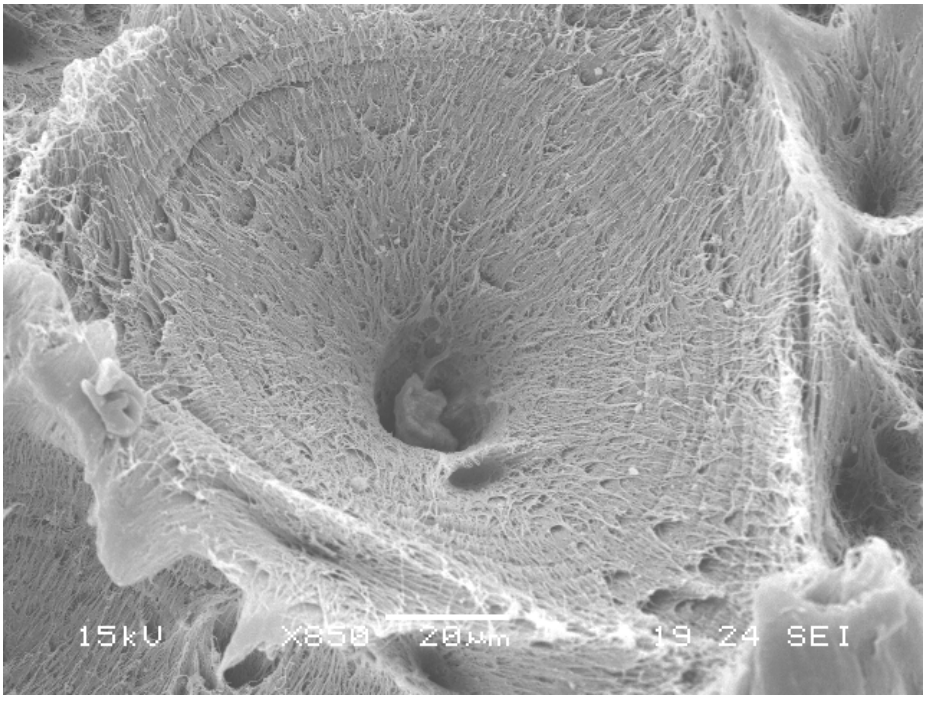

Figure 5.10 SEM micrographs of impact fracture surface of HDPE/PCC9 nanocomposites in Zone D

Moreover, Zone E in HDPE nanocomposites shows the striation-type fracture morphology similar to that observed for pure HDPE; however, there is evidence of an enhanced plastic deformation of the polymer matrix accompanying the local fracture process as shown in Fig. 5.9(j). The formation of these striations features of Zone E is probably connected to the nucleation of secondary cracks in Zone D, extending outwards along the direction of fracture propagation, as shown in Fig. 5.11 at high magnification. The secondary cracks are connected with the "*layered fibrillation*" or "*striation*" perpendicular to the crack propagation direction and consisting of the significant plastically deformed fibrils of the polymer matrix due to the existence of nanocomposites.

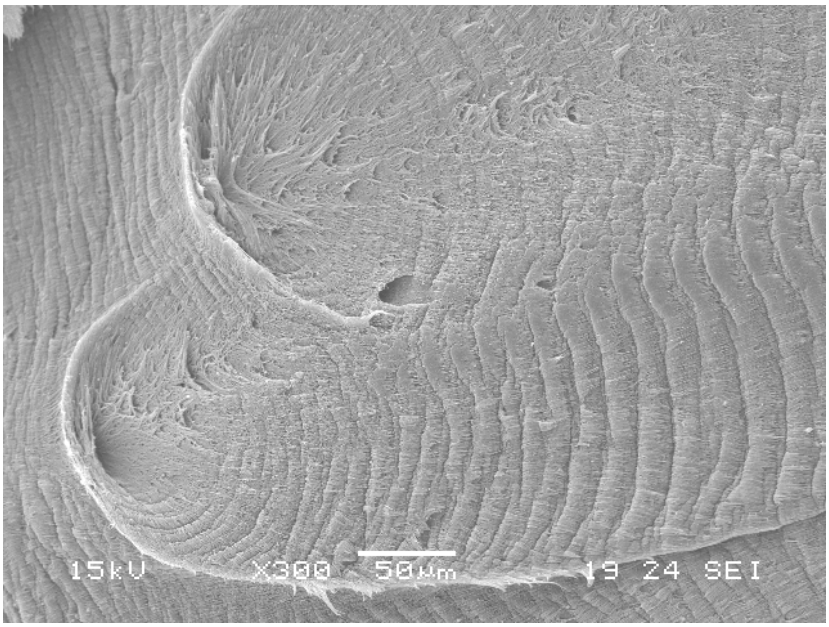

Figure 5.11 SEM micrographs of impact fracture surface of HDPE/PCC9 nanocomposites in Zone D-E

5.4.3 Comparison of HDPE nanocomposites with PCC particles coated with different methods

As we discussed in former work on Charpy tests, the impact strength of the HDPE composites increases with the increasing of the amount of surface coating. In this thesis, the SEM micrographs of HDPE nanocomposites with PCC fillers coated with different methods are also compared in Fig. 5.12, which represents micrographs of the same zone (Zone B) of the fracture surface of each sample. PE01 is the code for nanocomposites with the pure calcium carbonate, while PE07 and PE09 represent the nanocomposites with water-coated PCC, but different coating amounts, 10.3 wt% and 12.9 wt% respectively. Sample PES4 is the nanocomposite prepared with the solvent-coated PCC from the PCC1 powder to reach full monolayer coverage.

In all cases, the pure PCC or the coated PCC fillers can distribute very well in the HDPE polymer but with different degrees of dispersion. In fact, the level of aggregation of four different nanoparticles differs one from one another. Obviously, pure PCC shows relatively large aggregates compared to the water-coated PCC particles. Large agglomerates are observed also for solvent-coated PCC. This might be more difficult to elucidate. A possible explanation is related to the manufacturing process. In fact, it is possible that particle agglomeration occurs during the drying step, when the particles are brought together at very small distances from each other, and strong adhesion forces can establish among the particles due to the high polarity of the surface. The solvent coating process is probably not able to break down these agglomerates and thus survive even during the extrusion stage.

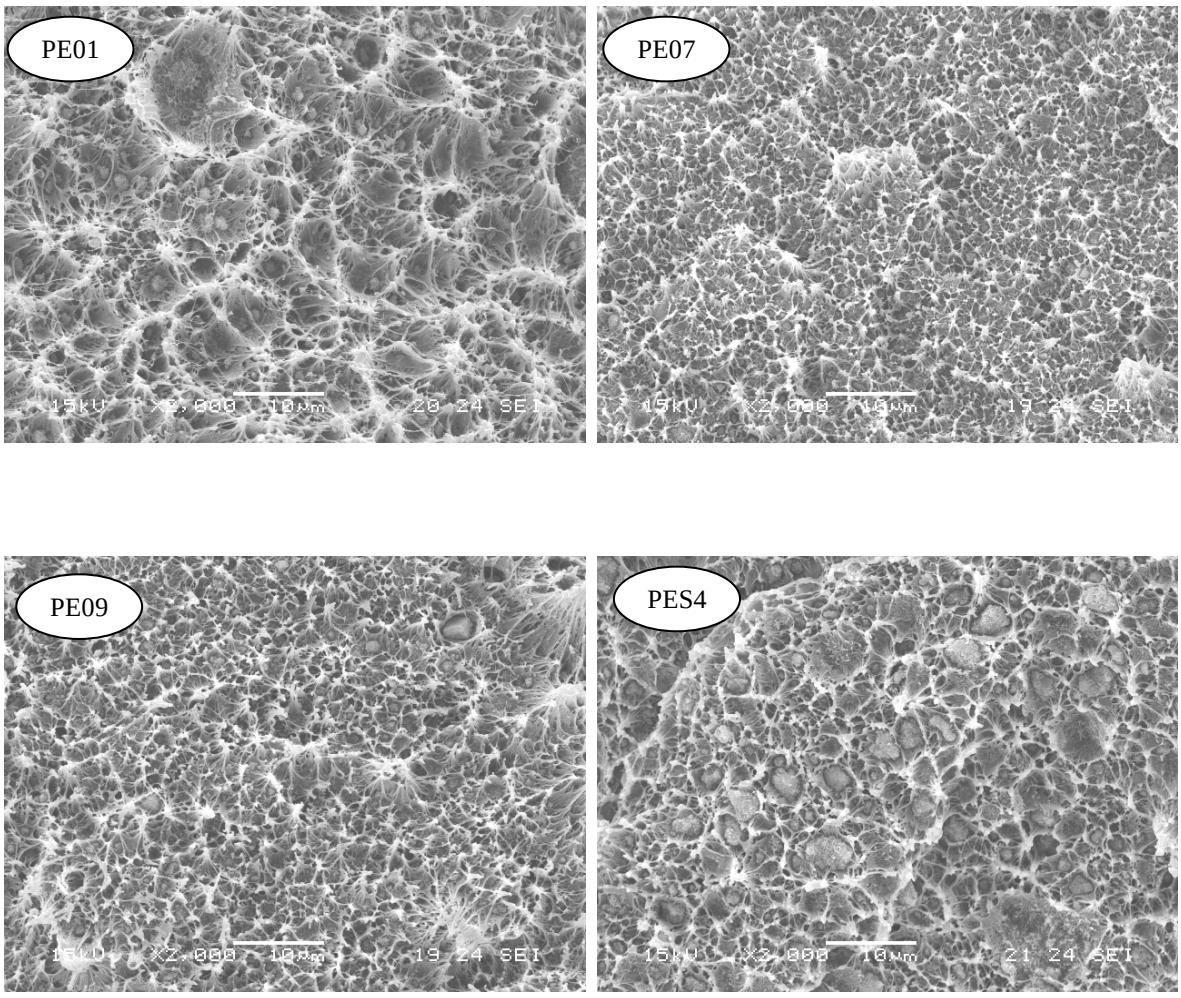

Figure 5.12 SEM micrographs of the fracture surface of HDPE/PCC nanocomposites with particles coated with different methods at the same location from the notch tip.

It is known that the aggregates are related to the surface free energy of PCC fillers. If the surface energy of calcium carbonate fillers is large, aggregates of nanofillers can survive during the shearing process during melt extrusion and then remain in the polymer nanocomposites, leading to deleterious effects on the mechanic performance. The SEM micro-morphology structure perfectly matches with our former result on the PCC surface characteristics and supported the IGC results, which suggested the lower surface energy and then lower interfacial adhesion. In other words, we can predict that improvements in the toughness of nanocomposites in the filler-toughened polymers strongly depend on the better dispersion of the nanofillers, which can be achieved by the surface coating process with suitable organic materials. Good dispersion of nanoparticles means that very fine microvoids formed during the fracture process as well as the extensively plastic deformation of the polymer matrix, localized in the ligament leading to the formation of fibrils between neighboring voids.

5.4.4 Filler toughening mechanism

After the comparison of the crack initiation and propagation zones in the impact fracture surface, it is clear that both zones in HDPE nanocomposites undergo significant larger plastic deformation than that of the pure polymer as shown in the SEM micrographs. The toughness of a material mainly depends on the energy dissipating events that can be activated in the vicinity of a sharp crack. The crack initiation zone in the pure HDPE shows mainly the crazing and tearing of the polymer itself. However, when PCC particles are added to the HDPE, the crack initiation zone shows evidence of microvoids around the nanoparticles on the surface. The formation of microvoid zones will continuously release the plastic constraint in the polymer matrix and then will trigger a significantly large plastic deformation of the polymer. This is accompanied by the consequent tearing of the matrix ligaments bridging the microvoids, which further leads to the formation of polymer fibrils. The fibrils of the polymer matrix can reach very large elongations, which are related to the energy absorption. The formation of crazes in the pure polymer, the formation of microcavitation around the particles, or the fibrillation of plastic deformed polymer ligaments, the yielding are also strongly related to the energy absorption of the polymer. Here, the SEM micrographs of the fracture surface of Charpy specimens tested in impact are consistent with the tensile mechanical properties. We reported a decreased yield stress and yield strain of the HDPE/PCC nanocomposites with an increase in the amount of surface coating on the PCC surface. As reported elsewhere in the literature [23, 35, 169, 170], debonding between nanofillers and the polymer matrix is the main mechanism for further inducing further plastic deformation of the matrix followed by the fibrillation of the polymer. Debonding is not an important process for energy absorption itself, but it is very important to nucleate a chain of following events and processes, which are effectively responsible for the toughness improvement.

Considering both the tensile and impact tests in this work, the balance between stiffness and toughness of the filler-toughened plastics is achieved by the addition of stearin-coated PCC particles, which are commercially available by means of water-based processes and low cost products. In other words, the organic coating on the PCC surface produces an alkanoate multilayer and decreases the surface free energy significantly. Then when the particles are applied to the polymers during the melt-blending process, the interfacial adhesion is also weakened and the special interphase region that is formed is very important for the mechanical performance of HDPE nanocomposites. The increase in stiffness is

mainly attributed to the internal properties of rigid inorganic particles, while the toughness is improved by the addition of PCC particles due to the easier and also earlier debonding and formation of microvoids, which are the key factors for triggering other processes for energy absorption. However, our study is main focuses on the microdeformation process, governed by the structural characteristics of the HDPE/PCC nanocomposites by the SEM technique. This will be also interesting for a further study on other factors, such as the presence of preferred polymer layers around the interface zone, the polymer lamellar thickness, and even the crystallinity of the polymer.

5.5 HDPE nanocomposites with PCC coated with different fatty acids

In the former part of this Chapter, we discussed the application of the stearin-coated PCC fillers in the HDPE polymer. Those nanoparticles were coated with stearin, a mixture of palmitic acid and stearic acid, in aqueous medium according to the currently used industrial process. Except stearic acid, which is the most common chosen surfactants for the PCC surface coating, we also considered other fatty acids to study the influence of the chain length on the mechanical properties of the polymer nanocomposites. In principle, the main purpose is to try to decrease the high surface energy of the hydrophilic calcium carbonate surface to make it more compatible with the low surface energy and hydrophobic surface of polyethylene. Our former work mainly focused on the different amount of surface coating on the PCC surface and different surface coating methods. In the literature [171-173], the surface tension of calcium carbonate nanoparticles and, consequently, the interfacial adhesion between nanoparticles and the polymer matrix are expected to depend on the type of fatty acids. The mechanical properties of HDPE composites are directly related to the deformation processes, such as the crazing, debonding, yielding, propagation and fibrillation [174, 175]. Therefore, a series of fatty acids were chosen with the carbon number from 10 to 20 in the alkyl chains. The surface coating of PCC particles with those fatty acids was carried out in acetone as shown in Chapter 2.2.2 and the coated PCC particles were added to the HDPE by extrusion blending.

The mechanical properties of HDPE/PCC nanocomposites are analyzed as a function of the number of carbon atoms in fatty acid and also the particle content in the HDPE polymer. Fig. 5.13 shows the effect of nanofiller contents on the tensile properties of nanocomposites. Here the specimens of HDPE with PCC particles coated with the capric acid were chosen as an example. The yield stress increases slowly, while the elongation-at-break shows a linear decrease with increasing filler content.

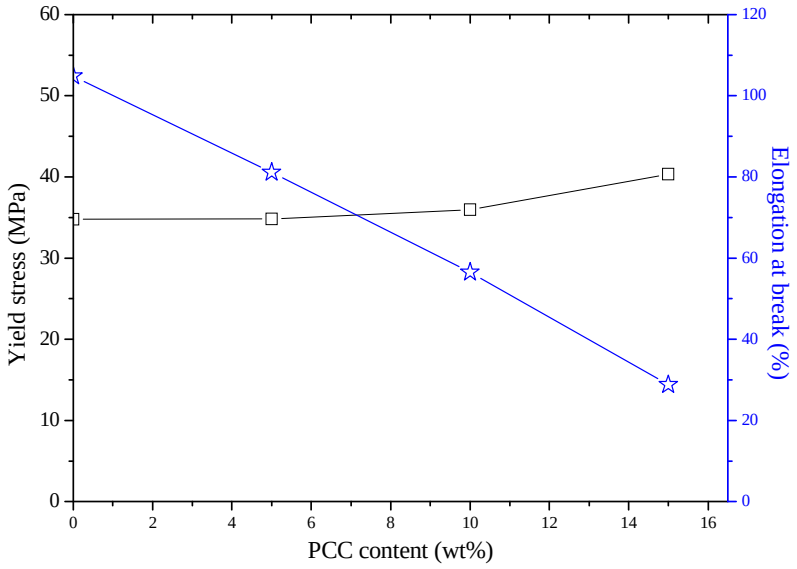

Figure 5.13 Tensile properties of HDPE/PCC nanocomposites
(PCC coated with capric acid marked as C10 as an example) versus the PCC nanoparticles content

Fig. 5.14, Fig. 5.15 and Fig. 5.16 show the dependence of yield stress, Young's modulus and elongation-at-break on the number of carbon atoms in the chain length of the fatty acids, respectively. The number of carbon atoms in the fatty acids used in this thesis vary from 10 (capric acid) to 20 (arachidic acid). Each coated PCC particle was added to the HDPE with a range of loading from 5 wt% to 15 wt%.

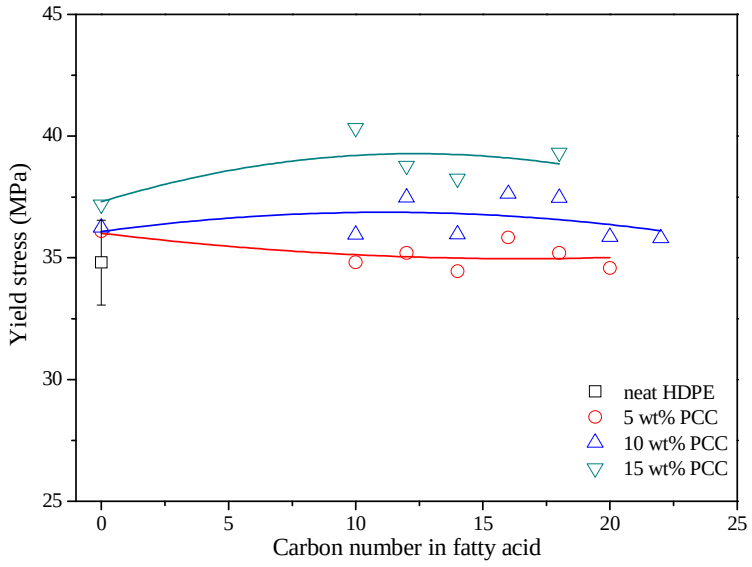

Figure 5.14 Yield stress of HDPE/PCC nanocomposites as a function of number of carbon atoms

The yield stress of this series of HDPE nanocomposites with solvent-coated PCC particles shows a higher value than for pure HDPE as shown in Fig. 5.14. At lower loadings (5 wt%), the yield stress indicates a very slight tendency to decrease with the number of

carbon atoms present in the fatty acids, reaching a plateau value of around 35 MPa. For the nanocomposites with a higher filler loading, the yield stress increases when the PCC particles were coated with fatty acid compared to that of pure PCC. The influence of the carbon chain length on the yield stress is less defined. A similar result of the elastic modulus is shown in Fig. 5.16, which suggests no significant change of the stiffness with increasing of carbon number in the fatty acid. This is similar to Young's modulus of HDPE nanocomposites with PCC particles coated in water. The stiffness appears to be mainly related to the filler loading and practically independent on the surface coating amount.

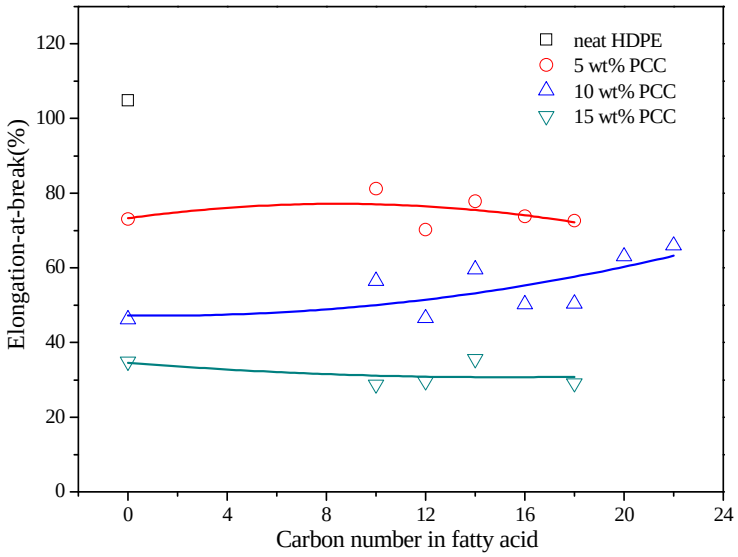

Figure 5.15 Elongation-at-break of HDPE/PCC nanocomposites as a function of number of carbon atoms

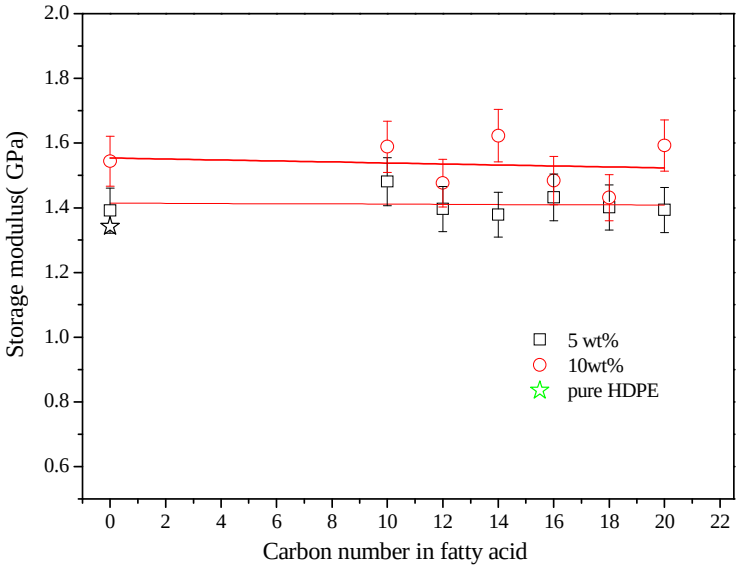

Figure 5.16 Elastic modulus of HDPE/PCC nanocomposites as a function of number of carbon atoms

The elongation-at-break of HDPE nanocomposites is shown in Fig. 5.15 as a function of the number of carbon atoms in the fatty acids. With increasing the filler loading in the

nanocomposites, the elongation-at-break value decreases. However, the relationship between the elongation-at-break and the type of fatty acids seems not so clear for three different loadings. In other words, when the fatty acids have a carbon number from 10 to 20, there is no influence of the alkyl chain length on the final fracture strain of polymer nanocomposites. One interesting result is that the elongation-at-break of HDPE/10wt% PCC nanocomposites increases when the fatty acids have a number of carbon atoms between 20 and 22. It seems that the increased length of the alkyl chain in the fatty acids changes the interfacial adhesion.

5.6 Conclusion

In this Chapter, the mechanical properties and the morphology of HDPE/PCC nanocomposites have been studied. The effect of stearin-coated PCC particles treated in water on the final performance of nanocomposites has been discussed.

The stiffness and toughness of HDPE/PCC nanocomposites appear to be well balanced. The addition of nanoparticles can increase the yield stress and Young's modulus significantly. However, the yield stress slightly decreased when the PCC surface coating amount increased probably due to earlier debonding between the fillers and polymer matrix. This is attributed to lower interfacial adhesion as an effect of the surface coating and matches well with the IGC determination in Chapter 4. The most interesting result is the Charpy impact strength, which also showed a linear dependence on the amount of surface coating on PCC particles.

The comparison of the microdeformation process by the SEM technique suggested that the main toughening mechanism of the HDPE/PCC nanocomposites is not the crazing such as in pure HDPE. In fact, the addition of nanoparticles lead to the formation of microvoids and of microfibrils in the matrix, clearly connected to the improved toughness deserved. The morphology of nanocomposites filled with different amounts of surface coating confirmed that a lower surface energy produced better dispersion of nanoparticles in the polymer matrix.

We also discussed the effect of carbon chain length of fatty acids on the final tensile properties. The carbon number in the fatty acid varied from 10 to 20. The yield stress and Young's modulus of HDPE/PCC nanocomposites seems relatively constant with the varying number of carbon atoms in the fatty acid. The elongation-at-break shows a slight increase when PCC fillers were coated with fatty acid with carbon atoms between 20 and 22. Future work is needed for studying the effect of chain length on the toughness.

Chapter 6 PLA/PCC nanocomposites

6.1 Introduction

Polylactic acid (PLA) is a biodegradable thermoplastic derived from a renewable resource [176-181]. PLA has received a lot of attention not only as an alternative to petrochemical plastic but also because of its high strength and stiffness, biocompatibility, and thermal processability. PLA is considered as a potential material in many fields such as biomedicine, packaging and films [181, 182]. However, its toughness, heat resistance and gas barrier properties are not satisfactory, and therefore its application for commercial products is limited because of those inherent weaknesses. PLA has been bulk modified mainly to improve the toughness and degradation rate. The toughness improvement is a crucial necessity for many applications, while the improved degradation rate could be important in biomedical applications.

The most extensively used methodology for improving toughness of PLA is to blend it with different plasticizers and (biodegradable or nonbiodegradable) polymers. Known plasticizers are glycerol, citrate ester, polyethylene glycol (PEG), polypropylene glycol (PPG) which are used to lower the glass transition temperature, increase ductility and processability [183, 184]. The addition of 5 and 10 wt% PEG with a lower molecular weight (400 and 600 g/mol) was reported to decrease the glass transition temperature from around 57 °C to about 45 °C and 34 °C, respectively [185]. Meanwhile, many research papers have been published on PLA blended with other biodegradable polymers such as poly (3-hydroxy butyrate) (PHB) and poly(e-caprolactone) (PCL) without compromising its biodegradability [186, 187]. Recently, PLA-based nanocomposites have also been investigated with nanoparticles, such as calcium carbonate, montmorillonite clay, cellulose fibers [177, 188-190]. In principle, rigid nanoparticles can substantially improve toughness more efficiently than rubber particles when a good dispersion is achieved, since both stiffness and toughness can be balanced [7, 11]. The properties of biodegradable PLA might be enhanced by the incorporation of nanoscale reinforcements.

The crystallization behavior of PLA is strongly related to the physical, mechanical and barrier properties. PLA can be either amorphous or semi-crystalline depending on its stereochemistry (L-Lactide, D-Lactide and meso-Lactide) and thermal history, which is a very important parameter for the PLA processing technology. More particularly, the increase of crystallinity is important for the injection-molded articles with good thermal

stability. A very important strategy for increasing the crystallinity of PLA is to add nucleating agents to the polymer matrix during melt extrusion. The nucleating agents will lower the surface free energy barrier for nucleation and make the crystallization start at a higher temperature during cooling. Talc is reported by Kolstad as a nucleating agent when added to PLLA [191].

In this chapter, we discuss the effect of the addition of precipitated calcium carbonate (PCC) nanoparticles to PLA as filler-toughening agents. Calcium carbonate is the most widely used filler in polymers and enables to increase toughness without a loss in stiffness. In Chapter 5, precipitated calcium carbonate nanoparticles coated with fatty acids were added into high-density polyethylene, and the impact strength of the polymeric composites was increased as the amount of stearic acid increased. We believed that the interfacial adhesion between PCC and HDPE was affected by the surface coating amount for the PCC nanoparticles. A weaker interfacial interaction between fillers and the matrix can lead to both a good dispersion of nanoparticles and easy debonding between two components during the fracture process, which are necessary factors for the improvement of toughness in polymer composites. The toughening mechanism for polymer nanocomposites with calcium carbonate has been well discussed for HDPE, PP, PVC and ABS [12, 89]. However, little research work has been reported in the literature on PCC/PLA nanocomposites. In this chapter, this polymeric system was studied in relation to its thermal and mechanical properties, building upon our former experience on the application of calcium carbonate nanoparticles into polymers, with the purpose of improving the toughness of PLA.

Another type of nanofillers, tubular clay, Halloysite NanoTubes (HNTs) was also added to PLA for the purpose of comparison. HNTs with a molecular formula of $Al_2Si_2O_5(OH)_4 \bullet nH_2O$ are naturally occurring, multi-walled inorganic nanotubes which have a similar geometry to carbon nanotubes (CNTs) [115, 192, 193], but with a much lower cost. Xu and co-workers [194] carried out some research on polylactide-based composites with functionalized multiwalled carbon nanotubes (F-MWCNTs), which exhibited remarkable improvements in rheological properties in the molten state compared with pure PLA. Moreover, F-MWCNTs acted as a nucleating agent when applied to PLA. With similar structures and physical properties as CNTs, HNTs are receiving increasing attention in the field of polymeric composites based on the their following facts: HTNs possess high mechanical strength and modulus, a high aspect ratio, and they can easily be dispersed by shearing in the polymer matrix due to their relative low hydroxyl density compared to other layer silicates.

The aim of this study is to test the capability of PCC nanoparticles as toughening fillers for PLA. We also try to compare two different types of inorganic fillers on the final performance of PLA composites, such as the thermal behavior and mechanical properties, especially fracture toughness. The nucleating effect of inorganic rigid nanoparticles on the crystallization behavior of PLA nanocomposites was evaluated by the isothermal crystallization analysis. Meanwhile, the macro-mechanical properties and the micro-deformation morphology of PLA composites were investigated.

6.2 Mechanical properties

Pure PLA is well known with its high strength and stiffness. The strain-stress curves of PLA composites with PCC, halloysite or both nanoparticles are shown in Fig. 6.1. The yield stress and Young's modulus of PLA binary or ternary composites are recorded in Table 6.1. The pure PLA shows the highest tensile strength but with a very small elongation-at-break of about 3.5 %. The specimens of pure PLA fractured without any whitening or necking. Both the addition of halloysite nanotubes and PCC particles into PLA decreases the tensile strength as shown in Fig. 6.1. The most impressive effect of nanofillers on PLA is that the addition of PCC can increase the elongation-at-break from about 3.5 % for pure PLA to about 10 % for the PLA composites filled with 10 wt% of PCC as shown in Fig. 6.1 (a). Meanwhile, all the specimens of composites with PCC fillers show the extensive stress-whitening band over the whole gauge length. However, the elongation-at-break first increases to reach a maximum of about 12 % when the PCC particles loading increase up to 15 wt%, then decreases with the further addition of PCC particles. However, the addition of the HNT nanotubes has little effect on the elongation-at-break of nanocomposites, which is also probably related to the dispersion of nanotubes in the PLA matrix. From Fig. 6.1 (b), it is evident that the increase in elastic modulus of PLA/HNT composites compared to pure PLA. This result confirms that the HNT nanotubes are effective in the improvement of stiffness. The PLA/HNT/PCC ternary composites in Fig. 6.1 (c) show unstable mechanical properties as the increasing of PCC content in the composites except the relative increase of elongation-at-break. Similar to the PLA/PCC system, the elongation-at-break of PLA/HNT/PCC composites first increases and then decreases with rising levels of loading of PCC fillers, while the yield stress keeps decreasing when the fillers content increases.

From the stress-strain curves of three different PLA composites and the recorded yield stress values, the effect of PCC coated with stearic acid can be explained by a decreased interfacial adhesion between PCC fillers and the PLA matrix in the presence of stearic acid

in the interfacial region. Similar to the situation in HDPE/PCC nanocomposites, the physisorbed stearate layer on the PCC surface effectively weakens the interfacial adhesion between the PLA and the PCC surfaces, therefore debonding between the PCC fillers and the PLA matrix can take place at lower stresses. In the work of Jiang [177], similar tensile properties were reported. The elongation-at-break was improved to about 13 % with 7 wt% NPCC from 4.1% of pure PLA. The most widely used method to improve the toughness is to add plasticizer to PLA, which produces a substantial reduction of the glass transition temperature and a parallel increase in ductility and impact strength. Murariu [195] and coworkers reported that the strain-at-break can be increased from 11 % of pure PLA to 75 % with the addition of 10 wt% glyceryl triacetate into PLA/calcium sulfate composites. However, they reported the parallel decrease of both tensile strength and Young's modulus.

Table 6.1 Mechanical properties of PLA binary and ternary composites with PCC or HNT fillers

Code	Composition PLA/HNT/PCC	Young's modulus (*GPa*)	Yield stress (*MPa*)
PLA	100/0/0	4.15	84.99
PLAPCC5	95/0/5	4.39	80.17
PLAPCC10	90/0/10	4.44	72.91
PLAPCC15	85/0/15	4.78	65.03
PLAPCC20	80/0/20	4.92	61.88
PLAPCC25	75/0/25	4.8	59.49
PLAHNT2	98/2/0	4.63	85.41
PLAHNT5	95/5/0	4.71	83.59
PLAHNT8	92/8/0	4.94	83.53
PLAHNT10	90/10/0	4.99	84.18
PHC1	90/5/5	6.89	67.3
PHC2	85/5/10	5.12	60.97
PHC3	80/5/15	4.39	55.93
PHC4	75/5/20	6.03	62.35
PHC5	70/5/25	6.21	56.2

Young's modulus and the tensile stress of those three types of PLA nanocomposites are compared in Fig. 6.2 and Fig. 6.3 as a function of the contents of nanoparticles in the PLA matrix. The tensile strength tends to decrease gradually as the filler content increases in PLA composites. The addition of 20 wt% of PCC decreased the tensile strength by 27%.

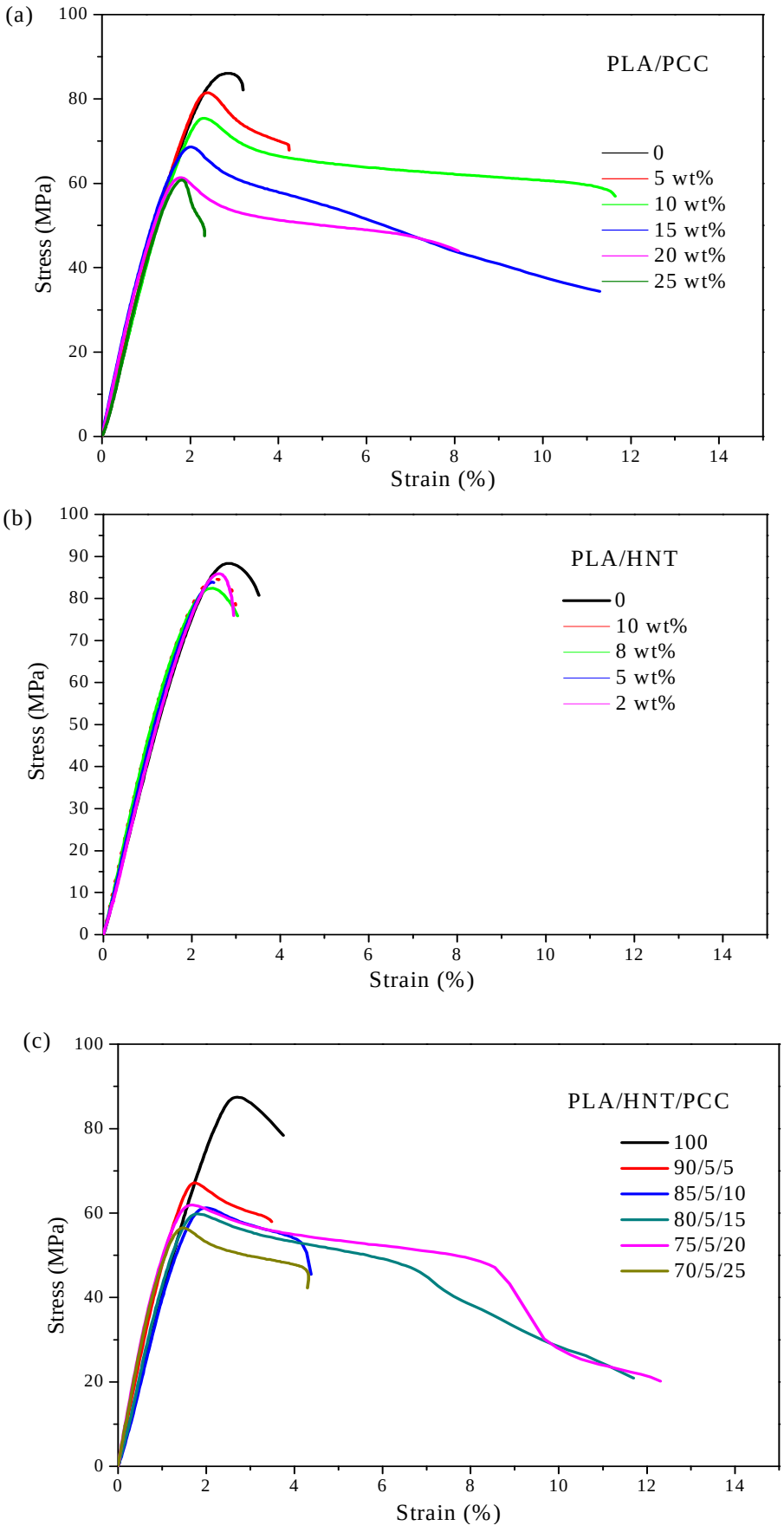

Figure 6.1 Strain-stress curves for PLA composites

Considering that the elongation-at-break of PLA/PCC composites is much larger than that of pure PLA, the decreased tensile stress is a reflection of both a weaker interface adhesion between the nanoparticles and the polymer matrix, and the plasticizing effect of the surface coating. In Chapter 5 for the HDPE composites toughened by PCC nanoparticles coated with stearin, a similar weaker interface interaction between polymer and particles allowed the improvement of the toughness of final nanocomposites. Here we believe that the surface modified PCC particles with stearate multilayer also have a suitable interfacial interaction with PLA, which is responsible for the decreasing yield stress in Fig. 6.2. The weaker interfacial adhesion between rigid nanoparticles and the polymer is also reported to achieve easier debonding of nanoparticles from the matrix and therefore improved toughness [84, 88]. The PLA/HNT nanocomposites also showed a similar decrease of the yield stress but to a lesser extent. However, the PLA/HNT/PCC ternary nanocomposites show much lower yield stress than the PLA/PCC system.

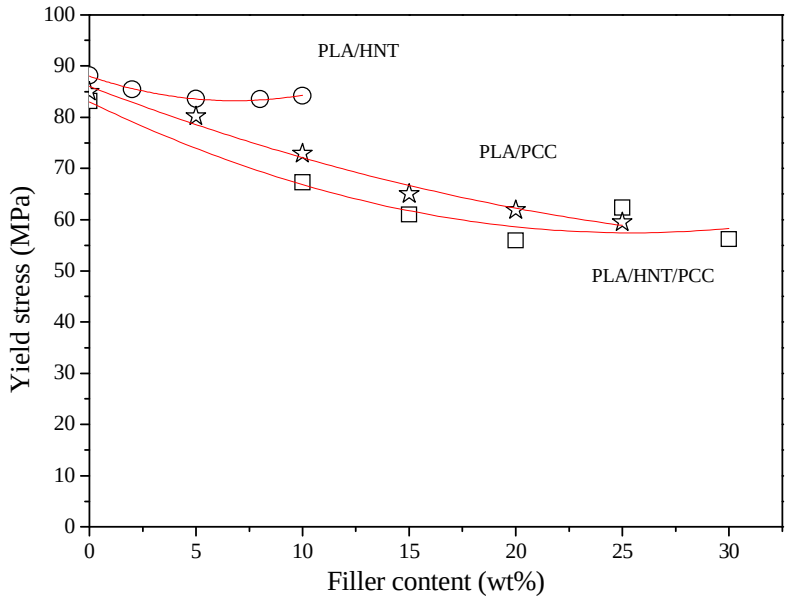

Figure 6.2 Comparison of yield stress for PLA nanocomposites versus the filler content

In Fig. 6.3 the addition of both PCC and HNT nanoparticles to PLA shows an increased Young's modulus. However, the effect of HNT nanotubes in the PLA shows a higher Young's modulus with respect to the addition of PCC to PLA, which is due to the higher aspect ratio of HNT nanofillers. Those tensile results indicated that the HNT nanotubes and PCC particles have different effects on the toughness and stiffness of the polymer. The PLA/HNT/PCC ternary nanocomposites show the lowest yield stress and unstable Young's modulus when compared to the single filler systems. The lower tensile strength can be related to the lower particles/polymer interfacial adhesion or to the presence

of flaws due to the possible aggregation of the fillers. Further micro-morphology analysis will be able to clarify the resulted decreasing of yield stress.

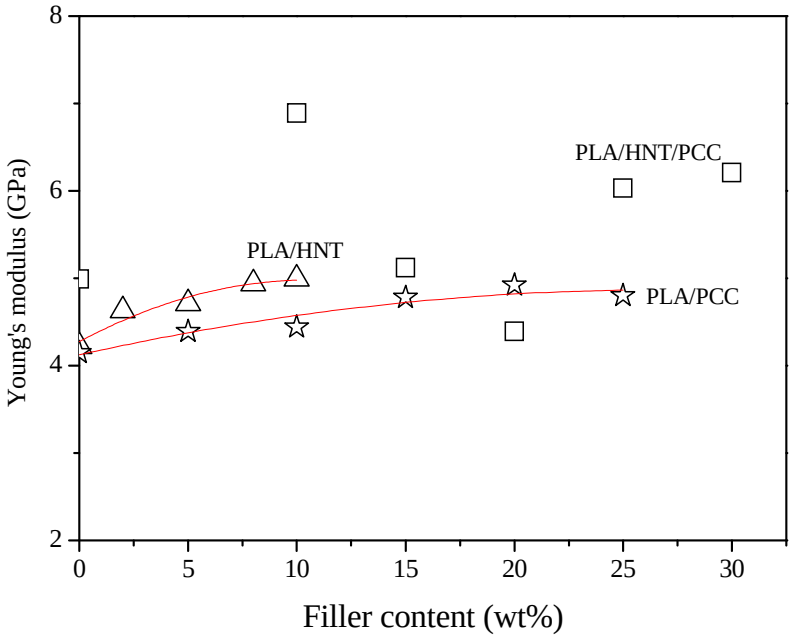

Figure 6.3 Comparison of Young's modulus for PLA nanocomposites versus the filler content

6.3 Dynamic thermal mechanical properties

DMTA is a useful and sensitive technique for the analysis of the microstructure and macromolecular conformations and motions as a function of temperature. Fig. 6.4 and Fig. 6.5 show the temperature dependence of dynamic storage modulus E' and loss modulus E'' of pure PLA and PLA composites with PCC or HNT nanoparticles over a temperature range from -100 °C to 150 °C. Generally, the storage modulus of both pure PLA and PLA composites remains stable in the temperature from -100 °C to about 55 °C, which is below its glass transition temperature. Then the storage modulus of neat PLA drops rapidly due to the glass transition around 55 °C. However, after this temperature range, the storage modulus increases rapidly with temperature, which is attributed to the well-known cold crystallization. However, in the cases of PLA composites with both PCC and HNT, the storage modulus is not stable and shows a much lower value with respect to that of PLA in the cold crystallization region. There are two possibilities in order to explain the low storage modulus in PLA nanocomposites; one can be the enhanced mobility of the PLA chain, and the other is the smaller number of PLA molecular chains involved. At room temperature, the storage modulus shows no significant difference between the neat PLA and PLA composites except the PLA composites with 5 wt% PCC. This result is consistent with the tensile

results of the decreased yield stress. However, in other research work [196, 197], the addition of inorganic particles shows a huge increase in the storage modulus when the temperatures are both below and above the glass transition temperature, which is attributed to the improvement of stiffness. Therefore, our storage modulus result matches well with the decreased tensile strength with the addition of PCC particles due to the weaker interfacial adhesion between fillers and the matrix.

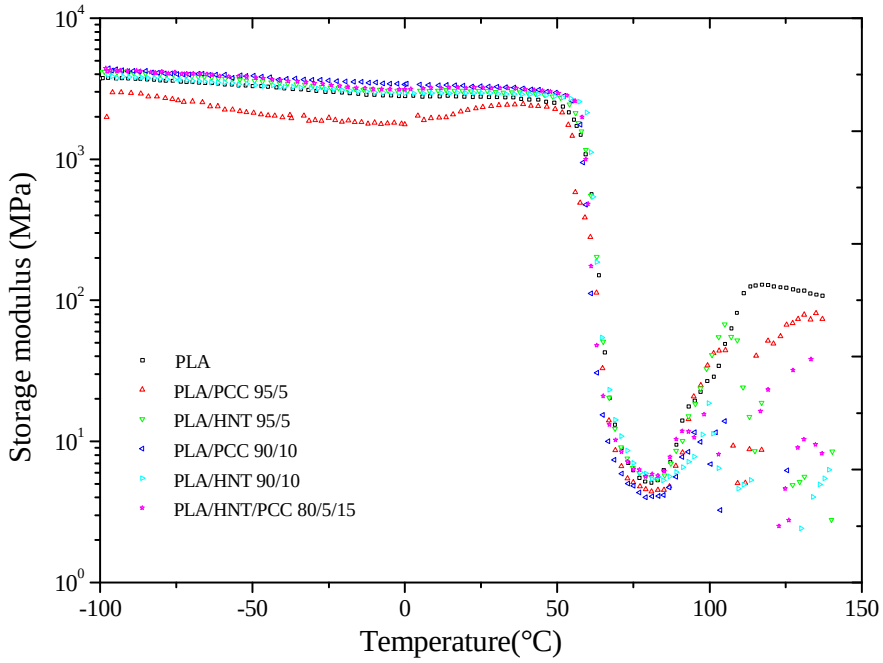

Figure 6.4 Temperature dependence of storage modulus of PLA nanocomposites

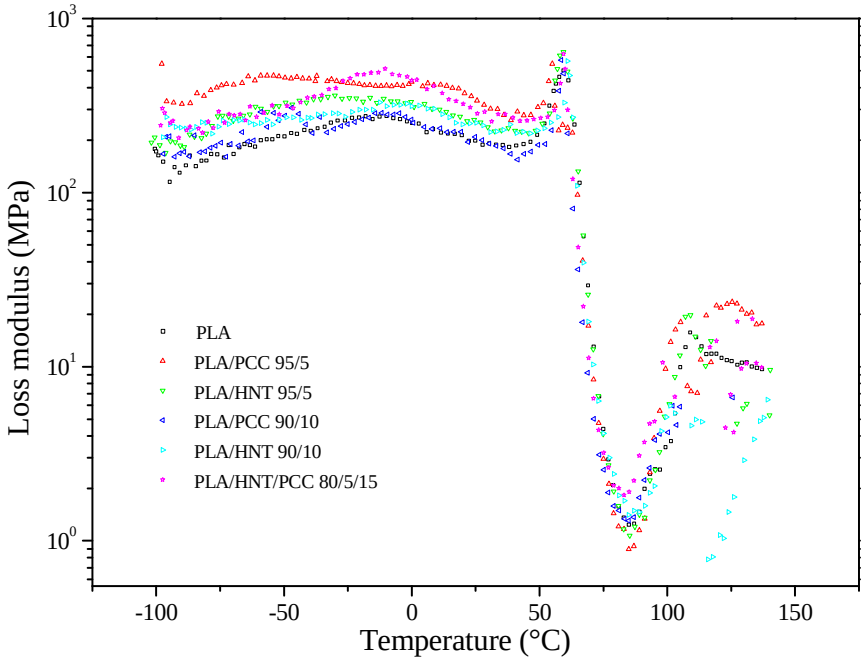

Figure 6.5 Temperature dependence of loss modulus of PLA nanocomposites

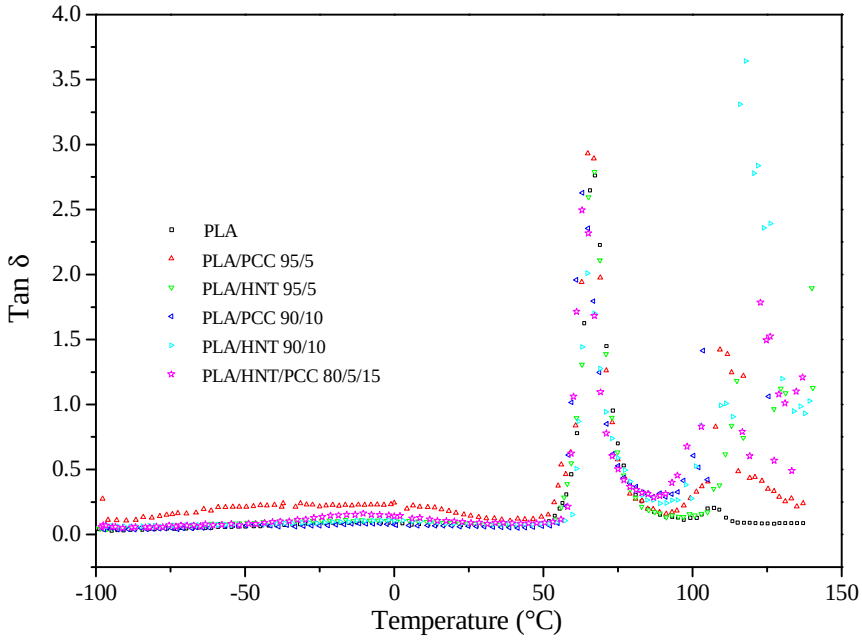

Figure 6.6 Temperature dependence of Tan δ of PLA nanocomposites

In Fig. 6.6, the tan δ curves of pure PLA, PLA binary nanocomposites with PCC or HNT or PLA ternary nanocomposites with both are plotted against temperature. The pure PLA show a glass transition temperature T_g at about 67.1 °C according to the peak value of the tan δ curve. For the PLA composites, the T_g values decreases to about 63.0 °C for PLA/PCC composites. The slight decrease of T_g is consistent with tensile tests when the stearin-coated PCC caused both a good dispersion of PCC nanoparticles and weak interfacial adhesion with the PLA matrix. However, the addition of HNT nanotubes to PLA also showed a slight decrease of the T_g temperature, which contradicts other reports that maintain that the glass transition temperature tends to increase due to the addition of inorganic fillers [196]. In other words, the addition of fillers to the PLA induced increased polymer chain mobility in the interphase zone. As it is well known, the glass transition is a complex phenomenon related to many factors such as chain flexibility, molecular weight, branching, crossing-linking and intermolecular interaction. Papageorgiou [196] and coworkers discussed the thermal properties of PLA composites with multi-walled carbon nanotubes, montmorillonite and silica nanoparticles. They reported impressive enhancement in the storage modulus for all three types of composites and a small increase of T_g (1-2 °C), which was attributed to the physical crossing-link caused by the interaction between fillers and PLA. Similar results were recorded for PLA composites with other nanoparticles such as clay [188], bentonite [196], microcrystalline cellulose [197] and natural fibers [189]. However, a lower T_g transition temperature was reported for PLA modified with plasticizer, such as PPG [185], PEG [198] and glyceryl triacetate [195]. A similar shift in T_g shows for

our PLA/PCC composites with PLA modified with plasticizers, which is consistent with the conclusion of Pukanszky [199] that states that the stearic acid on the PCC surface acts as plasticizer. Another work by Mahboobeh [200] reported the improved flexibility of PLA composites with stearate-modified layered double hydroxide, which showed seven times the elongation-at-break with 1.0 wt% stearate-Mg_3AlLDH, while keeping the same level of tensile strength and elastic modulus. Therefore, the alkanoate layers on the PCC surface showed a similar plasticizer effect in the PLA/PCC nanocomposites.

Considering the cold crystallization occurring in a temperature range from about 80 °C to 120 °C, the pure PLA showed a very small peak, while the PLA composites give a much higher intensity peak also due to the cold crystallization of the polymer matrix. In other words, this result can be explained by the fact that there are more PLA chains involved in the crystallization around the soft interphase zone. Meanwhile, there is a larger improvement in the spherulites due to the presence of the inorganic fillers separated in the PLA matrix. The tan δ curves of PLA composites indicate an effect of PCC as nucleating agents.

6.4 Thermal behavior of PLA nanocomposites

6.4.1 Isothermal crystallization of PLA nanocomposites

PLA crystallinity is a very important factor related to the mechanical and durability performance in molded applications. In this work, the isothermal crystallization of PLA composites was investigated at 120 °C as the crystallization temperature from the melt state. The effect of the PCC particles and halloysite nanotubes on the PLA crystallization kinetics was compared by measuring the crystallization half-time determined during the isothermal tests. Fig. 6.7 shows the DSC isothermal curves for pure PLA and a selection of PLA nanocomposites. It is clear that pure PLA has a very slow crystallization rate from the melt state, which is a well-known result, especially for the injection-molded products where PLA shows a low crystallinity or is almost amorphous. The degree of crystallinity is largely controlled by the ratio of D to L enantiomers used, and to a lesser extent on the type of catalyst used [201]. The crystallization half-time of pure PLA is about 37.7 min in this work. Our results are consistent with other works which reported a half-crystallization time in the range of 17-45 min, depending on the crystallization temperature, stereochemistry and molecular weight [202]. Many papers [203-205] discussed the influence of the stereochemistry of PLA on the crystallization behaviour, since two optically active forms of

lactic acid exist: L-lactic acid and D-lactic acid. Schmidt and Hillmyer [204] showed that the self-nucleation of PLA with stereocomplex (0.25-15 wt% PDLA into PLLA) was extremely effective when compared to the traditional nucleating agents such as talc. Self-nucleation is considered to be an ideal case for homopolymer crystallization due to an optimum dispersion of crystallites and the favourable interactions between the polymer melt and the polymer crystal fragments. In this work, only the effect of nanoparticles is considered for the crystallization of PLA composites. PCC nanoparticles were applied as nucleating agents into polypropylene for the formation of β phase PP [40, 65]. A similar enhanced crystallization behaviour was also found when the HNT nanotubes were added to PP, which was attributed to the unique morphology with multi-walled inorganic tubes and rolled by some aluminosilicate layers [206]. Both the PCC particles and halloysite sharply increase the crystallization rate from the melt and shorten the crystallization half time $t_{1/2}$, which is shown in Table 6.2. Similar results were found in other research for PLA/talc composites [202], where it was found that the addition of talc to the PLA can speed up the crystallization rate 65-fold over pure PLA for an isothermal temperature of 115 °C. The most impressive increase in the crystallization rate has been found for the PLA/HNT/PCC composite with a composition of 90/05/05, which showed crystallization half-time of only 12.4 min. The comparison between PCC and halloysite nanoparticles shows that PCC has a much better nucleation effect on the PLA matrix.

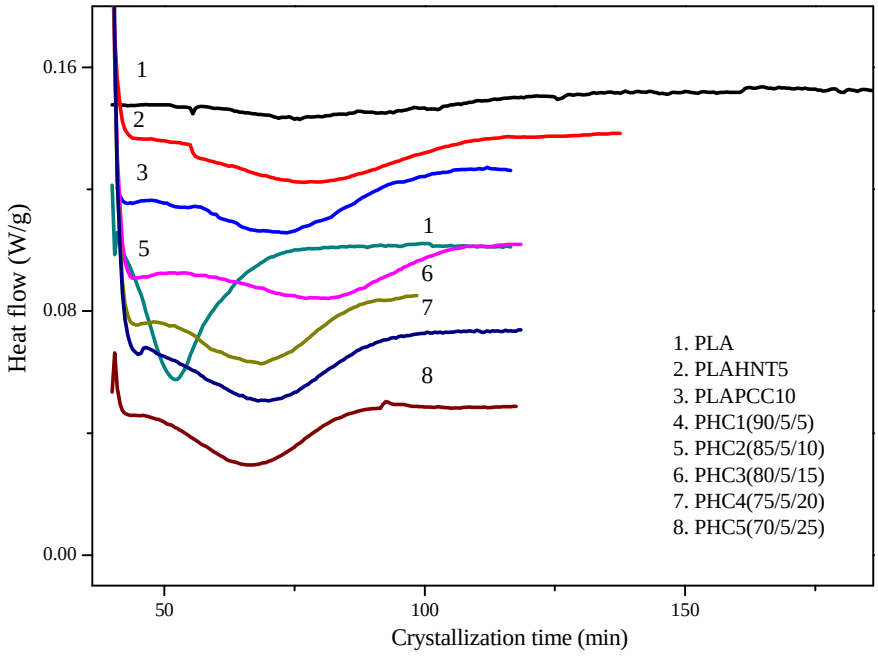

Figure 6.7 DSC isothermal traces of PLA and PLA nanocomposites

In this work, the results of obtained for PLA nanocomposites during the DSC isothermal measurements were analyzed by Avrami equation 6.1:

$$1 - X(t) = \exp(-Kt^n) \tag{6.1}$$

where constant K is the crystallization rate, n is the Avrami exponent, and $X(t)$ is the relative crystallinity at time t. Parameters K and n are related to the crystallization rate and to the type of nucleating and the geography of crystal growth. Fig. 6.8 shows the plots of relative crystallinity of selected PLA composites against crystallization time. The crystallization half-time is defined by the time where a relative crystallinity of 50% is reached. Pure PLA has the longest time to finish the crystallization from the melt state. The Avrami plots of $log(-ln(1 - X(t))$ versus $log(t)$ are shown in Fig. 6.9, where the intercept and slope of the best fitting lines are calculated to be the values of $logK$ and n, respectively. The Avrami exponent n of both pure PLA and PLA composites is just below 3 as shown in Table 6.2. In other words, this value means that the crystal growth occurred in 3 dimensions. In general, the nucleation stage and the crystal growth are more complicated for the polymeric composites due to the fact that fillers can act as nucleating agents, by increasing the crystallization or by limiting the normal crystal growth in some certain areas such as the interphase between fillers and the polymer matrix [207], depending upon the interfacial adhesion.

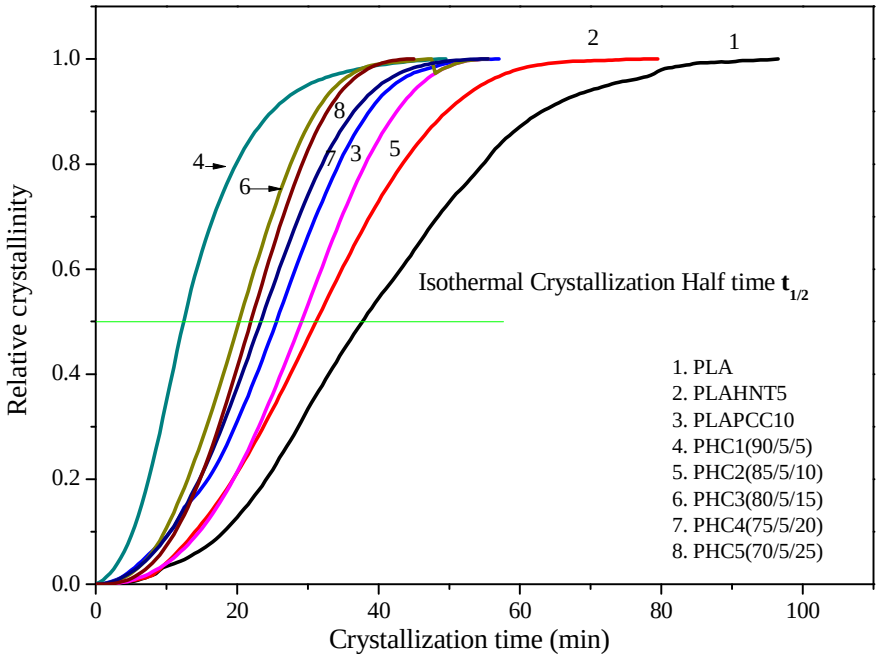

Figure 6.8 Plots of the relative crystallinity of PLA and PLA nanocomposites versus crystallization time when the isothermal temperature is 120 °C

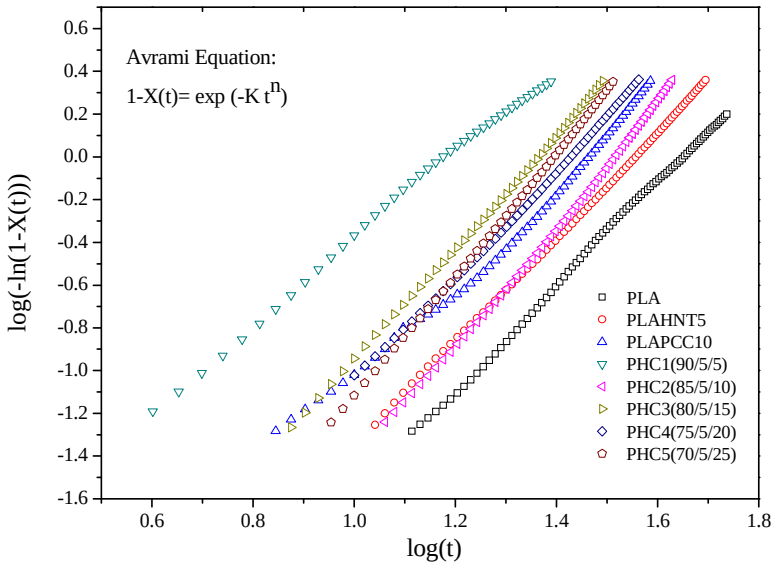

Figure 6.9 Linear Avrami plots of $log(-ln(1-X(t))$ versus $log(t)$ of the selected PLA composites

6.4.2 Non-Isothermal crystallization of PLA nanocomposites

In the literature, it is generally accepted that slowly crystallizing polymers tend to form a multilayer structure with an amorphous skin, a semicrystalline layer, and an amorphous core in their injection molded specimens [177]. However, the crystallization of PLA from melt usually occurs in the temperature range from 80 to 120 °C [208]. The crystallization properties of PLA-molded samples showed no structural gradient in PLA nanocomposites [208], which was explained by the combined effect of material crystallization ability and the injection molding conditions (50 °C). In our work, the neat PLA exhibited no crystallization peak during cooling from the molten state with a cooling speed of 20 °C/min as shown in Fig. 6.10, and this is consistent with the literature results that reported no crystal formation during cooling at this speed for pure PLA [208].

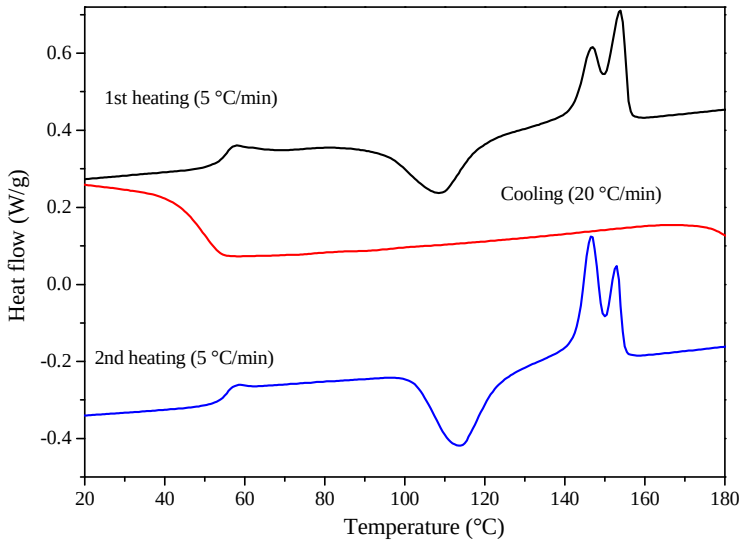

Figure 6.10 DSC trace of pure molded PLA specimen during the heating-cooling-reheating program

Table 6.2 Composition and crystallization properties of PLA composites

Code	Composition				Isothermal crystallization			Thermal properties of PLA composites					
					n	logK	$t_{1/2}$	T_g (°C)	Tcc (°C)	ΔH_{CC} (J/g)	T_{m1} (°C)	T_{m2} (°C)	ΔH_m (J/g)
PLA	PLA	HNT	PCC	100/0/0	2.30	-3.79	37.7	61.8	109.9	25.56	148.2	156.0	30.69
PLAHNT5	PLA	HNT	PCC	95/5/0	2.48	-3.83	31.2	62.1	103.8	25.62	146.9	155.0	27.94
PLAPCC10	PLA	HNT	PCC	90/0/10	2.23	-3.20	25.5	60.3	96.9	25.03	145.9	155.8	29.31
PHC1	PLA	HNT	PCC	90/5/5	1.81	-2.18	**12.4**	57.9	98.4	27.41	146.8	156.7	30.68
PHC2	PLA	HNT	PCC	85/5/10	2.66	-3.99	29.1	57.8	100.1	27.79	146.5	156.2	29.91
PHC3	PLA	HNT	PCC	80/5/15	2.18	-3.36	20.3	58.9	99.0	25.65	145.7	156.2	30.83
PHC4	PLA	HNT	PCC	75/5/20	2.34	-3.30	23.3	58.4	99.0	27.93	146.3	156.4	33.17
PHC5	PLA	HNT	PCC	70/5/25	2.94	-4.06	21.9	58.7	97.6	19.34	145.6	155.5	32.91
PLAPCC10*	PLA	HNT	PCC	90/0/10				60.5	119.69	26.93	152.8	---	28.32
PLAPCC15*	PLA	HNT	PCC	90/0/15				59.7	118.1	22.45		154.70	24.13
PLAPCC20*	PLA	HNT	PCC	90/0/20				59.9	118.79	24.40	152.2	155.8	24.61
PLAPCC25*	PLA	HNT	PCC	90/0/25				59.9	110.70	22.10	150.4	156.5	21.63

Therefore, the PLA nanocomposites for the DSC tests were taken from the injected molded specimens, which are already quenched from the melt state by a fast cooling speed in 15 seconds to 50 °C as the molding temperature. The characteristic thermal properties, such as glass transition temperature (T_g), cold crystallization temperature (T_{cc}), enthalpy of cold crystallization (ΔH_{cc}), melting temperature (two peaks T_{m1} and T_{m2}), and enthalpy of fusion (ΔH_m), are marked in Fig. 6.11, and those values are shown in Table 6.2.

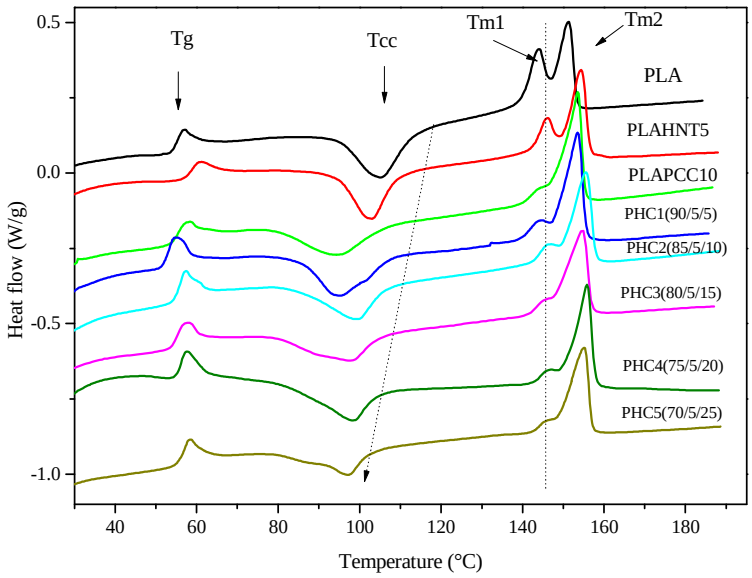

Figure 6.11 DSC thermographs of pure PLA and PLA nanocomposites extruded at 180 °C and molded at 50 °C first heating process at heating speed 5 °C/min

All the data shown in Table 6.2 have been corrected by considering the filler content in PLA nanocomposites. The addition of both PCC particles and halloysite nanotubes to PLA decreases the T_g by about 3 °C. More impressively, the cold crystallization temperature (109.9 °C) of pure PLA was decreased by the incorporation of PCC and HNT fillers by about 10 °C, which also indicated the improved crystallization behaviour of PLA matrix in the presence of nanoparticles. The decrease of both the glass transition and the cold crystallization temperatures can be attributed to the enhanced chain mobility of the PLA matrix at lower temperatures and the decreased crystallization induction period due to the presence of the already existed crystalline nuclei. This result confirms the Avrami isothermal study that rigid inorganic particles such as PCC can behave as nucleating agents for PLA. Meanwhile, the enthalpy of cold crystallization was slightly increased by the addition of nanoparticles compared to that of pure PLA. This enhanced crystallization behaviour can be explained by the high surface area supplied by the nanoparticles and thus by the increasing number of nucleating sites for the PLA matrix. The crystallinity of PLA nanocomposites can be determined from the difference between the enthalpy of fusion and

that of cold crystallization, which is quite small compared to the theoretical melting enthalpy (93 J/g) [209], which means that the injection-moulded PLA composites are almost amorphous in structure. There is not too much of a difference in PCC composition on the crystallization behavior, even if all nanocomposites can increase the crystallizing speed of PLA in isothermal tests.

The influence of the filler amount in the PLA nanocomposites on the glass transition and cold crystallization temperatures was plotted in Fig. 6.12. The addition of nanofillers can effectively decrease both the T_g and T_{cc}, but further increasing filler amount does not lead to additional effects. Fig. 6.13 shows that the DSC heating process for PLA/PCC nanocomposites and the cold crystallization temperature continuously decrease with increasing filler contents. This can be explained by the more available surface area of PCC nanoparticles for the nucleation of the PLA matrix. However, the cold crystallization temperature in Fig. 6.13 is different than that in Fig. 6.11 due to the different heating speeds. The label * in Table 6.2 represents a different thermal speed for the first heating of 10 °C/min, while the other data were calculated with a thermal speed of 5 °C/min. In the literature, plasticizers were applied to PLA in order to lower the glass transition for the moulding process [184]. According to the tan δ peak, measured in DMTA and the DSC results, the glass transition temperature clearly decreased by about 3 °C. The enhanced mobility of the PLA chains can be attributed to the plasticizer effect by the alkanoate layers on the PCC surface, which decrease the interfacial adhesion between polymer and PCC particles. The improved mobility also gives a faster growth rate for the PLA crystal leading to an increase in crystallinity.

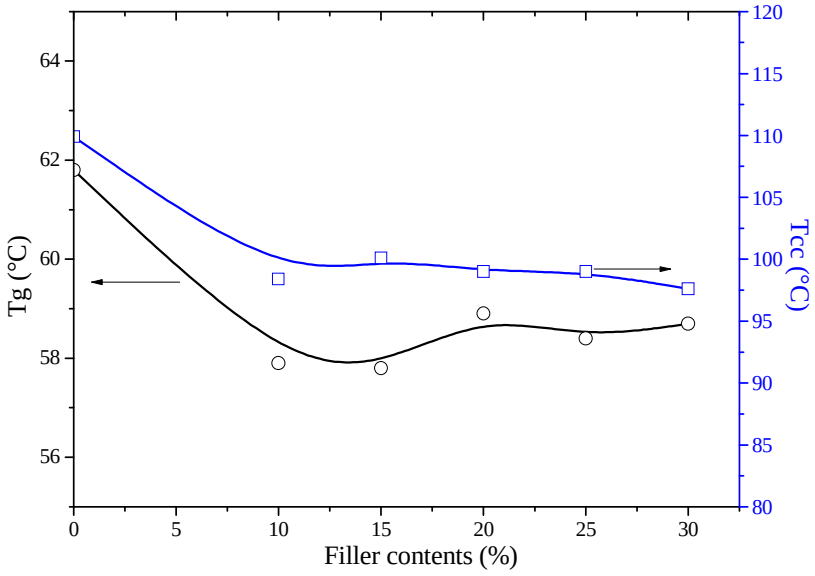

Figure 6.12 Glass transition and cold crystallization temperature of PLA ternary composites versus the filler contents

Another interesting point is that two melting peaks show up in the DSC curves for pure PLA as shown in Fig. 6.11. For the PLA nanocomposites with the PCC and HNT fillers, there is a progressive shift of low temperature peak to high temperature. The two melting peaks are classic for PLA thermal behavior due to the reorganization of less perfect crystals, which have the same structure of the more perfect crystals but with a smaller lamella thickness. Fig. 6.11 clearly shows the shift of the first melting peak to higher temperature in PLA nanocomposites. We believe that the improved crystallization favors the nucleation of larger amounts of less perfect crystals with respect to the pure PLA [194]. Generally speaking, the multiple melting behaviors are related to the presence of crystals with different forms or different perfection degrees during the heating process [210, 211].Here PCC nanoparticles have a much more impressive influence on the reorganization of the PLA crystals compared to HNT. Fig. 6.12 also indicates that the addition of 25 wt% PCC nanoparticles gives a clear melting peak at a higher temperature.

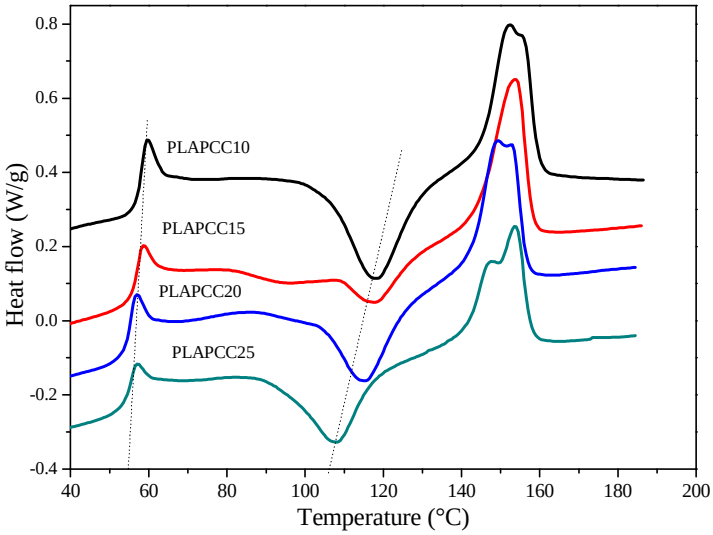

Figure 6.13 DSC thermographs of PLA/PCC nanocomposites extruded at 180 °C and molded at 50 °C first heating process at heating speed of 10 °C/min

6.5 Morphology of PLA nanocomposites

The fracture surface of the tensile samples was investigated by the SEM technique and shown in Fig. 6.14 from (a) to (d). The fracture surface in the presence of crazing has a more brittle aspect compared to that associated to shear yielding. The dispersion or distribution of nanofillers into the polymer matrix is an important topic for the high performance of polymeric nanocomposites, in particular for the mechanical and thermal properties. Pure PLA and PLA/HNT, PLA/PCC, PLA/HNT/PLA composites are compared in Fig. 6.14. The surface of pure PLA (Fig. 6.14 (a)) is smooth without significant plastic deformation and a few fibrils were formed, typical of a fracture process dominated by

crazing. Fig. 6.14 (b) shows the fracture surface of PLA with only halloysite natural tubes at different magnifications. The whole fracture surface in Fig. 6.14 (b1) shows the presence of a large aggregation of halloysite natural nanotubes, and causing an early fracture, which can explain for the decreased yield strength in the tensile tests. However, a part of the PLA/HNT surface consists of the exfoliated nanotubes as shown in Fig. 6.14 (b2), some of which are pulled out and with some holes left on the surface. This shows the potential of the application of HNT nanotubes taking advantage of their high surface area and their unique structure, in the case that homogeneous dispersion could be reached. This will be left to some future work to try to carry out a surface coating for the natural nanotubes to decrease their aggregation, while increasing their compatibility between those hydrophilic fillers and the relatively hydrophobic polymer. The tensile specimens of PLA/PCC nanocomposites, which exhibited stress whitening during the tensile test, show a homogeneous fracture surface with the well-separated PCC particles in Fig. 6.14 (c1) compared to the HNT nanotubes. The PLA matrix in the PLA/PCC composites showed enhanced plastic deformation (in Fig. 6.14 (c2)) compared to that of pure PLA. This better dispersion of PCC particles is achieved by the surface coating with stearic acid, which effectively decreased the surface free energy of the calcium carbonate nanoparticles as reported in our former work as mentioned in Chapter 5. Meanwhile, the interfacial adhesion between the PCC particles and PLA polymer is also influenced by the surface coating, since the debonding of calcium carbonate particles from the PLA matrix occurred during the tensile test, and evidence of the cavitation is shown in the Fig. 6.14 (c2). In other words, this debonding is responsible for the decreasing tensile strength and the increasing elongation-at-break for PLA composites when PCC particles are added and is also one of the most critical factors for the toughness improvement of PLA nanocomposites.

The addition of both PCC and HNT nanofillers to PLA does not change the aggregation of HNT. The fracture surface showed different zones in Fig. 6.14 (d). At high magnification, Fig. 6.14 (d1), noting a typical aggregate of HNTs, represents a material flaw that will induce a decrease of the mechanical properties. Another different zone is shown in Fig. 6.14 (d2) where PCC nanoparticles are clearly visible as well as many microvoids due to the debonding of PCC particles from the PLA polymer. There is also the combination of the fibrillation of the PLA around the nanoparticles and the stretching of ligament between the microvoids, which plays an important role in enhancing the toughness of the polymer material. Considering the mechanical properties in the tensile part, we believe that PCC nanoparticles are also potential nanofillers for the improvement in toughness of PLA.

Based on the SEM micrographs, we can conclude that the toughening mechanisms and failure behaviors of PLA nanocomposites under uniaxial tension, the pure PLA yields mainly by crazing of the polymer. However, in PLA/PCC nanocomposite, microvoids form by debonding at the PLA/PCC region, followed by enhanced plastic deformation of the polymer matrix and also by its fibrillation.

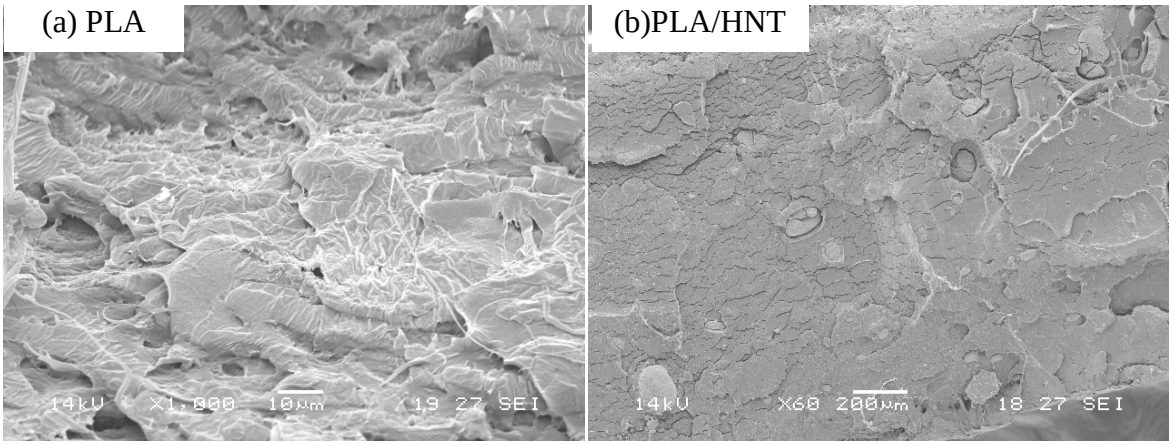

(a) (b)

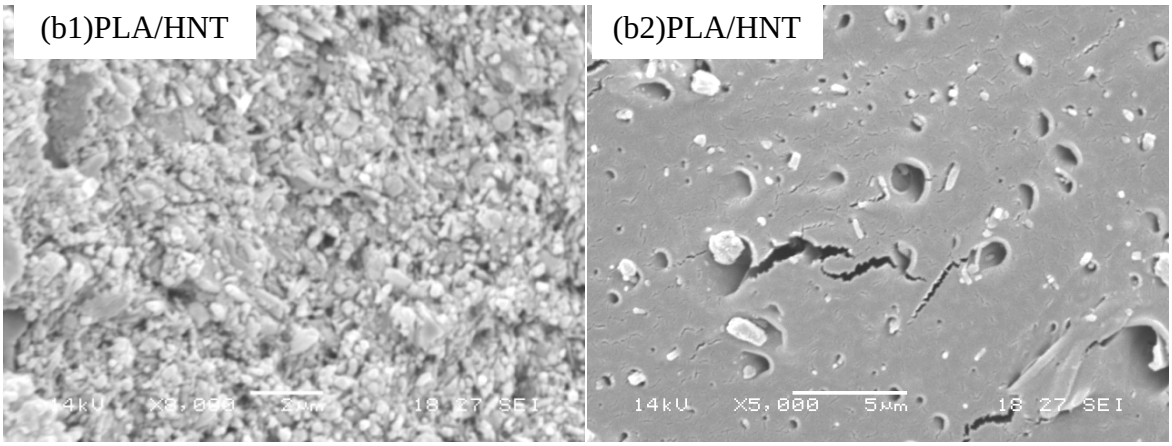

(b1) (b2)

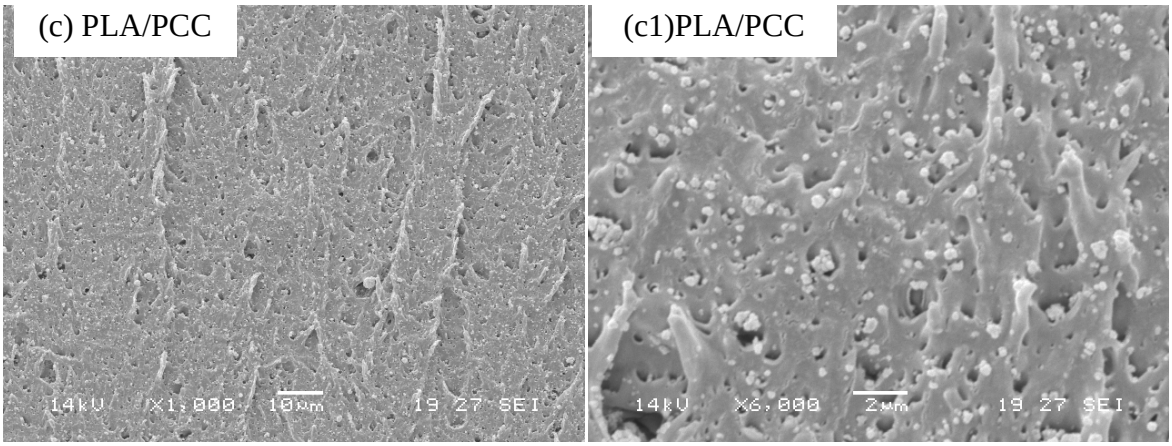

(c) (c1)

Fig. 6.14 (to be continued)

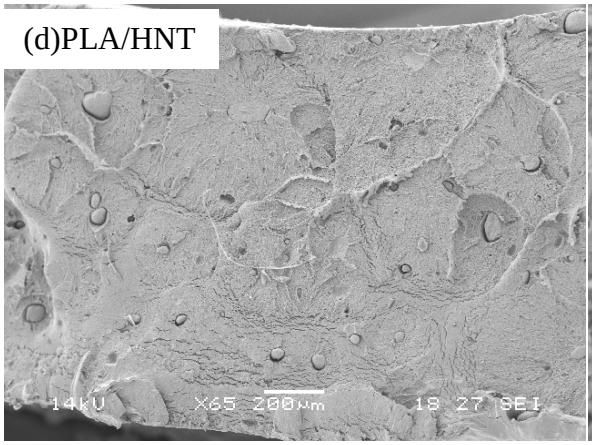

(d)

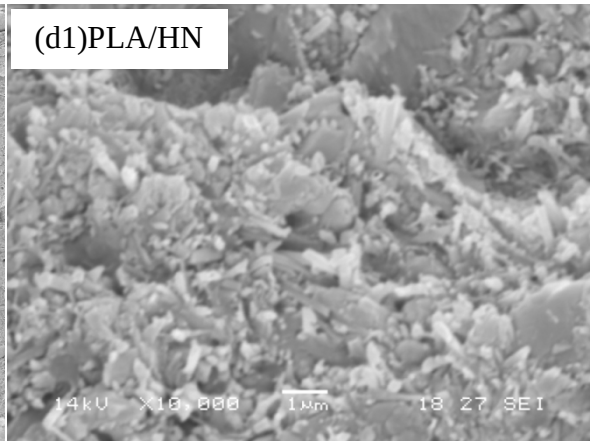

(d1)

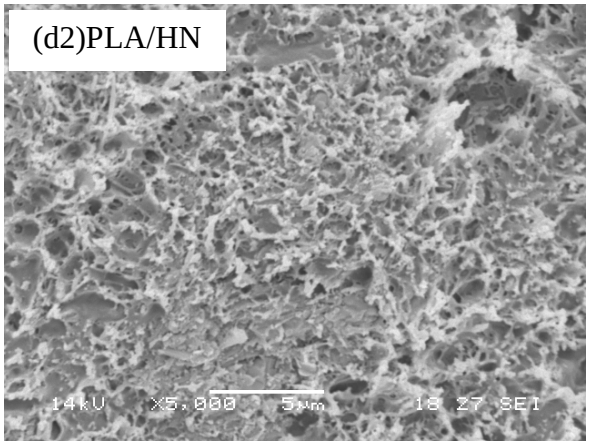

(d2)

Figure 6.14 SEM micrographs for the fracture surface of PLA specimens after tensile measurement: (a) pure PLA, (b) PLA/HNT (95/5) nanocomposites, (c) PLA/PCC (90/10) nanocomposites, (d) PLA/HNT/PCC (80/5/15) ternary nanocomposites

6.6 Conclusion

PLA composites with PCC (coated with stearic acid) and HNT nanotubes were compared in this study. An isothermal crystallization study indicated that two nanofillers acted as nucleating agents by decreasing the half-crystallization-time and increasing the crystal growth rate. Additionally, the glass transition temperature was decreased by about 3 °C when the PCC particles were added to the PLA due to the enhanced mobility of PLA chains. A similar T_g decrease resulted from the DMTA tests, which indicated a shift of Tan δ peak (corresponding to T_g) to the lower temperature in PLA composites.

The tensile tests of PLA composites with PCC, HNT or both of them showed different effects on the mechanical performance such as the yield stress, Young's modulus and the

elongation-at-break. The most impressive increase of ultimate deformation of PLA composites occurred when PCC fillers were present and the maximum elongation-at-break reached about 15 %. However, the addition of HNT nanotubes resulted in a decreased elongation-at-break of the PLA composites. Such a mechanical difference is attributed to the nanoparticle dispersion in the matrix as the PCC was surface coated with stearate for achieving a uniform distribution, and the HNTs were not coated, thereby achieving a much higher surface energy leading to aggregation.

These considerations were confirmed by the SEM morphological analysis. A weaker interfacial adhesion is proposed for the PCC surface coating with stearate, which is necessary for the microvoid formation and higher plastic deformation of the polymer matrix during the fracture process of PLA composites. Therefore, a good dispersion and easy debonding of the PCC particles together with the fibrillation of PLA matrix indicated the potential possibility of PCC for the toughness improvement of PLA composites.

Chapter 7 Conclusions

The main purpose of this thesis is to better understand filler-toughened polymer systems, in particular the relationship between the surface coating of nanoparticles and the final performance of polymer nanocomposites, to elucidate the toughening mechanisms that can be activated in filled plastics. Precipitated calcium carbonate nanoparticles are commercially available and widely applied in the industrial fields for polymer composites. However, little information has been disclosed in the open literature about a careful characterization of the structure of the surface of PCC particles coated with stearin under typical industrial conditions. Moreover, the connection between surface coating and mechanical properties, thermal behavior and morphology of the resulting polymer nanocomposites has not been investigated in a thorough manner. This work can be separated into four main parts.

Part 1:

The surface characterization of PCC nanoparticles coated with stearin in aqueous medium has been studied using DRIFT, TGA and DSC techniques. The organic groups on the surface by DRIFT indicate that only the COO^- group is present on the surface without any free stearic acid. The determination of the total organic coating amount shows the presence of calcium alkanoate multilayers on the PCC surface. The DTG analysis successfully showed two separate decomposition peaks and indicated two types of alkanoate layers on the surface. One is the chemisorbed alkanoate layer strongly bonded on the PCC surface, while the other is the physisorbed multilayer bonded to the internal chemisorbed layer by weak van der Waals forces.

DSC measurements suggested that the physisorbed multilayer had a complicated thermal behavior, showing a series of peaks due to (a) evaporation of water, (b) crystalline-to-smectic, (c) smectic-to-nematic and (d) nematic-to-liquid crystal transitions. The amount of chemisorbed layer on the PCC surface was determined by the relationship between the enthalpies of those transitions and the total organic amount on the PCC surface. The most interesting result is that the chemisorbed amount keeps at a constant level with a maximum coverage of about 3.0 wt% for all of the coated PCCs. However, the physisorbed multilayer increases linearly with the totally organic coating amount on the surface.

Micelles adsorption is proposed as the dominating mechanism for the water coating process of PCC particles with stearin. In fact, the low solubility of stearin in water results in the formation of micelles, which, during the drying steps, later deform into flattened

micelles with the bottom part chemically-bonded to the active sites of the PCC surface. The salt exchange between calcium ions and the sodium ions produces the formation of physisorbed alkanoate layers on the outer side of the coating. However, the solvent coating process of PCC particles with stearic acid follows the Langmuir adsorption and a full covered monolayer can be achieved.

Part 2:

Since some free active sites and physisorbed multilayers are present on the PCC surface, it is important to understand the dependence of surface free energy on the PCC surface coating. Meanwhile, the complicated thermal behavior of physisorbed alkanoate layer shows a strong connection between the molecular arrangement and the temperature. Therefore, the thermal transition behavior and the molecular arrangement of alkanoate layers are discussed in Chapter 4.

DSC and XRD techniques were used for the investigation of the thermal transition behavior of calcium carboxylate layers. It was found that the drying process after the water coating is of critical importance for the molecular rearrangement, which undergoes a transition from the α phase, formed originally in the water medium, to the C2 phase at the critical temperature of 104 °C, and then back to the β′ phase during cooling. This rearrangement of alkanoate molecules strongly modifies the structure of the coating and causes the organic group to orient outwards. This has a remarkable effect on the surface free energy of the coated PCC particles.

The surface free energy of coated PCC nanoparticles has been determined by the IGC technique. A decreasing tendency was found for both the dispersion and specific components of surface free energy with an increase in the surface coating amount. However, there is a much stronger dependence of specific component of PCC surface energy on the organic coating amount. The dependence of PCC surface free energy on the preconditioning and measurement temperatures is also discussed, especially in relation to the drying process and the conditions of melt blending with polymers. It is known from previous studies that the interfacial adhesion between particles and polymers largely depend on the surface free energy. Our study has revealed how this is also related to the surface coating amount.

A molecular arrangement model is proposed based on the DSC, XRD and XPS results. The chemisorbed monolayer is vertical to the PCC surface, but only partially covers the surface. The physisorbed multilayer can be arranged in different forms depending on the thermal treatment. After drying, the alkanoate molecules are perpendicular to the chemisorbed layer and show the alkyl chains oriented outwards. This proposed model

matches very well with the surface free energy determined by IGC and with the thickness of coating layers measured by XPS.

Part 3:

HDPE/PCC nanocomposites were prepared using the extrusion process with a fixed particle loading of 10% by volume. The mechanical properties, including the tensile properties and the impact response, were discussed mainly in relation to the effect of the surface coating amount on the PCC surface.

The addition of pure PCC particles significantly increases the yield stress and Young's modulus of HDPE composites compared to that of pure HDPE. However, on progressively increasing the amount of PCC surface coating, the yield stress shows a decreasing trend, while the elastic modulus keeps at a relatively constant value. This effect of the surface organic coating is related to the debonding process occurring between the PCC particles and the polymer matrix under the uniaxial applied load. Higher levels of surface coating, as determined in Chapter 4, mean a lower surface energy and consequently a lower interfacial adhesion. This results in an easier debonding of nanoparticles from polymer matrix. Therefore, the dependence of the yield strain on the amount of surface coating also reflects an earlier debonding during the tensile tests.

Impact tests showed a tendency to a linear increase of the Charpy impact strength on increasing the amount of PCC coating. This result supports our approach to filler-toughening, which mainly consists of achieving an optimum balance between toughness and stiffness of polymer nanocomposites.

The micro-morphology of the fracture surface of specimens of HDPE nanocomposites, after the Charpy test has been studied by SEM. Both the crack initiation and crack propagation zones of HDPE/PCC composites are compared with that of pure HDPE. The nanocomposites showed an enhanced plastic deformation and cooperative fibrillation of polymer matrix, which are related to the formation of the microvoids around nanoparticles. The degree of aggregation in HDPE/PCC composites was found to be smaller when compared to that of uncoated PCC particles. A better dispersion of nanoparticles in the polymer matrix can be achieved by a lowering of surface free energy and would produce finer microvoids during the impact process.

Part 4:

PLA is a biodegradable polymer and received much attention in recent years due to its high stiffness and strength. However, one of the main problems is its intrinsic poor

toughness that constrains some further applications. Therefore, PCC particles coated with stearin in the water medium were added to the PLA as toughening fillers.

The mechanical properties of PLA/PCC nanocomposites are compared with another PLA nanocomposite with halloysite nanotubes (HNT). The addition of PCC particles to the PLA shows a large increase of the elongation-at-break from about 3.5% for pure PLA to about 12% for the nanocomposites with 15 wt% PCC particles. The yield stress of PLA composites shows a decreasing tendency with increasing the nanofillers loading. For PCC particles, the decreasing of yield stress suggests a larger extent of debonding of PCC particles from the PLA matrix, similar to that mentioned for the HDPE/PCC nanocomposites. On the contrary, the HNT fillers showed a strong effect on the elastic modulus of PLA nanocomposites.

The dynamic thermal mechanical behavior of PLA/PCC nanocomposites was studied using the DMTA technique. It was found that the storage modulus of PLA composites keeps at the same level with that of pure PLA and some PLA/PCC composites show an even lower elastic modulus. This can be a reflection of the lower interfacial adhesion between PCC fillers and the PLA. The temperature dependence of tan δ suggests a decreased Tg of PLA nanocomposites by about 3 °C, which indicated an enhanced mobility of PLA chains due to the plasticizing effect of the stearate coating on the PCC particles.

The crystallization behavior of PLA/PCC nanocomposites was analyzed using both isothermal and non-isothermal DSC analysis. The addition of coated PCC particles effectively decreases the crystallization half-time and the cold crystallization temperature. It was confirmed that the glass transition temperature was decreased in the PLA/PCC nanocomposites. We believe that the coated PCC nanoparticles act as nucleating agents for the PLA, and the surface coating multilayer of stearate show a plasticizing effect decreasing the glass temperature.

The morphology investigation of PLA nanocomposites by SEM analysis showed a good dispersion of PCC nanoparticles, while large aggregates have been noted for HNT fillers. Considering the fracture surface of specimens broken in a tensile test, PLA/PCC nanocomposites showed the presence of debonding of PCC nanofillers from the PLA matrix and the fibrillation of this polymer. PCC particles are considered to be the toughening nanoparticles, while HNT particles the strength enhancing nanofillers.

References

1. Bucknall, C.B. and Drinkwat.Ic, *Rubber-Toughening of Plastics .4. Creep Mechanisms in Abs Emulsion Polymer*. Journal of Materials Science, 1973. **8**(12): p. 1800-1808.
2. Pearson, R.A., H.J. Sue, and A.F. Yee, *Toughening of Plastics : Advances in Modeling and Experiments*. 2000, Washington, DC: American Chemical Society ; Oxford : Oxford University Press [distributir]. x, 254 p.
3. Wu, S.H., *Phase-Structure and Adhesion in Polymer Blends - a Criterion for Rubber Toughening.* Polymer, 1985. **26**(12): p. 1855-1863.
4. Muratoglu, O.K., et al., *Toughening Mechanism of Rubber-Modified Polyamides.* Polymer, 1995. **36**(5): p. 921-930.
5. Bartczak, Z., et al., *Toughness Mechanism in Semi-Crystalline Polymer Blends: I. High-density Polyethylene Toughened with Rubbers.* Polymer, 1999. **40**(9): p. 2331-2346.
6. Levita, G., A. Marchetti, and A. Lazzeri, *Fracture of Ultrafine Calcium-Carbonate Polypropylene Composites.* Polymer Composites, 1989. **10**(1): p. 39-43.
7. Lazzeri, A., et al., *Filler Toughening of Plastics. Part 1 - The Effect of Surface Interactions on Physico-Mechanical Properties and Rheological Behaviour of Ultrafine $CaCO_3$/HDPE Nanocomposites.* Polymer, 2005. **46**(3): p. 827-844.
8. Rothon, R., *Particulate-Filled Polymer Composites*. 2nd ed. ed. 2003, Shrewsbury: Rapra Technology.
9. Fu, Q.A. and G.H. Wang, *Polyethylene Toughened by Rigid Inorganic Particles.* Polymer Engineering and Science, 1992. **32**(2): p. 94-97.
10. Fu, Q., G.H. Wang, and C.X. Liu, *Polyethylene Toughened by $CaCO_3$ Particles - the Interface Behavior and Fracture Mechanism in High-Density Polyethylene/ $CaCO_3$ Blends.* Polymer, 1995. **36**(12): p. 2397-2401.
11. Bartczak, Z., et al., *Toughness Mechanism in Semi-Crystalline Polymer Blends: II. High-Density Polyethylene Toughened with Calcium Carbonate Filler Particles.* Polymer, 1999. **40**(9): p. 2347-2365.
12. Thio, Y.S., et al., *Toughening of Isotactic Polypropylene with $CaCO_3$ Particles.* Polymer, 2002. **43**(13): p. 3661-3674.
13. Margolina, A. and S.H. Wu, *Percolation Model for Brittle-Tough Transition in Nylon Rubber Blends.* Polymer, 1988. **29**(12): p. 2170-2173.
14. Wu, S.H., *A Generalized Criterion for Rubber Toughening - the Critical Matrix Ligament Thickness.* Journal of Applied Polymer Science, 1988. **35**(2): p. 549-561.
15. Yee, A.F., *Yield and Deformation-Behavior of Some Polycarbonate Blends.* Journal of Materials Science, 1977. **12**(4): p. 757-765.
16. Maxwell, M.A. and A.F. Yee, *The Effect of Strain Rate on the Toughening Mechanisms of Rubber-Modified Plastics.* Polymer Engineering and Science, 1981. **21**(4): p. 205-211.
17. Pearson, R.A. and A.F. Yee, *Toughening Mechanisms in Elastomer-Modified Epoxies .2. Microscopy Studies.* Journal of Materials Science, 1986. **21**(7): p. 2475-2488.
18. Yee, A.F. and R.A. Pearson, *Toughening Mechanisms in Elastomer-Modified Epoxies .1. Mechanical Studies.* Journal of Materials Science, 1986. **21**(7): p. 2462-2474.
19. Parker, D.S. and A.F. Yee, *A Petrographic Thin Sectioning Technique for Evaluating Composite-Materials.* Journal of Materials Science Letters, 1989. **8**(8): p. 921-924.

20. Muratoglu, O.K., A.S. Argon, and R.E. Cohen, *Crystalline Morphology of Polyamide-6 near Planar Surfaces.* Polymer, 1995. **36**(11): p. 2143-2152.

21. Muratoglu, O.K., et al., *Microstructural Processes of Fracture of Rubber-Modified Polyamides.* Polymer, 1995. **36**(25): p. 4771-4786.

22. Muratoglu, O.K., et al., *Microstructural Fracture Processes Accompanying Growing Cracks in Tough Rubber-Modified Polyamides.* Polymer, 1995. **36**(25): p. 4787-4795.

23. Lazzeri, A. and C.B. Bucknall, *Dilatational Bands in Rubber-Toughened Polymers.* Journal of Materials Science, 1993. **28**(24): p. 6799-6808.

24. Lazzeri, A. and C.B. Bucknall, *Applications of a Dilatational Yielding Model to Rubber-Toughened Polymers.* Polymer, 1995. **36**(15): p. 2895-2902.

25. Bucknall, C.B., P.S. Heather, and A. Lazzeri, *Rubber Toughening of Plastics .12. Deformation Mechanisms in Toughened Nylon 6,6.* Journal of Materials Science, 1989. **24**(6): p. 2255-2261.

26. Bucknall, C.B. and A. Lazzeri, *Rubber Toughening of Plastics - Part XIII - Dilatational Yielding in PA6.6/EPR Blends.* Journal of Materials Science, 2000. **35**(2): p. 427-435.

27. Bucknall, C.B., et al., *The Role of Rubber Particle Cavitation in Deformation and Fracture of Toughened Plastics.* Abstracts of Papers of the American Chemical Society, 1998. **216**: p. U824-U824.

28. Gurson, A.L., *Continuum Theory of Ductile Rupture by Void Nucleation and Growth .1. Yield Criteria and Flow Rules for Porous Ductile Media.* Journal of Engineering Materials and Technology-Transactions of the Asme, 1977. **99**(1): p. 2-15.

29. Yee, A.F., D.M. Li, and X.W. Li, *The Importance of Constraint Relief Caused by Rubber Cavitation in the Toughening of Epoxy.* Journal of Materials Science, 1993. **28**(23): p. 6392-6398.

30. Lazzeri, A. and B. Bucknall Clive, *Recent Developments in the Modeling of Dilatational Yielding in Toughened Plastics*, in *Toughening of Plastics*. 2000, American Chemical Society. p. 14-35.

31. Zebarjad, S.M., et al., *Deformation, Yield and Fracture of Elastomer-Modified Polypropylene.* Journal of Applied Polymer Science, 2003. **90**(14): p. 3767-3779.

32. Cheng, C., et al., *Deformation of Rubber-Toughened Polycarbonate - Microscale and Nanoscale Analysis of the Damage Zone.* Journal of Applied Polymer Science, 1995. **55**(12): p. 1691-1702.

33. Cheng, C., et al., *Cooperative Cavitation in Rubber-Toughened Polycarbonate.* Journal of Materials Science, 1995. **30**(3): p. 587-595.

34. Kim, G.M. and G.H. Michler, *Micromechanical Deformation Processes in Toughened and Particle-filled Semicrystalline Polymers: Part 1. Characterization of Deformation Processes in Dependence on Phase Morphology.* Polymer, 1998. **39**(23): p. 5689-5697.

35. Kim, G.M. and G.H. Michler, *Micromechanical Deformation Processes in Toughened and Particle Filled Semicrystalline Polymers. Part 2: Model Representation for Micromechanical Deformation Processes.* Polymer, 1998. **39**(23): p. 5699-5703.

36. Argon, A.S., et al., *Novel Mechanisms of Toughening Semi-Crystalline Polymers*, in *Toughening of Plastics*. 2000, American Chemical Society. p. 98-124.

37. Argon, A.S. and R.E. Cohen, *Toughenability of Polymers.* Polymer, 2003. **44**(19): p. 6013-6032.

38. Wilbrink, M.W.L., et al., *Toughenability of Nylon-6 with $CaCO_3$ Filler Particles: New Findings and General Principles.* Polymer, 2001. **42**(26): p. 10155-10180.

39. Lehmann, B., et al., *Improvement of Notch Toughness of Low Nano-SiO_2 Filled Polypropylene Composites.* Journal of Materials Science Letters, 2003. **22**(14): p. 1027-1030.

40. Chan, C.M., et al., *Polypropylene/Calcium Carbonate Nanocomposites.* Polymer, 2002. **43**(10): p. 2981-2992.

41. Lin, Y., et al., *The Toughening Mechanism of Polypropylene/Calcium Carbonate Nnanocomposites.* Polymer, 2010. **51**(14): p. 3277-3284.

42. Badran, B.M., A. Galeski, and M. Kryszewski, *High-Density Polyethylene Filled with Modified Chalk.* Journal of Applied Polymer Science, 1982. **27**(10): p. 3669-3681.

43. Tjong, S.C., S.A. Xu, and Y.W. Mai, *Impact Fracture Toughness of Short Glass Fiber-Reinforced Polyamide 6,6 Hybrid Composites Containing Elastomer Particles using Essential Work of Fracture Concept.* Materials Science and Engineering a-Structural Materials Properties Microstructure and Processing, 2003. **347**(1-2): p. 338-345.

44. Nair, S.V., L.A. Goettler, and B.A. Lysek, *Toughness of Nanoscale and Multiscale Polyamide-6,6 Composites.* Polymer Engineering and Science, 2002. **42**(9): p. 1872-1882.

45. Wang, G., et al., *Nano- $CaCO_3$/Polypropylene Composites Made with Uultra-High-Speed Mixer.* Journal of Materials Science Letters, 2002. **21**(13): p. 985-986.

46. Osman, M.A., A. Atallah, and U.W. Suter, *Influence of Excessive Filler Coating on the Tensile Properties of LDPE-Calcium Carbonate Composites.* Polymer, 2004. **45**(4): p. 1177-1183.

47. Jancar, J., A.T. Dibenedetto, and A. Dianselmo, *Effect of Adhesion on the Fracture-Toughness of Calcium Carbonate-Filled Polypropylene.* Polymer Engineering and Science, 1993. **33**(9): p. 559-563.

48. Price, G.J. and D.M. Ansari, *Surface Modification of Calcium Carbonates Studied by Inverse Gas Chromatography and the Effect on Mechanical Properties of Filled Polypropylene.* Polymer International, 2004. **53**(4): p. 430-438.

49. Dasari, A., et al., *Toughening Polypropylene and Its Nanocomposites with Submicrometer Voids.* Macromolecules, 2010. **43**(13): p. 5734-5739.

50. Zhu, S., Y. Zhang, and Y.X. Zhang, *Deformation and Fracture of Mg(OH)(2)-Filled Polyolefin Composites under Tensile Stress.* Journal of Applied Polymer Science, 2003. **89**(12): p. 3248-3255.

51. Mai, K., Y. Qiu, and Z. Lin, *Mechanical Properties of Mg(OH)(2)/Polypropylene Composites Modified by Functionalized Polypropylene.* Journal of Applied Polymer Science, 2003. **88**(9): p. 2139-2147.

52. Dekkers, M.E.J. and D. Heikens, *The Effect of Interfacial Adhesion on the Tensile Behavior of Polystyrene Glass-Bead Composites.* Journal of Applied Polymer Science, 1983. **28**(12): p. 3809-3815.

53. Xie, X.L., Y.W. Mai, and X.P. Zhou, *Dispersion and Alignment of Carbon Nanotubes in Polymer Matrix: A Review.* Materials Science & Engineering R-Reports, 2005. **49**(4): p. 89-112.

54. Kim, G.M., et al., *Influence of Nanofillers on the Deformation Process in Layered Silicate/Polyamide-12 Nanocomposites.* Polymer, 2001. **42**(3): p. 1095-1100.

55. Debowska, M., et al., *Polyamide 6/Layered Silicate Nanocomposites.* Acta Physica Polonica A, 2008. **113**(5): p. 1321-1329.

56. Tjong, S.C., *Structural and Mechanical Properties of Polymer Nanocomposites.* Materials Science & Engineering R-Reports, 2006. **53**(3-4): p. 73-197.

57. Zhang, Y.H., et al., *Studies on Characterization and Cryogenic Mechanical Properties of Polyimide-Layered Silicate Nanocomposite Films.* Polymer, 2004. **45**(22): p. 7579-7587.

58. Yang, K., et al., *Morphology and Mechanical Properties of Polypropylene/Calcium Carbonate Nanocomposites.* Materials Letters, 2006. **60**(6): p. 805-809.

59. Xie, X.L., et al., *Rheological and Mechanical Properties of PVC/ $CaCO_3$ Nanocomposites Prepared by in Situ Polymerization.* Polymer, 2004. **45**(19): p. 6665-6673.

60. Zuiderduin, W.C.J., et al., *Toughening of Polypropylene with Calcium Carbonate Particles.* Polymer, 2003. **44**(1): p. 261-275.

61. Chow, T.S., *Effect of Particle Shape at Finite Concentration on Elastic-Moduli of Filled Polymers.* Journal of Polymer Science Part B-Polymer Physics, 1978. **16**(6): p. 959-965.

62. Chow, T.S., *Effect of Particle Shape at Finite Concentration on Thermal-Expansion of Filled Polymers.* Journal of Polymer Science Part B-Polymer Physics, 1978. **16**(6): p. 967-970.

63. Lazzeri, A., Y.S. Thio, and R.E. Cohen, *Volume Strain Measurements on $CaCO_3$/Polypropylene Particulate Composites: The effect of particle size.* Journal of Applied Polymer Science, 2004. **91**(2): p. 925-935.

64. Kowalewski, T. and A. Galeski, *Influence of Chalk and Its Surface-Treatment on Crystallization of Filled Polypropylene.* Journal of Applied Polymer Science, 1986. **32**(1): p. 2919-2934.

65. Lin, Y., et al., *Nucleating Effect of Calcium Stearate Coated $CaCO_3$ Nanoparticles on Polypropylene.* Journal of Colloid and Interface Science, 2011. **354**(2): p. 570-576.

66. Thomason, J.L. and A.A. Vanrooyen, *Transcrystallized Interphase in Thermoplastic Composites .1. Influence of Fiber Type and Crystallization Temperature.* Journal of Materials Science, 1992. **27**(4): p. 889-896.

67. Chen, E.J.H. and B.S. Hsiao, *The Effects of Transcrystalline Interphase in Advanced Polymer Composites.* Polymer Engineering and Science, 1992. **32**(4): p. 280-286.

68. Varga, J. and J. Kargerkocsis, *Interfacial Morphologies in Carbon-Fiber-Reinforced Polypropylene Microcomposites.* Polymer, 1995. **36**(25): p. 4877-4881.

69. Quan, H., et al., *On transcrystallinity in Semi-Crystalline Polymer Composites.* Composites Science and Technology, 2005. **65**(7-8): p. 999-1021.

70. Dasari, A., Z.Z. Yu, and Y.W. Mai, *Transcrystalline Regions in the Vicinity of Nanofillers in Polyamide-6.* Macromolecules, 2007. **40**(1): p. 123-130.

71. Halpin, J.C., *Stiffness and Expansion Estimates for Oriented Short Fiber Composites.* Journal of Composite Materials, 1969. **3**(4): p. 732-734.

72. Kerner, E.H., T*he Electrical Conductivity of Composite Media*. Proc. Phys. Soc., 1956. **69**(8): p. 802.

73. Nielsen, L.E., *Generalized Equation for Elastic Moduli of Composite Materials.* Journal of Applied Physics, 1970. **41**(11): p. 4626-&.

74. Nielsen, L.E., *Dynamic Mechanical-Properties of Polymers Filled with Agglomerated Particles.* Journal of Polymer Science Part B-Polymer Physics, 1979. **17**(11): p. 1897-1901.

75. Lewis, T.B. and L.E. Nielsen, *Dynamic Mechanical Properties of Particulate-Filled Composites.* Journal of Applied Polymer Science, 1970. **14**(6): p. 1449-1471.

76. Ishai, O. and L.J. Cohen, *Elastic Properties of Filled and Porous Epoxy Composites.* International Journal of Mechanical Sciences, 1967. **9**(8): p. 539-546.

77. Fu, S.Y., G.S. Xu, and Y.W. Mai, *On the Elastic Modulus of Hybrid Particle/Short-Fiber/Polymer Composites.* Composites Part B-Engineering, 2002. **33**(4): p. 291-299.

78. Nielsen, L.E., *Simple Theory of Stress-Strain Properties of Filled Polymers.* Journal of Applied Polymer Science, 1966. **10**(1): p. 97-103.

79. Nicolais, L. and L. Nicodemo, *Strength of Particulate Composite.* Polymer Engineering and Science, 1973. **13**(6): p. 469-469.

80. Nicolais, L. and M. Narkis, *Stress-Strain Behavior of Styrene-Acrylonitrile/Glass Bead Composites in Glassy Region.* Polymer Engineering and Science, 1971. **11**(3): p. 194-199.

81. Turcsanyi, B., B. Pukanszky, and F. Tudos, *Composition Dependence of Tensile Yield Stress in Filled Polymers.* Journal of Materials Science Letters, 1988. **7**(2): p. 160-162.

82. Demjen, Z., B. Pukanszky, and J. Nagy, *Evaluation of Interfacial Interaction in Polypropylene Surface Treated $CaCO_3$ Composites.* Composites Part a-Applied Science and Manufacturing, 1998. **29**(3): p. 323-329.

83. Pukanszky, B., *Interfacial Interactions in Particulate Filled Thermoplastics - Mechanism, Strength, Properties.* Makromolekulare Chemie-Macromolecular Symposia, 1993. **70-1**: p. 213-223.

84. Thio, Y.S., A.S. Argon, and R.E. Cohen, *Role of Interfacial Adhesion Strength on Toughening Polypropylene with Rigid Particles.* Polymer, 2004. **45**(10): p. 3139-3147.

85. Ahsan, T. and D.A. Taylor, *The Influence of Surface Energetics of Calcium Carbonate Minerals on Mineral-Polymer Interaction in Polyolefin Composites.* Journal of Adhesion, 1998. **67**(1-4): p. 69-79.

86. Evans, A.G., et al., *Mechanisms of Toughening in Rubber Toughened Polymers.* Acta Metallurgica, 1986. **34**(1): p. 79-87.

87. Bohse, J., W. Grellmann, and S. Seidler, *Micromechanical Interpretation of Fracture Toughness of Particulate-Filled Thermoplastics.* Journal of Materials Science, 1991. **26**(24): p. 6715-6721.

88. Wang, K., et al., *Mechanical Properties and Toughening Mechanisms of Polypropylene/Barium Sulfate Composites.* Composites Part a-Applied Science and Manufacturing, 2003. **34**(11): p. 1199-1205.

89. Lin, Y., et al., *High Impact Toughness Polypropylene/ $CaCO_3$ Nanocomposites and the Toughening Mechanism.* Macromolecules, 2008. **41**(23): p. 9204-9213.

90. Yoo, Y., et al., *Morphology and Mechanical Properties of Rubber Toughened Amorphous Polyamide/MMT Nanocomposites.* Macromolecules, 2010. **43**(2): p. 615-624.

91. Kiss, A., E. Fekete, and B. Pukanszky, *Aggregation of $CaCO_3$ Particles in PP Composites: Effect of Surface Coating.* Composites Science and Technology, 2007. **67**(7-8): p. 1574-1583.

92. Fekete, E., et al., *Aggregation, Fracture Initiation, and Strength of PP/ $CaCO_3$ Composites.* Journal of Macromolecular Science-Physics, 1999. **B38**(5-6): p. 885-899.

93. Pukanszky, B. and E. Fekete, *Adhesion and Surface Modification.* Mineral Fillers in Thermoplastics I, 1999. **139**: p. 109-153.

94. Matienzo, L.J. and T.K. Shah, *Surface-Treatment of Phlogopite Particles for Composite Applications - Xps and Drift Studies.* Surface and Interface Analysis, 1986. **8**(2): p. 53-59.

95. Rong, M.Z., et al., *Analysis of the Interfacial Interactions in Polypropylene/silica Nanocomposites.* Polymer International, 2004. **53**(2): p. 176-183.

96. Demjen, Z., et al., *Interaction of Silane Coupling Agents with $CaCO_3$.* Journal of Colloid and Interface Science, 1997. **190**(2): p. 427-436.

97. Osman, M.A., M. Ploetze, and P. Skrabal, *Structure and Properties of Alkylammonium Monolayers Self-assembled on Montmorillonite Platelets.* Journal of Physical Chemistry B, 2004. **108**(8): p. 2580-2588.

98. Papirer, E., J. Schultz, and C. Turchi, *Surface-Properties of a Calcium-Carbonate Filler Treated with Stearic-Acid.* European Polymer Journal, 1984. **20**(12): p. 1155-1158.

99. Fekete, E., et al., *Surface Modification and Characterization of Particulate Mineral Fillers.* Journal of Colloid and Interface Science, 1990. **135**(1): p. 200-208.

100. Osman, M.A. and U.W. Suter, *Surface Treatment of Calcite with Fatty Acids: Structure and properties of the organic monolayer.* Chemistry of Materials, 2002. **14**(10): p. 4408-4415.

101. Kaully, T., A. Siegmann, and D. Shacham, *Highly Filled Natural $CaCO_3$ Composites, III. Filler surface treatment and its structure.* Composite Interfaces, 2008. **15**(1): p. 49-74.

102. Wu, S., *Interfacial and Surface Tensions of Polymers.* Journal of Macromolecular Science-Reviews in Macromolecular Chemistry and Physics, 1974. **C 10**(1): p. 1-73.

103. Cavalier, K., et al., *Acid Resistant Particles of an Akaline Earth Metal Carbonate*. 2006: WO/2006/067144.

104. Nover, C. and D. Helmut, *Process for the Continuous Production of Precipitated Calcium Carbonate*. 2002: U.S Patent No. 2002/0,172,636 A1.

105. Nover, C. and D. Helmut, *Bimolecular Coated Calcium Carbonate And Process Of Production Thereof.* 2002: U.S Patent No. 6,342,100 B1.

106. Garnier, P., et al., *Polymorphism of Crystalline Phases of Calcium Stearate.* Journal of Materials Science, 1988. **23**(9): p. 3225-3231.

107. Vold, M.J., G.S. Hattiangdi, and R.D. Vold, *Crystal Forms of Anhydrous Calcium Stearate Derivable From Calcium Stearate Monohydrate.* Journal of Colloid Science, 1949. **4**(2): p. 93-101.

108. Mohai, M. and I. Bertoti, *Calculation of Overlayer Thickness on Curved Surfaces Based on XPS Intensities.* Surface and Interface Analysis, 2004. **36**(8): p. 805-808.

109. Mohai, M. and I. Bertóti. *Correction for Surface Contamination in XPS: A Practical Approach.* . in *Proc. 6th European Conference on Applications of Surface and Interface Analysis*. 1995. Chicheste.

110. Evans, S., R.G. Pritchard, and J.M. Thomas, *Relative Differential Subshell Photoionization Cross-Sections (Mgk-Alpha) from Lithium to Uranium.* Journal of Electron Spectroscopy and Related Phenomena, 1978. **14**(5): p. 341-358.

111. Reilman, R.F., A. Msezane, and S.T. Manson, *Relative Intensities in Photoelectron-Spectroscopy of Atoms and Molecules.* Journal of Electron Spectroscopy and Related Phenomena, 1976. **8**(5): p. 389-394.

112. Price, G.J. and D.M. Ansari, *An Inverse Gas Chromatography Study of Calcination and Surface Modification of Kaolinite Clays.* Physical Chemistry Chemical Physics, 2003. **5**(24): p. 5552-5557.

113. Schmitt, P., et al., *Characterization, by Inverse Gas-Chromatography, of the Surface-Properties of Calcium-Carbonate before and after Treatment with Stearic-Acid.* Chromatographia, 1988. **25**(9): p. 786-790.

114. Fekete, E., J. Moczo, and B. Pukansky, *Determination of the Surface Characteristics of Particulate Fillers by Inverse Gas Chromatography at Infinite Dilution: a Critical Approach.* Journal of Colloid and Interface Science, 2004. **269**(1): p. 143-152.

115. Yuan, P., et al., *Functionalization of Halloysite Clay Nanotubes by Grafting with Gamma-Aminopropyltriethoxysilane.* Journal of Physical Chemistry C, 2008. **112**(40): p. 15742-15751.

116. Rong, M.Z., M.Q. Zhang, and W.H. Ruan, *Surface Modification of Nanoscale Fillers for Improving Pproperties of Polymer Nanocomposites: a Review.* Materials Science and Technology, 2006. **22**(7): p. 787-796.

117. Leong, Y.W., et al., *Comparison of the Mechanical Properties and Interfacial Interactions between Talc, Kaolin, and Calcium Carbonate Filled Polypropylene Composites.* Journal of Applied Polymer Science, 2004. **91**(5): p. 3315-3326.

118. Fu, S.Y., et al., *Effects of Particle Size, Particle/Matrix Interface Adhesion and Particle Loading on Mechanical Properties of Particulate-Polymer Composites.* Composites Part B-Engineering, 2008. **39**(6): p. 933-961.

119. Pukanszky, B., *Influence of Interface Interaction on the Ultimate Tensile Properties of Polymer Composites.* Composites, 1990. **21**(3): p. 255-262.

120. Zhang, Z.S., et al., *Preparation and Characteristics of Nano- $CaCO_3$ Supported Beta-Nucleating Agent of Polypropylene.* European Polymer Journal, 2008. **44**(7): p. 1955-1961.

121. Gilbert, M., P. Petiraksakul, and I. Mathieson, *Characterisation of Stearate/Stearic Acid Coated Fillers.* Materials Science and Technology, 2001. **17**(11): p. 1472-1478.

122. Suess, E., *Calcium Carbonate Interaction with Organic Compounds* 1968, Lehigh University: Bethlehem.

123. Gilbert, M., I. Sutherland, and A. Guest, *Characterization of Coated Particulate Fillers.* Journal of Materials Science, 2000. **35**(2): p. 391-397.

124. Jiang, L., et al., *The Influence of Fatty Acid Coating on the Rheological and Mechanical Properties of Thermoplastic Polyurethane (TPU)/Nano-Sized Precipitated Calcium Carbonate (NPCC) Composites.* Polymer Bulletin, 2006. **57**(4): p. 575-586.

125. Fenter, P. and N.C. Sturchio, *Structure and Growth of Stearate Monolayers on Calcite: First Results of an in Situ X-Ray Reflectivity Study.* Geochimica Et Cosmochimica Acta, 1999. **63**(19-20): p. 3145-3152.

126. Lee, S.J. and K. Kim, *Diffuse Reflectance Infrared Spectra of Stearic Acid Self-Assembled on Fine silver Particles.* Vibrational Spectroscopy, 1998. **18**(2): p. 187-201.

127. Rothon, R., *Particulate-Filled Polymer Composites*. 2nd ed. ed. surface modification and surface modifiers 2003, Shrewsbury: Rapra Technology. 153-206.

128. Ukrainczyk, M., J. Kontrec, and D. Kralj, *Precipitation of Different Calcite Crystal Morphologies in the Presence of Sodium Stearate.* Journal of Colloid and Interface Science, 2009. **329**(1): p. 89-96.

129. Wright, E.H.M. and N.C. Pratt, *Solid/Solution Interface Equilibria for Aromatic-Molecules Adsorbed from Non-Aromatic Media .2. Aromatic Carboxylic-Acids.* Journal of the Chemical Society-Faraday Transactions I, 1974. **70**(8): p. 1461-1471.

130. Lelann, P. and J.F. Berar, *Synchrotron High-Resolution Powder Study of Molecular Packing in Hydrate Calcium Stearate.* Materials Research Bulletin, 1993. **28**(4): p. 329-336.

131. Valor, A., et al., *Thermal Decomposition of the Calcium Salts of Several Carboxylic Acids.* Thermochimica Acta, 2002. **389**(1-2): p. 133-139.

132. Valor, A., E. Reguera, and F. Sanchez-Sinencio, *Synthesis and X-ray Diffraction Study of Calcium Salts of Some Carboxylic Acids.* Powder Diffraction, 2002. **17**(1): p. 13-18.

133. Ho\hne, G., W. Hemminger, and H.J. Flammersheim, *Differential Scanning Calorimetry*. 2nd rev. and enl. ed. ed. 2003, Berlin ; London: Springer. xii, 298 p.

134. Montmitonnet, P., et al. *Physical Properties of Metal Soap Lubricants: Rheology, Phase Transitions under High Pressure*. in *Proc. Conf. "Tribology: friction, lubrication and wear - 50 years on"*. 1987. Londres: Inst. Mech. Engrs.

135. Lawrence, A.S.C., *In Surface Activity and Detergency*, ed. K. Durham. 1961, London.

136. Vold, R.D. and G.S. Hattiangdi, *Characterization of Heavy Metal Soaps by X-Ray Diffraction.* Industrial & Engineering Chemistry, 1949. **41**(10): p. 2311-2320.

137. Vold, R.D., J.D. Grandline, and M.J. Vold, *Polymorphic Transformations of Calcium Stearate and Calcium Stearate Monohydrate.* Journal of Colloid Science, 1948. **3**(4): p. 339-361.

138. Song, M.-G., J.-Y. Kim, and J.-D. Kim, *Effect of Sodium Stearate and Calcium Ion on Dispersion Properties of Precipitated Calcium Carbonate Suspensions.* Colloids and Surfaces A: Physicochemical and Engineering Aspects, 2003. **229**(1-3): p. 75-83.

139. Chen, S.H. and C.W. Frank, *Infrared and Fluorescence Spectroscopic Studies of Self-Assembled N-Alkanoic Acid Monolayers.* Langmuir, 1989. **5**(4): p. 978-987.

140. Ontko, A.C. and R.J. Angelici, *Effects of Alkyl Chain Length on the Adsorption of n-Alkyl Isocyanides (R-N C) on Gold Powder.* Langmuir, 1998. **14**(7): p. 1684-1691.

141. de Mul, M.N.G., et al., *Solution Phase Behavior and Solid Phase Structure of Long-Chain Sodium Soap Mixtures.* Langmuir, 2000. **16**(22): p. 8276-8284.

142. Spegt, P.A. and A.E. Skoulois, *La structure des colloides d'association. X. Description de la structure des savons de calcium a temperature ordinaire et a temperature elevee.* Acta Crystallographica, 1964. **17**(2): p. 198-207.

143. Heryanto, R., et al., *Solubility of Stearic Acid in Various Organic Solvents and Its Prediction using Non-ideal Solution Models.* ScienceAsia, 2007. **33**: p. 469-472.

144. Sircar, S., *Adsorption of Gases on Heterogeneous Adsorbents.* Journal of the Chemical Society-Faraday Transactions I, 1984. **80**: p. 1101-1111.

145. Palit, S. and J. McBain, *The Solubility of Heavy Metal Soaps in Co-solvent Mixtures of Chloroform and Propylene Glycol.* Journal of the American Oil Chemists' Society, 1947. **24**(6): p. 190-193.

146. Calhoun, A. and E. Chiang, *Determination of the Surface Energetics of Surface Modified Calcium Carbonate using Inverse Gas Chromatography.* Journal of Vinyl & Additive Technology, 2006. **12**(4): p. 174-182.

147. Moczo, J., E. Fekete, and B. Pukanszky, *Acid-base Interactions and Interphase Formation in Particulate-Filled Polymers.* Journal of Adhesion, 2002. **78**(10): p. 861-875.

148. Kontoyannis, C.G. and N.V. Vagenas, *Calcium Carbonate Phase Analysis using XRD and FT-Raman Spectroscopy.* Analyst, 2000. **125**(2): p. 251-255.

149. Mohai, M., *Development and Applications of Quantitative. X-ray Photoelectron Spectroscopy*, in *Institute of Materials and Environmental Chemistry, Chemical Research Center, Hungarian Academy of Sciences*. 2005: Budapest.

150. Schultz, J., L. Lavielle, and C. Martin, *The Role of the Interface in Carbon-Fiber Epoxy Composites.* Journal of Adhesion, 1987. **23**(1): p. 45-60.

151. Dorris, G.M. and D.G. Gray, *Adsorption of Normal-Alkanes at Zero Surface Coverage on Cellulose Paper and Wood Fibers.* Journal of Colloid and Interface Science, 1980. **77**(2): p. 353-362.

152. Gutmann, V., *The Donor-Acceptor Approach to Molecular Interactions*. 1978, New York ; London: Plenum Press. xvi,279p.

153. Riddle, F.L. and F.M. Fowkes, *Spectral Shifts in Acid-Base Chemistry .1. Vanderwaals Contributions to Acceptor Numbers.* Journal of the American Chemical Society, 1990. **112**(9): p. 3259-3264.

154. Papirer, E., J. Kuczynski, and B. Siffert, *Characterization of the Surface-Properties of Heavy Residues of Oil Distillation by Inverse Gas-Chromatography.* Chromatographia, 1987. **23**(6): p. 401-406.

155. Papirer, E., H. Balard, and A. Vidal, *Inverse Gas-Chromatography - a Valuable Method for the Surface Characterization of Fillers for Polymers (Glass-Fibers and Silicas).* European Polymer Journal, 1988. **24**(8): p. 783-790.

156. Bogillo, V.I., V.P. Shkilev, and A. Voelkel, *Chemical Heterogeneity of Metal Oxide Surfaces as Studied by Inverse Gas Chromatography at Finite Concentrations.* Adsorption Science & Technology, 1996. **14**(3): p. 189-198.

157. Rodriguez, M.A., et al., *Application of Inverse Gas Chromatography to the Study of the Surface Properties of Slates.* Clays and Clay Minerals, 1997. **45**(5): p. 670-680.

158. Bosse, F., et al., *Igc Study of Surface-Properties of Adsorbed Styrene Methacrylic-Acid Diblock Polymers.* Journal of Applied Polymer Science, 1994. **51**(3): p. 521-527.

159. Ma, D., et al., *The Effect of Donor-Acceptor Interactions on the Mechanical-Properties of Wood.* Journal of Adhesion Science and Technology, 1990. **4**(5): p. 411-429.

160. Shafrin, E.G. and W.A. Zisman, *Constitutive Relations in the Wetting of Low Energy Surfaces and the Theory of the Retraction. Method of Preparing Method of Preparing Monolayers1*. The Journal of Physical Chemistry, 1960. **64**(5): p. 519-524.

161. Fowkes, F.M., *Attractive Forces at Interfaces.* Industrial & Engineering Chemistry, 1964. **56**(12): p. 40-52.

162. Fowkes, F.M., *Determination of Interfacial Tensions, Contact Angles, and Dispersion Forces in Surfaces by Assuming Additivity of Intermolecular Interactions in Surfaces.* The Journal of Physical Chemistry, 1962. **66**(2): p. 382-382.

163. Jordan, J., et al., *Experimental Trends in Polymer Nanocomposites - a Review.* Materials Science and Engineering a-Structural Materials Properties Microstructure and Processing, 2005. **393**(1-2): p. 1-11.

164. Fu, Q., G. Wang, and J. Shen, *Polyethylene Toughened by $CaCO_3$ Particle Asterisk - Brittle-Ductile Transition of $CaCO_3$-Toughened HDPE.* Journal of Applied Polymer Science, 1993. **49**(4): p. 673-677.

165. Fu, Q. and G.H. Wang, *Polyethylene Toughened by $CaCO_3$ Particles Percolation Model of Brittle-Ductile Transition in HDPE/$CaCO_3$ Blends.* Polymer International, 1993. **30**(3): p. 309-312.

166. Fu, Q. and G.H. Wang, *Effect of Morphology on Brittle-Ductile Transition of HDPE/$CaCO_3$ Blends.* Journal of Applied Polymer Science, 1993. **49**(11): p. 1985-1988.

167. Parsons, E.M., et al., *Three-Dimensional Large-Strain Tensile Deformation of Neat and Calcium Carbonate-Filled High-Density Polyethylene.* Polymer, 2005. **46**(7): p. 2257-2265.

168. Tanniru, M. and R.D.K. Misra, *On Enhanced Impact Strength of Calcium Carbonate-Reinforced High-Density Polyethylene Composites.* Materials Science and Engineering a-Structural Materials Properties Microstructure and Processing, 2005. **405**(1-2): p. 178-193.

169. Borggreve, R.J.M., R.J. Gaymans, and H.M. Eichenwald, *Impact Behavior of Nylon Rubber Blends .6. Influence of Structure on Voiding Processes - Toughening Mechanism.* Polymer, 1989. **30**(1): p. 78-83.

170. Bartczak, Z., et al., *The Morphology and Orientation of Polyethylene in Films of Sub-Micron Thickness Crystallized in Contact with Calcite and Rubber Substrates.* Polymer, 1999. **40**(9): p. 2367-2380.

171. Osman, M.A. and A. Atallah, *Interfacial Adhesion and Composite Viscoelasticity.* Macromolecular Rapid Communications, 2006. **27**(16): p. 1380-1385.

172. Tao, Y.T., *Structural Comparison of Self-Assembled Monolayers of N-Alkanoic Acids on the Surfaces of Silver, Copper, and Aluminum.* Journal of the American Chemical Society, 1993. **115**(10): p. 4350-4358.

173. Osman, M.A. and A. Atallah, *Surfactant Chain Length and Tensile Properties of Calcium Carbonate-Polyethylene Composites.* Macromolecular Chemistry and Physics, 2007. **208**(1): p. 87-93.

174. Sahebian, S., et al., *Effect of both Uncoated and Coated Calcium Carbonate on Fracture Toughness of HDPE/$CaCO_3$ Nanocomposites.* Journal of Applied Polymer Science, 2007. **104**(6): p. 3688-3694.

175. Zhang, L., C.Z. Li, and R. Huang, *Toughness Mechanism in Polypropylene Composites: Polypropylene Toughened with Elastomer and Calcium Carbonate.* Journal of Polymer Science Part B-Polymer Physics, 2004. **42**(9): p. 1656-1662.

176. Jiang, L., B. Liu, and J. Zhang, *Properties of Poly(lactic acid)/Poly(butylene adipate-co-terephthalate)/Nanoparticle Ternary Composites.* Industrial & Engineering Chemistry Research, 2009. **48**(16): p. 7594-7602.

177. Jiang, L., J. Zhang, and M.P. Wolcott, *Comparison of Polylactide/Nano-Sized Calcium Carbonate and Polylactide/Montmorillonite Composites: Reinforcing Effects and Toughening Mechanisms.* Polymer, 2007. **48**(26): p. 7632-7644.

178. Gandini, A., *Polymers from Renewable Resources: A Challenge for the Future of Macromolecular Materials.* Macromolecules, 2008. **41**(24): p. 9491-9504.

179. Ray, S.S. and M. Okamoto, *Biodegradable Polylactide and its Nanocomposites: Opening a New Dimension for Plastics and Composites.* Macromolecular Rapid Communications, 2003. **24**(14): p. 815-840.

180. Avérous, L., *Polylactic Acid: Synthesis, Properties and Applications*, in *Monomers, Polymers and Composites from Renewable Resources*, B. Mohamed Naceur and G. Alessandro, Editors. 2008, Elsevier: Amsterdam. p. 433-450.

181. Bordes, P., E. Pollet, and L. Avérous, *Nano-biocomposites: Biodegradable Polyester/Nanoclay Systems.* Progress in Polymer Science, 2009. **34**(2): p. 125-155.

182. Rasal, R.M., A.V. Janorkar, and D.E. Hirt, *Poly(lactic acid) Modifications.* Progress in Polymer Science, 2010. **35**(3): p. 338-356.

183. Martin, O. and L. Averous, *Poly(lactic acid): Plasticization and Properties of Biodegradable Multiphase Systems.* Polymer, 2001. **42**(14): p. 6209-6219.

184. Piorkowska, E., et al., *Plasticization of Semicrystalline Poly(L-lactide) with Poly(propylene glycol).* Polymer, 2006. **47**(20): p. 7178-7188.

185. Kulinski, Z. and E. Piorkowska, *Crystallization, Structure and Properties of Plasticized Poly(L-lactide).* Polymer, 2005. **46**(23): p. 10290-10300.

186. Takagi, Y., et al., *Morphologies and Mechanical Properties of Polylactide Blends with Medium Chain Length Poly(3-hydroxyalkanoate) and Chemically Modified Poly(3-hydroxyalkanoate).* Journal of Applied Polymer Science, 2004. **93**(5): p. 2363-2369.

187. Broz, M.E., D.L. VanderHart, and N.R. Washburn, *Structure and Mechanical Properties of Poly(D,L-lactic acid)/Poly(epsilon-caprolactone) Blends.* Biomaterials, 2003. **24**(23): p. 4181-4190.

188. Pluta, M., J.K. Jeszka, and G. Boiteux, *Polylactide/Montmorillonite Nanocomposites: Structure, Dielectric, Viscoelastic and Thermal Properties.* European Polymer Journal, 2007. **43**(7): p. 2819-2835.

189. Oksman, K., M. Skrifvars, and J.F. Selin, *Natural Fibres as Reinforcement in Polylactic Acid (PLA) Composites.* Composites Science and Technology, 2003. **63**(9): p. 1317-1324.

190. Balakrishnan, H., et al., *Novel Toughened Polylactic Acid Nanocomposite: Mechanical, Thermal and Morphological Properties.* Materials & Design, 2010. **31**(7): p. 3289-3298.

191. Kolstad, J.J., *Crystallization Kinetics of Poly(L-lactide-co-meso-lactide).* Journal of Applied Polymer Science, 1996. **62**(7): p. 1079-1091.

192. Joussein, E., et al., *Halloysite Clay Minerals - A review.* Clay Minerals, 2005. **40**(4): p. 383-426.

193. Lecouvet, B., et al., *Structure-Property Relationships in Polyamide 12/Halloysite Nanotube Nanocomposites.* Polymer Degradation and Stability, 2011. **96**(2): p. 226-235.

194. Xu, Z.H., et al., *Morphology, Rheology and Crystallization Behavior of Polylactide Composites Prepared through Addition of Five-armed Star Polylactide Grafted Multiwalled Carbon Nanotubes.* Polymer, 2010. **51**(3): p. 730-737.

195. Murariu, M., et al., *Polylactide (PLA)-$CaSO_4$ Composites Toughened with Low Molecular Weight and Polymeric Ester-like Plasticizers and Related Performances.* European Polymer Journal, 2008. **44**(11): p. 3842-3852.

196. Papageorgiou, G.Z., et al., *PLA nanocomposites: Effect of Filler Type on Non-isothermal Crystallization.* Thermochimica Acta, 2010. **511**(1-2): p. 129-139.

197. Petersson, L. and K. Oksman, *Biopolymer Based Nanocomposites: Comparing Layered Silicates and Microcrystalline Cellulose as Nanoreinforcement.* Composites Science and Technology, 2006. **66**(13): p. 2187-2196.

198. Pluta, M., *Morphology and Properties of Polylactide Modified by Thermal Treatment, Filling with Layered Silicates and Plasticization.* Polymer, 2004. **45**(24): p. 8239-8251.

199. Molnar, K., et al., *Factors Affecting the Properties of PLA/$CaSO_4$ Composites: Homogeneity and Interactions.* Express Polymer Letters, 2009. **3**(1): p. 49-61.

200. Mahboobeh, E., et al., *Flexibility Improvement of Poly(lactic acid) by Stearate-Modified Layered Double Hydroxide.* Journal of Applied Polymer Science, 2010. **118**(2): p. 1077-1083.

201. Nampoothiri, K.M., N.R. Nair, and R.P. John, *An Overview of the Recent Developments in Polylactide (PLA) Research.* Bioresource Technology, 2010. **101**(22): p. 8493-8501.

202. Harris, A.M. and E.C. Lee, *Improving Mechanical Performance of Injection Molded PLA by Controlling Crystallinity.* Journal of Applied Polymer Science, 2008. **107**(4): p. 2246-2255.

203. Anderson, K.S. and M.A. Hillmyer, *Melt Preparation and Nucleation Efficiency of Polylactide Stereocomplex Crystallites.* Polymer, 2006. **47**(6): p. 2030-2035.

204. Schmidt, S.C. and M.A. Hillmyer, *Polylactide Stereocomplex Crystallites as Nucleating Agents for Isotactic Polylactide.* Journal of Polymer Science Part B-Polymer Physics, 2001. **39**(3): p. 300-313.

205. Tsuji, H., H. Takai, and S.K. Saha, *Isothermal and Non-Isothermal Crystallization Behavior of Poly(L-lactic acid): Effects of Stereocomplex as Nucleating Agent.* Polymer, 2006. **47**(15): p. 5430-5430.

206. Liu, M.X., et al., *Halloysite Nanotubes as a Novel Beta-Nucleating Agent for Isotactic polypropylene.* Polymer, 2009. **50**(13): p. 3022-3030.

207. Lee, S.-H., S. Wang, and Y. Teramoto, *Isothermal Crystallization Behavior of Hybrid Biocomposite Consisting of Regenerated Cellulose Fiber, Clay, and Poly(lactic acid).* Journal of Applied Polymer Science, 2008. **108**(2): p. 870-875.

208. Li, H.B. and M.A. Huneault, *Effect of Nucleation and Plasticization on the Crystallization of Poly(lactic acid).* Polymer, 2007. **48**(23): p. 6855-6866.

209. Fischer, E.W., H.J. Sterzel, and G. Wegner, *Investigation of the Structure of Solution Grown Crystals of Lactide Copolymers by Means of Chemical Reactions.* Colloid & Polymer Science, 1973. **251**(11): p. 980-990.

210. Li, J., et al., *Isothermal Crystallization Kinetics and Melting Behavior of Multiwalled Carbon Nanotubes/Polyamide-6 Composites.* Journal of Applied Polymer Science, 2007. **105**(6): p. 3531-3542.

211. Qiu, J., et al., *New Insights into the Multiple Melting Behaviors of the Semicrystalline Ethylene-Hexene Copolymer: Origins of Quintuple Melting Peaks.* Journal of Polymer Science Part B-Polymer Physics, 2008. **46**(19): p. 2100-2115.

Acknowledgement

First and foremost I am heartily thankful to my supervisor, Prof. Andrea Lazzeri, whose encouragement, guidance and support from the initial to the final level during this thesis. I would like to thank the precious offer from Prof. Lazzeri to fulfill my PhD in the Department of Chemical Engineering, Industrial Chemistry and Materials Science of Pisa University. I also appreciated his supervision during the last three years towards to the scientific way of thinking and researching. The thesis would not be possible without his contributions of time, ideas and funding to my PhD study. He also shows me the enthusiasm for doing research work in some tough time and I am thankful for the excellent example he provides to me as a successful professor.

Special thanks to Prof. Béla Pukánszky from Laboratory of Plastics and Rubber Technology in Department of Physical Chemistry and Materials Science of Budapest University of Technology and Economics. The same sincere thankfulness to Prof. Imre Bertóti from Institute of Materials and Environmental Chemistry, Chemical Research Center of the Hungarian Academy of Sciences. I appreciate my experience in Budapest and the training from both professors. I would like to thank Dr. Roberto Rosa, from TechDesign in Ranco for his contribution to this thesis and particularly for the information on the industrial technology for preparation of PCC particles and their coating.

I am grateful to all my colleagues in the Multifunctional, Bio-Ecocompatible Materials Laboratory. Thanks to the technician Irene Anguillesi for teaching me about the laboratorial skills and kinds of instruments. Thanks to Dr. Patrizia Cinelli, Dott.sa Letizia Bachechi, Ing. Thanh Vu Phuong, Dott.sa Fabia Galantini, Ing. Silvia Farsetti, Ing. Enrico Galli for the time working collaboratively in the laboratory. They are so nice to me making the life in Pisa much easier.

I gratefully acknowledge the funding sources that made my Ph.D. work possible from China Scholarship Council and the support from FP7–KBBE project n° 212239 Forbioplast (Forest Resource Sustainability through Bio-Based Composite Development). I also want to show my gratitude to my former university, Northwestern Polytechnic University in Xi’an, for offering me a teaching position to continue research work in the future.

My time in Pisa was enjoyable in large part due to my many friends and my roommates. Special thanks to Chen fang, who always supports me in some tough time.

I would also like to thanks my parents, my younger brother and all my family members to support me for the three years study outside of China.

Publication List

Publications:

Xuetao Shi, Roberto Rosa and Andrea Lazzeri [*]. On the Coating of Precipitated Calcium Carbonate with Stearic Acid in Aqueous Medium. ***Langmuir***, 2010, *26* (11), 8474–8482.

Xuetao Shi, Imre Bertóti, Béla Pukánszky, Roberto Rosa, Andrea Lazzeri[*]. Structure and Coverage of Water-based Stearate Coatings on Calcium Carbonate Nanoparticles. Submitted to *Journal of Colloid and Interface Science*.

Xuetao Shi, Enrico Galli, Cristina Siligardi, Andrea Lazzeri[*]. Comparison of Polylactic Acid/ Nano Precipitated Calcium Carbonate and Polylactic Acid/ Halloysite composites. Finished and planned to submit *to The Journal of Applied Polymer Science.*

Xuetao Shi, Andrea Lazzeri[*]. Effect of surface coating of precipitated calcium carbonate on the mechanical properties of polymeric nanocomposites. Submitted to *RFP Rubber Fibres Plastics International.*

A. Lazzeri[*]**, X. Shi,** R. Rosa, G. Ramorino, L. Conzatti. Filler Toughening of Plastics. Part 2 – The Effect of Surface Interactions on Morphology and Fracture Behavior of Ultrafine $CaCO_3$/High Density Polyethylene Nanocomposites. Preparing paper for the journal *Polymer*.

Conferences:

X. T. Shi, B. Cioni and A. Lazzeri*. Surface Characterization of Precipitated Calcium Carbonate Coated with Stearic Acid. *7th Eurofillers international Conference*, Alessandria, Italy, 21-25th June, 2009.

Xuetao Shi, Andrea Lazzeri*. Determination of Surface Coating Coverage of Precipitated Calcium carbonate Nano-particles Coated in Aqueous Medium. *6th International ECNP conference on Nanostructured Polymers and Nanocomposites*, Madrid, Spain, 28-30th April, 2010.

X. T. Shi, I. Bertoti, A. Lazzeri[*]. Surface Energy Characterization of Nano Calcium Carbonate Fillers Coated with Stearic Acid in Aqueous Medium. *14th International Conference on "Polymer Materials"*, Halle, Germany, 15-19th September, 2010.

Xuetao Shi, Enrico Galli, Cristina Siligardi, Andrea Lazzeri[*]. Comparison of Polylactic Acid/ Nano Precipitated Calcium Carbonate and Polylactic Acid/ Halloysite composites. *4th Conference on Polymer Behavior-IUPAC*, Lodz, Poland, 20-23th, September, 2010.